Effect of Counterion and Solvent on the Self-Assembly of Perfluorocarbon Surfactants.

Scott Jonathan Thomsen

Department of Chemistry
Massey University
New Zealand

Submitted in accordance with the requirements for the degree of Doctor of Philosophy

February 1998

Addenda

p 57 The rod charge density ν is the effective charge per unit length of cylindrical micelle.

p 77 In equation [4-1] the square brackets [ ] denote the concentration in moles per litre of solution. In equilibrium constant expressions, *e.g.* equation [4-9] the square brackets denote a dimensionless number which is the molar concentration divided by the standard state concentration of 1 mole per litre.

p 77 Figure 5.5 should read Figure 4.5

p 86 In equation [4-11] and thereafter, the free energy ΔG_s° represents the free energy change with respect to a standard state in which concentrations are expressed as mole fractions

p 97 10 lines from bottom, $s_{n,app}$ should read $s_{w,app}$.

p 136 Figure 5.1 should read Figure 5.8

Abstract.

This work investigates the effects of changing the counterion and the solvent on the self-assembly and self-organisation of anionic perfluorocarbon surfactants. Specifically, the following investigations were carried out:

- The concentration dependence of the rheological behaviour of tetraethyl- and tetramethylammonium perfluorononanoate/H_2O has been examined. The behaviour at intermediate concentrations is consistent with solutions of very long and entangled self-assembled rodlike micelles which is not observed in systems with unalkylated ammonium ions as counterions. At higher surfactant concentrations their rheological behaviour suggests that the rodlengths go through a maximum. At higher concentrations still the systems exhibit liquid crystalline phase behaviour which is consistent with the presence of discotic micelles i.e. a rod-to-disk transition must occur.

- The effects of substituting D_2O for H_2O, and ethylene glycol (EG) for H_2O, on the self-assembly of ammonium perfluorooctanoate (APFO) has been examined by variations in the electrical conductivity of their solutions as functions of temperature and surfactant concentration. The effect of substituting EG/H_2O mixtures for H_2O on APFO micellisation at 298 K was also examined. The results were interpreted within a phenomenological statistical thermodynamic model which showed that differences in self-assembly arise largely from modification of the solution/fluorocarbon interfacial tension.

- The effects of changing the solvent from water to mixtures of water and the cosolvents formamide (FA), ethylene glycol (EG), *N*-methylformamide (NMF), *N,N*-dimethylformamide (DMF), and *N,N*-dimethylacetamide (DMA) on the phase behaviour of the micellar liquid crystal caesium perfluorooctanoate (CsPFO)/D_2O have been investigated using ^{133}Cs and ^{2}H NMR. With increasing concentration of cosolvent the isotropic I - to - discotic nematic N_D and N_D - to - smectic L sequences of transitions are displaced to lower temperatures, but the general phase behaviour is conserved. The efficacy of the cosolvents in depressing the phase transition temperatures parallels the order of their effect on the solution/fluorocarbon interfacial tension i.e. DMA>DMF>NMF>EG>FA. Measurement of the ^{2}H quadrupole splittings of D_2O reveal that increasing the cosolvent concentration at constant temperature results in a concomitant decrease in micelle size but the axial ratios of the discotic micelles have essentially singular values at both the I - to - N_D and N_D - to - L transitions. The effect of cosolvent on the phase transition temperatures can be qualitatively understood in terms of phase transitions driven by hard particle interactions and, separately, modifications in the micelle self assembly as a consequence

of changes in the solution/fluorocarbon interfacial tension with the addition of cosolvent.

- The effects of the cosolvents on the micellar size of APFO/H_2O at high surfactant concentration have been investigated by small angle x-ray diffraction (SAXS) and have also been shown to arise from changes in the solution/fluorocarbon interfacial tension.

Contents.

List of Symbols.

a	average headgroup area
α	free counterion fraction
A	area
β	bound ion ion fraction
c	molar concentration
χ	nuclear quadrupole coupling constant (or Flory interaction parameter)
δ	surfactant headgroup radius
ε	relative permittivity
ϕ	volume fraction
γ	surface or interfacial tension (or strain in Chapter 3 only)
G	electrical conductance (or stress relaxation modulus in Chapter 3 only)
η	viscosity
κ	conductivity
λ	ionic conductivity at infinite dilution
L	micelle long-axis length scale
Λ	molar ionic conductivity
m	molal concentration (or dipole moment)
r	radius
R	hydrophobic chainlength
s	surfactant aggregation number
σ	stress
t	time
τ	terminal relaxation time
u	electrophoretic mobility
v, V	volume
w	weight fraction of *surfactant only*
x	mole fraction
ξ	meshsize

List of Abbreviations

12-2-12	ethanediyl-α,ω-bis(dodecyldimethylammonium bromide)
CTAB	cetyltrimethylammonium bromide
DMA	*N*,*N*-dimethylacetamide
DMF	*N*,*N*-dimethylformamide
DTAB	dodecyltrimethylammonium bromide
EG	ethylene glycol
FA	formamide
HFN	heptadecafluorononanoate ion
NMF	*N*-methylformamide
NMR	nuclear magnetic resonance
PFO	pentadecafluorooctanoate ion
POS	perfluorooctanesulphonate ion
SAM	self-assembled perfluorocarbon monolayer
SANS	small-angle neutron scattering
SAXS	small-angle x-ray scattering
SDS	sodium dodecylsulphate
TAA	tetraalkylammonium ion
TEA	tetraethylammonium ion
TMA	tetramethylammonium ion
TPA	tetrapropylammonium ion
W	water (H_2O)

Acknowledgements.

My sincere thanks go to Associate Professor Ken Jolley for his guidance, generosity, good humour, patience and persistence.

My special thanks go to my family, especially my parents, Neville and Jennifer Thomsen, Silver Range, Elsthorpe.

I am grateful to, in no particular order, Assoc. Prof. Gavin Hedwig, Dr Pat Edwards, Dr Mark Smith, Dr Ashok Parbhu, Dr Richard Harding (Leeds), Prof. Andrew Brodie and Prof. Neville Boden (Leeds).

I thank the technical staff at Massey University: the Electronics Workshop, Science Workshop, and the Glass Blower, Mr Grant Platt.

My thanks go to my past and present flatmates for their support, especially Messrs Alton McDonald, Brendan Stevenson and Robert Blathwayt.

Finally, I wish to thank Kristine Jowett.

1. Introduction.

This thesis concerns the equilibrium behaviour of perfluoroalkylcarboxylate surfactants[†] in water and other polar solvents, with a focus on the role of interfacial tension in determining their self-assembly.

Perfluorinated surfactants have several advantages for study since they possess properties that circumvent complexities associated with their hydrocarbon counterparts. The perfluorocarbon chain is not only hydrophobic but solvophobic in general, and furthermore, it can be considered to be lyophobic, as shown[1] by the ability of molecules possessing both fluorocarbon and hydrocarbon portions to act as surfactants in a hydrocarbon solvent. From a theoretical standpoint, they are simpler to model since the configurational entropy of the hydrophobe may be considered to be negligible at "normal" temperatures, owing to the steric hindrance to carbon-carbon bond rotation introduced by the substitution of comparatively large fluorine atoms for hydrogen atoms. They are generally resistant to biological, chemical and thermal decomposition, which allows them to be studied and applied under conditions where hydrocarbon surfactants cannot. In view of their attractiveness for study, it is surprising that the volume of published work concerning them has only recently (in the past two decades) become significant. The first "stand alone" text[2] devoted to fluorinated surfactants was published a mere four years ago. Table 1.1 summarises published experimental studies concerning the effect of various perturbations on the self-assembly and self-organisation of perfluoroalkylcarboxylate surfactant systems. Theoretical treatments of perfluorinated surfactant self-assembly are conspicuously absent from the literature.

Table 1.1 Summary of published studies on perturbations to perfluoro-alkylcarboxylate surfactant systems.

Perturbation	References
Salt	3-12
Counterion	6, 12-22
Chainlength	12, 20, 22-28
Pressure	29
Water Isotope effect	30, 31
Solvent	32-34

At low concentrations, ionic surfactants dissolve to form molecular solutions. However, at constant temperature and pressure, as concentration is increased, it becomes favourable for surfactant molecules to self-assemble into aggregates or

[†] The word *surfactant* is a contraction of the term *surface active agent* and describes molecules that have chemically bonded parts that "prefer" different physical environments e.g. dissolved in water or dissolved in oil. Hence the origin of the synonym *amphiphile* (Gr. *amphi*, both + *philos*, liking).

micelles where the solvophobic chains orient themselves so as to maximise contact with other chains and minimise contact with the solvent. In water, the concentration range over which this occurs is very narrow and it is possible to define a *critical micelle concentration* (cmc). The micelle formed is a dynamic entity with surfactant molecules in solution undergoing rapid exchange with those in a micelle with mean lifetimes varying from 10^{-1} s for nonionic perfluorocarbon surfactants[14] to 10^{-6} s for ionic perfluorocarbon surfactants with alkali metal and ammonium counterions[14-17]. Interestingly, ionic surfactant exchange is affected by the counterion; the substitution of tetraalkylammonium ions for ammonium ions slows surfactant lifetimes by 1-2 orders of magnitude[15-17]. Counterions are radially distributed about the micelle as a consequence of the competition between the entropy of mixing and the predominantly electrostatic interaction with the electric field gradient created by the surfactant headgroups at the micelle surface (where the charge density is a maximum). Counterions can be considered to be "bound" to the surface with, for alkali metal ions[35], mean lifetimes from 10^{-7} s to 10^{-8} s. Water molecules[36] have mean lifetimes at the micelle surface from 10^{-8} s to 10^{-9} s. In addition, surfactant molecules are rapidly diffusing within the micelle, and water and counterions are rapidly diffusing around the micelle surface. As a consequence of this dynamic nature, the micelle/solvent interface is constantly fluctuating and "rough"[35, 37], with surfactant molecules protruding above it. However, in order to model surfactant self-assembly, it is convenient to assume "idealised" micelle geometries e.g. spherical, ellipsoidal, spherocylindrical (rodlike), discotic, closed (vesicular) or planar (lamellar) bilayer geometries. The geometry adopted by a surfactant is determined by the molecule's "preferred curvature", which is a maximum in spherical geometry and a minimum in a planar bilayer. The preferred curvature is determined by the following combination of surfactant- and solvent-dependent factors:

(i) the surfactant chain length and radius,

(ii) surfactant chain conformational freedom (restricted in fluorocarbons),

(iii) whether the surfactant is singly- or doubly-chained,

(iv) the headgroup charge (smaller in magnitude in fluorocarbon surfactants compared to hydrocarbon surfactants),

(v) the headgroup size,

(vi) the nature of the counterion*,

(vii) surfactant concentration, which affects both the solution ionic strength and whether intermicellar interactions are significant (the latter are assumed absent at cmc concentrations),

---

* factors varied in this work.

(viii) surfactant chain/solvent interfacial tension*, and

(ix) solvent relative permittivity*.

Figure 1.1 shows a possible evolution of micelle geometries with increasing surfactant concentration. Past the cmc, hydrocarbon surfactants can assume a spherical geometry with a radius that can be less than the extended length of the hydrophobic chain since the chain rearranges itself to conformations that fill the sphere volume. However, perfluorocarbon surfactants have restricted chain conformational freedom and can form spherical micelles with a radius determined by their hydrophobic chain's extended length. This may not coincide with the geometry that minimises unfavourable solvent-surfactant interactions and, in this case, another geometry must be adopted. The only two possibilities that allow for micelles of greater aggregation number are the formation of prolate (step A) or oblate (step B) ellipsoidal geometries. Prolate ellipsoids can be thought of as a precursor to the rodlike micelle formed from the addition of monomers to a cylindrical middle portion (the micelle "body") between hemispherical endcaps, and oblate ellipsoids can be viewed as the precursor to the discotic micelle formed from addition of monomer to a cylindrical bilayer enclosed by a semi-toroidal rim. Experimental evidence[38, 39] suggests that fluorocarbon surfactants should be modelled at the cmc by a prolate ellipsoidal geometry over an oblate one.

Increasing surfactant concentration causes micelles to grow, and in the case of rodlike micelles, where the growth is one-dimensional, the rodlength is governed by the competition between entropy, which favours short rods, and the energy difference between surfactant molecules in the cylindrical body and those in the endcaps. The energy difference is independent of rodlength since, once the endcaps have formed, there is no energy cost for the insertion of another surfactant molecule into the body. If the energy difference is large, very long rodlike micelles form. An increase in this energy difference, which can arise either by the energy of surfactant molecules in the body to be lowered or by the energy of surfactant molecules in the endcaps to be raised (or both), will be shown to occur in Chapter 3 by the substitution of tetramethylammonium (TMA^+) and tetraethylammonium (TEA^+) ions for ammonium ions as counterions to the heptadecafluorononanoate (HFN^-) ion in water. When the rods are very long they become flexible and can entangle. Solutions of very long and entangled self-assembled rods exhibit properties similar to conventional polymers in solution e.g. they are viscoelastic, and due to their dynamic nature, have been termed *equilibrium polymers*. The viscoelastic behaviour of aqueous solutions of TMAHFN and TEAHFN as a function of surfactant concentration will be presented in this Chapter and interpreted within the equilibrium polymer theory formulated by Cates *et al*[40, 41] and their model modified[42, 43] to include the role of electrostatics.

Figure 1.1 Micellisation and the evolution of micelle size with surfactant concentration. See text for details.

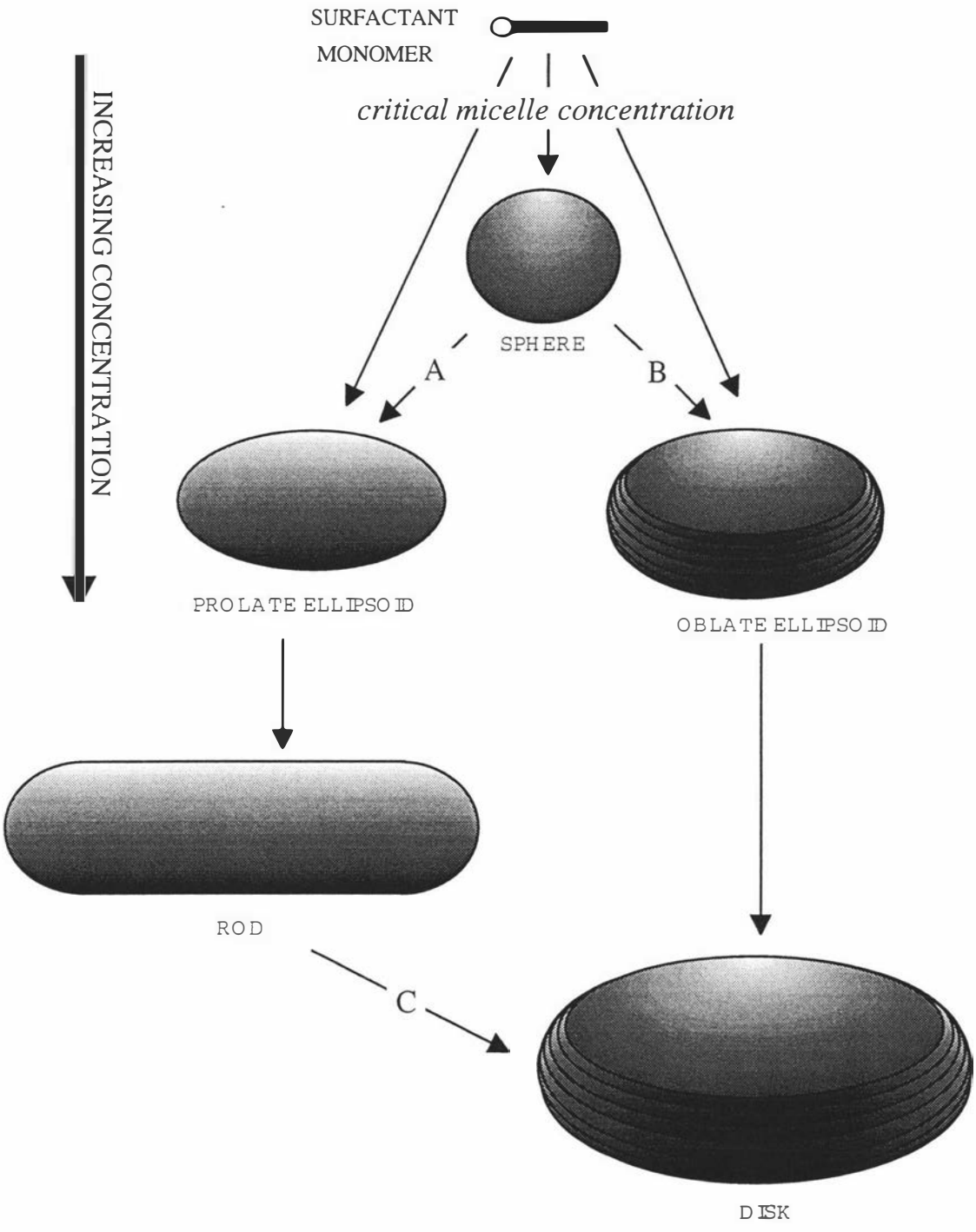

Interestingly, nuclear magnetic resonance (NMR)[44], small angle x-ray scattering (SAXS), and small angle neutron scattering (SANS)[45, 46] evidence has shown that at higher surfactant concentration the TMAHFN/D_2O system[44] (see Figure 1.2) forms ordered phases consisting of relatively small discotic micelles.

Figure 1.2 Partial phase diagram for the TMAHFN/D_2O system[44]. Nomenclature: cmc; critical micelle concentration; *I*, isotropic micellar solution phase; N_D, nematic phase with discotic micelles; *L*, lamellar phase; *K*, crystal; *T*p(*I*,*N*,*L*), the isotropic micellar solution-nematic-lamellar triple point; *T*p(*I*,*N*,*K*), the isotropic micellar solution-nematic-crystal triple point; *C*ep, the critical endpoint; *T*cp, the lamellar-nematic tricritical point; *T*c, the solubility curve. The isotherm along which rheological measurements were made is also shown.

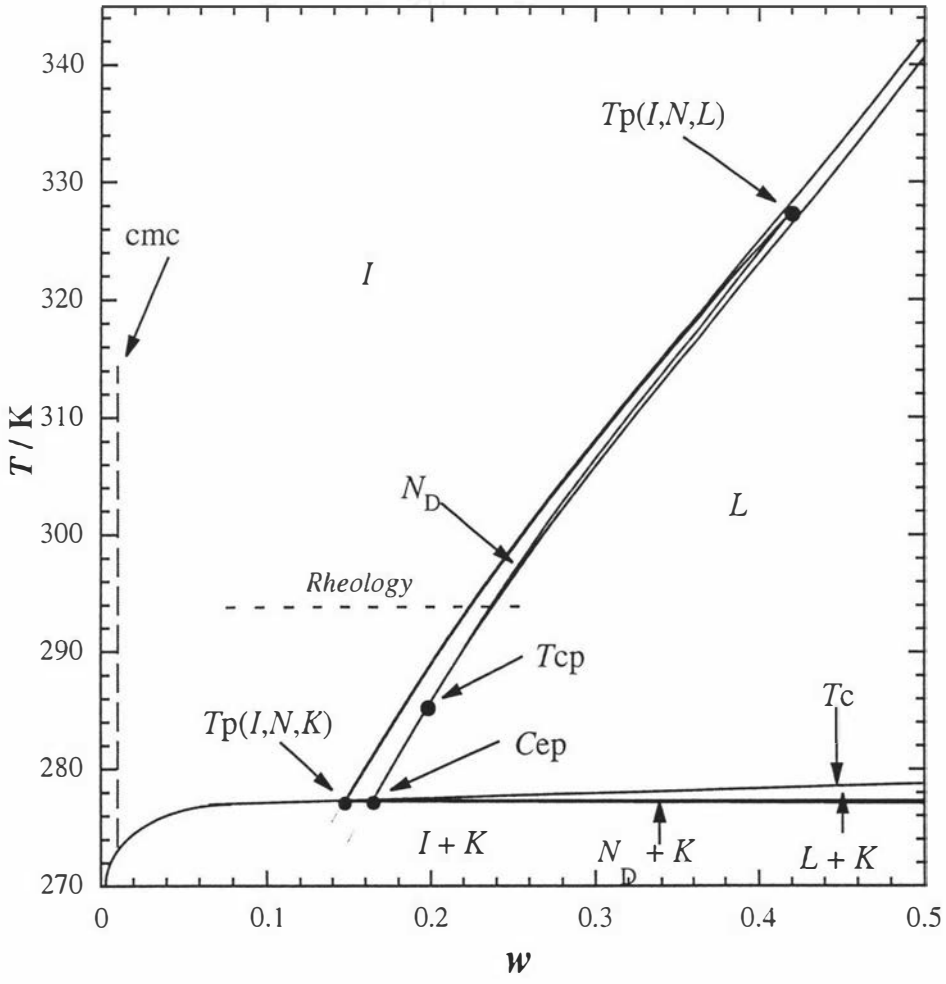

Israelachvili *et al*[47] argued that the existence of small discotic micelles was theoretically impossible, with two-dimensional aggregation necessarily leading to the formation of an infinite planar bilayer. An explanation for the stability of discotic micelles with respect to an infinite bilayer was first proposed by McMullen *et al*[48] who showed that small discotic micelles can be stable providing the energy of the surfactant in the semi-toroidal rim is only slightly greater than that in the oblate right-cylindrical body so that the entropy of mixing suppresses their explosive growth into infinite bilayers. Furthermore, Granek *et al*[49] have shown that it is possible to obtain discotic micellar liquid crystal phases with wide stability by introducing a curvature dependent "line tension" which includes a preferred ("spontaneous") curvature for the rim. Thus, for two-dimensional self-assembly there are good theoretical arguments to account for the stability of systems comprised of discotic micelles and for the existence of discotic-liquid-crystalline mesophases. However, current theories do not predict the rod-to-disk transition (step C in Figure 1.1) that must occur at, or before, the concentration at which the transition to ordered phases occurs in the TMAHFN/water system. That the rod-to-disk transition appears to be common to other binary perfluorocarbon surfactant/water systems can be inferred from SAXS[38] and SANS[39] measurements on the ammonium pentadecafluorooctanoate (APFO)/H_2O/NH_4Cl system. The addition of salt to the APFO/H_2O system allowed the detection of rodlike micelles since the effect of salt is to promote an increase in rodlength[42, 43, 51]. Similarly to the TMAHFN/water system, at higher APFO concentrations, in both the presence[3, 8] and absence[31, 52] of salt, the APFO/H_2O system shows liquid crystal phases characterised by ordered phases of discotic micelles. Brandao[38] also showed that, under the conditions of low temperature, low APFO concentration, and high NH_4Cl concentration, APFO/H_2O/NH_4Cl solutions separate into a dilute phase of rods and a concentrated phase of disks.

Chapter 4 examines the effect of changing the solvent on the micellisation of APFO. The experimental study of surfactant micellisation in solvents other than H_2O is receiving increasing attention in literature since the substitution probes the factors that govern the size and shape of micelles presented above. Table 1.2 summarises published studies of cmc's and liquid crystal phases in selected pure solvents or their aqueous mixtures along with relevant pure solvent physical properties.

Interestingly, the substitution of D_2O for H_2O was shown[30] to shift the temperature dependence of CsPFO cmc's to higher temperatures, whereas the same substitution has the *opposite* effect on hydrocarbon surfactant micellisation.

Table 1.2 Summary of published studies on cmc's and liquid crystals of surfactants in non-aqueous solvents or aqueous solvent mixtures. Relevant pure solvent physical properties were obtained from the references listed and are at 298 K for relative permittivities and at 295 K for surface tensions. References to aqueous systems are too numerous to include.

	cmc's	liquid crystals	ε	γ / mJ m^{-2}
H_2O	-	-	78.4	72.5
D_2O	30, 58, 64	-	77.9	72.1
Formamide (FA)	59, 65-72	73-83	109.1	58.2
Ethylene glycol (EG)	33, 84-90	74, 75, 82, 91, 92	37.7	47.7
N-methylformamide (NMF)	65, 72	75, 82, 93	182.4	40.1
N,N-dimethylformamide (DMF)	63, 72, 94, 95	75	36.7	36.8
N,N-dimethylacetamide (DMA)	65, 72	no refs	37.8	32.4
Acetamide	59, 96	no refs	41.1	39.0
Urea	53-63	no refs	n/a	n/a
Glycerol	58, 65, 88	82	42.5	63.4
Hydrazine	97, 98	no refs	51.7	66.7
Ethylammonium nitrate	no refs	99	∞	46.0
N-methylsydnone	no refs	75, 77	144	57
Ethanol	33, 53, 63, 100, 101	no refs	24.3	22.8

Previous non-aqueous solvent studies have generally concerned solvents of high relative permittivity and/or high surface tension and they have almost exclusively concerned hydrocarbon surfactants. Many of these studies have superficially attempted to correlate variations in solvent properties with the variation in cmc's values. However, only one approach, that by Nagarajan[86, 87, 102, 103], has attempted to interpret hydrocarbon surfactant cmc variation with changes in solvent within a phenomenological statistical thermodynamic model for surfactant self-assembly. Phenomenological models attempt to quantify the factors presented above that govern the "preferred curvature" of a surfactant molecule in a micelle as a function of the micelle aggregation number *s* in order to predict *a priori* the cmc's and optimum values of *s*. Theoretical interpretations concerning hydrocarbon surfactant self-assembly in non-aqueous solvents suffer from the possible invalidity of the assumption of non-solubilisation of the solvent within the micelle. However, in view of the lyophobicity of perfluorocarbons, this assumption can be made with confidence for perfluorocarbon surfactants. No phenomenological models exist specifically for perfluorocarbon surfactant self-assembly but Chapter 4 adapts Nagarajan's theory to model the micellisation of the APFO/H_2O, APFO/EG and APFO/EG/H_2O systems. Ethylene glycol was chosen in this study because it is the only solvent among 17 non-aqueous solvents examined[91] in which liquid crystal phases of APFO have been observed.

They were only observable by supercooling $w > 0.65$ APFO/EG solutions to low temperatures < 250 K.

Chapter 5 examines the effect of several cosolvents on surfactant self-assembly at high surfactant concentrations by two methods: nuclear magnetic resonance (NMR) and small angle x-ray diffraction (SAXS). NMR gives a measure of micelle size *via* the variation of ^{2}H quadrupole splittings in liquid crystal phases. The liquid crystal phases of perfluorocarbon surfactants have been well studied and it has been shown[30, 104-109] that, generally, at high concentration, salts of short chain perfluorocarboxylic acids form solutions of discotic micelles which are stable over wide concentration and temperature intervals. With increasing concentration the discotic micelles undergo a sequence of disorder-order transitions from the isotropic phase *I* to form, first, a nematic phase and, subsequently, a smectic lamellar phase[30, 52, 104] (see Figure 1.3).

Figure 1.3 Partial phase diagram for the CsPFO/D_2O system[104]. Nomenclature: *I*, isotropic micellar solution phase; N_D, nematic phase with discotic micelles; *L*, lamellar phase; *K*, crystal; *T*p(*I*,*N*,*L*), the isotropic micellar solution-nematic-lamellar triple point; *T*p(*I*,*N*,*K*), the isotropic micellar solution-nematic-crystal triple point; *C*ep, the critical endpoint; *T*cp, the lamellar-nematic tricritical point; *T*c, the solubility curve. The isopleth along which NMR measurements were made is also shown.

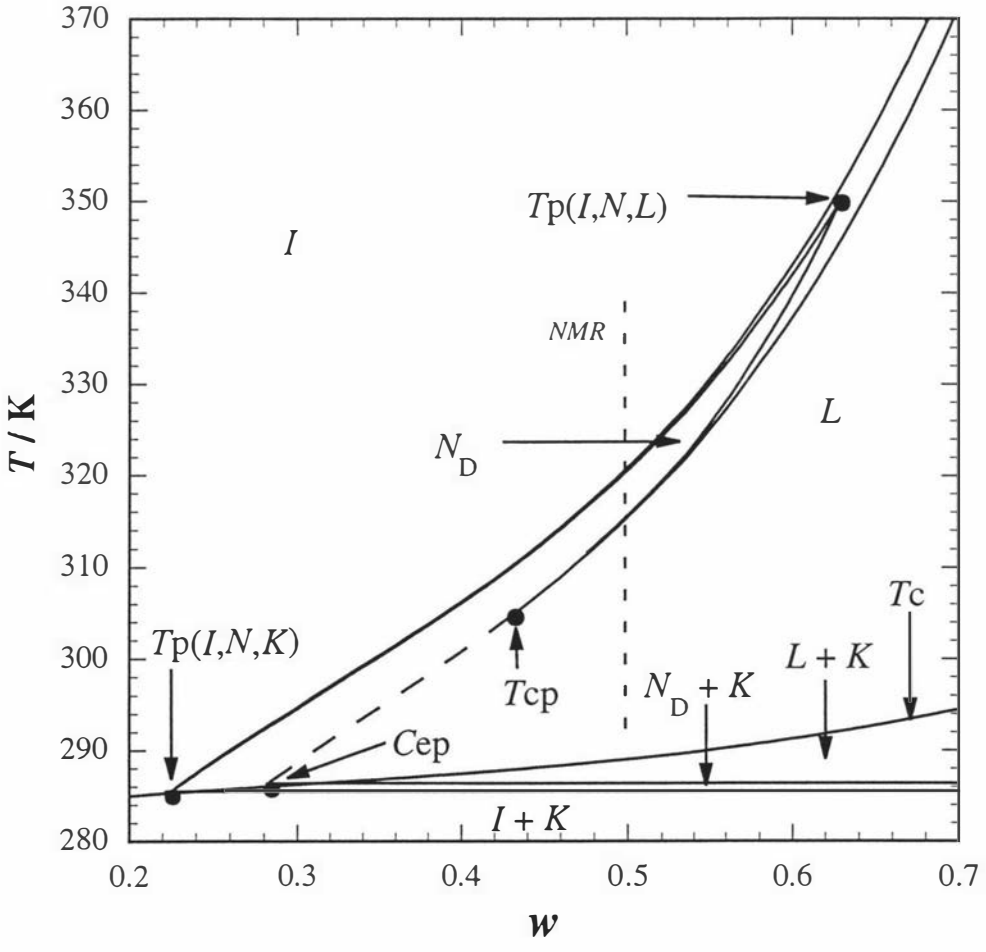

The nematic phase N_D is characterised by long-range correlations in the orientation of the symmetry axes of the micelles. At low concentrations, where the N_D-to-L phase transition is apparently second order, the first-formed lamellar phase is a smectic-A-like state comprised of micelles arranged on equidistant planes[105, 110]. In a recent study[23] of the surfactant systems $CF_3(CF_2)_nCOO^-Cs^+$ (n = 5-8)/D_2O it was shown that increasing n results in a progressive displacement of the phase transitions to higher temperatures, and that the behaviour of all the surfactant systems can be represented on a universal phase diagram in reduced temperature T *vs* volume fraction ϕ co-ordinates. This result was explained in terms of phase transitions which were driven by hard particle interactions between discotic micelles and changes in micellar self-assembly, that is, in micelle size, brought about by changes in the value of n. In the above study, the effect of chain length on the micelle self-assembly was exposed simply by measuring the I - to - N_D transition temperature T_{IN} at a given surfactant volume fraction, that is, an increase in transition temperature signals larger micelles and *vice verca*. In the present study, this method has been used to investigate how the presence of cosolvent affects the size of micelles. Specifically, the effect of the addition of small amounts of formamide (FA), *N*-methylformamide (NMF), ethylene glycol (EG), *N,N*-dimethylformamide (DMF) and *N,N*-dimethylacetamide (DMA) on the phase behaviour and self-assembly of the w = 0.5 CsPFO/D_2O system will be examined.

SAXS was used to obtain a direct measure of a micelle size variation with increasing cosolvent concentration. However, aqueous CsPFO solutions are not amenable to SAXS study owing to the strong absorption of x-rays by the heavy Cs^+ atom. The very similar APFO/H_2O system[31] shown in Figure 1.4 does not suffer this drawback and thus the strategy employed was to examine the effect on the w = 0.5 APFO/H_2O system at temperatures just higher than the I - to - N_D transition temperature T_{IN} i.e. in the isotropic phase. The cosolvents examined have widely different relative permittivities and surface tensions and are all miscible with water. It will be shown that the effect of addition of cosolvent is to dramatically suppress both the I - to - N_D and N_D -to -L transitions which will be explained in terms of the effect of cosolvent on the solvent/micelle interfacial tension.

In order to discuss the role of interfacial tension in self-assembly, measurements of the interfacial tension between solvent mixtures and a self-assembled perfluorocarbon monolayer were conducted and the results are presented in Chapter 6 along with a novel method for estimating these interfacial tensions from known data.

Experimental details and a description of an automated conductivity and NMR data acquisition system developed specifically for this study are presented in Chapter 2.

Figure 1.4 Partial phase diagram for the APFO/H_2O system[31]. Nomenclature: *I*, isotropic micellar solution phase; N_D, nematic phase with discotic micelles; *L*, lamellar phase; *K*, crystal; *T*p(*I*,*N*,*L*), the isotropic micellar solution-nematic-lamellar triple point; *T*p(*I*,*N*,*K*), the isotropic micellar solution-nematic-crystal triple point; *C*ep, the critical endpoint; *T*cp, the lamellar-nematic tricritical point; *T*c, the solubility curve. The isopleth along which SAXS measurements were made is also shown.

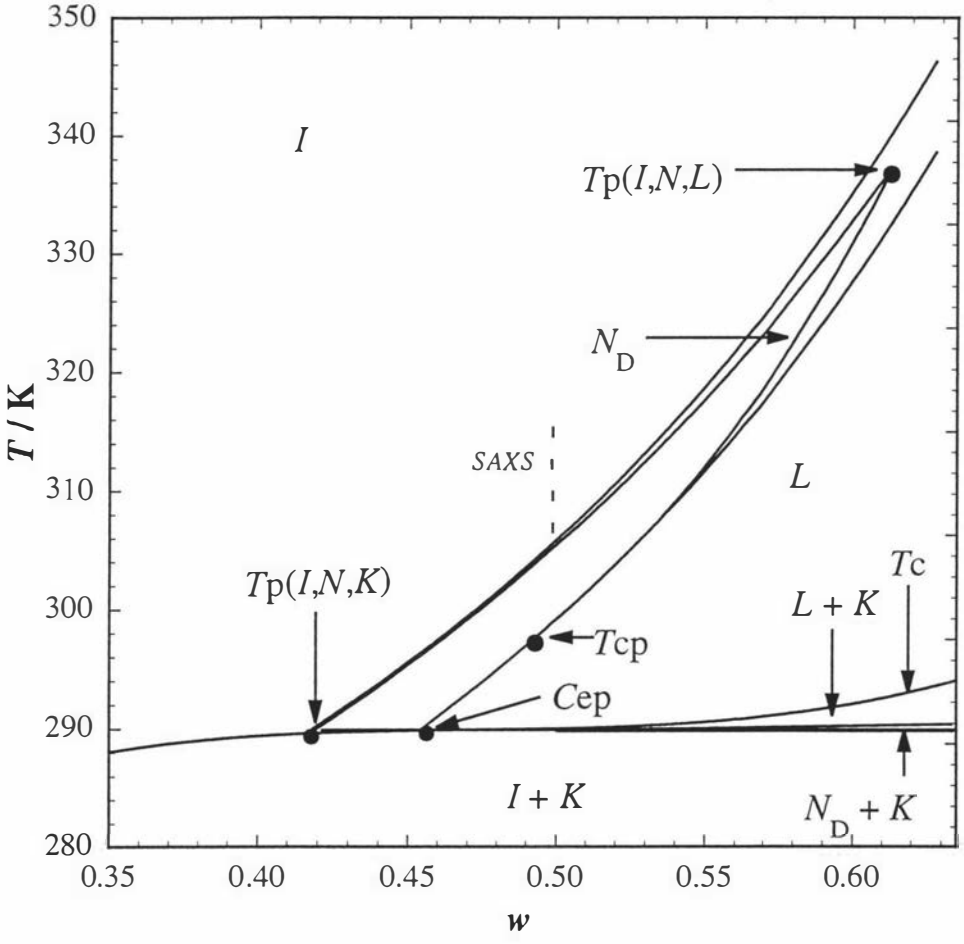

1.1 References.

1. Yoshino, N., *et al.*, *Bull. Chem. Soc. Japan* **1991**, *64*, 3262.

2. Kissa, E. *Fluorinated Surfactants*; Marcel Dekker, Inc: New York, 1994; Vol. 50, 469.

3. Cull, B., *et al.*, *Liq. Cryst.* **1994**, *17*, 507.

4. Bahadur, P., *et al.*, *Langmuir* **1992**, *8*, 1903.

5. Downes, N., G. Ottewill, and R. Ottewill, *Coll. Surf. A* **1995**, *102*, 203.

6. Fontell, K. and B. Lindman, *J. Phys. Chem.* **1983**, *87*, 3289.

7. Mendez Sierra, J., *et al.*, *Coll. Surf. A* **1996**, *117*, 143.

8. Parbhu, A.N., Ph.D. Thesis, Dept. of Chemistry, Massey University, New Zealand. **1994**

9. Rosenblatt, C. and N. Zolty, *J. Physique Lett.* **1985**, *46*, L.

10. Yu, Z.-J. and R. Neumann, *Langmuir* **1994**, *10*, 377.

11. Wong, A., P. Wiltzius, and B. Yurke, *Physical Review Letters* **1992**, *68*, 3583.

12. Mukerjee, P., *et al.*, *J. Phys. Chem.* **1990**, *94*, 8832.

13. Rosenblatt, C., *J. Colloid. Interface. Sci.* **1989**, *131*, 236.

14. Guo, W., T.A. Brown, and B.M. Fung, *J. Phys. Chem.* **1991**, *95*, 1829.

15. Hoffmann, H., W. Ulbricht, and B. Tagesson, *Zeitschrift fur Physikalische Chemie Neue Folge* **1978**, *113*, 17.

16. Hoffmann, H. and W. Ulbricht, *Zeitschrift fur Physikalische Chemie Neue Folge* **1977**, *106*, 167.

17. Hoffmann, H. and B. Tagesson, *Zeitschrift fur Physikalische Chemie Neue Folge* **1978**, *110*, 113.

18. Mukerjee, P., *Coll. Surf. A* **1994**, *84*, 1.

19. Mukerjee, P., *et al.*, *J. Phys. Chem.* **1985**, *89*, 5308.

20. Muzzalupo, R., G. Ranieri, and C. La Mesa, *Coll. Surf. A* **1995**, *104*, 327.

21. Reizlein, K. and H. Hoffmann, *Progress in Colloid and Polymer Science* **1984**, *69*, 83.

22. Shinoda, K., M. Hato, and T. Hayashi, *J. Phys. Chem.* **1972**, *76* , 909.

23. Boden, N., *et al.*, *J. Chem. Phys.* **1995**, *103*, 5712.

24. Tamaki, K., S. Watanabe, and Y. Daikyoji, *Bull. Chem. Soc. Japan* **1990**, *63*, 3681.

25. Tamaki, K., Y. Ohara, and S. Watanabe, *Bull. Chem. Soc. Japan* **1989**, *62*, 2497.

26. Perron, G. and J.E. Desnoyers, *J. Chem. Eng. Data* **1997**, *42*, 172.

27. Mukerjee, P. and T. Handa, *J. Phys. Chem.* **1981**, *85*, 2298.

28. Weber, R. and H. Hoffmann, *Liq. Cryst.* **1988**, *3*, 203.

29. Ikawa, Y., *et al.*, *J. Sol. Chem.* **1988**, *17*, 125.

30. Boden, N., K.W. Jolley, and M.H. Smith, *J. Phys. Chem.* **1993**, *97*, 7678.

31. Edwards, P., *et al.*, *Langmuir* **1997**, *13*, 2665.

32. Harding, R., *to be submitted,* in *Chemistry*. 1997, Leeds University: Leeds.

33. Esumi, K. and S. Ogiri, *Coll. Surf. A* **1995**, *94*, 107.

34. Thomsen, S., M.Sc. Thesis, Dept. of Chemistry, Massey University, New Zealand, **1994**.

35. Lindman, B., *et al.*, *J. Phys. Chem.* **1984**, *88*, 5048.

36. Lindman, B. and H. Wennerstrom, *Micelles. Amphiphile Aggregation in Aqueous Solution,* in *Micelles,* F.L. Boschke, Editor. 1980, Springer-Verlag: p. 1.

37. Laaksonen, L. and J. Rosenholm, *Chemical Physics Letters* **1993**, *216*, 42.

38. Brandao, M., Ph.D. Thesis, Dept. of Chemistry, Leeds University, United Kingdom. **1997**

39. Burkitt, S., *et al.*, *Colloid and Polymer Science* **1987**, *265*, 619.

40. Cates, M.E., *Macromolecules* **1987**, *20*, 2289.

41. Granek, R. and M.E. Cates, *J. Chem. Phys.* **1992**, *96*, 4758.

42. Safran, S.A., *et al.*, *J. Phys. France* **1990**, *51*, 503.

43. MacKintosh, F.C., S.A. Safran, and P.A. Pincus, *Europhysics Letters* **1990**, *12*, 697.

44. Dombroski, J.P., *et al.*, *Liquid Crystals* **1995**, *18*, 51.

45. Froba, G. and J. Kalus, *J. Phys. Chem.* **1995**, *99*, 4450.

46. Herbst, L., *et al.*, *Ber. Bunsenges. Phys. Chem.* **1985**, *89*, 1050.

47. Israelachvili, J.N., D.J. Mitchell, and B.W. Ninham, *Faraday Trans. II* **1976**, *72*, 1525.

48. McMullen, W.E., A. Ben-Shaul, and W.M. Gelbart, *Coll. Int. Sci.* **1984**, *98*, 523.

49. Granek, R., *et al.*, *Journal of Chemical Physics* **1994**, *101*, 4331.

50. Burkitt, S.J., *et al.*, *Coll. Poly. Sci.* **1987**, *265*, 619.

51. Odijk, T., *Macromolecules* **1986**, *19*, 2313.

52. Boden, N., *et al.*, *J. Chem. Phys.* **1990**, *93*, 9096.

53. Almgren, M. and S. Swarup, *Coll. Int. Sci.* **1983**, *91*, 256.

54. Asakawa, T., *et al.*, *Langmuir* **1995**, *11*, 2376.

55. Caponetti, E., *et al.*, *J. Phys. Chem.* **1992**, *96*, 4950.

56. Causi, S., *et al.*, *J. Phys. Chem.* **1991**, *95*, 5664.

57. Choudhury, N.R. and J.C. Ahluwalia, *J. Chem. Soc., Faraday Trans. 1* **1981**, *77*, 3119.

58. Emerson, M.F. and A. Holtzer, *J. Phys. Chem.* **1967**, *71*, 3320.

59. Miyagishi, S., *Bull. Chem. Soc. Japan* **1974**, *42*, 2972.

60. Mukerjee, P. and A. Ray, *J. Phys. Chem.* **1963**, *67*, 190.

61. Ravey, J. and M. Stebe, *Coll. Surf. A* **1994**, *84*, 11.

62. Schick, M.J., *J. Phys. Chem.* **1964**, *68*, 3585.

63. Treiner, C., *Coll. Int. Sci.* **1982**, *90*, 444.

64. Chang, J.N. and E.W. Kaler, *J. Phys. Chem.* **1985**, *89*, 2996.

65. Almgren, M., S. Swarup, and J.E. Lofroth, *J. Phys. Chem.* **1985**, *89*, 4621.

66. Ceglie, A., *et al.*, *Langmuir* **1993**, *9*, 1449.

67. Gamboa, C., H. Rios, and V. Sanchez, *Langmuir* **1994**, *10*, 2025.

68. Jonstromer, M., M. Sjoberg, and T. Warnheim, *J. Phys. Chem.* **1990**, *94*, 7549.

69. Olofsson, G., *J. Chem. Soc., Faraday Trans. 1* **1991**, *87*, 3037.

70. Perche, T., *et al.*, *Langmuir* **1997**, *13*, 1475.

71. Rico, I. and A. Lattes, *J. Phys. Chem.* **1986**, *90*, 5870.

72. Singh, H.N., *et al.*, *J. Phys. Chem.* **1980**, *84*, 2191.

73. Auvray, X., *et al.*, *Langmuir* **1993**, *9*, 444.

74. Auvray, X., *et al.*, *Langmuir* **1991**, *7*, 2385.

75. Auvray, X., *et al.*, *Langmuir* **1992**, *8*, 2671.

76. Auvray, X., *et al.*, *J. Phys. Chem.* **1989**, *93*, 7458.

77. Auvray, X., *et al.*, *J. Phys. Chem.* **1990**, *94*, 8604.

78. Belmajdoub, A., *et al.*, *J. Phys. Chem.* **1988**, *92*, 3569.

79. Belmajdoub, A., *et al.*, *J. Phys. Chem.* **1992**, *96*, 1011.

80. Perche, T., *et al.*, *Journal De Physique I* **1992**, *2*, 923.

81. Schubert, K.V., *et al.*, *J. Phys. Chem.* **1993**, *97*, 248.

82. Warnheim, T. and A. Jonsson, *Journal of colloid and Interface Science* **1988**, *125*, 627.

83. Perche, T., *et al.*, *Journal de Physique IV* **1993**, *3*, 133.

84. Backlund, S., *et al.*, *Journal of Colloid and Interface Science* **1989**, *131*, 393.

85. Callaghan, A., *et al.*, *Langmuir* **1993**, *9*, 3422.

86. Nagarajan, R., *Journal of Colloid and Polymer Science* **1998**, *submitted for publication*,

87. Nagarajan, R. and C. Wang, *Journal of Colloid and Interface Science* **1996**, *178*, 471.

88. Palepu, R., *et al.*, *Langmuir* **1993**, *9*, 110.

89. Ray, A., *J. Am. Chem. Soc.* **1969**, *91*, 6511.

90. Tamori, K., *et al.*, *Journal of Colloid and Interface Science* **1991**, *147*, 33.

91. Boden, N., *et al.*, *Molecular Crystals Liquid Crystals* **1998**, *submitted for publication*,

92. Funari, S., M. Holmes, and G. Tiddy, *J. Phys. Chem.* **1992**, *96*, 11029.

93. Auvray, X., *et al.*, *Liquid Crystals* **1994**, *17*, 109.

94. Ionescu, L., T. Tokuhiro, and J. Czerniawski, *Bull. Chem. Soc. Japan* **1979**, *52*, 922.

95. Gopal, R. and J.R. Singh, *J. Phys. Chem.* **1973**, *77*, 554.

96. Akhter, M., *Colloids and surfaces A* **1997**, *121*, 103.

97. Ramadan, M.S., D.F. Evans, and R. Lumry, *J. Phys. Chem.* **1983**, *87*, 4538.

98. Ramadan, M.S., D.F. Evans, and S. Philson, *J. Phys. Chem.* **1985**, *89*, 3405.

99. Evans, D.F., E.W. Kaler, and W.J. Benton, *J. Phys. Chem.* **1983**, *87*, 533.

100. Backlund, S., *et al.*, *Journal of Colloid and Interface Science* **1981**, *79*, 578.

101. Onori, G. and A. Santucci, *Chemical Physics Letters* **1992**, *189*, 598.

102. Nagarajan, R. and C.-C. Wang, *Langmuir* **1995**, *11*, 4673.

103. Nagarajan, R. and E. Ruckenstein, *Langmuir* **1991**, *7*, 2934.

104. Boden, N., S.A. Corne, and K.W. Jolley, *J. Phys. Chem.* **1987**, *91*, 4092.

105. Boden, N., *et al.*, *J. Physique* **1986**, *47*, 2135.

106. Boden, N., *et al.*, *Mol. Cryst. Liq. Cryst.* **1987**, *152*, 37.

107. Boden, N., K.W. Jolley, and M.H. Smith, *Liq. Cryst.* **1989**, *6*, 481.

108. Boden, N., *et al.*, *Phys. Rev. Lett.* **1991**, *66*, 2883.

109. Boden, N., P.J.B. Edwards, and K.W. Jolley, *Self-Assembly and Self-Organization in Micellar Liquid Crystals,* in *Structure and Dynamics of Strongly Interacting Colloids and Supramolecular Aggregates in Solution,* S.-H. Chen, J. Huang, andP. Tartaglia, Editor. 1992, Kluwer academic Publishers: Dordrecht. p. 433.

110. Boden, N. and K.W. Jolley, *Phys. Rev. A* **1992**, *45*, 8751.

2. Materials and Methods.

2.1 Chemicals, Purification and General Sample Preparation.

2.1.1 Chemicals Used and Surfactant Synthesis.

Pure water was obtained by passing it through a reverse-osmosis (R.O.) column and then doubly-distilling it. Deuterium oxide (Aldrich, 99.9 atom %), *N*,*N*-dimethylacetamide, *N*,*N*-dimethylformamide, *N*-methylformamide, formamide and ethylene glycol (all from Merck, >99%) were of the highest purity available and were used without further purification. All of these solvents are hygroscopic and the amides can decompose over time in the presence of oxygen so were stored under dry nitrogen. The caesium, ammonium, tetramethylammonium and tetraethylammonium salts of heptadecafluorononanoic and pentadecafluorooctanoic acids (Aldrich) were made by neutralising the acids with appropriate hydroxides (Merck) in doubly-distilled R.O. water until the solutions were slightly alkaline to indicator paper. Water was then removed by freeze-drying.

2.1.2 Purification of Surfactants.

Pure surfactant salts were obtained by double recrystallisation from acetone in the case of tetraethylammonium heptadecafluorononanoate and from 50% $^{v}/_{v}$ butanol/hexane for the other salts. Residual solvent was removed by prolonged heating (at least 48 hours) at 30°C under vacuum (0.5 mmHg). The salts are hygroscopic (especially the tetraalkylammonium salts) and were stored in a dessicator. Prior to use they were further dried under the same conditions. Purity was checked by the NMR determination of liquid crystal phase transition temperatures of 50% $^{w}/_{w}$ aqueous solutions, values for which have been well established[1-8].

It was observed that APFO had a tendency to sublime under the conditions used in the solvent removal stage and this phenomenon was exploited in an alternative method for its purification. An existing glass sample-drying apparatus was modified by the incorporation of a cold finger into one of the endcaps (see Figure 2.1).

Figure 2.1 Purifying APFO by sublimation.

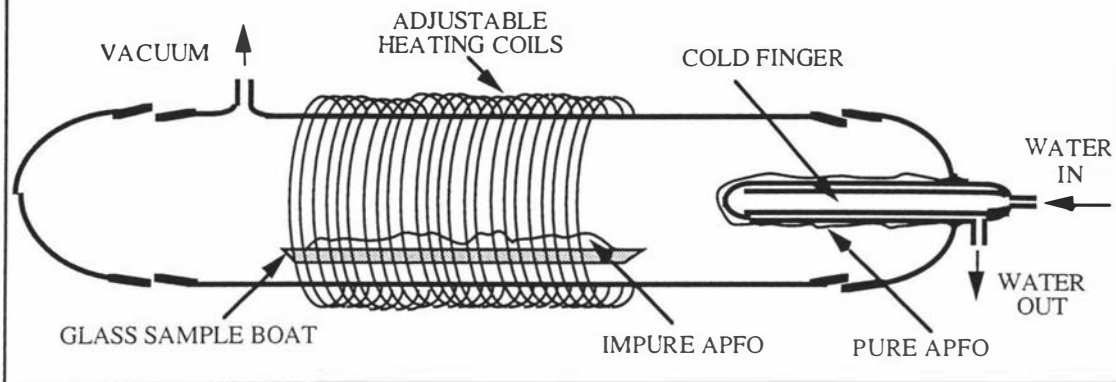

First, the apparatus was evacuated to 0.5 mmHg and the heating coils were adjusted *via* rheostats so that the temperature at the sample boat level was 45 °C, as measured by a glass thermometer. A higher temperature and vacuum may have increased the yield but also may have increased the likelihood of the APFO decomposing. The thermometer was replaced by impure APFO contained in the sample boat and the apparatus re-evacuated. Tap water was passed through the cold finger and the apparatus monitored over time. After about 48 hours a white layer about 5 mm thick had built up over the cold finger. This layer was recovered and a 50% $^{w}/_{w}$ aqueous solution of the compound was tested by NMR as above. There was virtually no difference in liquid crystal phase transition temperature between this sample and a sample made from doubly-recrystallised APFO. Since purification by recrystallisation had a greater yield in a shorter time it was the preferred method.

2.1.3 General Sample Preparation.

All sample vessels were thoroughly cleaned before use. In preparing samples, both solids and liquids were measured gravimetrically to a precision of ±0.00002 g using a Mettler AT 261 Delta Range balance. Organic solvents were handled with glass syringes to preclude the possibility of dissolution of plastic disposable syringes. Specific sample preparation is treated separately in each experimental section.

2.2 Temperature Control and Measurement.

Precise temperature control and accurate temperature measurement are crucial in the determination of liquid crystal phase transition temperatures and critical micelle concentrations. Systems previously developed at Massey University[9-11] that achieve a high standard of temperature control and measurement have been further refined in this work.

2.2.1 Temperature Control.

Double-pass water flow sample cells have been previously developed for NMR determination of phase transition temperatures[9, 10] and conductivity measurements[11] and were used in this work. However, the temperature of the waterbath (a Colora wk3 cryostat) supplying these cells was previously altered by the manual operation of coarse and fine analogue rheostats which controlled its heating and cooling elements. This manual control was rather clumsy and often small changes in temperature were difficult to achieve. An improvement implemented here was the modification of the rheostats to allow digital as well as manual control. The voltage supplied to the heating elements could now be governed by the value of four-digit hexadecimal number sent *via* an IEEE cable. An IEEE "uP" interface was manufactured by the Electronics Workshop at Massey University to communicate with the waterbath temperature control system *via* a computer. The benefits of digital control were two-fold: it enabled (a) temperature incrementation by smaller intervals (approximately 0.025 °C), and (b) remote data collection (see section 2.9) thus allowing improved calibration of thermocouples and the performance of experiments overnight.

Figure 2.2 shows the non-linear response of the the waterbath heating elements to changes in output integer. The Figure plots the (decimal) integer sent to the waterbath as a function of waterbath temperature measured *via* a Hewlett-Packard 2804A Digital Quartz Thermometer.

Figure 2.2 Colora wk3 waterbath calibration curve showing the decimal integer sent to the waterbath as a function of temperature measured *via* a Hewlett-Packard 2804A Digital Quartz Thermometer. The solid line is a degree-three polynomial fitted through the data.

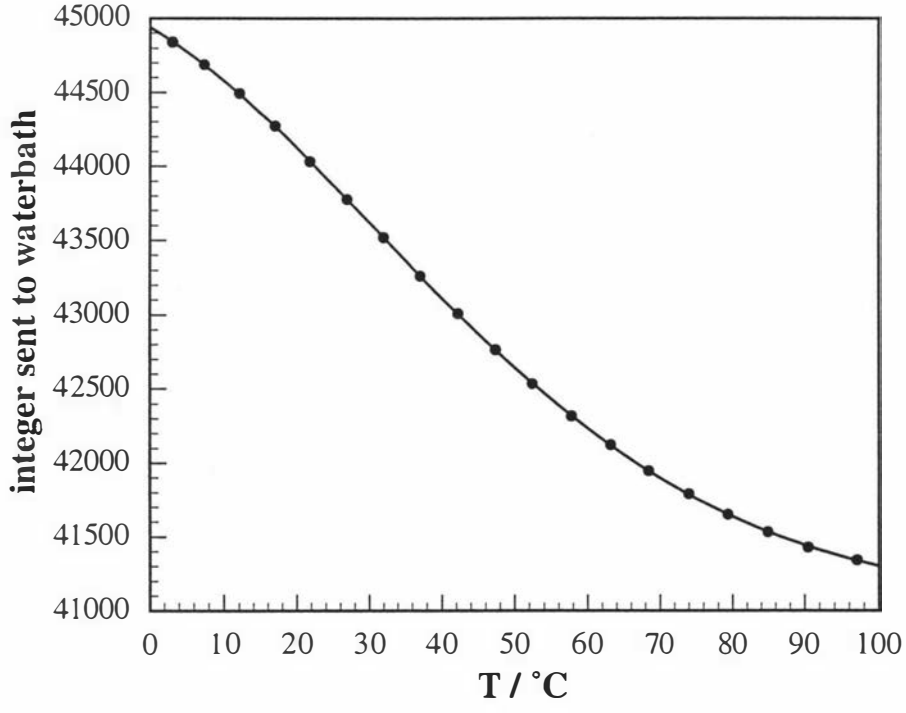

2.2.2 Temperature Measurement.

Temperature was monitored by the measurement of the potential difference (to a precision of 0.1 μV using a Philips PM2535 System Multimeter) between copper-constantin thermocouples inserted into the sample cells' waterjackets as close as possible to the analyte and a constant reference temperature. Previous methods used an ice slurry as the reference temperature (assumed to be 0°C). Disadvantages of using an ice slurry are its short lifetime, the possible variation in ice purity and a moderate temperature stability. However, a 10-fold increase in temperature stability (±0.5 mK as opposed to ±5 mK)[12] and a 20-fold increase in lifetime (a few hours as opposed to up to week) can be achieved by the use of the triple-point of water as the temperature reference.

2.2.3 The water triple-point cell.

As a consequence of the phase rule

$$F = C - P + 2$$

where F is the number of degrees of freedom, C is the number of components, and P is the number of phases in equilibrium, the temperature and pressure of a one-component system ($C = 1$) with solid, liquid and vapour co-existing in equilibrium ($P = 3$) must be fixed ($F = 0$). The triple-point of water occurs at 273.16 K (0.01 °C) and 4.58 mmHg[12].

A triple-point cell was constructed and employed as the reference temperature wherever practicable. Figure 2.3 shows the dimensions of the unprimed cell. The cell consists of a borosilicate glass cylinder with rounded ends and a hollow central well or 'finger' running almost fully down its central axis. The protrusions on the top of the cell were necessary in its construction and were where the cell was sealed after the insertion of water.

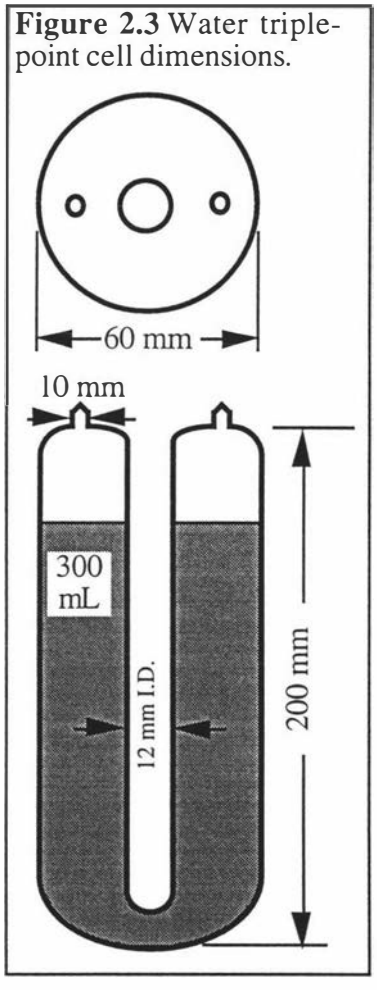

Figure 2.3 Water triple-point cell dimensions.

2.2.3.1 Construction of the cell.

Figure 2.4 shows the apparatus used to construct the triple-point cell. The apparatus was cleaned with conc. nitric acid and flushed several times with doubly-distilled R.O. water. Water of the same purity was then fed into the 500mL flask *via* the teflon tap on the left. The tap was closed and the system evacuated *via* the tap on the right. The water was degassed by several freeze-thaw cycles, distilled into the triple-point cell and the cell flame-sealed.

Figure 2.4 Apparatus used to construct the water triple-point cell.

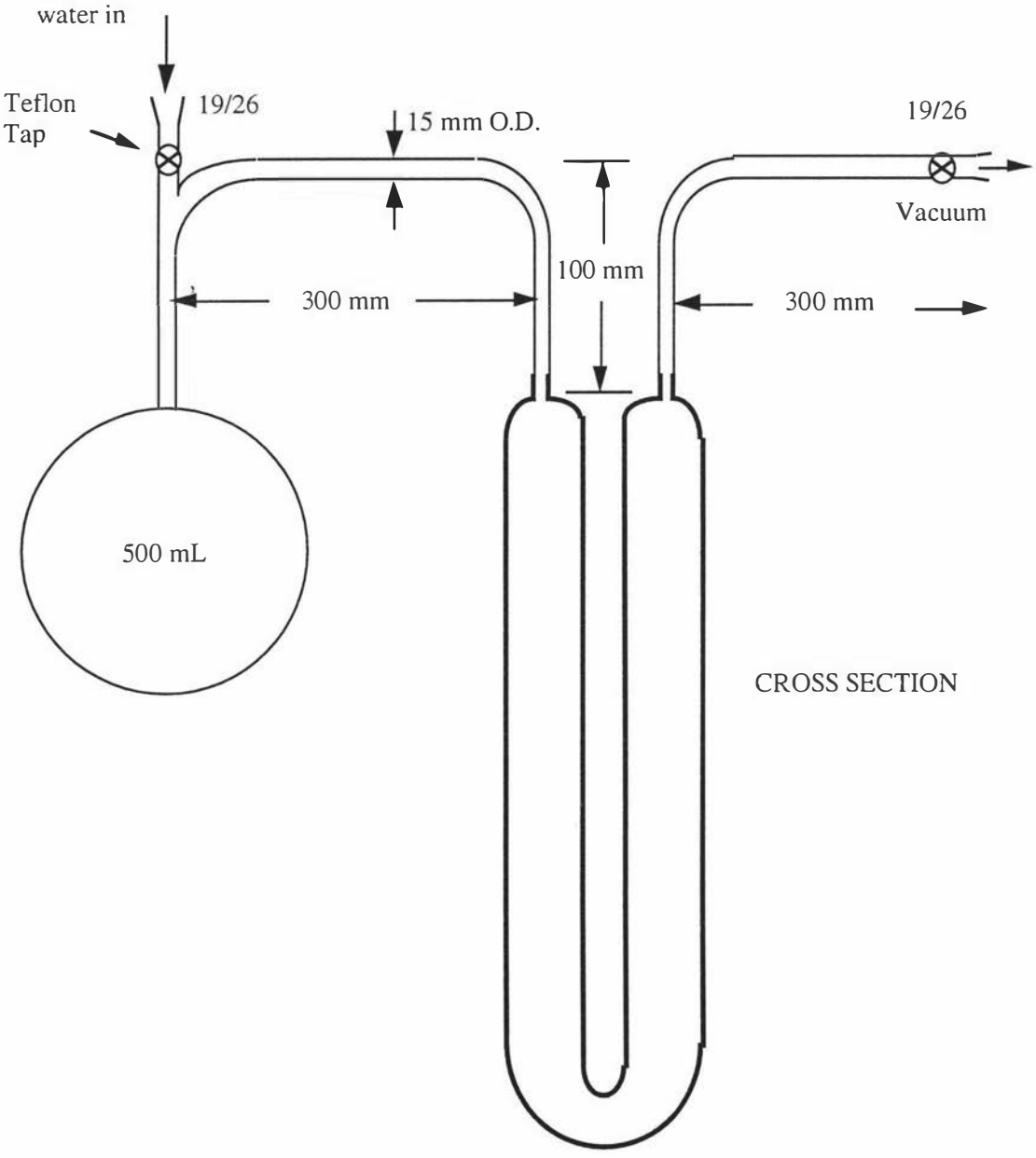

2.2.3.2 Priming and using the cell.

The cell was primed by forming a layer of ice internally about the central finger by the insertion of dry ice or a flow of liquid nitrogen into the finger. Ice was prevented from forming at the liquid/vapour interface by occasional warming. Once a thick (2-3 cm) ice layer was formed, a few mL of glycerol were inserted into the finger to aid thermal conduction, and the cell was placed into an ice slurry in a specially designed vacuum flask with a drain at the bottom. Since the ice in the slurry is colder than the ice in the cell (by 0.01 °C) it helped to maintain the longevity of the cell by preferentially melting and draining *via* the hole at the bottom of vacuum flask. The triple-point cell is shown ready for use in Figure 2.5.

Figure 2.5 The water triple-point cell in use.

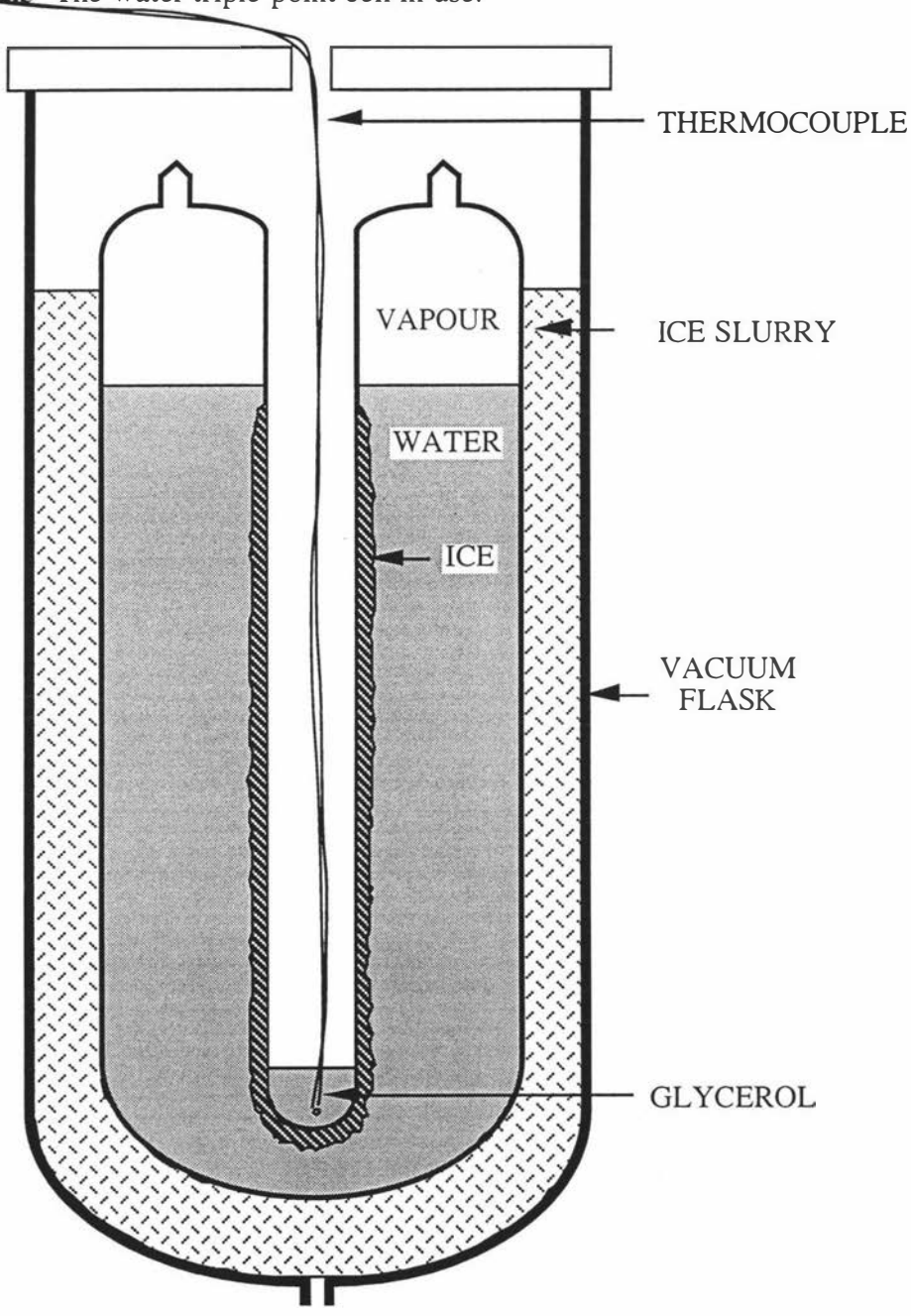

2.2.3.3 Testing the cell.

To test the accuracy of the measured water triple-point temperature, the quartz thermometer was inserted into the finger of the cell and monitored at about 20 minute intervals over 12 hours. Figure 2.6 shows that the measured equilibrium temperature was equal to the literature value of 0.01 °C to quoted precision[12]. More importantly, once thermal equilibrium had been achieved, the temperature did not vary significantly i.e. by >±0.0001 °C after 6 hours had elapsed. Thus, when the cell was required as a temperature reference, the thermocouple junction was allowed to thermally equilibrate in it for at least this time.

To test the longevity of the cell it was monitored *via* the quartz thermometer at eight hour intervals over eight days. Figure 2.7 shows that the cell temperature remained constant at 0.0090±0.0001 °C for approximately six days.

Having established a high stability and longevity of the temperature reference, thermocouples were calibrated against the quartz thermometer. The high temperature junction of the thermocouple was tied to the quartz thermometer probe and then placed into the waterbath. The calibration curve relating temperature to the thermocouple potential difference *E*/mV between the triple-point of water cell and the waterbath is shown in Figure 2.8 and is given by the polynomial

$$T/^{\circ}\mathrm{C} = 0.22141E^3 - 1.7110E^2 + 27.089E - 0.28667.$$

Figure 2.6 The water triple-point cell temperature monitored *via* quartz thermometer at 20 minute intervals over 12 hours.

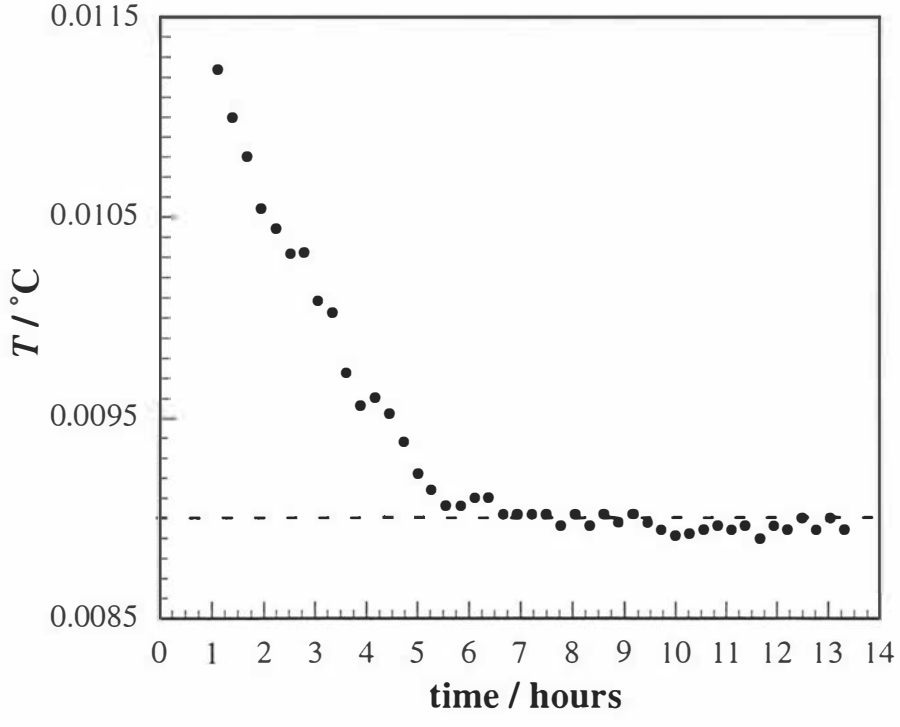

Figure 2.7 The water triple-point cell temperature monitored *via* quartz thermometer at eight hour intervals over eight days.

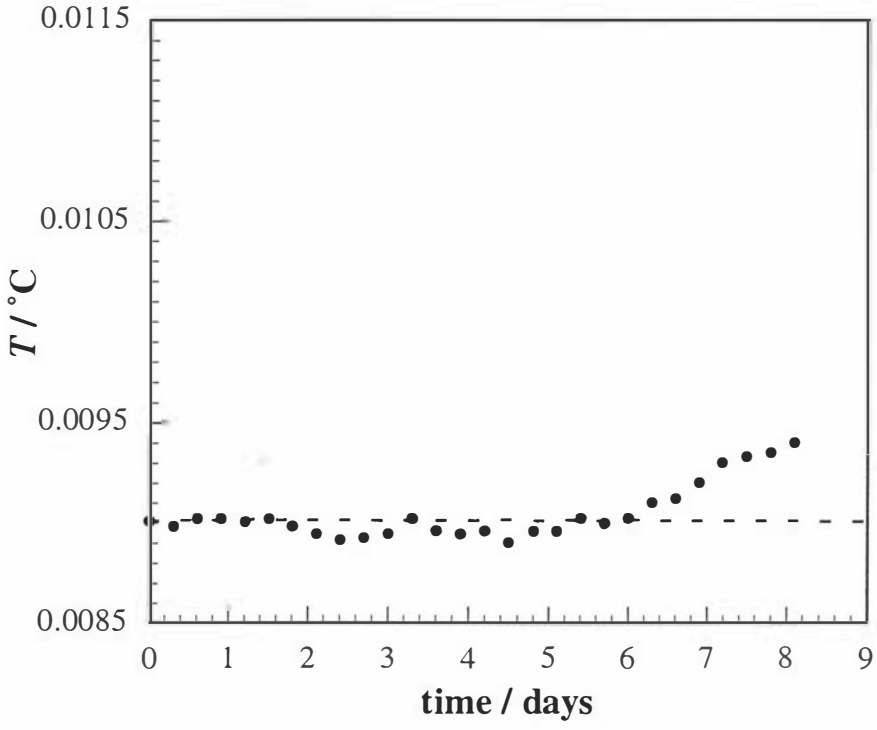

Figure 2.8 Temperature calibration curve for a copper-constantin thermocouple with the triple-point of water as reference. The solid line is a degree-three polynomial through data points.

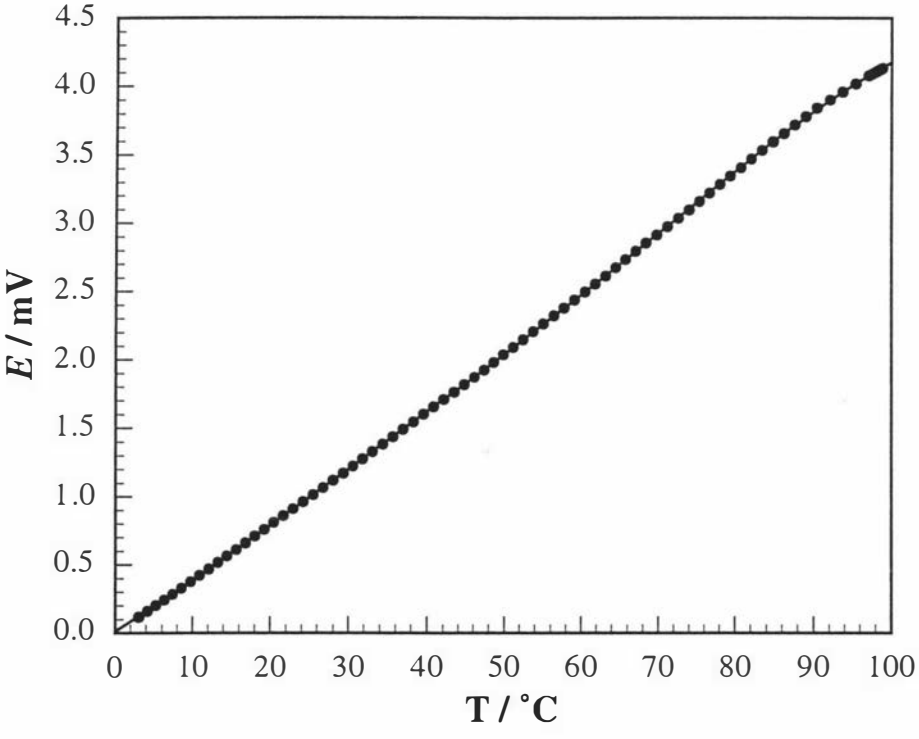

2.3 Conductivity.

2.3.1 Sample Preparation.

Stock solvent/water solutions were gravimetrically prepared in 25 cm^3 volumetric flasks. A dilution method[10] was used whereby, after measurement, the analyte was recovered from the conductivity cell, weighed and diluted with the solvent stock.

2.3.2 Conductivity Measurement.

The conductance *G*/S of surfactant solutions was measured to four significant figures by a Philips PW9512/61 conductivity probe connected to a Hewlett-Packard HP 4192A LF Impedance Analyzer operating at 0.5 V and 25 kHz. The temperature-dependence of the conductance was obtained by cooling, usually from approximately 90 °C down to 3 °C at 2 °C intervals. Ten conductance measurements were sampled at 10 s intervals at each temperature, and the mean and variance (<0.01%) of the data were automatically calculated. The cooling time to thermal equilibrium had been established to be ≈5 min/°C but usually 15 minutes were allowed between each 2 °C temperature decrement. Details of temperature control and measurement have been outlined above. A degree-four polynomial was fitted through the data points and the conductivity κ/S cm^{-1} at any temperature within that range was obtained as the product of the conductance interpolated from the polynomial and the conductivity probe cell constant previously determined to be 0.75 cm^{-1} at 298 K[10].

2.4 NMR.

2.4.1 Sample Preparation.

Surfactant was weighed into previously cleaned and dried 100 mm long 5 mm o.d. NMR tubes *via* a specially manufactured funnel (preventing the decomposition of surfactant at the tube mouth upon flame sealing). Solvent was then weighed in by glass syringe. The tubes were covered with parafilm and centrifuged. The tubes were cooled to reduce the vapour pressure of the solvent then flame sealed. Samples could be prepared in this manner to an accuracy of ±0.001 mass fraction. The samples were then thoroughly mixed in an isotropic phase (determined by cross polarisers. The polarisers also revealed any undissolved surfactant.) The viscosity of the tetraalkylammonium surfactants made mixing difficult. When a constant surfactant:D_2O mass ratio was required e.g in the determination of the effect of solvent on 50% $^{w}/_{w}$ surfactant solutions, a stock solution of this concentration was made up and introduced to the NMR tube and solvent added rather than individually making up solutions.

Before use, the samples were attached to an approximately 650 mm length of 5 mm o.d. glass rod *via* a copper sleeve and inserted into the sample cell and mixed again in the isotropic phase. Details of NMR temperature control and measurement have been outlined above.

2.4.2 NMR Measurement.

^{133}Cs NMR was used for precise determination of phase transition temperatures and ^{2}H NMR was used for following variations in micelle size (see Chapter 5). The spectrometer used was a JEOL JNM-GX270 spectrometer with an Oxford Instruments 6.34 tesla wide bore superconducting magnet. The spectrometer's data acquisition system had been recently upgraded to a tecmag™ system driven by MacNMR™ software on a Macintosh Power PC. ^{133}Cs spectra were obtained using an NM-G27T10 10 mm tuneable probe. ^{2}H spectra were obtained simultaneously by monitoring the ^{2}H frequency on the lock channel. Typical experimental parameters used to obtain spectra are shown in Table 2.1.

Table 2.1 Typical experimental parameters used to obtain NMR spectra.

Nucleus	^{2}H	^{133}Cs
Acquisition mode	Single Pulse	Single Pulse
Obervation frequency	41.47 MHz	35.44 MHz
Sweep Width	2 kHz	10-60 kHz
Data Points	8192	32768
Broadening Factor	0.1 Hz	1 Hz
Accumulations	4	16
$\pi/2$ Pulse Width	20 μs	19 μs
Pulse delay	2 s	0.5 s

2.5 Optical Microscopy.

Optical microscopy was used for coarse phase detection only, thus precise and accurate temperature control and measurement was not required. A hotstage developed specially[7] for this type of microscopy consisted of two cartridge heaters inserted into a brass block either side of a sample cavity and controlled by an Omron E5AX temperature controller. The brass block was mounted on a cast iron ring acting as a heat sink through which thermostatted water was passed. This then fitted onto the stage mount of a Nikon 104 Polarising Microscope.

Samples were weighed into 1 mL glass vials, flame sealed and thoroughly mixed. Before use, the solutions were heated into the isotropic phase (established by examination of the sample placed between crossed polarisers), transferred to glass

microslides and flame sealed. Slides were then placed into the sample cavity and allowed to thermally equilibrate to a temperature in the isotropic phase. While cooling slowly (about 0.5 K min^{-1}) samples were observed under crossed polarisers and transitions to ordered phases were established by the observation of birefringence. Nematic, lamellar and mixed phases have characteristic textures[5], and transitions between these could be determined to within 0.1 K.

2.6 Rheology.

2.6.1 Sample Preparation.

Solutions of TEAHFN and TMAHFN (previously dried for 24 hours under vacuum) in water (doubly-distilled R.O. water) were gravimetrically made up and thoroughly mixed. The solutions were allowed to stand until no bubbles were present (usually overnight). The volume of solution required per sample was approximately 0.45 cm^3.

2.6.2 Temperature Control and Measurement.

Measurements were carried out on two machines: a Rheometrics Dynamic Analyzer RDA II (The University, Leeds) and a Bohlin VOR Rheometer (Massey University). The machines had a similar design and response but had different temperature control systems. The Rheometrics machine used an air-flow unit to control temperature and the Bohlin rheometer used a water bath. Both methods have their pros and cons. The air-flow temperature control tended to evaporate solvent, introducing undesirable concentration gradients within the sample. To avoid this, ambient temperature conditons (21±2)°C were used with the trade-off of less control over temperature *between* samples. Once equilibrated the temperature did not vary by more than ±0.05°C over the timescale of a single experiment. Whilst solvent evaporation was minimised with the waterbath system, the Bohlin rheometer had the disadvantage that only the stage beneath the fixed plate was thermostatted, which required longer equilibration times. Despite these problems, comparison of measurements between machines did not show significant differences. Temperature measurement on both machines was by factory-installed thermocouples positioned below the fixed plate.

2.6.3 Rheology Measurements.

Dynamic measurements of viscoelasticity are usually made by placing a sample between circular plates (made from a light metal e.g. aluminum or magnesium) of a specific geometry, disturbing the system from equilibrium by applying an oscillating stress or strain, and observing the relaxation. In relaxing, some of the energy is dissipated as heat (viscosity) and some is stored and relaxed by other mechanisms

(elasticity). Rheology theory is covered more fully in Chapter 3. Figure 2.9 shows the fixed cone and plate geometry used to measure viscoelasticity (cone and plate diameter = 25 mm; cone angle $\theta = 0.1$ rad; gap between cone and plate = 0.05 mm). This geometry is commonly used in rheology and has the advantages of a uniform strain rate at small cone angles i.e. where $\tan\theta \cong \theta$, a small sample volume, and good sample retention (by surface tension) between the plates.

Figure 2.9 Cone and plate geometry used in rheology experiments.

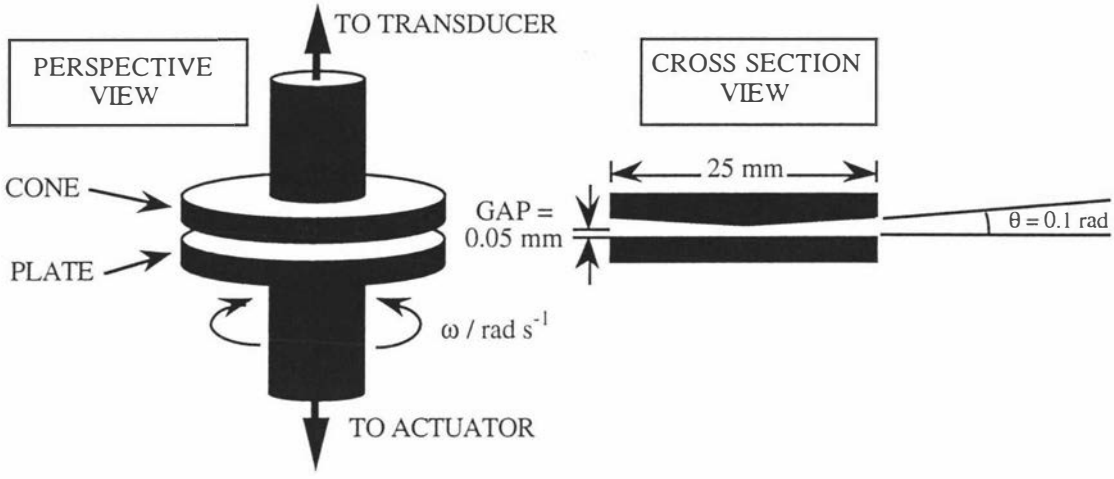

Both Rheometrics and Bohlin rheometers measured viscoelasticity by applying a deformation (strain) *via* an actuator (a motor) at the lower plate and the torque (stress) was detected by a transducer (a torsion bar with known deflection characteristics) connected to the upper cone. Measurements were made in the following manner. After the cone and plate were thermally equilibrated samples were poured or placed by spatula onto the plate ensuring no bubbles were introduced, the cone lowered to a gap just greater than 0.05 mm, the excess sample removed, and the system allowed to thermally equilibrate. The gap was then readjusted to exactly 0.05 mm and dynamic frequency sweeps were carried out typically over ($10^{-1} \leq \omega \leq 10^{2}$) rad s^{-1}. The complex stress relaxation modulus $G^{*}(\omega)$ was measured, and the complex loss modulus $G''(\omega)$ (the viscous component) and storage modulus $G'(\omega)$ (the elastic component), and the magnitude of the complex viscosity $|\eta^{*}|$ were automatically calculated and output to files. Between samples the apparatus was cleaned with acetone, allowed to dry and recalibrated.

2.6.4 Data Analysis: Extracting η_0, G_0 and τ.

The rheological behaviour of the samples was close to "ideal" i.e. the form of the storage and loss moduli could be modelled on a simple Maxwell element - a spring with constant G_0 and and dashpot of viscosity η_0. For a full treatment of rheology theory see Chapter 3. This model was applied and the parameters of interest, the 'spring constant' G_0, relaxation time τ and the zero-shear viscosity η_0 were extracted in the follwing manner:

(a) Curves of the form $G'' = \sqrt{G_0^2 - \left(G' - G_0\right)^2}$ were fitted to Cole-Cole plots (G'' plotted against G', see Chapter 3) using Delta*Graph*™, and G_0 extracted.

(b) Values of τ were obtained by calculating for each data point

$$\tau = \frac{G'}{G''\omega}$$

(c) The zero-shear viscosity η_0 was obtained from extrapolation of the plateau of the magnitude of the complex viscosity $|\eta^*|$ plotted against frequency to the y-axis.

2.7 Surface Tension of Binary Solvent Mixtures.

The surface tensions of binary solvent mixtures of NMF/H_2O and DMA/H_2O at mole fractions of 0, 0.2, 0.5, 0.8 and 1 were measured by the Wilhelmy plate method[13] using a Kruess Processor Tensiometer K12. The apparatus is shown in Figure 2.10 and consists of a rectangular platinum plate of precisely known geometry connected to a balance and suspended over a sample vessel. The vessel is thermostatted by a waterbath and measurements were carried out at (25.0±0.1)°C. The volume of sample per measurement was less than 40 cm^3. The plate method is based on force measurement. The balance is tared with the plate suspended above the sample. The bottom edge of the plate is then lowered to the liquid surface and the liquid jumps to meet it. The plate is returned to its zero position and the downward 'Wilhelmy' force F exerted on the plate is measured. The surface tension γ is calculated by the equation $\gamma = F/(L\cos\theta)$ where L is the wetted length of the plate and $\cos\theta = 1$ since the contact angle between the tangent at the wetting line of most liquids and the roughened platinum plate surface is 0°. Figure 2.11 shows the experimentally determined surface tensions of binary NMF/water and DMA/water solutions at 25.1 °C.

Figure 2.10 Wilhelmy plate method for surface tension measurement. The insert shows a cross section of the wetted plate. The surface tension $\gamma = F/(L\cos\theta)$.

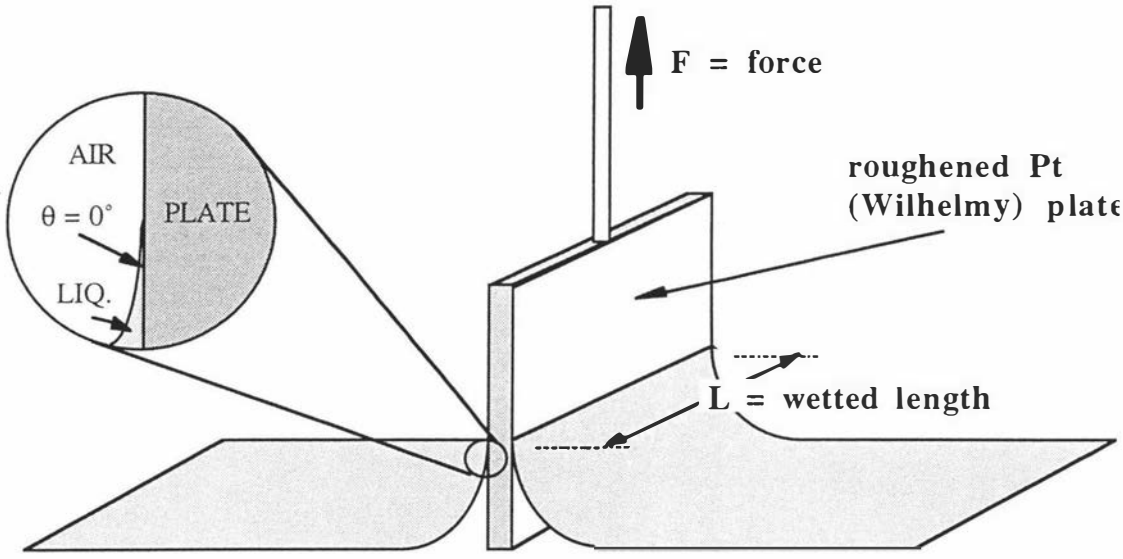

Figure 2.11 Surface tensions of the binary FA/water[14], NMF/water, DMA/water solvent mixtures.

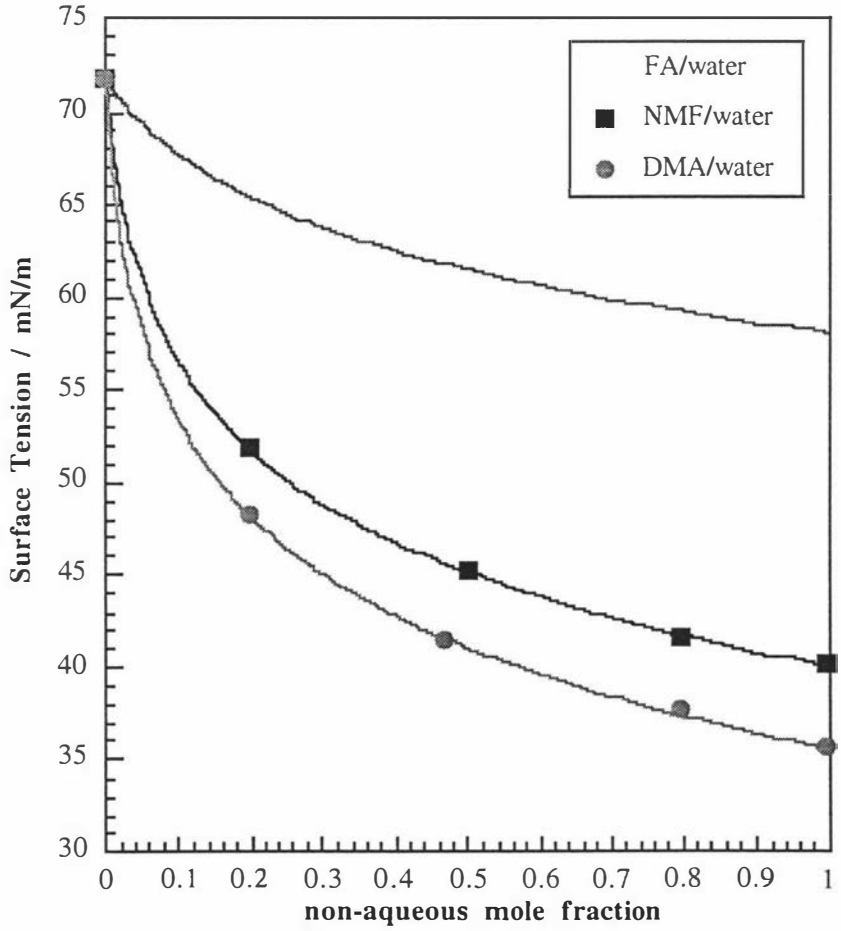

2.8 Small-angle x-ray diffraction (SAXS).

2.8.1 Sample Preparation.

Binary solvent/water mixtures with the non-aqueous solvents EG, DMF and DMA were made up gravimetrically. 50% $^{w}/_{w}$ CsPFO and 50% $^{w}/_{w}$ APFO solutions were made up using these solvent mixtures and transferred to 0.5 mm i.d. x-ray sample tubes after thorough mixing.

2.8.2 Temperature Control and Measurement.

Temperature control was *via* a water flow system controlled by a Colora WK3 cryostat passed through a brass sample block. Temperature measurement was by the potential difference measured by a Keithley 181 digital voltmeter between a previously calibrated copper/constantin thermocouple inserted into the sample block and an ice slurry as the reference. Each sample was equilibrated for at least 15 minutes prior to x-ray exposure.

2.8.3 X-ray Measurement.

All samples were measured in the isotropic phase. Nickel-filtered Cu K_{α} radiation (λ=0.154 nm) from a Philips generator operating at 30 mA and 40 kV was passed through the sample and the x-ray diffraction pattern was obtained using a simple pinhole camera. The distance L from the photographic plate to the sample was 112 mm. Before development, films were typically exposed for two hours for ammonium surfactant systems. Sufficiently intense diffraction patterns were unobtainable within the limited time available on the x-ray machine for CsPFO systems owing to the strong absorption of x-rays by the heavy Cs^{+} atom and thus measurements on this system were discontinued. The appearance of the diffraction patterns as diffuse rings was consistent with the expected isotropic distribution of diffracting sites. Figure 2.12 shows a typical photographic plate after development. The clear "C" shape leading from the ring center is from the x-ray beam stop.

Figure 2.12 Photographic plate after exposure to x-rays diffracted through a 50% $^{w}/_{w}$ APFO in 1:9 EG:water mole ratio at 308 K.

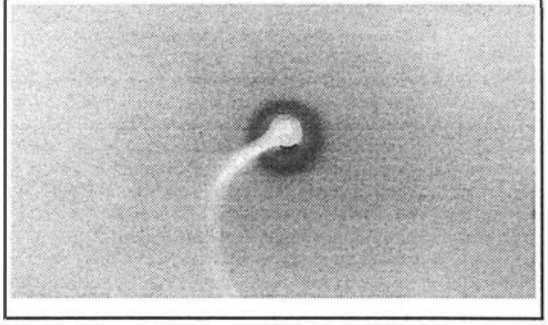

2.8.4 Data Analysis: micelle size from SAXS.

The diffraction ring diameter *d* was determined from the exposed and developed films by scanning with a densitometer and measuring the peak-to-peak distance. A typical trace is shown in Figure 2.13. The peak-to-peak distance was measured using the graphics packages CorelDraw™ and Delta*Graph*™.

Figure 2.13 A densitometer trace of 50% $^{w}/_{w}$ APFO/(1:9 EG:W) at 311 K.

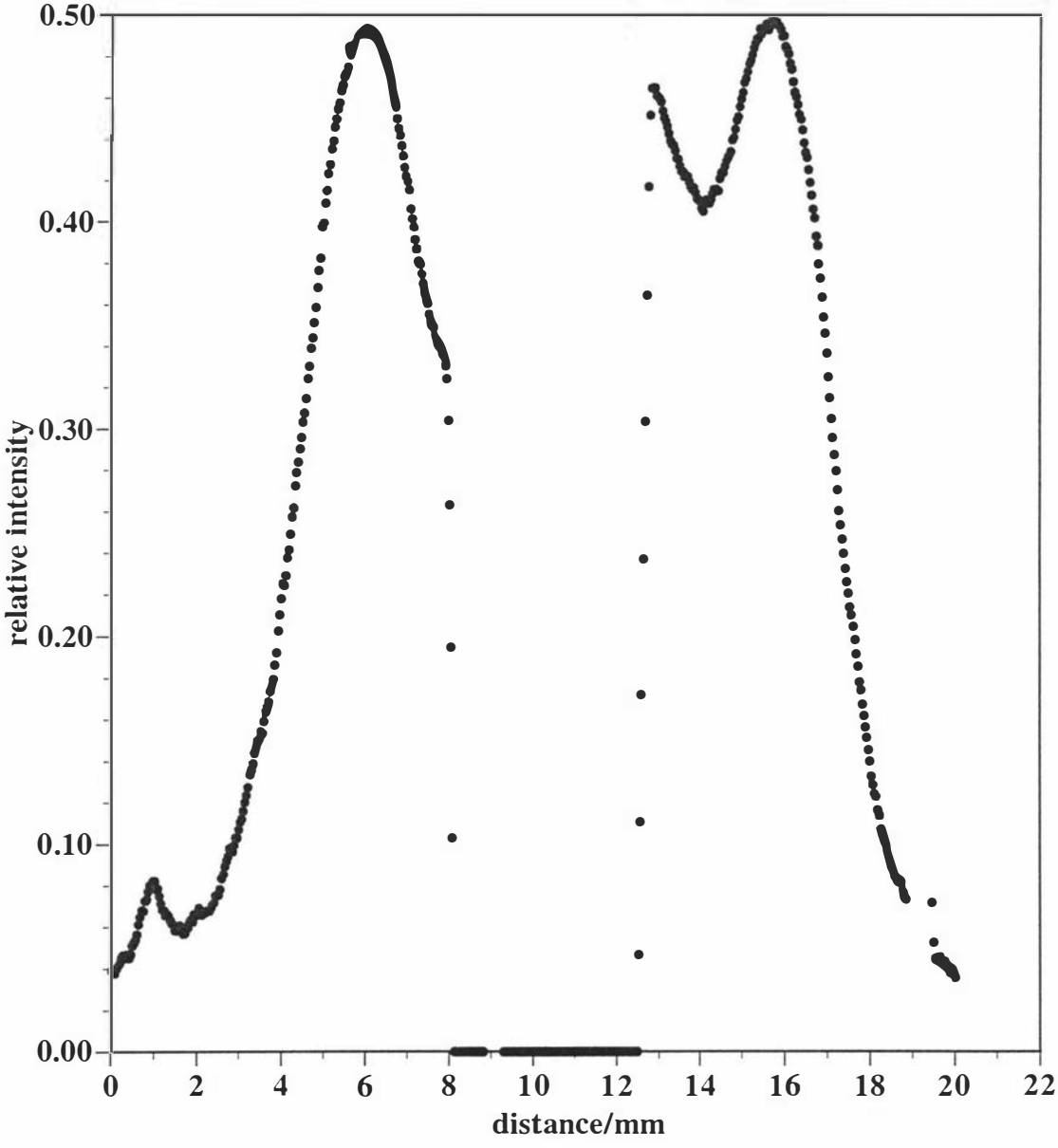

The aggregate center-to-center separation distance d_0 was calculated assuming x-rays are scattered from the (111) planes of a face-centered cubic lattice[15]. Using the parameters shown in Figure 2.14 and the Bragg condition for constructive interference

$$n\lambda = 2d_0 \sin\theta$$

where n = 1 and $\theta = \frac{1}{2}\tan^{-1}(d/L)$, the center-to-center separation distance d_0 is given by

$$(d_0/\text{nm}) = 36.96 / (d/\text{mm}).$$

The micelle volume V_m is calculated *via*

$$V_m = 3\sqrt{3}\,\phi d_0^3/4$$

where ϕ is the volume fraction.

Figure 2.14 X-ray diffraction from a face-centred cubic (fcc) lattice.

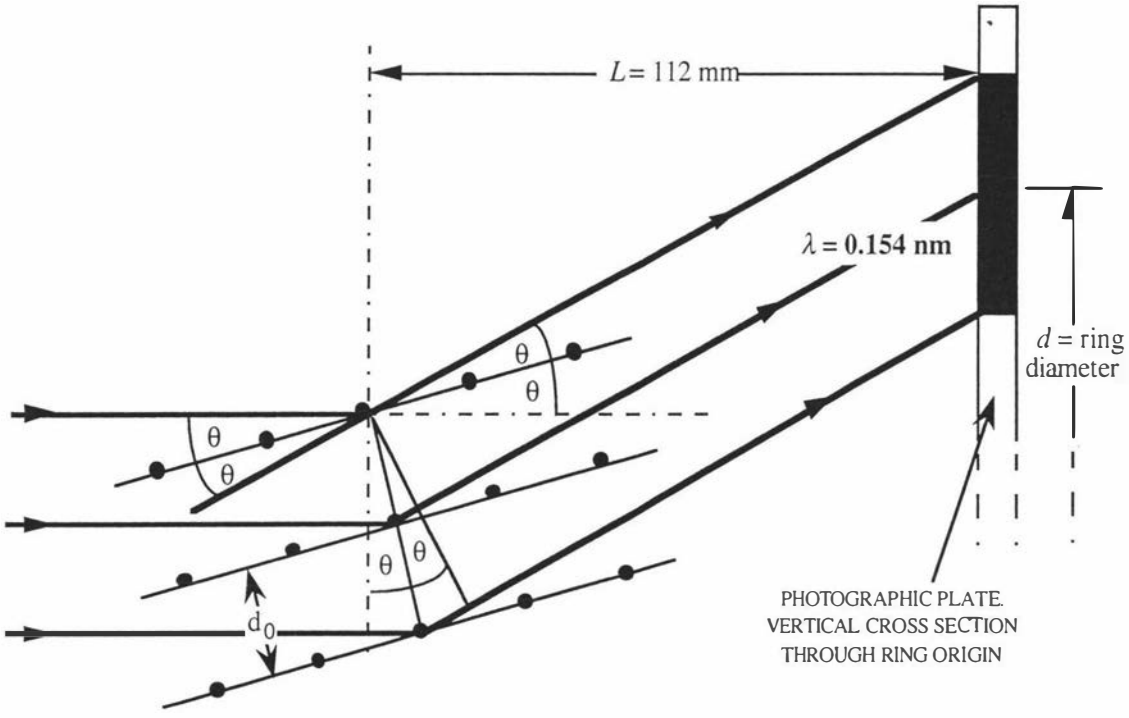

2.9 Automated data collection.

The improvements to existing methods for NMR and conductivity measurement outlined above i.e digital control of the waterbath temperature and the longevity of the water triple-point cell, allowed the implementation of an automated data collection system.

The Philips PM2535 digital voltmeter and the Hewlett-Packard HP 4192A LF Impedance Analyzer had existing capacities for remote operation. The recent upgrading of the JEOL GX-270 NMR machine's data acquisition system to a tecmag™ system driven by MacNMR™ software operating on a Macintosh Power PC allowed automation of NMR measurements. The IEEE uP interface used to communicate with the waterbath was also designed to communicate with these devices.

A system was designed and software written in THINK C™ (the program listing is not included for brevity) and AppleScript™[16] to allow this automation. Figure 2.15 shows a schematic of the devices used for automated conductivity data collection where fat arrows indicate water flow and thin arrows indicate data flow. The devices were identifiable by a digital address which preceded commands. The automated NMR data collection scheme was qualitatively similar. Figure 2.16 shows the main structure diagram for remote control of the devices shown in Figure 2.15. "HP" refers to the Hewlett-Packard impedance analyser and "DVM" refers to the digital voltmeter. Structure diagrams should be read like normal text i.e. from the top down and from left to right, but they have associated notational conventions: Variable names have their first letter capitalised. Rectangles denote a set of operations to be performed. Procedures or functions accessed within a set of operations are indicated in boldface (structure diagrams for these are omitted). The symbol "←" should be read as "*takes the value of*". This symbol is necessary since "=" is reserved for logical comparisons e.g. line 4 in the Figure: the condition "*(Status=11)*" has a value of either *TRUE* or *FALSE* depending on whether the device has finished reading another voltage. Rounded rectangles indicate a loop to be performed until a condition is fulfilled e.g. line 3 in the Figure: the loop is to "*sample the devices and increment* [by unity, the variable] *SampleNum from zero until (Samplenum=Samples)*".

The requirement of overnight data collection over extremes of temperature meant the incorporation of two safety precautions: (a) if the waterbath temperature was outside specified limits e.g. $T/^{\circ}C < 0.5$ and $T/^{\circ}C > 99$, the system automatically reset the waterbath back to room temperature and shut down while preserving data collected to that point, and (b) if the main power supply was cut and then restored during an experiment, a cut-out switch prevented the devices from turning on again (and consequently being set to unpredictable values).

Figure 2.15 Automated conductivity data collection schematic (see text for details).

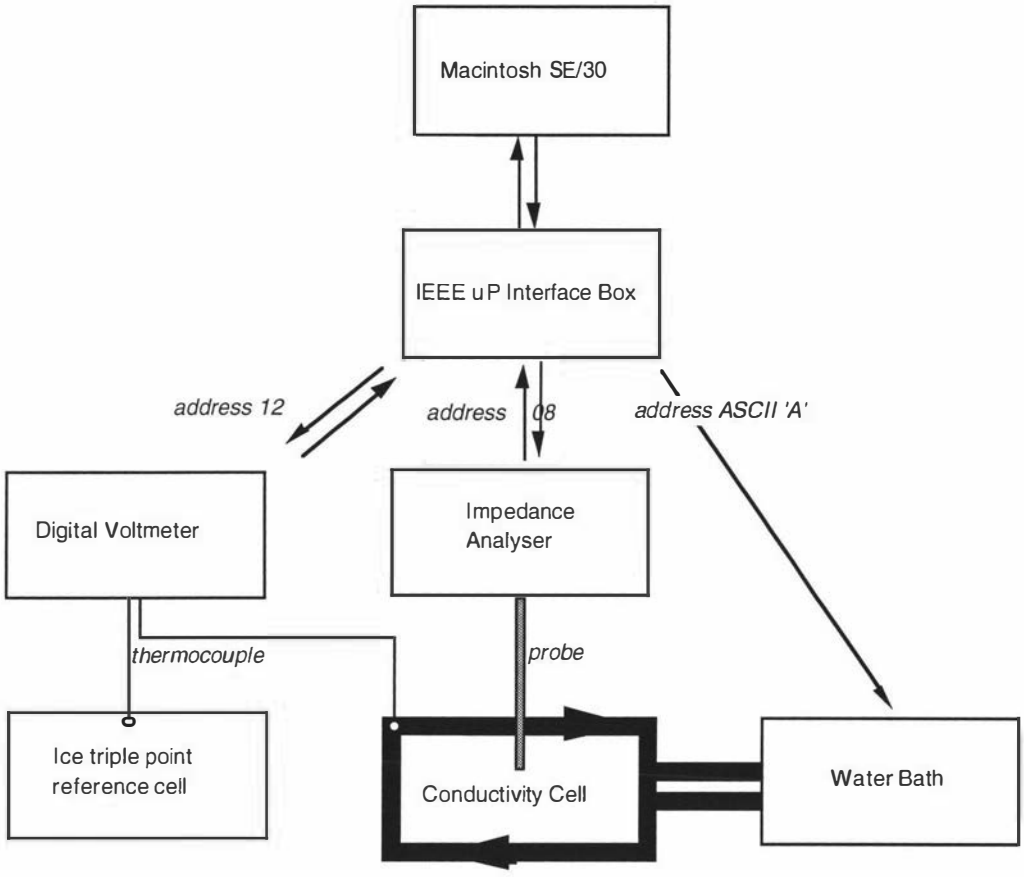

Figure 2.16 Main structure diagram for automated conductivity data collection.

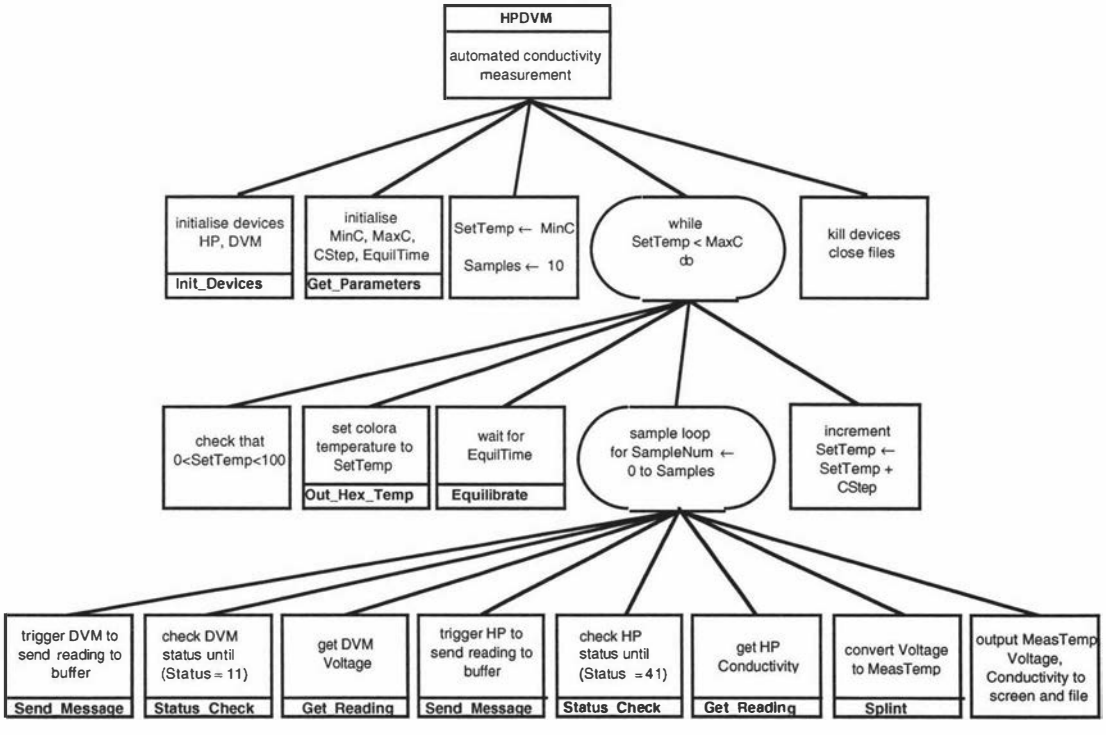

2.10 References.

1. Boden, N., *et al.*, *Phys. Rev. Lett.* **1991**, *66*, 2883.

2. Boden, N., K.W. Jolley, and M.H. Smith, *J. Phys. Chem.* **1993**, *97*, 7678.

3. Boden, N., *et al.*, *J. Chem. Phys.* **1995**, *103*, 5712.

4. Boden, N., *et al.*, *J. Chem. Phys.* **1990**, *93*, 9096.

5. Boden, N., S.A. Corne, and K.W. Jolley, *J. Phys. Chem.* **1987**, *91*, 4092.

6. Dombroski, J.P., *et al.*, *Liquid Crystals* **1995**, *18*, 51.

7. Parbhu, A.N., Ph.D Thesis, Dept. of Chemistry., Massey University, New Zealand. **1994**

8. Edwards, P., *et al.*, *Langmuir* **1997**, *13*, 2665.

9. Boden, N., *et al.*, *Journal of Magnetic Resonance* **1992**, *98*, 92.

10. Thomsen, S.J., M.Sc. Thesis, Dept of Chemistry, Massey University, New Zealand. **1994**.

11. Smith, M.H., Ph.D. Thesis, Dept of Chemistry, Massey University, New Zealand. **1990**

12. Nicholas, J. and D. White *Traceable Temperatures*; Science Information Division, DSIR: Wellington, New Zealand, 1982;

13. Kruess, *Kruess Processor Tensiometer K12 Users Manual GmbH*. 1994, Hamburg.

14. Schubert, K.V., *et al.*, *J. Phys. Chem.* **1993**, *97*, 248.

15. Parker, D., Ph.D. Thesis, Dept of Chemistry, Leeds University, United Kingdom. **1988**

16. Edwards, P., *Remote MacNMR Driver*. 1996, unpublished

3. Rheology of Aqueous Phases of TEAHFN and TMAHFN.

3.1 Introduction.

Rheology (Gr. *rhein*, to flow) is a principal experimental technique applied to the study of the behaviour of conventional polymers as melts or in solution. It has rapidly gained prominence in the study of self-assembled or 'equilibrium' polymers because the rheological behaviour of these systems is very close to theoretical. This will be shown in section 3.2.3. Equilibrium polymers consist of long entangled rodlike micelles and differ from conventional polymers by the reversibility of the self-assembly process which ensures the molecular weight distribution is in thermal equilibrium (this has brought about the term "living polymers"). As applied to the study of equilibrium polymers rheology involves disturbing a system from equilibrium by applying a shear and observing how it relaxes. Information on the equilibrium state can be obtained from dynamic measurements by using an oscillating shear force small enough that the underlying supermolecular structure is undisturbed e.g. by flow-induced alignment. Most surfactant systems studied to date either require added salt to access phases of equilibrium polymers or the extent of these phases is enhanced by the addition. This is not the case in this study, where the focus is to characterise the pure binary surfactant/water system. Theoretical treatments of equilibrium polymer formation in the presence[3, 4] and absence[13-15] of salt have been developed but they cannot fully explain the behaviour of salt-free equilibrium polymer systems at high surfactant concentrations.

Rheology theory will be reviewed first and then theoretical models for equilibrium polymers will be described and applied to the TEAHFN/water and TMAHFN/water systems.

3.2 Rheology theory.

Broadly, rheology is the study of the deformation of real bodies under the influence of an external stress. Specifically, rheology deals with the relationship between stress σ and strain γ[†] and their time dependencies. These quantities will be described first for a steady shear applied to the simplest cases and then in relation to the oscillatory experiments carried out on TEAHFN/water and TMAHFN/water

[†] The symbol for strain has traditionally been γ and will be used to refer to this quantity in this Chapter only. Elsewhere γ should be assumed to refer to surface or interfacial tension.

3.2.1 Shear Stress σ and shear strain γ.

3.2.1.1 Shear between rectangular parallel plates.

Two (hypothetical) extremes of materials i.e. a purely viscous fluid and a perfectly elastic solid subject to shear will be considered first. Figure 3.1 shows a side view of two rectangular parallel plates with areas A containing a purely viscous fluid. A shear is produced by a force F acting on the top plate and parallel to it and the fluid begins to flow. The shear strain γ is the deformation of the fluid dx/dy and since it is the ratio of two lengths $\gamma$is dimensionless. The shear rate is $\dot{\gamma} = d\gamma/dt$. The force acting on the top plate produces a shear stress defined as $\sigma = F/A$ (Pa). Purely viscous fluids obey Newton's Law i.e. the shear stress σ is proportional to the rate of deformation $\dot{\gamma}$, or

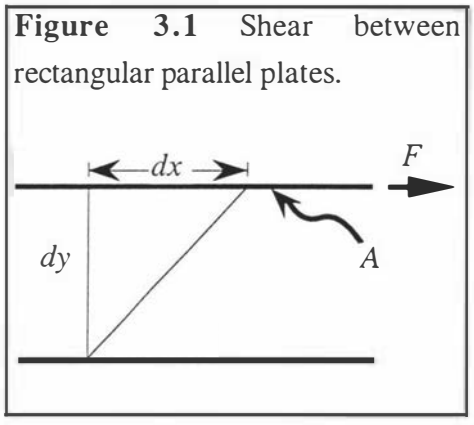

Figure 3.1 Shear between rectangular parallel plates.

$$\sigma = \eta_0 \dot{\gamma}$$

where η_0 is the static viscosity. Where a shear is acting on a purely elastic solid, the material does not flow but undergoes reversible deformation according to Hooke's Law i.e the shear stress is proportional to the deformation γ, or

$$\sigma = G_0 \gamma$$

where G_0 is the static shear modulus. Real materials behave in an intermediate manner to these extremes. Viscoelastic materials are those whose elastic and viscous responses to shear are roughly of the same order of magnitude. Provided the viscoleastic responses of real materials is linear (see the next section), the stress is simply the sum of the viscous and elastic responses to strain i.e.

[3–1] $$\sigma = G_0 \gamma + \eta_0 \dot{\gamma}.$$

3.2.1.2 Linear viscoelasticity.

Measurements performed with a very large imposed shear can alter the physical characteristics of the system under study. Since it is the equilibrium structure that is of interest the shear must be such that the material constants (G_0 and η_0) are independent

of its magnitude. Where this is so is termed the linear regime. The term stems from the British Standards Institution's formal definition[1] of linear viscoelasticity as "*viscoelasticity characterised by a linear relationship between stress and strain, and the time derivatives of strain*". I.e. a doubling of the strain will result in a doubling of the stress response. All experiments in this work were performed in the linear viscoelastic regime.

3.2.1.3 Shear between a cone and plate.

A cone and plate geometry was used in this work and the rheometers employed were designed to apply a strain γ to the bottom plate and measure the consequent torque Γ produced on the top cone as shown Figure 3.2. If the bottom plate of radius R rotates relative to the cone with a base radius R at a constant rate of $d\Theta/dt$ the strain rate at some ring of radius $r < R$ is given by

[3–2] $$\dot{\gamma} = \frac{r\frac{d\Theta}{dt}}{r\tan\theta}.$$

Since the cone angle to the base θ = 0.1 rad is small, $\tan\theta \cong \theta$, and equation [3-2] reduces to

$$\dot{\gamma} = \frac{1}{\theta}\frac{d\Theta}{dt}$$

Thus the strain γ at any time and position in the sample is constant and equal to

$$\gamma = \Theta/\theta$$

Figure 3.2 Shear between a cone and plate.

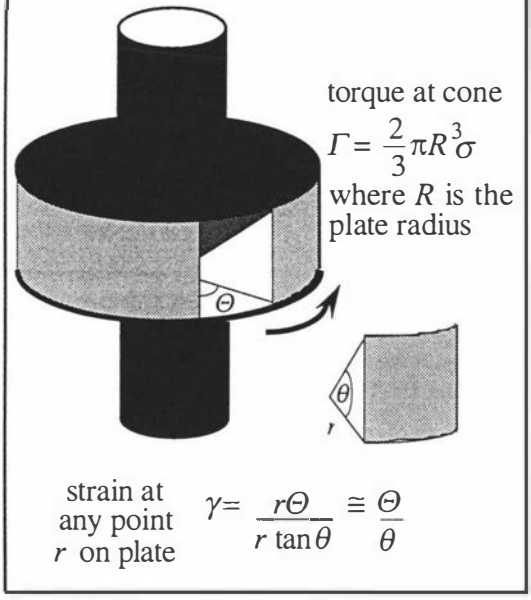

The stress at the cone can be obtained from the torque. The relation between the torque measured at the transducer and stress in the sample at some ring of radius r and thickness δr is given by[2]

$$\delta\Gamma = \sigma 2\pi r^2 \delta r.$$

The total torque can be obtained by summing the contributions of concentric rings between 0 and R i.e.

$$\Gamma = \int_0^R 2\pi r^2 \sigma dr = \tfrac{2}{3}\pi R^3\sigma.$$

3.2.2 Oscillating shear experiments.

Instead of a imposing a constant strain rate on the plate, information on the equilibrium state of a material can be obtained by examining the behaviour of the material under a small oscillating shear. The equations for stress and strain will be introduced and their representation as complex variables will be developed. A shear force oscillating at a frequency $\omega/2\pi$ imposed on the plate produces a strain in the material (in the linear viscoelastic regime) given as a function of time t by

[3–3] $$\gamma(t) = \hat{\gamma}\sin(\omega t)$$

where $\hat{\gamma}$ is the strain amplitude. The torque response detected at the cone will lag behind the strain due to the viscous component of the stress relaxation. The stress then is out of phase by an angle δ and is given by

[3–4] $$\sigma(t) = \hat{\sigma}\sin(\omega t - \delta).$$

If the material was purely viscous the stress would be 90° out of phase with the strain and if it were perfectly elastic the stress would be in phase with it. These functions are illustrated in Figure 3.3.

Figure 3.3 Stress and strain in oscillating shear. Also shown are the stress and strain amplitudes and the stress response delay as the phase angle δ.

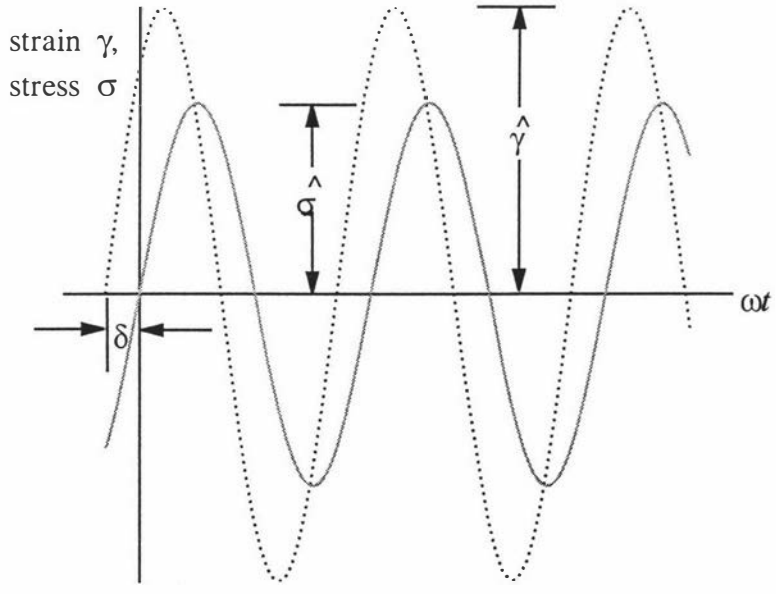

Equation [3–4] can be alternatively expressed as

[3–5]
$$\sigma(t) = \hat{\sigma}\sin\omega t\cos\delta - \hat{\sigma}\cos\omega t\sin\delta$$

$$= G'\,\hat{\gamma}\sin\omega t - G''\hat{\gamma}\cos\omega t$$

$$= G'\,\gamma + \frac{G''}{\omega}\dot{\gamma}$$

where $G' = \frac{\hat{\sigma}}{\hat{\gamma}}\cos\delta$ gives the in-phase stress amplitude and $G'' = \frac{\hat{\sigma}}{\hat{\gamma}}\sin\delta$ gives the quadrature (90° out of phase) stress amplitude. G' is called the storage or elastic modulus and G'' is called the loss or viscous modulus and are the main parameters of interest extracted from oscillatory experiments. It is usual to express the time-dependent stress response in terms of complex variables since this conveniently eliminates $\cos\omega t$ and $\sin\omega t$, thus

$$G^* = G' + \mathbf{i}G'' = \frac{\hat{\sigma}}{\hat{\gamma}}\cos\delta + \mathbf{i}\frac{\hat{\sigma}}{\hat{\gamma}}\sin\delta$$

This relation is depicted in Figure 3.4. The phase angle δ can be obtained from the relation $\tan\delta = G''/G'$. Another quantity of interest is the complex viscosity η^*. An expression for this can be obtained by substituting the amplitude of the strain rate $\dot{\hat{\gamma}} = \omega\hat{\gamma}$ (obtained by differentiating equation [3–3] with respect to time) into equation [3–5] i.e.

Figure 3.4 The components of the complex stress modulus G^*.

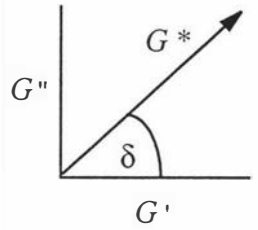

$$\sigma(t) = \hat{\dot{\gamma}}(-\eta''\sin\omega t + \eta'\cos\omega t)$$

where $\eta' = \frac{\hat{\sigma}}{\hat{\dot{\gamma}}}\sin\delta$ and $\eta'' = \frac{\hat{\sigma}}{\hat{\dot{\gamma}}}\cos\delta$. η' is called the dynamic viscosity and $\hat{\dot{\gamma}}\eta'$ is the amplitude of the component of stress in-phase with the strain rate $\dot{\gamma}$. The complex viscosity then is given by

$$\eta^* = \eta' - \mathbf{i}\,\eta''$$

and is related to the complex stress relaxation modulus by

[3–6]
$$\eta^* = G^*/\mathbf{i}\omega.$$

Thus it follows that $\eta'' = G''/\omega$ and $\eta' = G'/\omega$. Complex amplitudes of stress and strain can be converted to corresponding physical values by multiplying by $\exp(\mathbf{i}\omega t)$ and taking the real part. In practise a material is subjected to a range of frequencies (i.e. $\omega/2\pi$ is varied) and $G^*(\omega)$ is extracted. In order to calculate the material constants from the response of the material to dynamic frequency sweeps a model is required.

3.2.3 Modelling linear viscoelasticity.

Mechanical analogues can be used to describe the linear viscoelastic behaviour of materials over a frequency range. One such analogue is the Maxwell element shown in Figure 3.5, a spring with force constant G_0 connected in series to a dashpot filled with a purely viscous fluid of viscosity η_0. Here a force analogous to a shear stress is applied to the dashpot and the spring stretches instantaneously (analogous to the strain) while the dashpot elongates at the rate of σ/η_0. The behaviour[1] of the Maxwell model under harmonic oscillation can be characterised by the equations for the elastic and viscous components of the complex stress relaxation

Figure 3.5 A simple Maxwell model, a spring and dashpot.

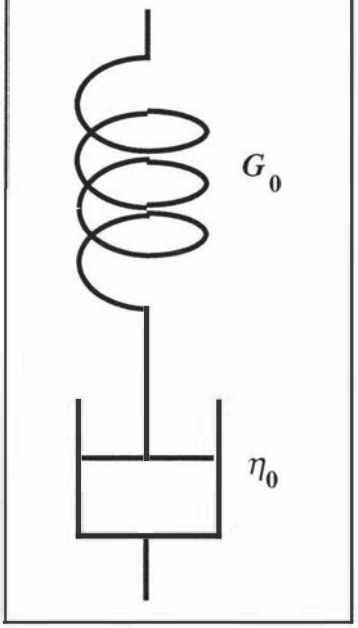

[3–7] $$G'(\omega) = G_0 \frac{\omega^2\tau^2}{1+\omega^2\tau^2} = \eta_0 \frac{\omega^2\tau}{1+\omega^2\tau^2}$$

[3–8] $$G''(\omega) = G_0 \frac{\omega\tau}{1+\omega^2\tau^2} = \eta_0 \frac{\omega}{1+\omega^2\tau^2}$$

where $\tau = \eta_0/G_0$. It is evident from the form of equation [3–7] that the elastic response of real bodies that can be modelled by Maxwell elements under oscillating shear always increases with frequency. The components of the complex viscosity are given by

[3–9] $$\eta'(\omega) = \frac{G''}{\omega} = \frac{\eta_0}{1+\omega^2\tau^2}$$

$$\eta''(\omega) = \frac{G'}{\omega} = \frac{\eta_0\omega\tau}{1+\omega^2\tau^2}$$

and its magnitude is given by

[3–10] $$|\eta^*| = \frac{\sqrt{G'^2 + G''^2}}{\omega}$$

The relation between steady shear and oscillatory shear experiments can be seen by the limit when $\omega\tau >> 1$, $G' \rightarrow G_0$ in equation [3–7], i.e at high frequencies the material behaves as an elastic solid. When $\omega\tau << 1$ in equation [3–9], $\eta' \rightarrow \eta_0$ i.e. at low frequencies the material behaves as a Newtonian fluid. In practise this was how the static viscosity η_0 was obtained in this work i.e. by extrapolation of the dynamic viscosity η' plotted against ω to the y-axis. Figure 3.6 illustrates the very good agreement between experimental data and theoretical curves generated by applying the Maxwell model.

Figure 3.6 Dynamic frequency sweep data from a $w = 0.14$ TEAHFN/water sample at 21°C. Plot (a) shows the elastic G' (squares) and viscous G'' (circles) components of the complex stress relaxation modulus G^*. Lines are fits to a Maxwell model using equations [3–7] and [3–8]. Plot (b) shows the magnitude of the complex viscosity $|\eta^*|$ fitted using equation [3–10].

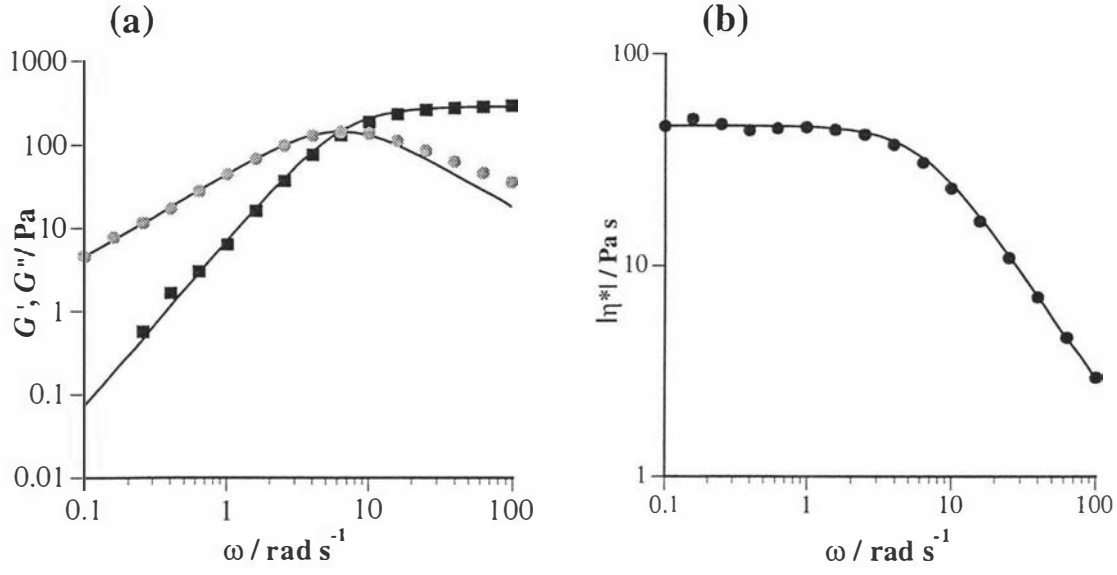

3.2.4 Cole-Cole representation.

A convenient way of representing experimental data is by plotting G' and G'' against each other. This representation is called a Cole-Cole plot (see Figure 3.7) and was used in this work to extract values of G_0, and hence η_0 and τ using equations [3-7], [3-8] and [3-10]. The data extraction method is described in detail in Chapter 2, and experimental data will be presented as Cole-Cole plots from here on.

The material constants G_0, η_0 and τ can be qualitatively related[1] to individual parts of the viscoelastic solution. G_0 may be pictured as the 'stiffness' of the spring due to elastically deforming chains between entanglement points, η_0 may be seen as the frictional movement of entangled chains past each other or through the solvent and τ may be seen as an upper limit to the total stress relaxation time. However it has been pointed out[2] that, though the Maxwell model is qualitatively useful it may be misleading to push the mechanical analogy too far. Indeed, examination of Figure 3.7 shows that the Maxwell model (equivalent to monoexponential stress relaxation in the time domain) breaks down at high frequency (at high G' in the figure). Thus Cole-Cole plots have the advantage of clearly showing deviations from Maxwellian (monoexponential) behaviour i.e. they reveal the existence of other modes of relaxation, with characteristic relaxation times τ. A theoretical explanation for the origin of these modes has been proposed by Cates *et al*[3], and a model for the dynamics of equilibrium polymer solutions in general developed and refined[4] which gives a more physically realistic picture of equilibrium polymer behaviour. Cates' model will be examined next.

Figure 3.7 Cole-Cole (G'' against G') representation of the data in Figure 3.6. The line is a fit to the equation for a circle, the diameter of which gives G_0, and describes the behaviour of G'' and G' subject to monoexponential relaxation decay in the time domain.

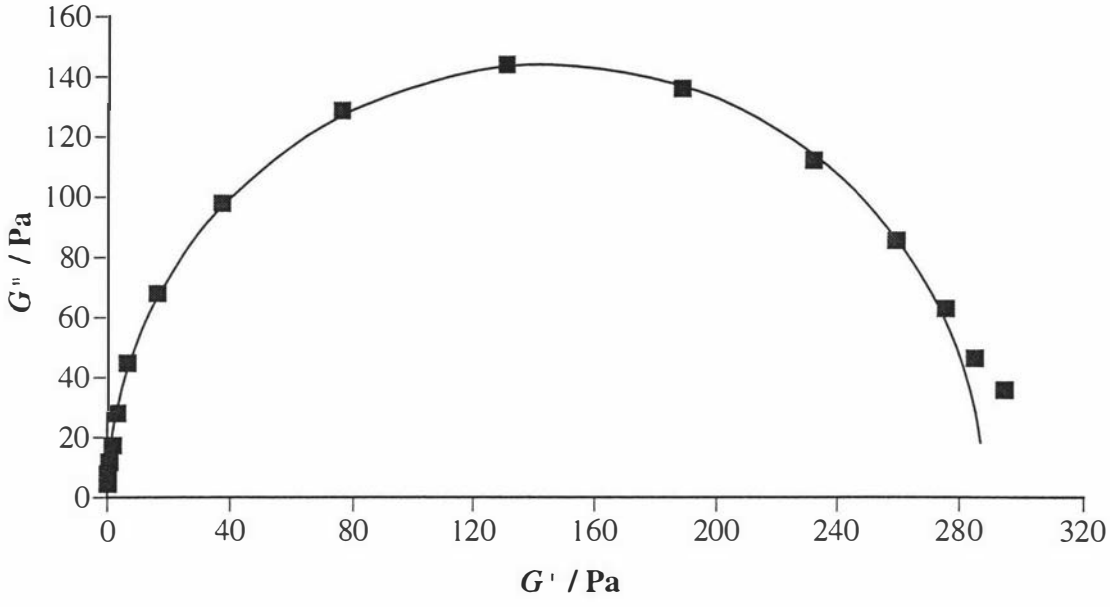

3.3 Cates' model for equilibrium polymer dynamics.

Cates' theory[3, 4] for equilibrium polymer dynamics uses the concept of polymer relaxation by reptation developed by Doi and Edwards[5] for the theory of conventional polymer dynamics but introduces other kinetic processes to take into account the molecular weight distribution being in thermal equilibrium (chainlength polydispersity). His model computes the theoretical contributions to the overall stress relaxation function $G(t)$ or its complex form $G^*(\omega)$. Once $G(t)$ is known all other properties of the system can be calculated and he produces a set of power laws which describe how these properties should vary as a function of concentration ϕ. His model successfully describes the behaviour of several real systems in the presence of salt[6-11] and the model will be applied to the viscoelastic systems in this work since it is the only known method of extracting equilibrium polymer chainlengths from viscoelastic measurements[12]. The systems under study here do not contain added salt and this introduces complications because the chainlength is no longer solely a function of surfactant concentration. The behaviour of equilibrium polymers in the absence of salt has been treated theoretically by Mackintosh *et al*[13, 14] and Odijk[15] but the viscoelastic behaviour of only a few real salt-free systems have been reported; the perfluorocarbon surfactant tetraethylammonium perfluorooctanesulphonate (TEAPOS)[16], the double-chain hydrocarbon surfactant ethanediyl-α,ω-bis(dodecyldimethylammonium bromide)

(12-2-12)[17-20] and the related single-chain surfactant cetyltrimethylammonium bromide (CTAB)[21].

The relaxation mechanisms considered by Cates will be examined first and then his model, with the modifications proposed by Mackintosh *et al* will be discussed in relation to the systems TEAHFN/water and TMAHFN/water.

3.3.1 Stress relaxation mechanisms.

3.3.1.1 Reptation.

If a strain is applied to system, a stress is induced and is associated with the entropy loss of polymer chain conformations. In the Doi polymer theory the main mechanism by which conventional polymers can relax is by reptation (L. *reptare*, to creep). This can be thought of as the curvilinear diffusive motion of a polymer chain along its own contour out of a hypothetical tube formed from contacts with neighbouring chains (see Figure 3.8) i.e. diffusion along the polymer axis is more probable than diffusion perpendicular to it. The chain reptates out of its original tube and a new tube is created in equilibrium with the strained environment and hence carries no stress. The time it takes to reptate its length is τ_{rept} and has an upper limit given by

$$\tau_{rept} \cong \frac{\overline{L}^2}{D_c}$$

where $\overline{L}$ is the mean chain length. $D_c(L)$ is the curvilinear diffusion constant of the chain in its tube, and since frictional drag is proportional to chain length $D_c(L) \sim 1/L$. The fraction of stress $\mu(t)$ (where $G(t) = G_0\,\mu(t)$) remaining at time t is simply the fraction of of the original tube still occupied at that time and for *monodisperse* systems

Figure 3.8 Stress Relaxation by Reptation. The first panel shows a polymer chain within a tube formed by contacts with other chains. The second shows the polymer chain subject to stress after a time t having reptated a distance out of its original (stressed) tube into a new piece of (unstressed) tube.

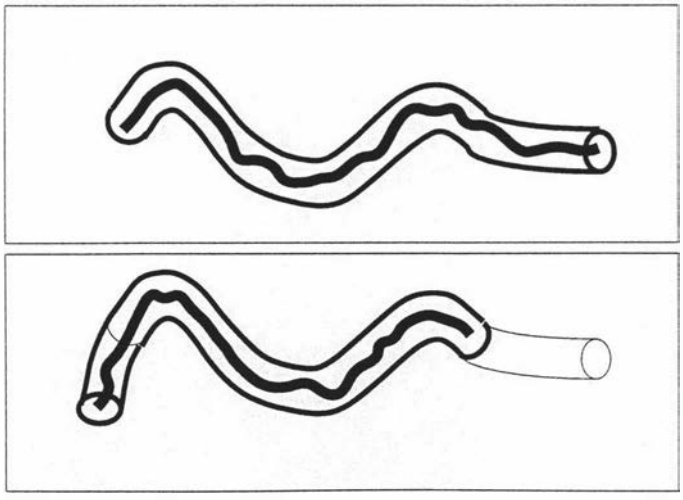

is easily computed[5] and is a nearly monoexponential function. For *polydisperse* systems the relaxation function shows a range of relaxation times i.e. is non-monoexponential.

3.3.1.2 Chain scission.

Chain scission is the reversible unimolecular scission process illustrated in Figure 3.9(a). It is characterised by a temperature dependent rate constant k_l per unit time per unit arc length and is associated with a scission energy E independent of ϕ. k_l is assumed to be the same for all elongated micelles and is independent of time and ϕ. This assumption leads to an expression of the time taken for a rod of mean length $\overline{L}$ to break as $\tau_{break} = (k_l \overline{L})^{-1}$. This assumption, and that of the ϕ-independence of E may not be valid for systems in the absence of salt[13], such as in the systems studied in this work.

Figure 3.9 Equilibrium polymer reactions. (a) scission; (b) bond interchange; (c) end interchange.

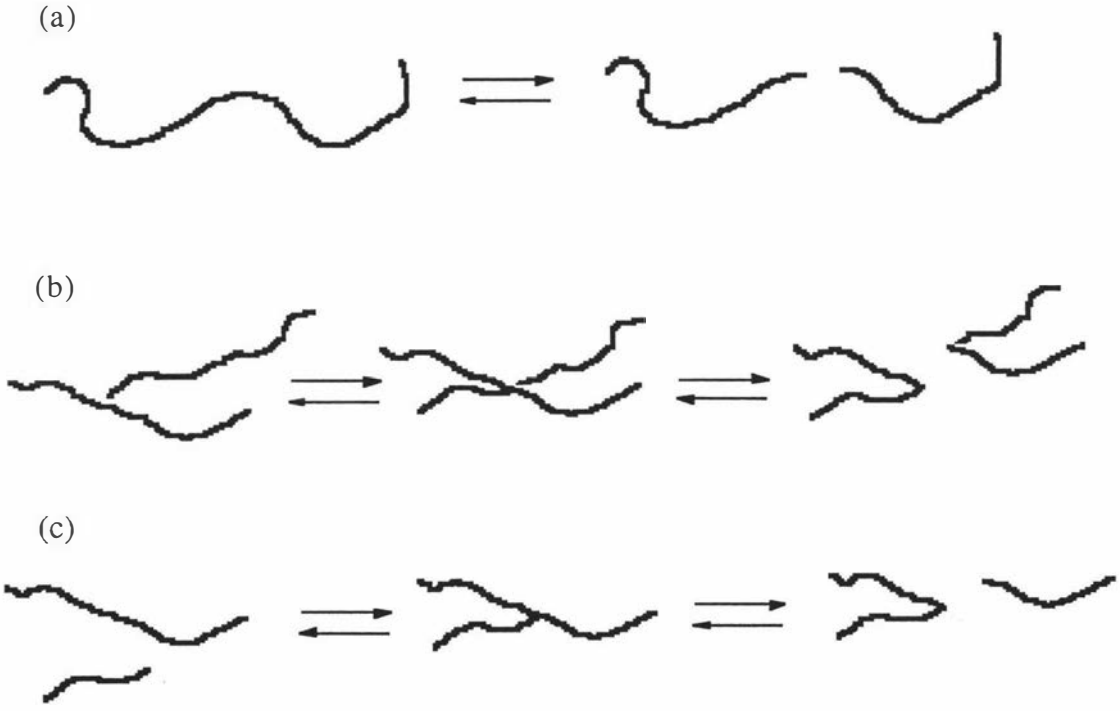

3.3.1.3 Bond interchange.

The bond-interchange mechanism is shown in Figure 3.9(b) and is the process where two chains pass through each other and interchange their broken segments. Cates concludes that this process does not contribute to stress relaxation since, contrary to what is experimentally observed the process shows non-monoexponential behaviour.

3.3.1.4 End interchange.

This reaction mechanism is shown in Figure 3.9(c) and involves one end of a micelle passing through the middle of another and swapping ends in the process. Cates model shows that the process has monoexponential behaviour and can be treated like scission.

3.3.1.5 End evaporation.

End evaporation is the relaxation process whereby surfactant monomers or groups of monomers (small micelles) in the end of a micelle "evaporate" into solution, effectively removing the micelle from a stressed environment. Such behaviour was shown to be non-monoexponential and does not contribute to the (experimentally found) stress relaxation process.

3.3.1.6 Rouse and breathing modes.

Rouse modes of relaxation can be visualised as contributions to the stress relaxation due to Brownian motion of "segments" in the equilibrium polymer chain. A polymer (both "conventional" and "equilibrium") has a randomly contorted configuration which is continually changing due to fluctuations in the local thermal energy i.e Brownian motion. Under a small stress (linear regime) these configurational changes are only slightly disturbed; the Brownian motion goes on just the same, but is influenced by the stress and, since the motion is very fast, shows up in the high frequency regime i.e. where the applied strain is so fast that the polymer cannot relax by Rouse modes before another perturbation. This type of relaxation was proposed by Rouse[5] who modelled a (conventional) polymer as a chain of beads (with properties of universal joints) connected by Hookean springs. These beads constitute the aforementioned "segments" within the equilibrium polymer.

Cates showed that these processes do contribute to the stress relaxation and manifest themselves as an upturn in the Cole-Cole plot at high frequency. His modified model[4] uses the height of this upturn to estimate rodlengths since it is found to scale with the number of entanglements along the chain. The relation is

[3–11] $$\frac{G''_{min}}{G'_{\infty}} \sim \frac{l_e}{\bar{L}}$$

where G'_{∞} is the value of the elastic component extrapolated to infinite ω and can be identified with G_0, G''_{min} is the value of the viscous component at the upturn, and l_e is the curvilinear length of a chain between two entanglement points. The entanglement length and another length scale, the mesh size ξ, the mean distance between entanglement points are depicted in Figure 3.10. Equation [3–11] will be used to obtain mean rodlengths in the TEAHFN/water system.

Figure 3.10 Length scales in an entangled network of rodlike micelles. ξ and l_e are, respectively, the mean distance (the mesh size) and curvilinear chain length between entanglement points.

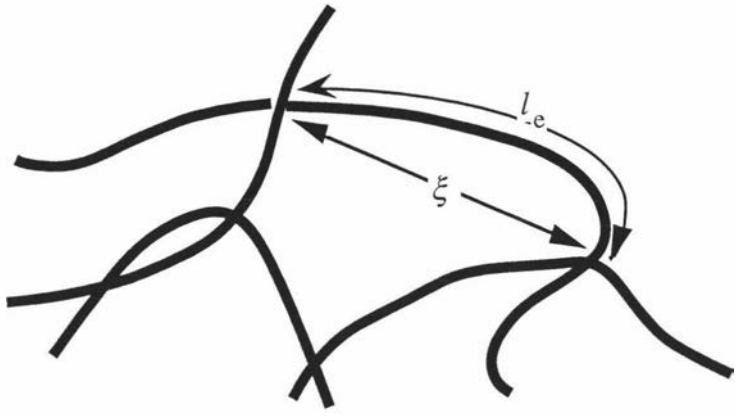

3.3.2 Cates' model predictions.

Cates considers two regimes: a **dilute regime** where the rods behave as essentially unbreakable chains, and a **semi-dilute regime** where the rods (or more correctly, their hydrodynamic radii) begin to overlap at the crossover concentration ϕ^* and scission reactions become important. In Cates' treatment, the mean rodlength $\bar{L}$ varies in both regimes by the same scaling law

[3–12] $$\bar{L} = 2\sqrt{\phi}\exp(E/2kT) \sim \phi^{0.5}$$

where E is the scission energy (assumed to be independent of ϕ). The size distribution represented by the volume fraction of micelles of size L, $C(L)$ is given by

[3–13] $$C(L) = \frac{\phi}{\bar{L}^2}\exp\left(-\frac{L}{\bar{L}}\right)$$

with the constraint of $\phi = \int L.C(L)\,dL$.

3.3.2.1 **Dilute regime** ($\phi < \phi^*$)

At low concentrations where rods are short there is no overlap of the micelles i.e. the sphere swept out by one rod (characterised by its hydrodynamic radius) typically does not contain parts of other rods. The scission/recombination reaction kinetics are very slow ($\tau_{rept} << \tau_{break}$) and the only effect of these reactions is to enforce chain polydispersity (thermal equilibrium of the molecular weight distribution). In the dilute regime the stress relaxation function $\mu(t)$ is mainly by reptation and has been shown to be an extremely non-exponential function. Below ϕ^* the zero-shear or static viscosity should increase weakly according to the Einstein relation $\eta_0 = \eta_{water}(1 + c\phi)$ where c~1.

3.3.2.2 Semidilute regime ($\phi > \phi^*$)

As surfactant concentration is increased rodlengths increase according to equation [3–12] and at ϕ^* the rods begin to overlap. Here chain scission and recombination reactions are fast enough ($\tau_{rept} >> \tau_{break}$) to directly affect the stress relaxation. Cates' model shows that when τ_{break} is fast with respect to τ_{rept} a nearly monoexponential stress relaxation is seen with a decay time given by

[**3–14**] $$\tau = \sqrt{(\tau_{rept}\tau_{break})}$$

The stress relaxation is monoexponential because the chainlength is being rapidly averaged i.e. before a given chain segment relaxes it undergoes many scission/recombination reactions so that there is no memory of the initial chain length or the position of the segment on the chain. Thus, since there is effectively no dispersion in chainlength, all segments relax at the same rate and there is no dispersion of relaxation times. Within the semidilute regime Cates' model predicts some power laws which describe the solution properties e.g. the zero-shear or static viscosity should vary according to $\eta_0 \sim \phi^{3.5}$. Theoretical exponents and those found experimentally elsewhere[16, 19, 21, 22] will be compared with those found in this work in section 3.4.3.

Now Cates' model will be applied to the systems under study here.

3.4 Application of Cates' model to TEAHFN and TMAHFN/water.

3.4.1 The TEAHFN/water system.

Viscoelastic spectra for the system TEAHFN/water represented as Cole-Cole plots are shown in Figure 3.11. The lines are fits to a Maxwell model with values of G_0 and τ shown in Table 3.1. The curves in Figure 3.11(a) all show monoexponential behaviour at low frequency but exhibit deviations at higher frequency, with the greatest

Figure 3.11 Cole-Cole Plots for TEAHFN/water at 21°C.

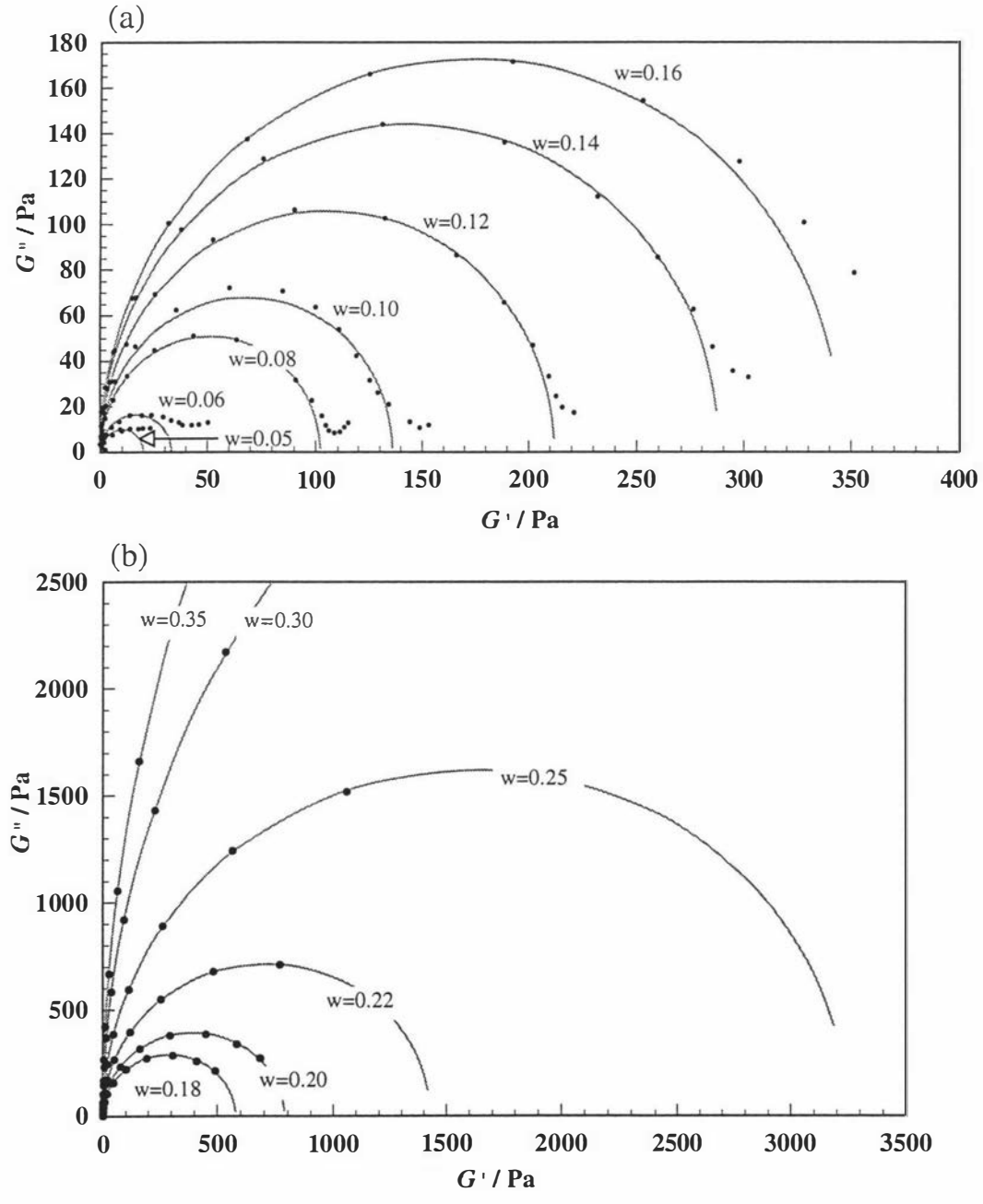

Table 3.1 Data extracted from fits to the Cole-Cole plots in Figure 3.11 for TEAHFN/water at 21°C.

w	ϕ	τ / s	G_0 / Pa	$G_0.\tau$ / Pa s	η_0 / Pa s
0.05	0.033	1	20	20	22
0.06	0.039	0.7	33	23	24
0.08	0.053	0.8	102	82	74
0.10	0.067	0.9	136	122	130
0.12	0.081	0.37	212	79	80
0.14	0.095	0.16	288	46	46
0.16	0.109	0.081	346	28	31
0.18	0.124	0.029	579	17	19
0.20	0.138	0.033	786	26	30
0.22	0.153	0.012	1427	17	20
0.25	0.176	0.0076	3244	25	-
0.30	0.216	0.0025	9212	23	-
0.35	0.257	0.0010	17196	17	-

deviation at the lowest concentrations examined (w = 0.05 and w = 0.06). At these concentrations the stress relaxation functions are non-monoexponential indicating a range of relaxation times. The dispersity in relaxation times is consistent with a dilute solution of unentangled rods where the dominant relaxation mode is *via* reptation i.e. where $\tau_{rept} < \tau_{break}$. As concentration is increased the relaxation time dispersity is rapidly lessened which can be seen in Figure 3.11 by the Cole-Cole curves becoming semi-circular. This is consistent with a crossover into the semidilute regime ($\phi > \phi^*$).

Figure 3.11(b) shows the highest concentrations examined. Here, any deviations from monoexponential behaviour are not evident because they fall outside the "experimental window" i.e. the rheometer used cannot physically reach high enough frequencies.

3.4.2 The TMAHFN/water system.

Viscoelastic spectra for the system TMAHFN/water represented as Cole-Cole plots are shown in Figure 3.12. The lines are fits to a Maxwell model with values of G_0 and τ shown in Table 3.2. The curves closely follow the form shown by TEAHFN/water in that the lowest concentration examined (w = 0.08) shows a dispersion of relaxation times indicative of the dilute regime ($\phi < \phi^*$) and, as concentration is increased, the the curves become more monoexponential. However at the highest concentrations at w = 0.18 and w = 0.20, where the data were collected

Figure 3.12 Cole-Cole Plots for TMAHFN/water at 21°C.

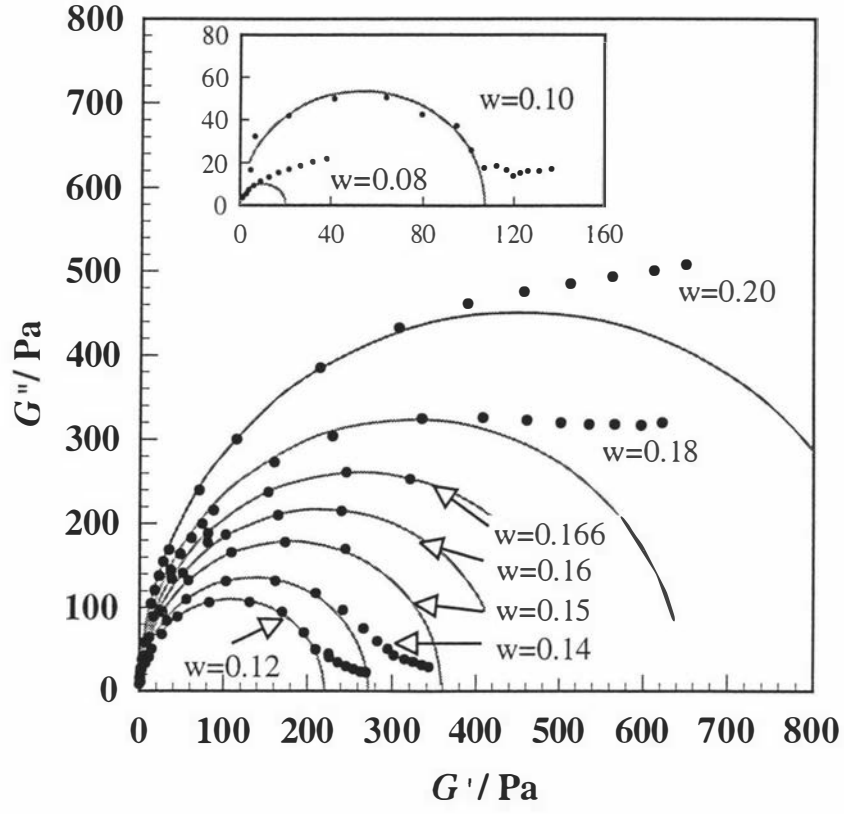

Table 3.2 Data extracted from fits to Cole-Cole plots for TMAHFN/water at 21°C.

w	ϕ	τ / s	G_0 / Pa	$G_0.\tau$ / Pa s	η_0 / Pa s
0.08	0.050	0.18	20	3.6	5
0.10	0.063	1.9	107	203	172
0.12	0.076	3.9	220	858	861
0.14	0.090	1.2	272	326	430
0.15	0.097	0.45	358	161	170
0.16	0.103	0.24	434	104	115
0.166	0.108	0.18	522	93	100
0.18	0.117	0.078	688	54	59
0.20	0.132	0.035	1004	35	42

using a Bohlin rheometer which could access slightly higher frequencies the curves appear to become less monoexponential. The origin of this is unclear, but by analogy to the low concentration spectra, it implies that reptative relaxation is becoming more important[21]. The spectra do not show sufficiently well-defined upturns at high frequency to extract estimates of rodlengths.

3.4.3 Comparison of scaling laws between experiment and theory.

The theoretical and experimentally[22] found exponents are contained in Table 3.3 for hydrocarbon systems in the presence (columns two and three) and absence (column four) of salt. Columns five and six contain the exponents calculated from fits to experimental data shown in Figures 3.13-3.16 for the TEAHFN/water and TMAHFN/water systems. These values will be compared individually in the next sections.

Table 3.3 Predicted and Experimental scaling law exponents.

	Systems with salt		Salt-free systems		
	theory[3, 4]	experiment[22]	12-2-12[19]	TEAHFN	TMAHFN
G_0	2.25	2.18	3.0	2.52	2.93
τ	1.24	1.13	-4.0	-5.0	-9.0
η_0	3.5	3.3	4.5	3.22	15
$\frac{}{L}$	0.5	0.36	-	-	-

3.4.3.1 The zero-shear viscosity η_0.

Figure 3.13 shows the zero-shear viscosity for both TEAHFN and TMAHFN systems. The low viscosity at low concentration is consistent with the dilute regime of a solution of essentially unbreakable rods ($\phi<\phi^*$). The onset of the rapid increase in viscosity with concentration indicates the crossover to the semi-dilute regime ($\phi>\phi^*$). ϕ^* cannot be estimated with accuracy from this data but a value for TMAHFN may be estimated from the kinetic measurements carried out by Hoffmann[23] using a pressure-jump technique. Here the disappearance of a slow relaxation process at $\phi = 0.0018$ at 20°C was interpreted as due to the presence of very large rod-like aggregates. This value can be compared to $\phi^* = 0.003$ in the similar perfluorocarbon surfactant TEAPOS/water system[16], $\phi^* = 0.015$ in the dimeric hydrocarbon surfactant 12-2-12/water system[19] and $\phi^* = 0.01$ for the single-chain hydrocarbon surfactant CTAB in 0.1M KBr (30°C)[24]. This comparison suggests that the estimates of the

absolute values of ϕ^* from the viscosities in Figure 3.13 i.e $\phi^* \approx 0.050$ for TMAHFN and $\phi^* \approx 0.039$ for TEAHFN are at least an order of magnitude too large and should be taken as upper limits, though the relative values may be useful for comparison. Interpretation of ϕ^* with respect to chainlength is ambiguous - in the absence of salt a higher ϕ^* could mean that (a) the rods are shorter, or (b) the rods are longer but more flexible and avoid entangling by being able to coil more tightly. It will be argued in section 3.5 that at corresponding ϕ *in the dilute regime* TMAHFN micelles are shorter than TEAHFN ones as a consequence of a lower bound-ion fraction and that this is responsible for the higher ϕ^*. Above ϕ^* the viscosity increases exponentially and the exponent of the viscosity power law of 3.22 for TEAHFN/water compares favourably with those predicted theoretically (3.5) and experimentally (3.3) for hydrocarbon systems however the value of 15.0 for TMAHFN/water is quite different. Anomalously high exponents were found in the TEAPOS/water system[16] with a value of 13 and CTAB/water[21] with a value of 12. It is significant that these systems do not contain salt, and the rapid increase in viscosity may reflect a rapid increase in rodlength which is theoretically predicted for highly charged equilibrium polymer systems. This too will be addressed in section 3.5.

The most striking feature of Figure 3.13 is the existence of maxima in viscosity. This phenomenon is not predicted theoretically but was seen in the TEAPOS/water and 12-2-12/water systems where it was interpreted as reflecting a maximum in rodlengths. This is consistent with the maximum in rodlengths calculated for TEAHFN shown in section 0. The values at which the maxima occur are shown in Table 3.4.

Table 3.4 Comparison of the maxima in zero-shear viscosity. ϕ_{max} is the concentration at the maximum.

	TEAHFN (21°C)	TMAHFN (21°C)	TEAPOS (25°C)	12-2-12 (20°C)
η_{max} / Pa s	130	861	50 000	1000
ϕ_{max}	0.067	0.076	0.023	0.07

The concentrations at which the TEAHFN and TMAHFN maxima occur compare well with the 12-2-12 system but ϕ_{max} is three times lower in the TEAPOS system. Correcting for the difference in temperature would shift ϕ_{max} of TEAPOS even lower which suggests that the value of ϕ_{max} may not be universal. Assuming η_{max} reflects mean rodlengths the higher value for TMAHFN would suggest longer rods than

TEAHFN *at this concentration*. The occurrence of maxima in viscosity is paralleled by an increasing zero-shear modulus G_0 and decreasing τ since η_0 varies as the product $G_0.\tau$. The variation of G_0 and τ with concentration is discussed below.

Figure 3.13 Concentration dependence of the zero-shear viscosity for (a) the system TEAHFN/water (the dotted line is $\eta_0 \sim \phi^{3.22}$), and (b) TMAHFN/water (the dotted line is $\eta_0 \sim \phi^{15.0}$)

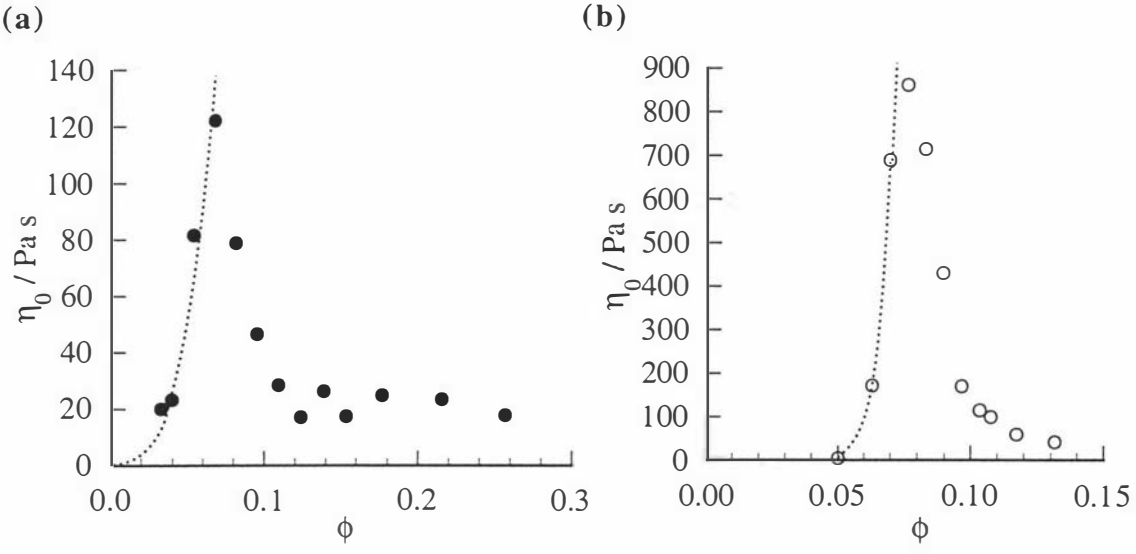

3.4.3.2 The zero-shear modulus G_0.

Figure 3.14 shows the concentration dependence of the zero-shear or plateau modulus for (a) TEAHFN/water and (b) TMAHFN/water. A significant feature is the apparent increase in the exponent near $\phi \approx 0.1$ from 2.52 to 4.76 in the TEAHFN system where none could be detected in the TMAHFN system. This phenomenon has not been seen in other systems and may in fact not be real. It should be noted that the values of G_0 at higher ϕ are subject to the most error since they were obtained from fits to data corresponding to only a very small portion of the semi-circle (see Figure 3.11(a)) which is a consequence of the physical limitations of the rheometer used. If the higher concentration data are neglected then the exponents of the two systems do compare favourably, both with each other and with those obtained in other systems. An exponent of 3.0 was found in the 12-2-12 system in the absence of salt. It may even be that there is no difference between the TEAHFN and TMAHFN data, suggested by the close correspondence of the absolute values as a function of ϕ shown in Figure 3.15.

Figure 3.14 Concentration dependence of the plateau modulus G_0 in (a) the system TEAHFN/water and (b) TMAHFN/water at 21°C.

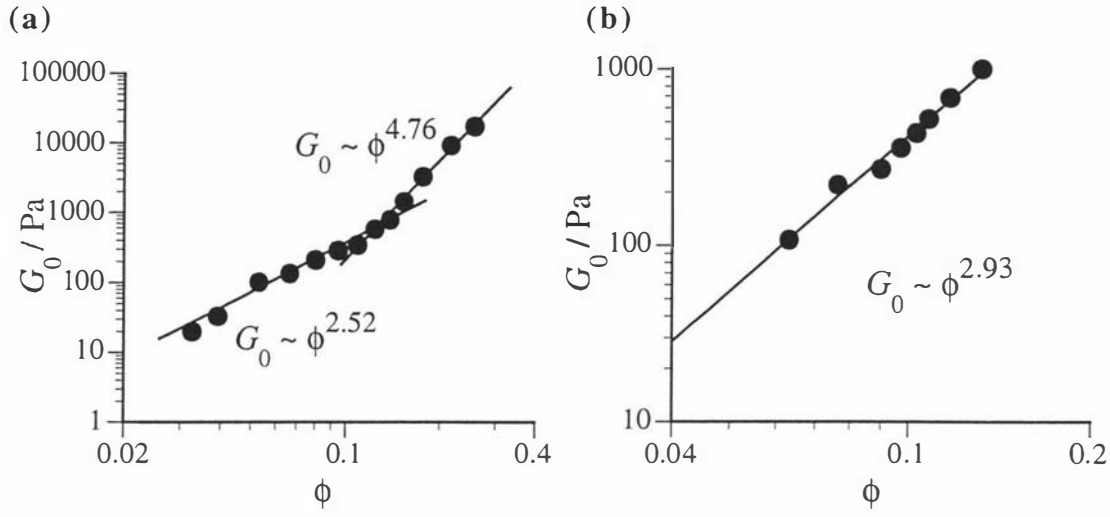

Figure 3.15 Comparison of TEAHFN and TMAHFN zero-shear moduli at 21°C

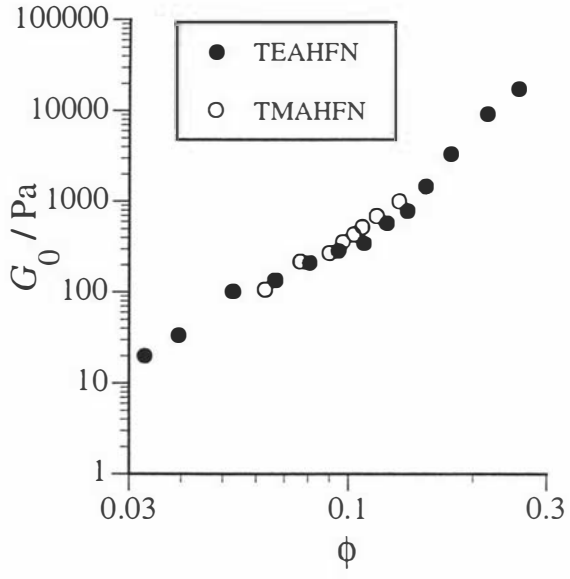

3.4.3.3 The terminal relaxation time τ.

Figure 3.16 shows the concentration dependence of the terminal relaxation time of TEAHFN and TMAHFN. The exponents of -5.0 (TEAHFN) and -9.0 (TMAHFN) are of opposite sign to those predicted and found experimentally for systems in the presence of salt contained in Table 3.3 but can be compared with -4.0 (20°C) and -2.6 (25°C) for the 12-2-12 system[19]. The anomalous difference in sign was left unexplained. Cappelaere *et al*[21] found an exponent of 62 for salt-free CTAB at 30°C. The variation of τ for salt-free systems is unclear since equation [3–14] applies to salt-containing systems in the semi-dilute regime while for inflexible chains τ varies according to[25] $\tau=\tau_{break}^{5/7}\tau_{rot}^{2/7}$ where τ_{rot} is the characteristic time scale for the angular relaxation of an unbreakable rod. Since the behaviour of TEAHFN and TMAHFN should be intermediate to these extremes a firm interpretation of a decreasing τ cannot be made - it could be a consequence of either a decreasing breaking time or of the rods getting shorter, or both. Figure 3.17 compares the absolute values of τ for the two systems and, ignoring a wayward point, there appears to be a real difference in their behaviour.

Figure 3.16 Concentration dependence of the terminal relaxation time in (a) the system TEAHFN/water and (b) TMAHFN/water at 21°C.

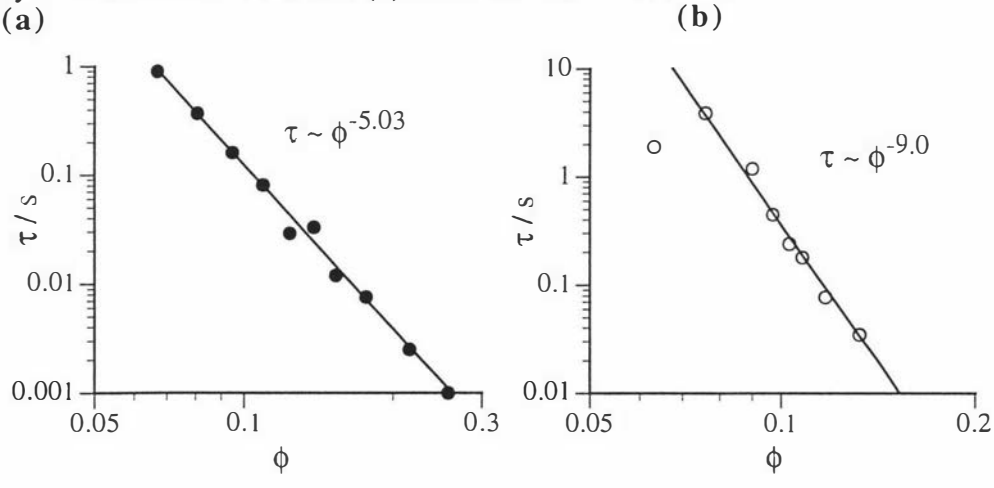

Figure 3.17 Comparison of TEAHFN and TMAHFN terminal relaxation times at 21°C.

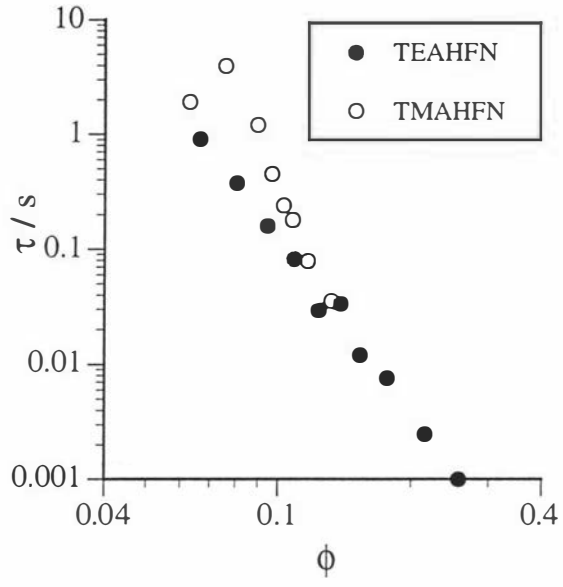

3.4.4 Mean rodlengths from rheology.

The only Cole-Cole plots that lend themselves to the determination of chainlengths i.e those that show an upturn at high frequencies occur over the range 0.6<w<0.14. In order to use equation [3–11], an estimate for the entanglement length l_e is required. Kern *et al*[19] in their investigation of 12-2-12 used

[**3–15**] $$G_\infty \cong \frac{kT}{\xi^3}$$

and the relation $\xi = l_e^{2/5} l_p^{2/5}$ where l_p, the persistence length, is that length over which the axis of the cylinder is constant in direction and can be viewed as a measure of the chain stiffness. Values of l_p for fluorocarbon systems are not known but a reasonable estimate is that used for 12-2-12 (l_p = 15 nm). This should represent an upper limit since the persistence length is a function of the electrostatic repulsion between surfactant headgroups (or alternatively, the effective charge per unit cylindrical chainlength v) and, neglecting counterion effects, it is reasonable to assume this to be less for fluorocarbons than hydrocarbons due to the electron-withdrawing effect of the fluorine atoms[26]. For the purpose of calculating the variation of $\bar{L}$ the absolute value of l_p is not critical if the assumption of its concentration independence[27] is correct. Values used to calculate mean rodlengths $\bar{L}$ using l_p = 15 nm are shown in Table 3.5 and plotted in Figure 3.18.

Table 3.5 Values used to calculate mean rodlengths.

w	ϕ	G''_{min} / Pa	G'_{∞} / Pa	G''_{min}/G'_{∞}	l_e / nm	$\bar{L}$ / nm
0.06	0.039	12	33	0.364	110.6	304
0.08	0.053	9	102	0.088	59.1	670
0.10	0.067	13	136	0.096	50.4	527
0.12	0.081	18	212	0.085	39.4	464
0.14	0.095	34	288	0.118	33.2	281

It should be noted by examination of Figure 3.11 that the upturns at high frequency used to calculate $\bar{L}$ are not well defined which could introduce significant error. However the trend is clear - the mean rodlengths go through a maximum as concentration is increased. This is contrary to the scaling laws predicted by Cates in Table 3.3 (where $\bar{L}$ should vary according to $\phi^{0.5}$) but in agreement with the trend found experimentally for 12-2-12 using rheology where the maximum rodlength found was 2000 nm (about twice the lengths found here) and Hoffmann *et al*[28] who studied alkylammonium bromides of various chainlengths using light scattering techniques and found the maximum rodlengths varied from about 300-700 nm (about the same as lengths found here).

Figure 3.18 Concentration dependence of mean rodlength in TEAHFN/water.

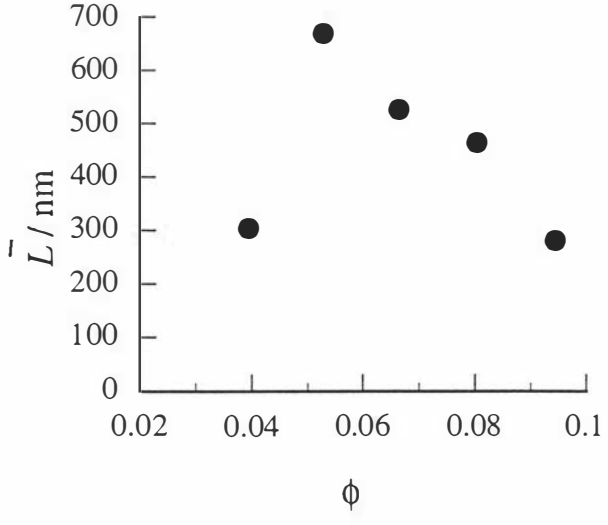

3.4.5 General summary of results and comparison of systems with and without salt.

In comparing systems with and without salt some generalisations may be made:

(a) The zero-shear modulus power law exponents of TEAHFN agrees more with those found in salt-containing systems than both 12-2-12 and TMAHFN.

(b) The exponent of τ for all salt-free systems is of opposite sign to that predicted and found experimentally in salt systems.

(c) TMAHFN (and some other systems without salt) have greatly enhanced viscosity exponents compared to TEAHFN and salt systems.

(d) Mean rodlengths go through a maximum in salt-free systems whereas they only increase in salt systems.

(e) The crossover concentration ϕ^* for TEAHFN is lower than that for TMAHFN.

These results expose real differences in behaviour between systems in the presence and absence of salt and it is appropriate to introduce the modified prediction of the growth of rodlike micelles in the absence of salt proposed by Mackintosh *et al*[13-15].

3.5 Modified prediction of growth of charged rodlike micelles.

It has been shown that any interaction dependent only on surfactant concentration ϕ does not affect the size distribution[29]. Two interactions which do not depend only on ϕ are (i) orientational interactions, which cause nematic ordering at high concentration (mean rodlengths experience an increase by a factor of 1.6 over the isotropic to nematic (phase of rods) transition[24]), and (ii) electrostatic interactions, important at low or zero salt, as is the case in these systems. Case (i) should not apply since the surfactant concentrations where rods exist are low and no ordered phase of *rods* has been observed. It would also be revealed in the zero-shear modulus which is predicted to decrease with nematic ordering[19, 21, 25] and no such decrease occurs. However the latter case has been treated theoretically[13-15] and E shown to be no longer ϕ-independent. For *uncharged* micelles or micelles in the presence of salt the scission energy E can be equated with the endcap energy E_{cap}, the energy required to form two hemispherical endcaps where there were none before. The addition of salt reduces the effective headgroup area by screening electrostatic interactions, destabilising endcaps relative to the cylindrical body (i.e. E_{cap}-E_{cyl} increases) and so causes an increase in mean rodlength. For *charged* micelles E is composed of E_{cap} and the repulsive energy of the surface charges E_{elect} which favours smaller micelles and is given by

[3–16] $$E_{elect} = \frac{l_B a v^2}{\sqrt{\phi}}$$

where $l_B = e^2/\varepsilon kT$ is the Bjerrum length, a is the micelle diameter and v is an effective charge per unit chainlength. An additional effect at high ϕ is the increased entropy of counterions near the endcaps. This leads to a complicated behaviour which cannot be described by a simple power law e.g. by equation [3–12]. Three regimes can be identified:

(i) A **dilute regime** ($\phi<\phi^*$) where the Debye length $\kappa^{-1} > \bar{L}$. Here the distribution is very narrow and $\bar{L}$ increases very slowly according to

[3–17] $$\bar{L} = \frac{1}{l_B a v^2}\left(E_{cap} + \log\frac{\phi}{\bar{L}}\right)$$

(ii) A **semi-dilute regime** where $\kappa^{-1} < \bar{L}$ and $\phi>\phi^*$ i.e micelles begin to overlap. Here a collective screening of the electrostatic interaction sets in (similar to the addition of salt) and $\bar{L}$ increases very rapidly. The distribution is broad as in equation [3–12] but E is replaced by (E_{cap}-E_{elect}). Mean rodlengths are thus given by

[3–18] $$\bar{L} = 2\sqrt{\phi}\exp\left[\frac{1}{2}\left(E_{cap} - E_{elect}\right)\right]$$

The value of ϕ^* is given by

[3–19] $$\phi^* \approx \left(\frac{kTl_B a v^2}{E_{cap}}\right)^2$$

(iii) A **concentrated regime** where $\phi>>\phi^*$. The dominant electrostatic contribution is that of the entropy of the counterions near the endcaps. This arises because the counterions are less tightly bound there relative to the cylindrical body. Both the fraction of counterions which escape and the volume they occupy depend on concentration[14]. $\bar{L}$ is characterised by an effective power law similar in form to equation [3–12] but with the exponent of 1/2 corrected by a term Δ thus

[3–20] $$\bar{L} \sim \phi^{0.5(1+\Delta)}$$

where Δ is related to the effective charge on an endcap (the degree of ionization) which depends logarithmically on the ambient charge density and hence, in the absence of salt, only on ϕ. The effect of this term is to *increase* the rate of growth of $\bar{L}$ relative to

systems with added salt (where $\Delta \rightarrow 0$). It is evident that the systems under study here do not behave in this manner in the concentrated regime.

Figure 3.19 shows the theoretical variation of mean rodlengths over the dilute and semi-dilute regimes predicted in (a) the presence (Cates' model) and (b) the absence of salt (Mackintosh' model). Cates' model assumes that the scission energy E is ϕ-independent and thus the size distribution is governed only by ϕ *via* equation [3–12]. The variation of the mean rodlength $\bar{L}$ by this equation is shown by curve (a) in Figure 3.19. Since the width of the distribution varies as $\bar{L}/\sqrt{2}$[24], this also increases according to $\sqrt{\phi}$. The corresponding rodlength distribution as a function of ϕ is depicted in Figure 3.20(a). The prediction of micellar growth modified by the presence of electrostatic interactions is shown by curve (b) in Figure 3.19. Initially $\bar{L}$ increases very slowly according to equation [3–17] until ϕ^* is reached (ϕ^* is given by equation [3–19] and shown by curve (c)) whereupon $\bar{L}$ increases steeply according to equation [3–18]. The corresponding distributions are shown in Figure 3.20(b) where it can be seen that the micelle distribution is very narrow below ϕ^* but broadens explosively above it.

Figure 3.19 Comparison of theoretical mean rodlengths $\bar{L}$ in (a) the presence and (b) the absence of salt. Curve (c) represents the crossover concentration ϕ^*.

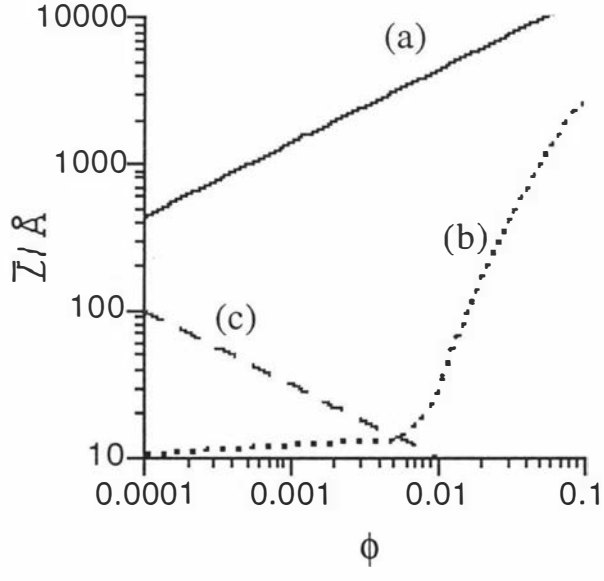

Figure 3.20 Comparison of theoretical rodlength distributions $C(L)$ in (a) the presence and (b) the absence of salt. $C(L)$ represents the volume fraction of micelles of size L given by equation [3–13]. The origin is at the top left corner. In the absence of salt (figure (b)) the micelle length L grows very slowly with total volume fraction ϕ and then rapidly increases around the crossover concentration ϕ^*. Note the condensed rodlength scale in (b).

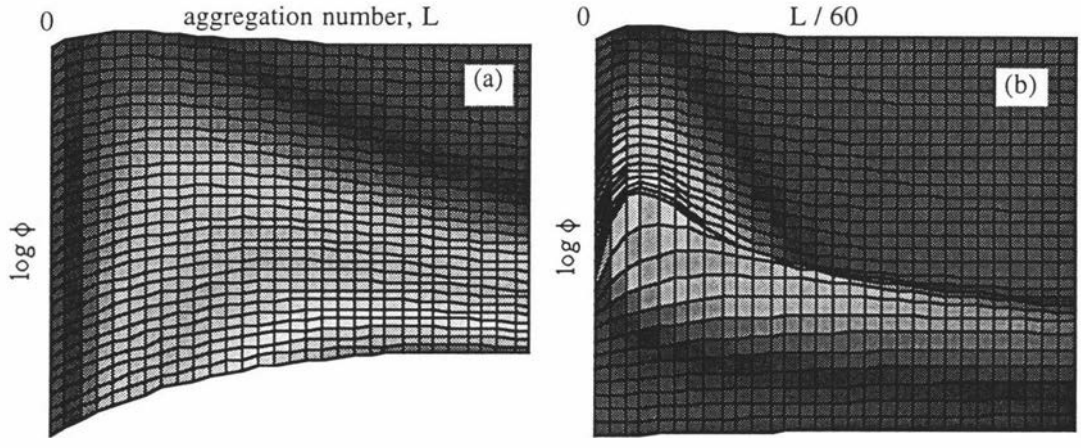

3.5.1 Application of the modified growth model to TEAHFN and TMAHFN/water systems.

Within the theoretical models presented above, the experimental results that (a) the crossover to an entangled regime at ϕ^* for TMAHFN occurs at a higher concentration than that for TEAHFN, and (b) TMAHFN has a much steeper increase in viscosity after ϕ^* than TEAHFN indicate that TMAHFN micelles are more highly charged than TEAHFN micelles. The closer agreement of the exponents of the power laws between TEAHFN and hydrocarbon surfactant systems with added salt supports this conclusion. Since the chainlength is the same in both systems, differences between the two systems must originate in differences in counterion binding. Evidence for differences in counterion binding will be presented at the end of this chapter.

However, neither of the theoretical treatments of micellar growth predict maxima in the ϕ-dependence of the rodlength which is implied by the maxima in viscosity. The modified prediction of rodlengths in the presence of electrostatic interactions assumes the effective charge per unit chainlength v is independent of ϕ. This is unrealistic since v varies with the degree of ionisation which has been shown[13] to increase with ϕ. An increasing v with ϕ would decrease micellar growth as a consequence of two effects: (i) by increasing E_{elect} *via* equation [3–16] and (ii) by decreasing E_{cap} since this represents the packing energy of surfactant *and* counterions. If the number of condensed counterions per surfactant decreases with increasing ϕ then

E_{cap} decreases[19]. This may be the origin of the decrease in rodlength†. In the absence of estimates of the electrostatic interactions at a molecular level i.e. knowledge of the ϕ-dependence of v and E_{cap} in these fluorocarbon systems, the effect on the rodlength calculations cannot be quantitatively assessed.

3.6 Behaviour of TMAHFN/water over the liquid crystal phase transitions.

In an attempt to delineate the transition from rods to disks in the isotropic phase rheological measurements on TMAHFN/water were extended to cover the behaviour on the approach to, and within, ordered phases. The liquid crystal phases have been extensively studied by NMR[30], SANS[31] and SAXS[32] and there is strong evidence to suggest they are formed from disklike aggregates (this will be presented in Chapter 5). Figure 3.21 shows a sequence of Cole-Cole plots for three concentrations in the isotropic phase (w = 0.18, 0.20, 0.22) and one each in the nematic (w = 0.23) and lamella phases (w = 0.24) at 21°C.

Figure 3.21 Rheological behaviour of TMAHFN/water in the isotropic (w = 0.18, 0.20, 0.22), nematic (w = 0.23) and lamellar (w = 0.24) phases at 21°C.

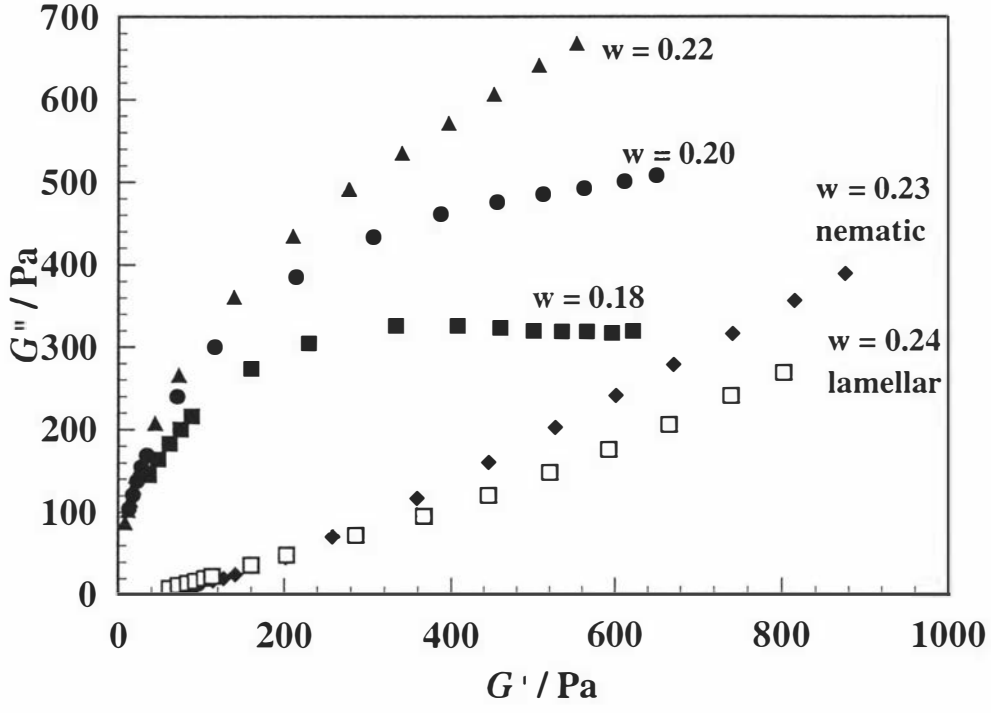

† An unfortunate consequence of invoking a variable charge per unit length with concentration is that the persistence length will vary as well which invalidates the assumption that l_p remains constant used in the calculation of mean rodlengths. However this also affects the entanglement length l_e in an opposing manner and the calculations may still be meaningful.

From the lowest concentration $w = 0.18$ to the concentration $w = 0.22$ immediately before the phase transition the curves show (i) an increasing dispersion in relaxation times consistent with increasing effect of reptation (of essentially unbreakable short rods, or possibly the relaxation of other particles - disks), and (ii) no decrease in G_0 which would be indicative of orientational ordering near the transition. At $w = 0.23$ (discotic nematic phase) the viscous modulus G'' drops away which is consistent with the ordering of anisometric particles[21] though the shape of the particles cannot be inferred. At $w = 0.24$ G'' is even lower and coincides with the lamella phase. No clear transition other than between those determined by other methods can be observed by these measurements. The behaviour of isotropic phase samples near to the transition may not preclude the existence of disks and that no pretransitional ordering occurs may even imply rod/disk co-existence.

3.7 Discussion of results from rheological measurements.

It has been shown here that the substitution of TEA^+ and TMA^+ ions for ammonium ions in HFN^- micelles in the isotropic phase promotes the formation of very long rod-like micelles, and that as surfactant concentration is increased, the rodlengths go through a maximum.

Interpretation of the concentration dependence of G_0 and τ with concentration is rather conjectural since current theories apply to systems in the presence of salt. However within Cates' model for flexible micelles G_0 $(=G_\infty)$ varies with the mean distance between entanglement points ξ according to equation [3–15]. As G_0 increases this implies the mean distance grows smaller, and this is supported by the decrease in l_e with concentration in Table 3.5. Since ξ is independent of chainlength this does not preclude a shortening of the mean rodlengths. Within the simplistic Maxwell model, an increasing G_0 can be interpreted as an increase in "stiffness of the spring" due to the entangled network of elastically deforming chains.

The terminal relaxation time τ appears to be responsible for the observed maxima in viscosity since (i) τ decreases with ϕ, (ii) the zero-shear moduli are comparable between the two systems and both increase with ϕ, and (iii) the viscosity is related by $\eta_0 = G_0 . \tau$. The product $G_0\tau$ closely follows the values of η_0 tabulated in Table 3.1 and Table 3.2. Physical interpretation of a decreasing τ as a consequence of decreasing τ_{break}, τ_{rept} and/or τ_{rot} does not rule out a shortening of rodlengths.

The rheological behaviour of TMAHFN/water approaching the liquid crystal phase boundary shows no diminishment in "rodlike" behaviour. This may not bar the existence of disks before the transition. Froba *et al*[32] using SANS and SAXS measurements found that the aggregate shape of TMAHFN before the I-to-N transition at 40°C could be modelled satisfactorily by a small ellipsoid. However the model they used was based on spherical interacting particles and it was admitted that their interpretation should be regarded with care.

The points above give the following picture of the behaviour of TEAHFN and TMAHFN between the cmc and the I-to-N transition (see Figure 3.22): Initially rodlike micelles grow with concentration ϕ until they become entangled at ϕ^*. The rodlengths increase rapidly and the network becomes more and more entangled until ϕ_{max} is reached, whereupon they begin to decrease in length as a consequence of (unknown) intermicellar interactions. This is not at odds with a decreasing meshsize - the number density of rods is increasing with ϕ as the rodlength decreases. The increasing ionisation causes a simultaneous decrease in rod flexibility consistent with a decreasing l_e and "stiffness" of the network. Nematic ordering of the rods does not occur because the cylindrical micellar length-to-diameter ratio is insufficiently large (and may also be inhibited by the presence of anisometric aggregates of a different shape i.e. disks), but excluded volume effects require some sort of ordering at a critical concentration and temperature, whereupon the disordered network of short rods (and/or disks) macroscopically rearranges to form a nematic phase of disk-like aggregates.

The question remains as to why rods give way to disklike aggregates either before or at the I-to-N transition. The answer may also lie in the degree and strength of the counterion binding coupled with intermicellar interactions all varying in a complicated way with concentration. Counterion interactions modify the optimal headgroup area to favour one shape over another. Gelbart *et al*[33] proposed a phenomenological model that allowed the coexistence of rods and disks but the model predicts, in contrast to these results, that disks should give way to rods as concentration is increased.

The differences in phase behaviour between TEAHFN/H_2O and TMAHFN/H_2O, and the un-alkyl-substituted ammonium system AHFN/H_2O, which does not exhibit viscoelasticity at any concentration in the isotropic phase, must lie in differences in the degree and strength of counterion binding to the micelle surface. A discussion of some unusual counterion effects encountered here and in other systems with alkyl-substituted ammonium counterions follows.

Figure 3.22 Schematic showing the evolution of the rod-like micelle length L and the mesh size ξ with concentration ϕ between the cmc and the isotropic-to-nematic (I-to-N) transition. Though L goes through a maximum, ξ can continue to decrease as a consequence of increased micelle number density. ϕ^* indicates the crossover concentration where the rods' hydrodynamic radii (represented by dashed circles) just begin to overlap. ϕ_{max} is the concentration at which the maximum in viscosity occurs. The last panel includes possible rod/disk co-existence.

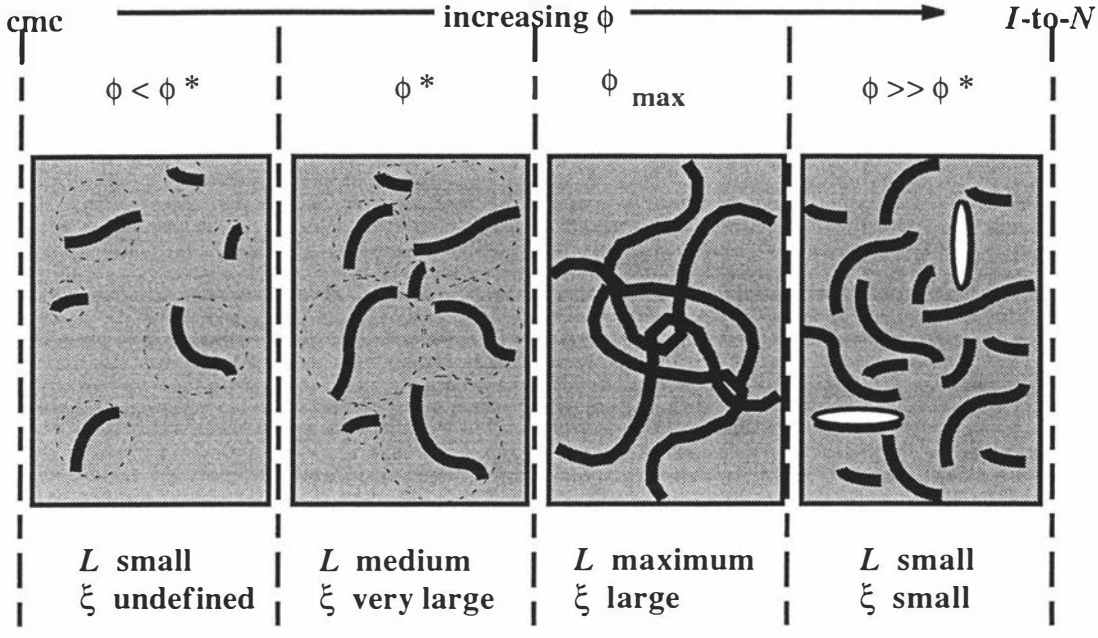

3.8 Unusual TMA^+ and TEA^+ counterion effects.

From the results presented above for the TMAHFN/water and TEAHFN/water systems, and the recent x-ray experiments[34] on the APFO/NH_4Cl/water system where it was shown that very short rods exist at low surfactant concentration, it can be generally concluded that salts of perfluorocarboxylic acid surfactants all show the same evolution of micelle shape with increasing concentration i.e. from a molecular solution→rods→disks, but with the concentration range over which each micelle type persists and the size of the aggregates formed varying with the counterion. Superimposed on this are intermicellar interactions which also affect the micelle size and shape[24]. The substitution of tetraalkylammonium ions for ammonium ions profoundly increases the concentration range over which rods occur and must originate in differences in the strength and degree of counterion binding. Evidence for other peculiar effects associated with tetraalkylammonium ions follows.

3.8.1 Evidence from cmc determination.

Cmc's determined in this work and elsewhere are summarised in Table 3.6. Those determined by conductivity allow an estimation of the free ion fraction ($1-\beta$) and these values are included in the table. The table shows that tetraalkylammonium (TAA^+) perfluorosurfactants have greatly reduced cmc's and are considerably less ionised with respect to their ammonium and alkali metal ion counterparts. Mukerjee[46, 47] used differential conductance methods to examine the micellisation of SDS/NaPFO mixtures and demonstrated the formation of fluorocarbon-rich and hydrocarbon-rich micelles.

Table 3.6 Comparison of cmc's and free counterion fractions ($1-\beta$) of the perflurocarbon surfactants perfluorooctanesulphonate (POS^-), perfluorononanoate (HFN^-) and perfluorooctanoate (PFO^-) at 25°C.

	[a] POS^-		HFN^-		PFO^-	
	cmc / mM	($1-\beta$)	cmc / mM	($1-\beta$)	cmc / mM	($1-\beta$)
Na^+	5.5	-	[b] 9.1	0.55	[c] 32	0.46
Li^+	6.4	0.70	[a] 10.8	0.49	[d] 37	-
NH_4^+	5.5	-	-	-	[e] 24.4	0.42
TMA^+	1.75	0.22	[e] 4.5	0.18	-	-
TEA^+	0.88	0.17	[e] 3.5	0.23	[f] 7.2	-

[a] refs 23, 42, 43

[b] ref 42 (30°C)

[c] ref 44

[d] ref 45

[e] this work

[f] ref 46

This was attributed to the nonideality of chain mixing[¥]. The apparent anomaly presented by the strong affinity of TEA^+ for the PFO^- micellar surface, evident from the much lower cmc of TEAPFO compared to NaPFO, was rationalised by making the distinction between contact hydrophobic interactions and hydrophobic processes in which chain mixing is involved. For contact interactions, it was asserted that water-structure effects were likely to be of greater importance, the driving force for the interaction deriving from the reorganisation of water around the hydrophobic counterion. Mukerjee attributes the much lower cmc's of fluorocarbon surfactants (in general) compared to their hydrocarbon analogues to water-structure effects, evident in the much greater volume change on fluorocarbon surfactant micellisation.

The conclusions by Mukerjee are intuitively correct since TAA^+ ions will have a greater affinity for the fluorocarbon/water interface on interfacial tension grounds. If three immiscible liquids having different interfacial tensions e.g. a fluorocarbon, a hydrocarbon and water are brought into contact, the liquid of intermediate interfacial tension (the hydrocarbon) will form between those most unalike[48] (fluorocarbon and water)(neglecting density considerations).

3.8.2 Evidence from kinetic measurements.

Hoffmann *et al*[23, 42, 43] compared the kinetics of LiHFN and TMAHFN above the cmc by a pressure jump technique and showed the micellar dissociation rate to be two orders of magnitude slower for the TMAHFN/water system. The authors also compared the lithium and TEA^+ salts of perfluorooctanesulphonic acid (POS) and found a similar result. This was interpreted as suggesting that the hydrophobic counterions form a barrier to the monomer exchange process. In comparing the effect of partial substitution of alkyl groups onto the ammonium counterion, the POS^- dissociation rate was found to decrease with increasing hydrophobicity according to $CH_3NH_3^+ > C_2H_5NH_3^+ > (CH_3)_2NH_2^+ > TEA^+$ and it would be reasonable to assume ammonium and TMA^+ ions form less of a barrier to monomer exchange than TEA^+ ions according to $NH_4^+ >> TMA^+ > TEA^+$.

[¥] The antipathy between fluorocarbons and hydrocarbons is a useful phenomenon exploited in this work. It allows the assumption of non-solubilisation of additives i.e co-solvents inside the micelle to be made for fluorocarbon surfactants whereas work on hydrocarbon surfactants suffers in this respect.

3.8.3 Evidence from light scattering.

Light scattering[49] was used to study the (purportedly unique) existence of a cloud point of NaPFO in the presence of tetrapropylammonium (TPA) bromide. Although this may be merely an example of general phase separation phenomena at high salt (the system could be viewed as TPAPFO in the presence of NaBr), it is interesting that the authors did not observe a cloud point with tetraalkylammonium counterions substituted with shorter alkyl-chainlengths.

3.8.4 The case for ion-specific interactions.

The experimental evidence presented above highlights the unusual effects encountered where alkyl-substituted ammonium ions form one component of a self-assembling system. Evans[50] has noted that specific ion-binding effects do not generally occur in anionic surfactants *unless the counterion is hydrophobic*, though no qualification was given to the significance of the amphiphile polarity.

Examples of unusual counterion effects abound in literature. A classic example is the Hofmeister effect, which describes the relative affinities of anions for self-assembled cationic surfaces according to $I^- > ClO_4^- > Br^- > Cl^- > F^-$. Another ion-specific effect[51] is the suppression of bubble coalescence by the addition of salts of only certain ion-pair combinations. Interestingly, one combination is the tetramethylammonium acetate ion-pair. Recently, Ninham[53] argued that present theories of self-assembly concentrate on the role of electrostatic forces and neglect the role of dispersion forces in determining ion adsorption, and that when they break down, rather than discard the theory as being inadequate, some "ion-specificity", varying from case to case, is invoked[†] (as it is being invoked here!). He demonstrated that dispersion forces can be quite large, and that under certain circumstances (where the debye length <1.2 nm) can even dominate. Using the Hofmeister series as an example, he argued that when dispersive forces are taken into account, ion-specificity emerges naturally. It should be noted that the debye length may be shorter in perfluorocarbon surfactants since the formal charge on e.g. a perfluorinated carboxylate ion is reduced with respect to its hydrocarbon analogue due to the electron-withdrawing effect of fluorine atoms. Dispersion forces increase with polarizability α (or polarizability volume $\alpha' = \alpha/(4\pi\varepsilon_0)$). Table 3.7 compares values of α' for some perfluorooctanoate salts, and the larger α' for the TMA^+ salt shows that there will be an increased dispersive component of the attraction potential for this counterion, albeit a small one.

[†] Nagarajan's model presented in Chapter 4 contains an ion-specific correction factor δ.

In summary, experimental evidence has been presented to show that TEA^+ and TMA^+ ions have a greater affinity than ammonium ions for the micellar interface and possible origins of this greater affinity have been suggested. This effect may explain the promotion of long rod-like micelles by these counterions. The greater/stronger binding of these ions to the micelle surface causes self-assembled HFN^- ions to "prefer" a more curved environment (rods over disks) by virtue of the greater counterion volume. The rods grow to very great lengths because the cylindrical body of the rod is stabilised with respect to the hemi-spherical endcaps. It is more favourable for alkyl-substituted counterions to be at the surface because this minimises (a) the fluorocarbon/water interfacial tension, and (b) the hydrophobic hydration of the counterions. However, the transition from rods to disks cannot be explained in terms of current theories for surfactant self-assembly and self-organisation and is probably the result of an exceedingly complex combination of intra- and intermicellar interactions and differences in counterion binding varying both with surfactant concentration and ionic strength.

Table 3.7 Polarizability Volumes α' of PFO^-M^+ surfactants [52].

M+	α' / 10^{-24} cm^3
Li^+	17.7 ± 0.2
Na^+	17.8 ± 0.2
NH_4^+	19.0 ± 0.1
TMA^+	25.9 ± 0.25

3.9 References.

1. Ferguson, J. and Z. Kemblowski *Applied Fluid Rheology*; Elsevier Science: London, 1991;

2. Whorlow, R.W. *Rheological Techniques*; Editor Ed.; Ellis Horwood: London, 1992;

3. Cates, M.E., *Macromolecules* **1987**, *20*, 2289.

4. Granek, R. and M.E. Cates, *J. Chem. Phys.* **1992**, *96*, 4758.

5. Doi, M. and S.F. Edwards *The Theory of Polymer Dynamics.*; Clarendon: Oxford, 1986;

6. Khatory, A., *et al.*, *Langmuir* **1993**, *9*, 1456.

7. Kern, F., R. Zana, and S.J. Candau, *J. Phys. Chem.* **1991**, *7*, 1344.

8. Appell, J., *et al.*, *Journal de physique II* **1992**, *2*, 1045.

9. Kern, F., *et al.*, *Langmuir* **1992**, *8*, 437.

10. Candau, S., *et al.*, *Journal de Physique IV* **1993**, *3*, 197.

11. Khatory, A., *et al.*, *Langmuir* **1993**, *9*, 933.

12. Cates, M.E., *Of Micelles and Many-Layered Vesicles.*, in *to be published.* 1995,

13. Safran, S.A., *et al.*, *J. Phys. France* **1990**, *51*, 503.

14. MacKintosh, F.C., S.A. Safran, and P.A. Pincus, *Europhysics Letters* **1990**, *12*, 697.

15. Odijk, T., *J. Phys. Chem.* **1989**, *93*, 3888.

16. Angel, M., *et al.*, *Ber. Bunsenges. Phys. Chem.* **1989**, *93*, 184.

17. Schmitt, V. and F. Lequeux, *Europhysics Letters* **1995**, *30*, 31.

18. Schmitt, V. and F. Lequeux, *Journal de Physique II* **1995**, *5*, 193.

19. Kern, F., *et al.*, *Langmuir* **1994**, *10*, 1714.

20. Candau, S.J., *et al.*, *Il Nuovo Cimento* **1994**, *16*, 1401.

21. Cappelaere, E., R. Cressely, and J. Decruppe, *Colloids and Surfaces A* **1995**, *104*, 353.

22. Berret, J.-F., J. Appell, and G. Porte, *Langmuir* **1993**, *9*, 2851.

23. Hoffmann, H., W. Ulbricht, and B. Tagesson, *Zeitschrift fur Physikalische Chemie Neue Folge* **1978**, *113*, 17.

24. Gelbart, W., A. Ben-Shaul, and D. Roux, ed. *Micelles, Membranes, Microemulsions, and Monolayers.* 1st ed. Partially Ordered Systems, ed. L. Lam and D. Langevin. 1994, Springer-Verlag, Inc: New York. 608.

25. Cates, M.E., C.M. Marques, and J.-P. Bouchard, *J. Chem. Phys.* **1991**, *94*, 8529.

26. Kissa, E. *Fluorinated Surfactants*; Marcel Dekker, Inc: New York, 1994; Vol. 50, 469.

27. Cates, M.E. and S.J. Candau, *J. Phys.: Condens. Matter* **1990**, *2*, 68669.

28. Angel, M., *et al.*, *Progress in Colloid and Polymer Science* **1984**, *69*, 12.

29. Cates, M., *Philosophical Transactions of the Royal Society of London Series A - Physical Sciences and Engineering* **1993**, *344*, 339.

30. Dombroski, J.P., *et al.*, *Liquid Crystals* **1995**, *18*, 51.

31. Herbst, L., *et al.*, *Ber. Bunsenges. Phys. Chem.* **1985**, *89*, 1050.

32. Froba, G. and J. Kalus, *Journal of Physical Chemistry* **1995**, *99*, 4450.

33. McMullen, W.E., A. Ben-Shaul, and W.M. Gelbart, *J. Colloid Interface Sci.* **1984**, *98*, 523.

34. Brando, M., , in *Chemistry*. 1996, Leeds University: Leeds.

35. Parbhu, A.N., Ph,D Thesis, Dept. of Chemistry. Massey University, New Zealand. **1994.**

36. Parbhu, A.N., M.Sc. Thesis, Dept. of Chemistry. Massey University, New Zealand. **1990.**

37. Boden, N., *et al.*, *J. Chem. Phys.* **1995**, *103*, 5712.

38. Smith, M.H., Ph.D. Thesis, Dept. of Chemistry. Massey University, New Zealand. **1990.**

39. Fontell, K. and B. Lindman, *J. Phys. Chem.* **1983**, *87*, 3289.

40. Reizlein, K. and H. Hoffmann, *Progress in Colloid and Polymer Science* **1984**, *69*, 83.

41. Boden, N., *et al.*, *Phys. Rev. Lett.* **1991**, *66*, 2883.

42. Hoffmann, H. and W. Ulbricht, *Zeitschrift fur Physikalische Chemie Neue Folge* **1977**, *106*, 167.

43. Hoffmann, H. and B. Tagesson, *Zeitschrift fur Physikalische Chemie Neue Folge* **1978**, *110*, 113.

44. Mukerjee, P., *et al.*, *J. Phys. Chem.* **1985**, *89*, 5308.

45. Guo, W., T.A. Brown, and B.M. Fung, *J. Phys. Chem.* **1991**, *95*, 1829.

46. Mukerjee, P., *Colloids and Surfaces A* **1994**, *84*, 1.

47. Mukerjee, P., *et al.*, *Journal of Physical Chemistry* **1990**, *94*, 8832.

48. Israelachvili, J. *Intermolecular and Surface Forces*; Academic Press Ltd: London, 1991; 353.

49. Yu, Z.-J. and R. Neumann, *Langmuir* **1994**, *10*, 377.

50. Evans, D. and H. Wennerstrom *The Colloidal Domain*; VCH Publishers, Inc.: New York, 1994; 515.

51. Craig, V., B. Ninham, and R. Pashley, *Journal of Physical Chemistry* **1993**, *97*,

52. Posnecker, G. and H. Hoffmann, *Ber. Bunsenges. Phys. Chem.* **1990**, *94*, 579.

53. Ninham, B. and V. Yaminsky, *Langmuir* **1997**, *13*, 2097.

4. Solvent Effects on Micellisation.

This Chapter probes the factors responsible for changes in surfactant self-assembly brought about by changing the solvent (a) from H_2O to D_2O, and (b) from H_2O to ethylene glycol (EG). Micellisation in EG/H_2O mixtures will also be investigated.

To date, the experimental investigation of the water isotope effect† has been limited to only a few hydrocarbon surfactants (SDS[1] and C_nTAB[2, 3] with n=12,14 and 16) and one fluorocarbon surfactant (CsPFO[4]) and the temperature dependence of the isotope effect was investigated in only two of these studies[3, 4], and at only a few temperatures. The work on CsPFO revealed a remarkable difference between hydrocarbon and fluorocarbon surfactants - the isotope effect on the cmc's is *opposite*, with values for fluorocarbon surfactants being greater in D_2O than H_2O. One aim of this work is to systematically investigate the temperature-dependence of the isotope effect on APFO micellisation.

Surfactant micellisation in non-aqueous solvents has attracted increasing attention. A summary of experimental surfactant-solvent studies can be found in the Introduction. To date, those surfactants investigated have, with one exception, been hydrocarbon surfactants, and only one investigation examines the effect of temperature[5]. Though the formation of "aggregates" has been inferred from these experiments, the evidence is conflicting and depends on the method employed. Hydrocarbon surfactants are a poor choice for investigation since the assumption that solvent does not penetrate the micelle interior i.e. partially solubilises the hydrophobe, cannot be made with confidence. Fluorocarbon surfactants, however, have the advantage of not only being hydrophobic but solvophobic (and, indeed, lipophobic) in general. The micellisation of CsPFO/D_2O in the presence of formamide (FA), *N*-methylformamide (NMF), *N,N*-dimethylformamide (DMF) and *N,N*-dimethylacetamide (DMA) has been studied[6] at 298 K as a precursor to this work. The only other fluorocarbon surfactant in mixed solvents studied to date is lithium perfluorooctanesulphonate (LiPOS)[7] in ethylene glycol/water and ethanol/water mixtures at one temperature (298 K). The work presented here investigates the aggregation of APFO in ethylene glycol as a function of temperature, and in ethylene glycol/water mixtures at 298 K.

The main parameter of interest in studying surfactant micellisation is the "critical micelle concentration" (**cmc**), the concentration at which surfactant appears to form aggregates. In this chapter, the experimental method for the determination of cmc's will

† Hereafter, the term *isotope effect* should be taken to mean the substitution of heavy water for water.

first be outlined, then the physical interpretation of the cmc values will be discussed in the context of current micellisation theory.

4.1 Experimental determination of cmc's.

4.1.1 Obtaining the temperature-dependence of the conductance.

The temperature-dependence of the conductance (*G*/S) of samples of known APFO/solvent concentration were obtained by cooling, from 90 °C to 3 °C for aqueous systems, and from 55°C in the ethylene glycol system, measurements being taken at approximately 2°C intervals in both cases. The conductance and thermocouple potential difference (*E*/mV) were automatically read at each temperature by the

Figure 4.1 Temperature (expressed as thermocouple potential differences) dependence of the conductance for APFO/H_2O. The points are the raw data obtained from the automated data acquisition system (see Chapter 2). The curves represent degree-four polynomials fitted to the raw data with correlations of >0.9994. Concentrations are presented as weight fractions *w*. All data were obtained by cooling the samples.

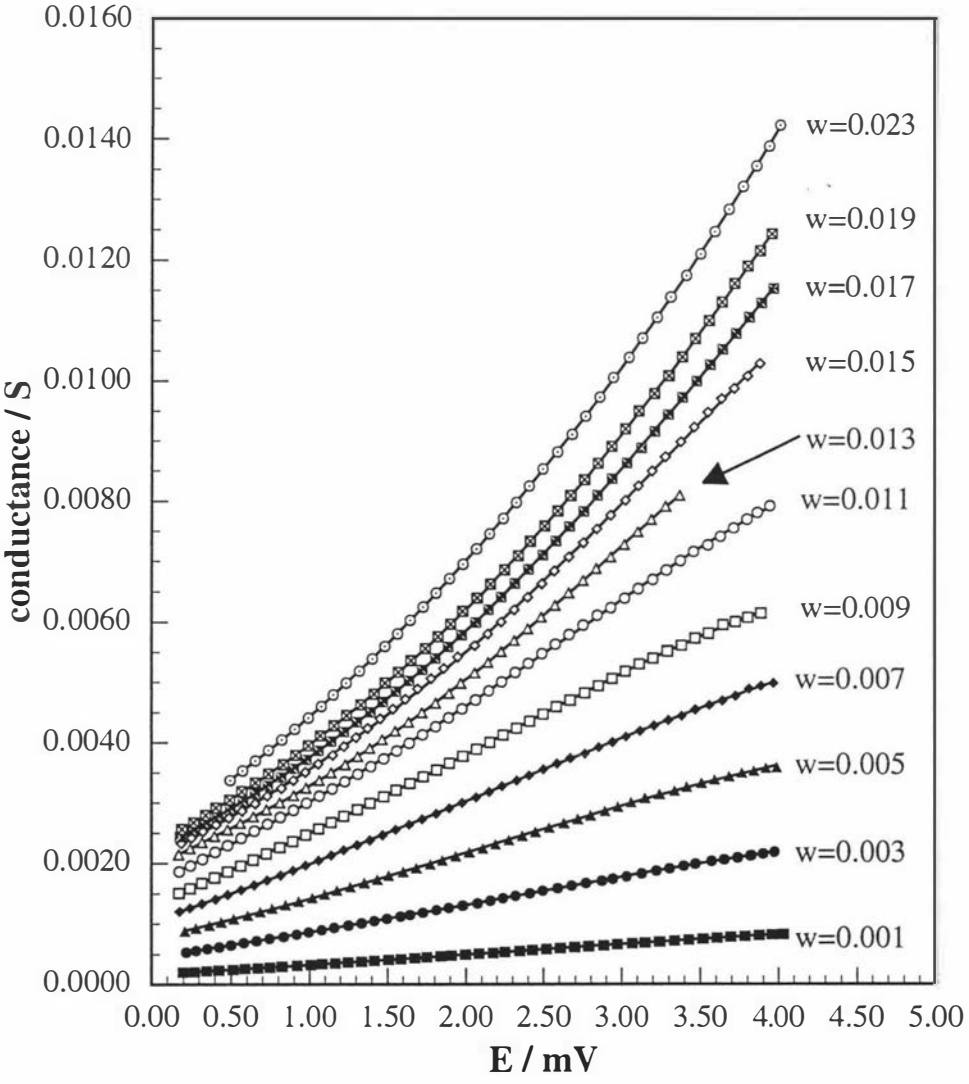

automated conductivity data acquisition system outlined in Chapter 2, and the raw data fitted with a degree-four polynomial. The temperature (expressed as thermocouple potential differences) dependence of the conductances for APFO/H_2O solutions is shown in Figure 4.1. The corresponding curves for APFO/D_2O and APFO/EG are shown in Figure 4.2 and Figure 4.3 respectively.

Figure 4.2 Temperature (expressed as thermocouple potential differences) dependence of the conductance for APFO/D_2O. The points are the raw data obtained from the automated data acquisition system (see Chapter 2). The curves represent degree-four polynomials fitted to the raw data with correlations of >0.9993. Concentrations are presented as weight fractions *w*. All data were obtained by cooling the samples.

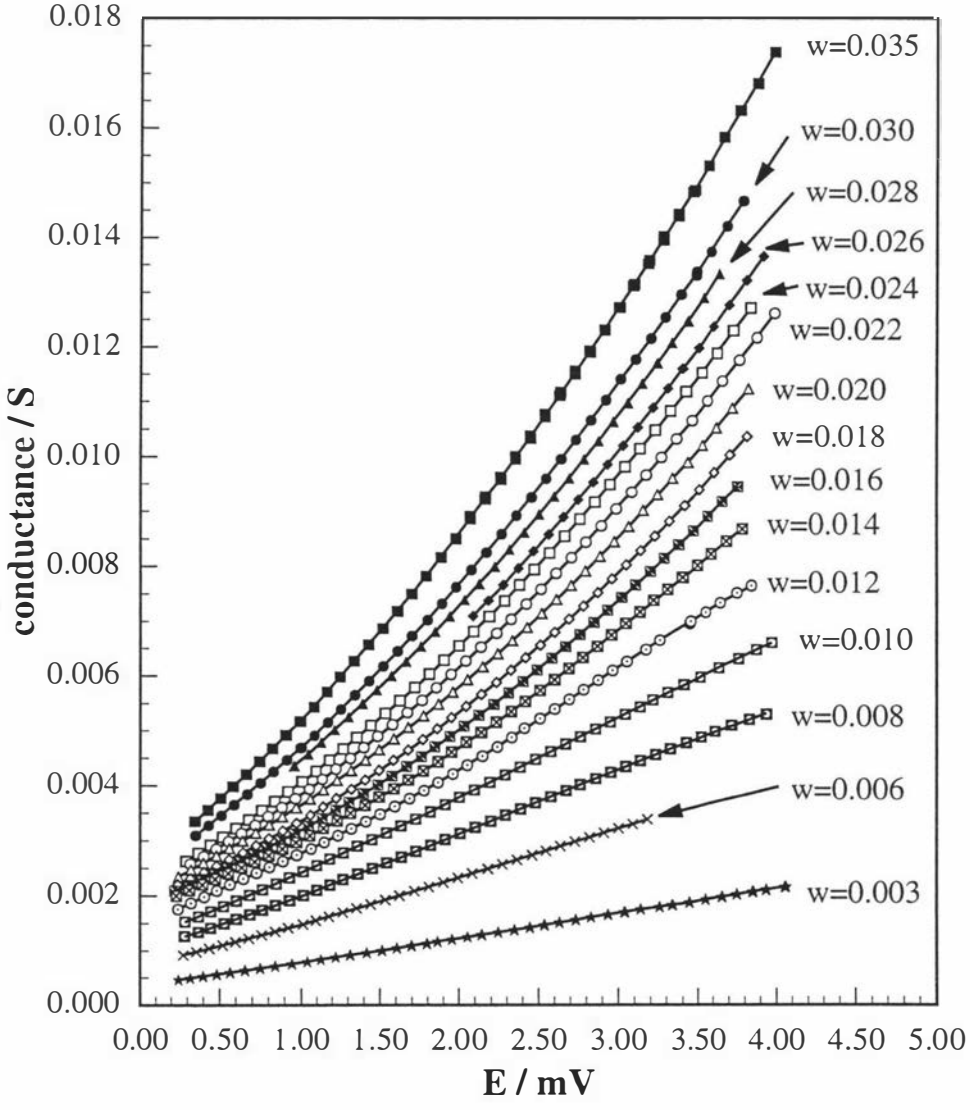

Figure 4.3 Temperature (expressed as thermocouple potential differences) dependence of the conductance for APFO/EG. The points are the raw data obtained from the automated data acquisition system (see Chapter 2). The curves represent degree-three polynomials fitted to the raw data with correlations of >0.9993. Concentrations are presented as weight fractions *w*. All data were obtained by cooling the samples.

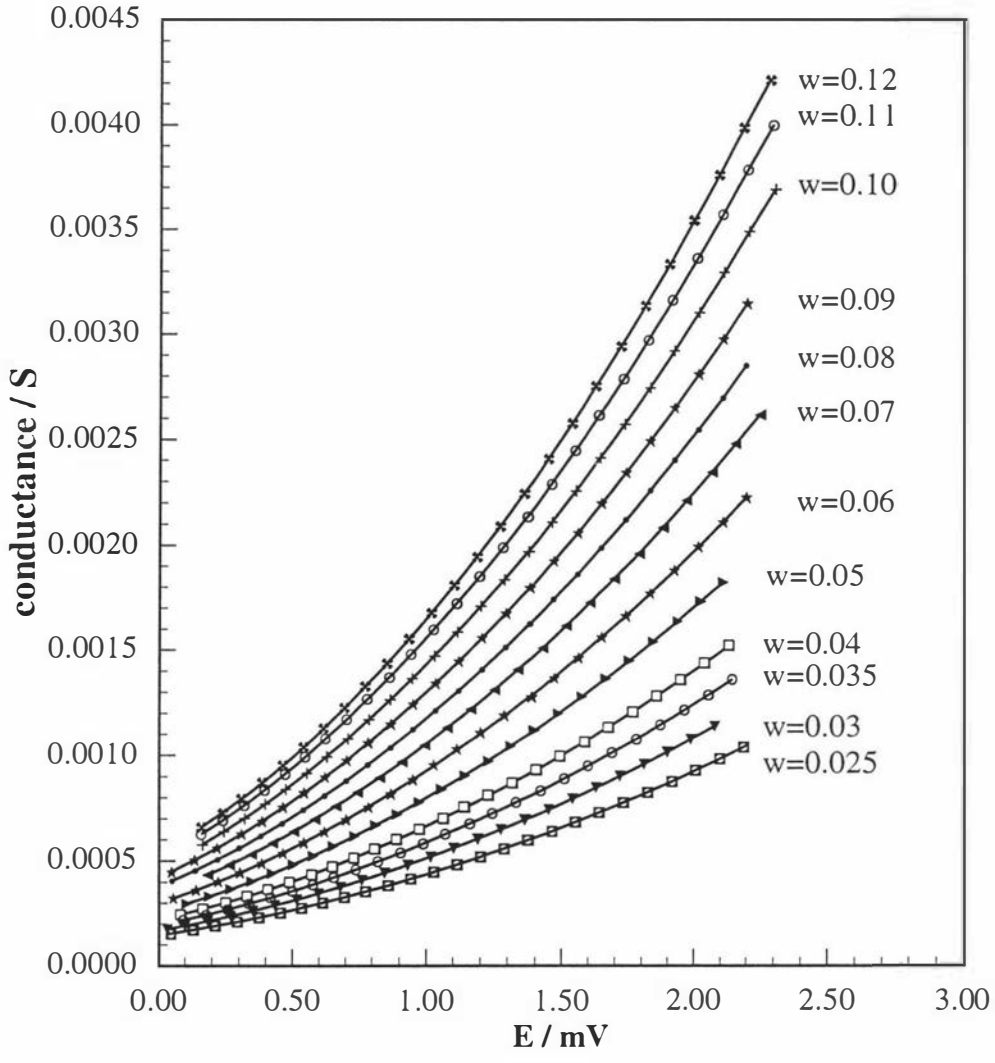

4.1.2 Extraction of cmc's.

Using the polynomials for the conductance as a function of potential difference $G/\mathrm{S} = f(E/\mathrm{mV})$ generated from the cooling curves (contained in Appendix A) and the polynomial used to calibrate the thermocouple potential difference against temperature (given in Chapter 2), the conductivity $\kappa/\mathrm{S\ cm^{-1}}$ at any temperature can be obtained as the product of the conductance and the cell constant = 0.75 $\mathrm{cm^{-1}}$ of the conductivity probe.

The total conductivity $\kappa/\mathrm{S\ cm^{-1}}$ below the cmc varies linearly with APFO concentration according to[8]

[4–1] $$1000\kappa = \lambda_{\mathrm{PFO^-}}\left[\mathrm{PFO^-}\right] + \lambda_{\mathrm{NH_4^+}}\left[\mathrm{NH_4^+}\right]$$

where $\lambda/\mathrm{S\ cm^2\ mol^{-1}}$ is the ionic conductivity at infinite dilution, and is given by

[4–2] $$\lambda = uF$$

where F is the Faraday constant and $u/\mathrm{cm^2\ s^{-1}\ V^{-1}}$ is the electrophoretic mobility of the ion. u depends on the ionic charge z, the solvent viscosity $\eta/\mathrm{N\ s\ m^{-2}}$ ($=\eta/\mathrm{cP}$) and the hydrodynamic radius of the ion r according to

[4–3] $$u = ze/6\pi\eta r$$

which is obtained by a combination of Einstein, Nernst and Stokes relations. Above the cmc there is an extra contribution from the micelle M with the total conductivity being given by

[4–4] $$1000\kappa = \lambda_{\mathrm{PFO^-}}\left[\mathrm{PFO^-}\right] + \lambda_{\mathrm{NH_4^+}}\left[\mathrm{NH_4^+}\right] + \lambda_{\mathrm{M}}[\mathrm{M}]$$

Thus the onset of aggregation with increasing APFO concentration is revealed as a change in conductivity (it actually decreases above the cmc since [$\mathrm{PFO^-}$] remains almost constant and [M] changes only slowly with concentration. This is discussed further in section 4.3.1). Cmc's can be obtained from conductivity *via* two methods - (i) by plotting ($\kappa/\mathrm{S\ cm^{-1}}$) *vs* concentration, or (ii) by plotting molar conductivity ($\Lambda/\mathrm{S\ cm^2\ mol^{-1}}$) *vs* $\sqrt{(m/\mathrm{mol\ kg^{-1}})}$. A comparison of the two methods is shown in Figure 4.4 for the aqueous APFO systems and in Figure 5.5 for the APFO/EG system. The first method involves calculating the intersection of linear fits to points above and below the breakpoint in κ *vs* concentration curves, and the second involves calculating the intersection of curve fits to points above and below the breakpoint. It has been previously noted[20] that the two methods can lead to different cmc values, but in this

instance, the results were the same within fitting error. The first method was adopted because it involves extrapolation of straight lines whilst the second method involves extrapolation of curves.

Figure 4.4 Comparison of methods for extracting cmc's from conductivity measurements of aqueous APFO systems at 298 K: (a) Conductivity *vs* concentration, (b) Molar conductivity *vs* √(molality). In both figures, dotted lines represent cmc values obtained as the points of intersection of best fit lines. Points in both plots are derived from the same raw data.

(a)

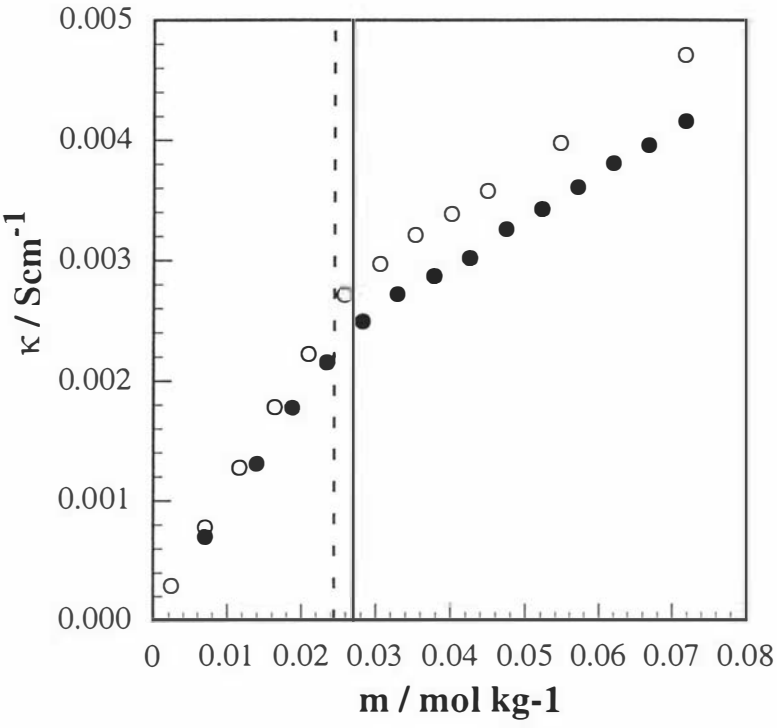

(b)

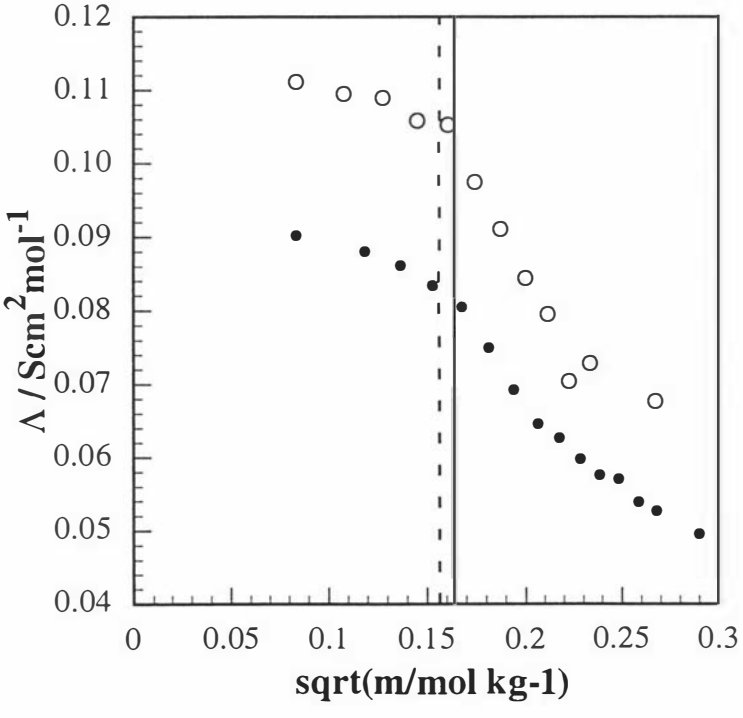

Figure 4.5 Comparison of methods for extracting cmc's from conductivity measurements of APFO/EG at 295 K: (a) Conductivity *vs* concentration, (b) Molar conductivity *vs* √(molality). In both figures, dotted lines represent cmc values obtained as the points of intersection of best fit lines. Points in both plots are derived from the same raw data. Note the smaller difference in $d\kappa/dm$ above and below the cmc in plot (a) with respect to the aqueous systems in Figure 4.4.

(a)

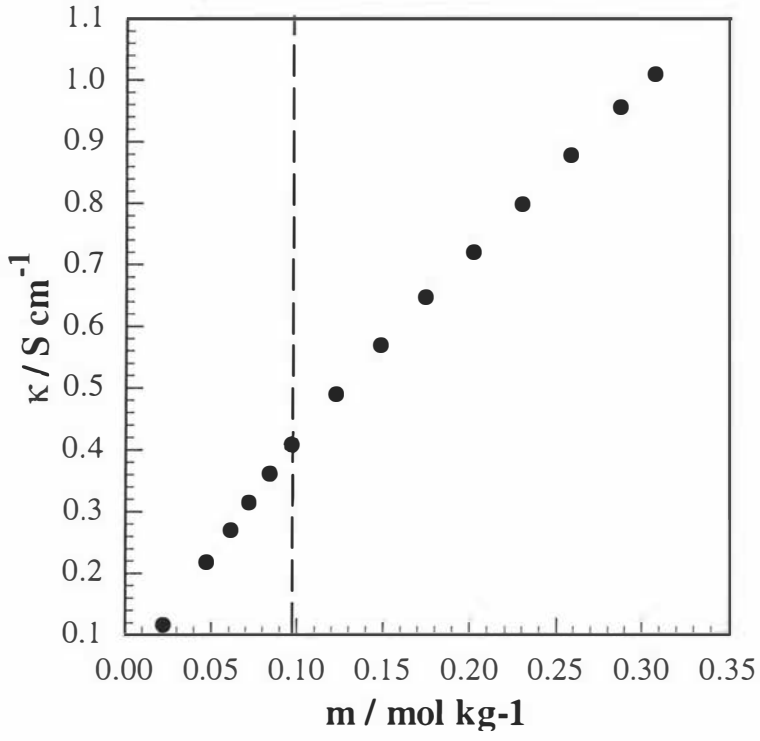

(b)

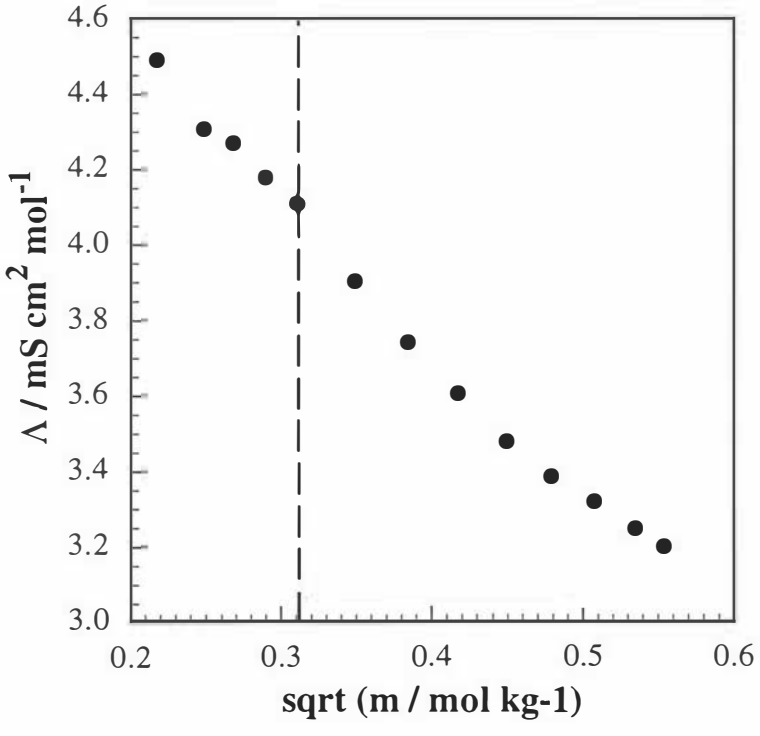

4.1.3 Experimental cmc results.

4.1.3.1 APFO/H_2O and APFO/D_2O systems.

The break points in conductivity with concentration (i.e. the cmc's) represented in (T, x, κ) space are shown in Figure 4.6 where the z-axis is the conductivity κ/S cm^{-1}, the x-axis is temperature T/K, and the y-axis is the APFO concentration x in mole fraction. The increase in conductivity with temperature and substitution of H_2O for D_2O at any given surfactant concentration is consistent with the decrease in solvent viscosity shown in Figure 4.7[9] accompanying both changes since κ and η are related by equations [4–1], [4–2] and [4–3]. The cmc's projected onto the temperature-concentration plane are shown in Figure 4.8. They are presented as full lines representing a fit to degree-four polynomials through 50 calculated cmc points with a correlation of >0.9996 in the case of APFO/H_2O (dotted line) and >0.9994 in the case of APFO/D_2O (solid line) with minima occurring at 317.3 K (D_2O) and 311.1 K (H_2O). Individual points are not shown since they do not represent directly-determined data, however the data from which the curves were generated are contained in Appendix B. The isotope effect on cmc's will be discussed in section 4.5.1.

Figure 4.6 Cmc's of APFO in H_2O and D_2O represented in (T, x, κ) space. The z-axis is the conductivity κ/S cm^{-1}, the x-axis is temperature T/K, and the y-axis is the APFO concentration x in mole fraction. The cmc's projected on to the T-x plane are shown in Figure 4.8

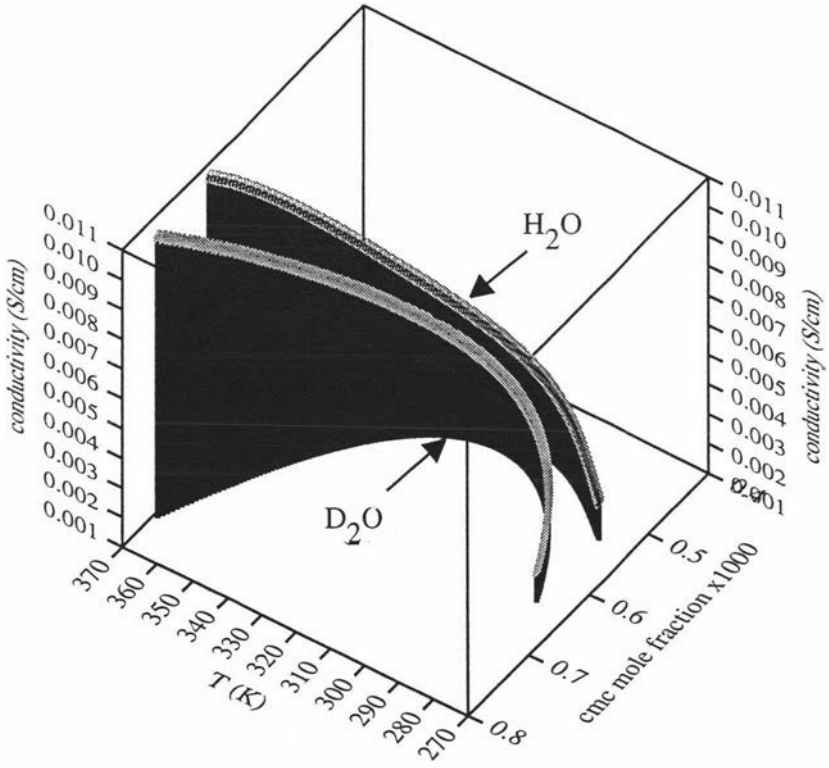

Figure 4.7 Temperature-dependence of the viscosity η/cP of H_2O (open circles) and D_2O (closed circles)[9].

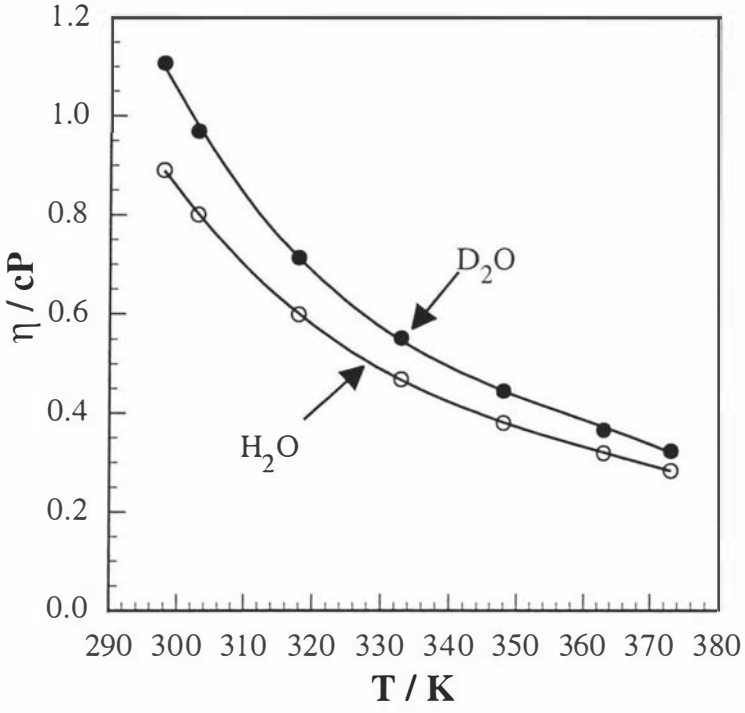

Figure 4.8 Temperature-dependence of cmc's in APFO/H_2O (dotted line) and APFO/D_2O (solid line). The lines represent degree-four polynomials through 50 evenly-distributed points with correlations of >0.9994 and minima occurring at 317.3 K (D_2O) and 311.1 K (H_2O). At all temperatures, the isotope effect displaces the cmc's to higher concentration whilst for hydrocarbon surfactants[1-3] the isotope effect displaces the cmc's to lower concentration.

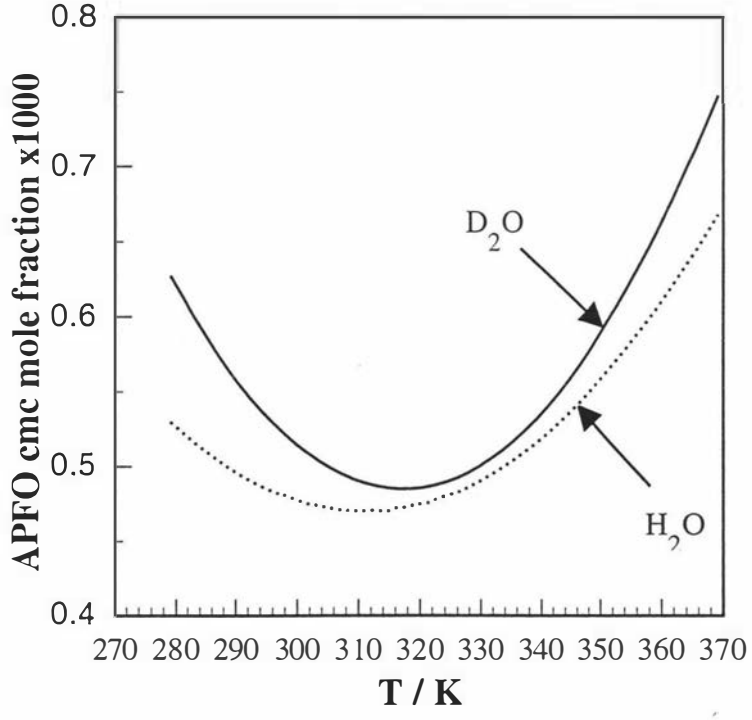

4.1.3.2 APFO/EG system.

The cmc's of APFO/EG are shown in Figure 4.9. The points from which the curves were generated are contained in Appendix B. The discovery of an apparent maximum in the temperature-dependence of the cmc was initially of great interest since the phenomenon has never been seen before. However, it will be shown that it is probably an artifact of the fitting procedure used. Though it can be assumed with reasonable certainty that the curve does not reflect actual APFO/EG "critical micelle concentrations", it is presented nevertheless since it reveals much about surfactant aggregation in ethylene glycol and the concept of a cmc in non-aqueous solvents in general. The origin of the maximum will be discussed in section 4.5.2.

Figure 4.9 Apparent temperature-dependence of cmc's in APFO/EG. The line represents a degree-four polynomial through 26 evenly-distributed data points with a correlation of >0.9994.

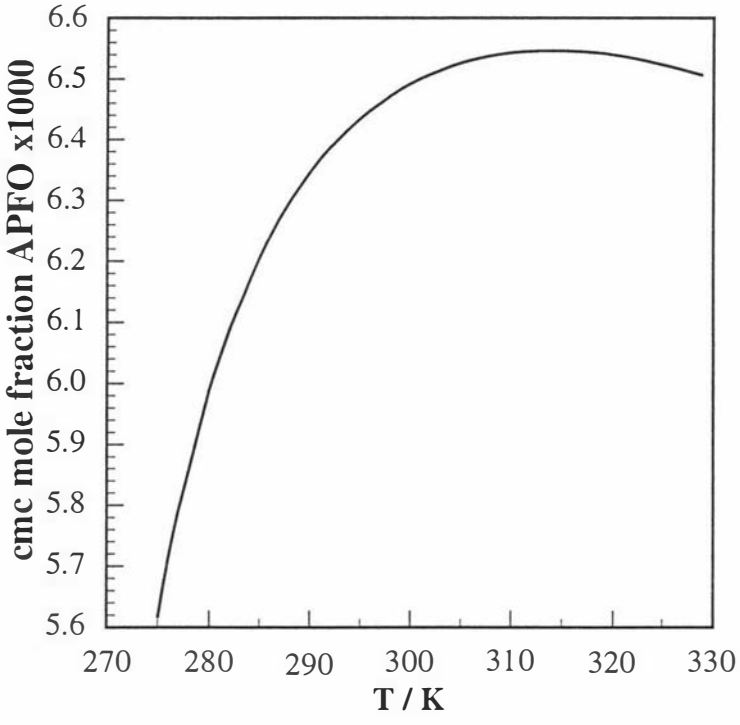

4.1.3.3 APFO/EG/H_2O systems.

The cmc's of APFO in EG/H_2O determined by conductivity at 298 K are shown in Figure 4.10. The only other fluorocarbon surfactant studied in these solvent mixtures is lithium perfluorooctanesulphonate (LiPOS)[7] at 298 K, the cmc's of which were determined by surface tension and are included in the Figure for comparison. The lower cmc of LiPOS at corresponding EG concentration is consistent with the greater solvophobicity of the chain conferred by the extra perfluoromethylene group. Both systems exhibit minima in the cmc *vs* EG composition curves. The trend in cmc's with increasing EG concentration will be discussed in section 4.5.2.

Figure 4.10 Cmc's of APFO (closed circles) and LiPOS[7] (open circles) in EG/H_2O mixtures at 298 K. Both systems exhibit minima in the cmc *vs* EG composition curves.

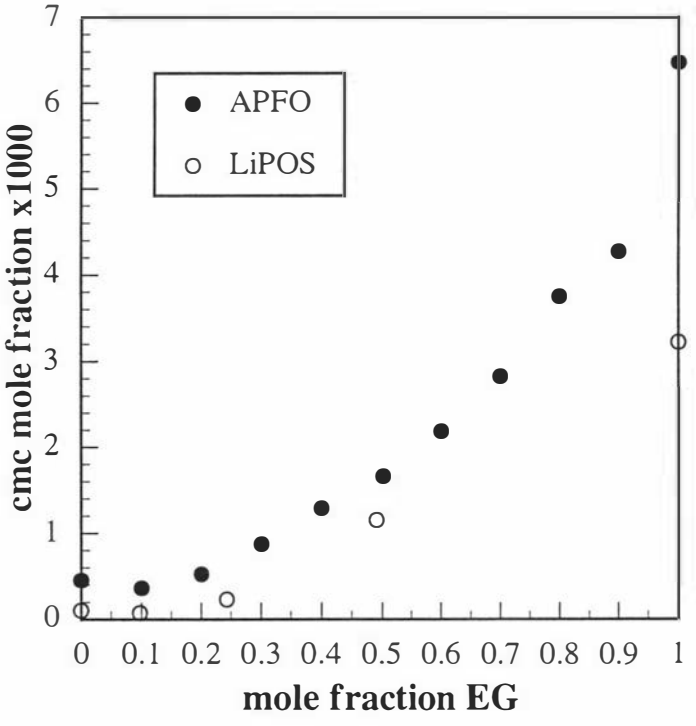

4.2 Theoretical treatments of the micellisation.

In order to discuss the cmc results and calculate thermodynamic quantities it is necessary to adopt a model. The process of surfactant aggregation can be represented generally as a step-wise addition of surfactant monomer A to a micelle M_s composed of s monomers.

[4–5] $$M_s + A \rightleftarrows M_{s+1}$$

Practically, the determination of s equilibrium constants for the formation of a micelle is unrealistic and simplified models are required. The two prevailing models applicable to ionic surfactants are the 'phase separation' (or 'pseudophase separation') model and the 'mass-action' (or 'closed association') model, both of which will be used to extract thermodynamic parameters.

The phase separation model treats the surfactant existing as monomer and micellised forms as separate phases with the monomer analagous to a gas phase and micelles as the condensed phase. The model assumes that the aggregation number s in equation [4–5] is infinite, and ignores the presence of counterions. Though the model correctly predicts certain features of micellisation, it has been criticised on the basis that it is inconsistent with the number of degrees of freedom in the system given by the phase rule, and that the assumption of an infinite s is unrealistic[10]. However, it has been applied before to ionic surfactant systems.

The mass-action model treats the micelle as a separate chemical species with one preferred aggregation number s which is assumed to be invariant with temperature, i.e

[4–6] $$sA \underset{k_s}{\overset{k_1}{\rightleftarrows}} M_s$$

where the rate of association = $k_1[A]^s$ and the rate of dissociation = $k_s[M_s]$. The equilibrium constant is given by

[4–7] $$K_s = \frac{k_1}{k_s} = \frac{[M_s]}{[A]^s}.$$

The general features of surfactant aggregation represented by equation [4–6] can be shown by the variation of the concentration of A in micellised form, $s[M_s]$ with total concentration. If the total surfactant concentration c is expressed as $c = s[M_s] + [A] = sK_s[A]^s + [A]$ then

[4–8] $$\frac{ds[M_s]}{dc} = \frac{ds[M_s]}{d[A]} \cdot \frac{d[A]}{dc} = \frac{s^2 K_s [A]^{s-1}}{s^2 K_s [A]^{s-1} + 1}$$

Figure 4.11 shows the abrupt onset of aggregation at the cmc marked by a rapid increase in $d\{s[M_s]\}/dc$ with c. The dotted line representing $s \rightarrow \infty$ corresponds to the phase separation model.

Figure 4.11 The theoretical variation of surfactant concentration in micellised form with total concentration calculated *via* equation [4–8] for two values of s and $K = 10^{-21}$. $s \rightarrow \infty$ (dotted line) corresponds to the phase separation model.

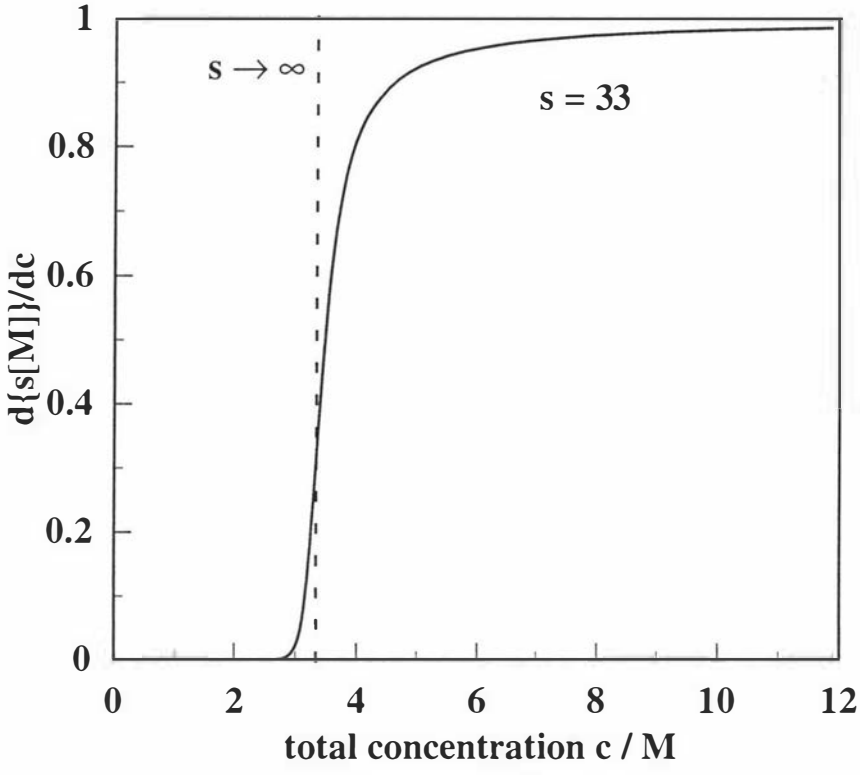

4.3 Thermodynamics of micellisation.

Applying the mass-action model to ionic surfactants, the expression for the free energy per mole of surfactant of forming a micelle is

$$\Delta G^0_{mic} = -RT\ln K_s$$

where for a 1:1 anionic surfactant AB the equilibrium constant is

[4–9]

$$K_s = \frac{\left[M_s^{-(s-p)}\right]}{\left[A^-\right]^s\left[B^+\right]^p}$$

representing the equilibrium

[4–10] $$sA^- + pB^+ \underset{k_s}{\overset{k_1}{\rightleftharpoons}} M_s^{-[s-p]}$$

For brevity, the micellar charge will now be omitted. The free energy per mole of forming a micelle becomes

$$\Delta G^0_{mic} = -RT \ln K_s = -RT\left(\ln[M_s] - s\ln[A^-] - p\ln[B^-]\right).$$

On a molecular level, the free energy per molecule in a micelle (now in terms of mole fractions) is

[4–11] $$\frac{\Delta G^0_s}{RT} = \frac{\Delta G^0_{mic}}{sRT} = \ln x_A + \frac{p}{s}\ln x_B - \frac{1}{s}\ln x_M$$

The ratio p/s is the bound B^+ ion fraction β defined as

[4–12] $$\beta = (1-\alpha) = p/s$$

where α is the fraction of free B^+ ions. ΔG^0_s can be obtained from cmc measurements by adopting two assumptions. The first is to assume that the concentrations of A^- and B^+ are equal at the cmc i.e $x_A = x_B = x_M/s = \text{cmc}$ and the second is that the term in x_M is negligble. Thus equation [4–11] becomes

[4–13] $$\Delta G^0_s = (1+\beta)RT \ln \text{cmc} = (2-\alpha)RT \ln \text{cmc}$$ **(mass-action model).**

Applying the phase separation model, which assumes $s \rightarrow \infty$, to equations [4–12] and [4–13] the expression for the free energy per mole of surfactant of forming a micelle is

[4–14] $$\Delta G^0_s = RT \ln \text{cmc}$$ **(phase separation model).**

The other thermodynamic quantities of interest, the enthalpy ΔH^0_s and entropy ΔS^0_s of micellisation, can be calculated using the Gibbs-Helmholtz equation

[4–15] $$\Delta H^0_s = \frac{\partial(\Delta G^0_s / T)}{\partial(1/T)}$$

and the Gibbs equation

[4–16] $$T\Delta S^0_s = \Delta H^0_s - \Delta G^0_s.$$

To use equations [4–13] and [4–15] knowledge of the free ion fraction α and its temperature-dependence is required. Determination of cmc's by conductivity can give an approximation for these quantities.

4.3.1 Obtaining the free ion fraction from conductivity.

The method for obtaining α uses the relation

[**4–17**] $$\alpha = S_2/S_1$$

where S_1 and S_2 are the slopes of the linear portions of the conductivity κ *vs* concentration curves below and above the cmc respectively. This relation has been widely used in other work[5, 11-18] but the origin of its derivation is not clear. The following is a derivation of equation [4–17] starting from the expressions for the conductivity given by equations [4–1] and [4–4] but with the adoption of some assumptions.

By consideration of the mass balance in the equilibrium represented by equation [4–10] the total surfactant concentration c is given by

[**4–18**] $$c = [A^-] + s[M_s]$$

or

[**4–19**] $$c = [B^+] + p[M_s],$$

and electroneutrality requires that

[**4–20**] $$[B^+] - [A^-] = (s - p)[M_s].$$

By the substitution of the expression obtained by rearrangement of equation [4-18] for $[M_s]$, equation [4-20] becomes

[**4–21**] $$[B^+] - [A^-] = (1 - \beta)(c - [A^-]).$$

The conductivity κ/S cm^{-1} below the cmc only has contributions from the completely dissociated A^- and B^+ ions and is given by equation [4–1]. The slope of the conductivity *vs* concentration curve below the cmc is thus given by

[**4–22**] $$S_1 = \frac{1000\kappa}{c} = \lambda_{A^-} + \lambda_{B^+}$$

Above the cmc there is an extra contribution from the micelle with the total conductivity being given by equation [4–4]. This equation, normalised to the point (κ_0,cmc), where κ_0 is the conductivity at the cmc, becomes

[**4–23**] $$1000(\kappa - \kappa_0) = \lambda_{A^-}([A^-] - cmc) + \lambda_{B^+}([B^+] - cmc) + \lambda_M[M_s]$$

The first assumption is that above the cmc the monomer concentration remains constant at $[A^-]$ = cmc. Using this assumption and equation [4-21], equation [4–23] becomes

[4–24] $$1000(\kappa - \kappa_0) = 0 + \lambda_{B^+}(1-\beta)(c - cmc) + \lambda_M[M_s]$$

The second assumption is that, just above the cmc, $[M_s]$ does not change significantly with concentration i.e $\delta[M_s]/\delta c \approx 0$ since for a unit increase in c, and hence $[B^+]$, $[M_s]$ only increases by c/s. Then the slope above the cmc S_2 is given by

[4–25] $$S_2 = \frac{1000(\kappa - \kappa_0)}{(c - cmc)} = \lambda_{B^+}(1-\beta)$$

i.e the change in conductivity above the cmc is dominated by the free counterion fraction and its molar conductivity. Equation [4-25] by itself is insufficient to obtain β since λ_{B^+} is temperature- and solvent-dependent. However, by taking the ratio of the slopes S_2 / S_1 (i.e. the ratio of equation [4–22] and equation [4–25]) β can be obtained as

[4–26] $$\frac{S_2}{S_1} = \left(\frac{\lambda_{B^+}}{\lambda_{A^-} + \lambda_{B^+}}\right)(1-\beta).$$

Here, the assumption is that the molar conductivities of monomer and counterion will vary in the same way with temperature and solvent.

The final assumption is that the prefactor to (1-β) should be of the order of unity i.e. $\lambda_{B^+} >> \lambda_{A^-}$. Boden *et al*[19] showed this generally to be the case on the grounds of the large difference in hydrodynamic radii of the ions r since λ is inversely proportional to r which can be seen by equations [4–2] and [4–3]. Mukerjee[20] made the same assumption in his work on NaPFO. However, a quantitative estimate of the prefactor is necessary. The molar ionic conductivity of the ammonium ion in water at 298 K is λ = 73.6 S cm^2 mol^{-1}[18]. The value for a PFO^- ion is unavailable but may be estimated by the value for a dodecylsulphate ion of λ = 18 S cm^2 mol^{-1}[21] leading to a value for the prefactor of 0.8. Though this would lead to an underestimation of α, it will be shown from the good agreement between α values obtained from S_2/S_1 and values obtained from Raman scattering[22] on APFO in water, ethylene glycol and their mixtures that the above assumptions are valid. In addition, Callaghan[5] compared α values obtained using the above method with values obtained from emf measurements for various surfactants in ethylene glycol/water mixtures and showed very close agreement (±0.01) between the two.

4.3.2 Experimentally determined free ion fractions α.

Figure 4.12 shows that, for aqueous APFO systems, the free ion fraction α increases with increasing temperature. This will be discussed in section 4.5.1. The values of α for the APFO/EG system, presented in Figure 4.13, also increase with increasing temperature but exhibit a minimum at low temperature which will be explained in section 4.5.2. The values of α for the APFO/EG/H_2O system shown in Figure 4.14 (closed circles, this work) are compared with values estimated from Raman scattering (open circles[22]). These will also be discussed in section 4.5.2.

Figure 4.12 Temperature-dependence of the estimated free counterion fraction α for APFO/H_2O (dotted line) and APFO/D_2O (solid line). The lines represent degree-four polynomials through 50 evenly-distributed points with correlations of >0.992. The crossover at low temperature may be an experimental artifact (see text).

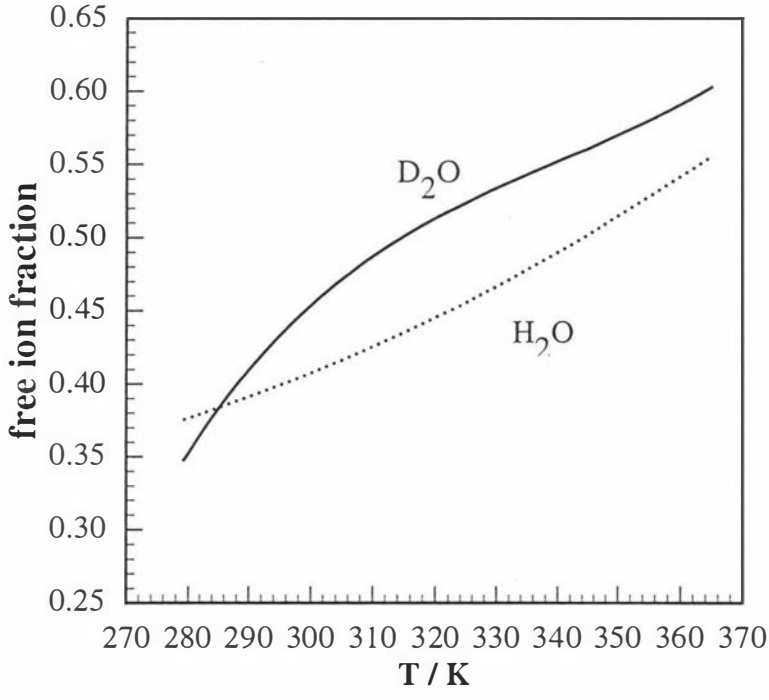

Figure 4.13 Temperature-dependence of the estimated free counterion fraction α for APFO/EG. The line represents a degree-four polynomial through 26 evenly-distributed points with a correlation of >0.991. The curve is probably only an approximation for the true free counterion fraction, i.e α is expected to increase with temperature but is not expected to go through a minimum. Note also that the total change in α with T is only ≈6% (*c.f.* Figure 4.12).

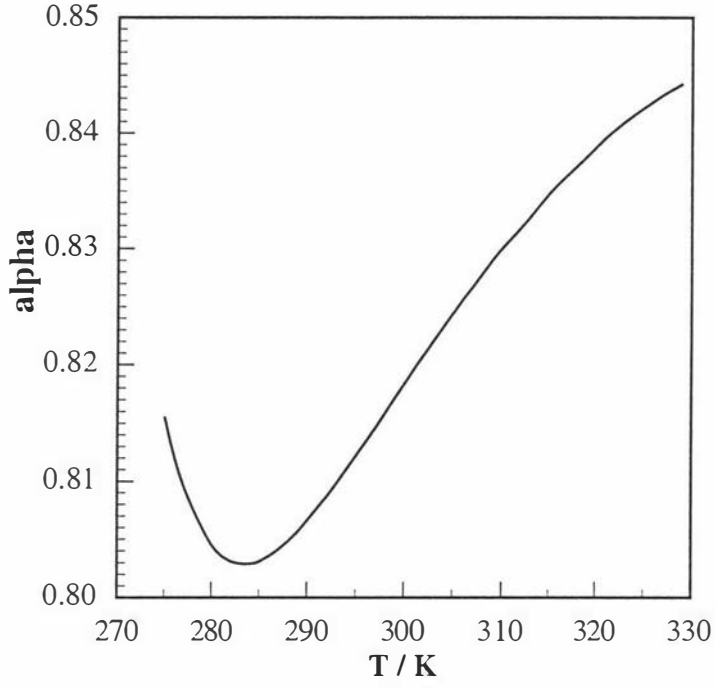

Figure 4.14 Estimated free counterion fraction α for APFO/EG/H_2O as a function of ethylene glycol composition at 298 K determined by conductivity (closed circles, this work) and Raman spectroscopy (open circles[22]).

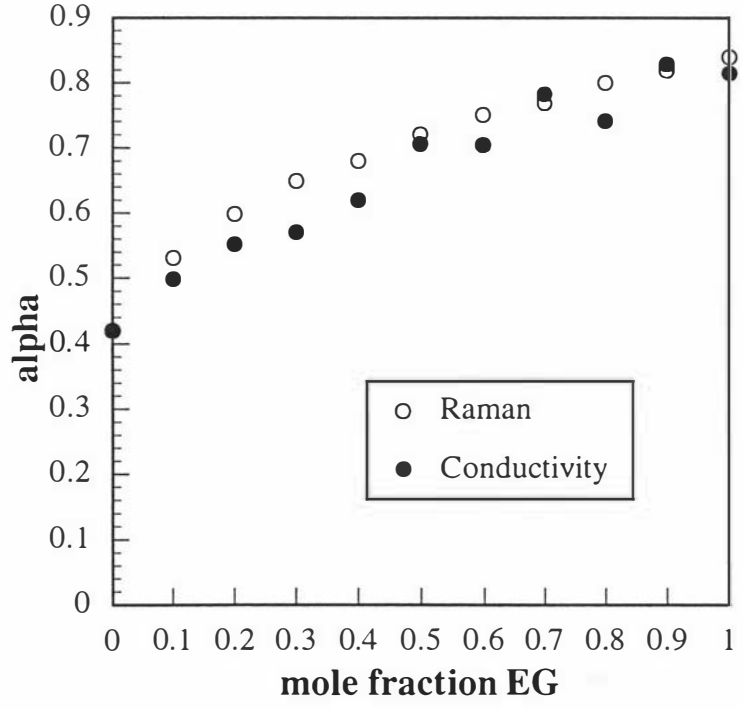

4.4 Phenomenological statistical thermodynamic models.

The thermodynamic models presented above are useful in describing surfactant self-assembly at a macroscopic level but suffer from the possible invalidity of some of the assumptions necessarily adopted in their derivation. It will be shown below that both the phase separation and mass-action models are inappropriate to apply to the APFO/EG system. Alternative descriptions of micellisation are provided by statistical thermodynamic models for surfactant self-assembly which attempt to explain and/or predict micellisation at a molecular level. However, rigorous statistical thermodynamic theories have only been successful at providing expressions for partition functions and cannot be usefully employed without invoking some gross approximations[23]. The most successful (i.e quantitative) theories combine classical thermodynamics with 'semi-empirical' or phenomenological models. Most phenomenological approaches start from an expression for the equilibrium size distribution of micelles derived from the chemical potentials of species in the equilibrium represented by equation [4–6], i.e. the process

$$s\mathrm{A} \underset{k_s}{\overset{k_1}{\rightleftharpoons}} \mathbf{M}_s$$

At equilibrium, the chemical potentials of surfactant as monomer and in a micelle must be equal, and if the chemical potential of monomers A is μ_1 and that of micelles M_s is μ_s, then $\mu_1 = \mu_s/s$ and hence

$$\mu_1^0 + kT\ln x_1 = (\mu_s^0 + kT\ln x_s)/s$$

where x_1 is the monomer mole fraction and x_s is the mole fraction of micelles of size s. This equation rearranges to give the micelle size distribution as

[**4–27**] $$x_s = x_1^s \exp\left[-s\Delta\mu_s^0 / kT\right]$$

where $\left(\Delta\mu_s^0\right) = \left(\mu_s^0 / s - \mu_1^0\right)$ and represents the difference in standard chemical potentials per molecule between surfactant in the micellised and monomer states.

Phenomenological approaches attempt to derive expressions for $\left(\Delta\mu_s^0\right)$ and use the equilibrium size distribution to predict *a priori* all size-dependent solution properties for example, cmc's, number and weight average aggregation numbers. Though many phenomenological approaches have been formulated[39, 57-79] for the aggregation behaviour of hydrocarbon surfactants in pure water and in salt solutions, no such formulation exists for perfluorocarbon surfactants. Furthermore, only one approach, that by Nagarajan[24-26], attempts to explicitly account for aggregation in non-aqueous solvents.

In this section Nagarajan's model will be modified for fluorocarbon surfactants and applied to both the APFO/H_2O and APFO/EG systems. The calculated cmc's will be compared to those determined experimentally in this work, and the origin of differences between the two systems discussed.

4.4.1 Nagarajan's model.

Nagarajan's model predictions for several ionic and nonionic hydrocarbon surfactants in water agree well with experimental cmc data. The recent extension of this model to the micellisation of alkyltrimethylammonium bromides and alkylpyridinium bromides in ethylene glycol and its mixtures with water, while demonstrating that an operational cmc can be defined, shows that aggregation occurs over a wide concentration range and that the location of the cmc may depend on the experimental method used. Cmc's calculated by Nagarajan using a plot of monomer *vs* total concentration are in reasonable agreement with those determined experimentally by emf measurements using surfactant specific electrodes.

Nagarajan's approach to calculating $\left(\Delta\mu_s^0/kT\right)$ shares many features with the other phenomenological models cited above. His approach is to consider the following changes in intermolecular interactions that accompany aggregation:

(a) the transfer of the surfactant tail from the solvent to the micellar core, $\left(\Delta\mu_s^0/kT\right)_{\text{trans}}$,

(b) the electrostatic repulsion between headgroups, $\left(\Delta\mu_s^0/kT\right)_{\text{ionic}}$,

(c) the creation of an interface between the solvent and the hydrophobic core of the micelle, $\left(\Delta\mu_s^0/kT\right)_{\text{int}}$,

(d) the steric repulsion between headgroups, $\left(\Delta\mu_s^0/kT\right)_{\text{steric}}$ and

(e) the deformation of the surfactant tail $\left(\Delta\mu_s^0/kT\right)_{\text{def}}$ from the conformation in a pure liquid hydrocarbon caused by packing constraints i.e. one end of the hydrophobe is anchored to the micelle surface. In the case of fluorocarbons, where fluorine atoms introduce steric hindrance to rotations about carbon-carbon bonds[10], this contribution will be assumed to be negligible i.e the conformation of the fluorocarbon chain dissolved in a polar solvent is the same as it is when dissolved in liquid fluorocarbon. Raman spectroscopy has recently[22] been used to study APFO in water and ethylene glycol and fluorocarbon chain conformations were shown to be essentially the same as that in solid polytetrafluoroethylene (PTFE). PTFE has been shown[27] to have a helical conformation with 15 CF_2 groups per seven turns of the helix at 293 K. The rigidity

of the chain imposes limitations on the dimensionality of micelle growth, the consequences of which will be addressed in section 4.4.1.3.

Next, the contributions (a)-(d) will now be examined (for both water and ethylene glycol) and modified if necessary for fluorocarbons.

4.4.1.1 Transfer free energy.

This contribution, $\left(\Delta\mu_s^0/kT\right)_{\text{trans}}$ is the free energy change for transferring the hydrophobe from contact with the solvent to the micellar core and is the main driving force for surfactant aggregation (the so-called 'hydrophobic effect') .

(i) From Water.

Nagarajan calculates the free energy of transfer for methylene and methyl groups as a function of temperature *via*

$$\left(\Delta\mu_s^0/kT\right)_{\text{trans}}=\left(\Delta\mu^0/kT\right)(\text{aq.}\rightarrow\text{gas})+\left(\Delta\mu^0/kT\right)\text{vap}$$

using solubility data compiled by Abraham[28, 29] for *n*-hydrocarbon gases to obtain $\left(\Delta\mu^0/kT\right)(\text{aq.}\rightarrow\text{gas})$ and vapour pressure-temperature data to obtain $\left(\Delta\mu^0/kT\right)\text{vap}$.

(ii) From Ethylene Glycol.

$\left(\Delta\mu_s^0/kT\right)_{\text{trans}}$ for ethylene glycol was calculated from *n*-hydrocarbon infinite dilution activity coefficients compiled by Pierotti[30] *via* $\left(\Delta\mu_s^0/kT\right)_{\text{trans}}=-\ln\gamma_A^\infty$.†

Literature data on the solubility of fluorocarbons appears to be limited to CF_4 and C_2F_6 in H_2O and D_2O over a narrow temperature range (<30°C)[32-34], and that in other solvents non-existent. This may be due to experimental difficulties presented by their very low solubility[35]. Pierotti[30] did not measure *n*-perfluorocarbon infinite dilution activity coefficients. Thus an alternative approach to the estimation of $\left(\Delta\mu_s^0/kT\right)_{\text{trans}}$ is required. From the dependence of cmc's on chainlength, Shinoda[36] estimated the transfer free energy from water to the micelle interior per CF_2 group to be $-1.6kT$ and $-1.08kT$ per CH_2 group and further suggested that a fluorocarbon hydrophobe is 'equivalent' to the ratio -1.6 / -1.08 = 1.48 times the length of a hydrocarbon one. In view of the significant difference between Shinoda's value of $-1.08kT$ and Nagarajan's value of $-0.606kT$ per CH_2 group the approach used here will be to approximate the transfer free energies of fluorocarbon methylene and methyl groups by applying the factor of 1.48 to the values calculated by Nagarajan for their hydrocarbon analogues in both water and ethylene glycol i.e

---

† Such data for hydrocarbons in other non-aqueous solvents is limited but Nagarajan has provided a method for estimation of the transfer free energies for a range of polar solvents based on an empirical correlation between available data and the Hildebrand[31] solubility parameter.

[4–28] $$\left(\Delta\mu_s^0\right)_{\text{trans,FC}} = 1.48\left(\Delta\mu_s^0\right)_{\text{trans,HC}}$$

This assumption may not reflect their absolute values but since it is the *difference* between the aggregation behaviour of APFO in these solvents that is of interest it provides a reasonable starting point for defining $\left(\Delta\mu_s^0/kT\right)_{\text{trans}}$. In the course of this work it was noted that the ratio of 1.48 is very close to the fluorocarbon/hydrocarbon volume ratio of 1.47 calculated from the data in Table 4.1 for n=6¥. This correlation could be merely fortuitous but use of a volume-derived factor may have a physical basis in that the solubilisation of a non-polar solute in a 'structured' medium involves the necessary formation of a 'hole' about which the solvent must order itself. The transfer of the solute out of the solvent is entropically favourable since it 'frees up' the solvent.

Table 4.1 Hydrophobic Chain Properties of Surfactants

	Chain Volume v_{mon} / nm^3	Chain Length R / nm
Fluorocarbon[37, 38]	0.0884+0.0381n	0.306+0.130n
Hydrocarbon[39]	0.0546+0.0269n	0.270+0.127n

4.4.1.2 Electrostatic headgroup repulsion.

This contribution is assumed independent of the hydrophobe (an arguable assumption in view of the greater acidity of perfluorocarboxylate ions compared to their hydrocarbon analogues as a consequence of the electron-withdrawing effect of fluorine atoms[10]). $\left(\Delta\mu_s^0/kT\right)_{\text{ionic}}$ was estimated by Nagarajan using an approximate analytical solution to the Poisson-Boltzmann equation in spherical geometry (originally derived by Mitchell and Ninham[40]) i.e (in units of kT)

[4–29] $$(\Delta\mu_s^0)_{\text{ionic}} = 2\left[\ln\left(S+\sqrt{1+S^2}\right)+\frac{1}{S}\left(1-\sqrt{1+S^2}\right)-\frac{2}{S\kappa(R+\delta)}\ln\left(\frac{1}{2}\left(1+\sqrt{1+S^2}\right)\right)\right]$$

where the dimensionless parameter S is defined as $S=\sigma/\sqrt{8ckT\varepsilon}$ with $\sigma = e/a_\delta$ the surface charge density at a distance of $R+\delta$. R is the hydrophobe length defined in Table 4.1 and δ is the headgroup radius δ = 0.118 nm[38]. c is the concentration of APFO in molecules/dm^3 and $\varepsilon=\varepsilon_0\varepsilon_r$ is the solvent permittivity. ε_0 is the vacuum

¥ As n→∞ the fluorocarbon/hydrocarbon volume ratio tends to 1.42, a value not too dissimilar from Shinoda's value of 1.48.

permittivity and ε_r is the solvent relative permittivity given in Table 4.2. The inverse Debye screening length κ is given by $\kappa = \sqrt{2ce^2 / \varepsilon kT}$.

Table 4.2 Bulk properties of solvents[25].

	H_2O	EG
ε_r	87.74exp[-0.0046(T/°C)]	46.6exp[-0.00516(T/°C]
γ/ mJ m^{-2}	72.0-0.16[(T-298)/K]	48.5-0.1[(T-298)/K]

4.4.1.3 Fluorocarbon/solvent interfacial free energy.

Micelle formation generates an interface between the solvent and the micellar core. This contribution $\left(\Delta\mu_s^0 / kT\right)_{\text{int}}$ is given (in units of kT) by

[**4–30**] $$\left(\Delta\mu_s^0\right)_{\text{int}} = \frac{\gamma_{\text{int}}}{kT}\left(a - a_p\right)$$

where γ_{int}, the macroscopic fluorocarbon/solvent interfacial tension is calculated *via* a modified form of the Fowkes[41-43] equation (see Chapter 6) $\gamma_{\text{int}} = \gamma_{FC} + \gamma_{solvent} - 2\psi\sqrt{\gamma_{FC}\gamma_{solvent}}$ with γ_{FC} = 19 mJ m^{-2}, $\gamma_{solvent}$ given in Table 4.2, $\psi_{water} = 0.55$ and $\psi_{EG} = 0.78$. a_p is the area of the fluorocarbon surface shielded by the carboxylate headgroup and is taken to be 0.15 nm^2[44]. a is the area/molecule at the interface defined by the following geometric considerations. Nagarajan assumed a spherical geometry for hydrocarbon surfactants at the cmc with the radius of the sphere determined by sv_{mon} where v_{mon} is the monomer volume defined in Table 4.1. However, in the case of fluorocarbon surfactants, where the carbon chain can be assumed to be rigid, only one sphere can form with a radius determined by the extended chainlength. In order to allow for the presence of larger micelles a non-spherical geometry must be envisaged. Independent SANS[45] and SAXS[46] evidence on APFO in the presence of salt suggests that the APFO micelles in water just above the cmc are rodlike with a long axis <5 nm. In the absence of salt we would expect shorter rods[47, 48] and for the purposes of this calculation a prolate ellipsoidal geometry will be assumed. This has the advantage of being mathematically tractable i.e. the semi-minor axis is fixed at R and the dimensionality of growth is provided by the semi-major axis b

defined as $b = 3v_{mon}s/4\pi R^2$. With the aggregate eccentricity E defined as $E = \sqrt{1-(R/b)^2}$, the area/molecule at the interface is given by

$$a = \frac{2\pi R^2}{s}\left[1 + \frac{\sin^{-1} E}{E\sqrt{1-E^2}}\right].$$

4.4.1.4 Steric headgroup repulsion.

The constraining of headgroups to the micelle surface introduces steric hindrance to surfactant translational motion within the aggregate. Assuming these are hard particle interactions Nagarajan models the interactions from a van der Waals approach. Thus $\left(\Delta\mu_s^0/kT\right)_{\text{steric}}$ (in units of kT) is

[4–31] $$\left(\Delta\mu_s^0\right)_{steric} = -\ln\left(1 - \frac{a_p}{a}\right)$$

with parameters previously defined. This term is small and solvent-independent.

4.4.2 Calculations using Nagarajan's model.

Calculations for APFO/H_2O and APFO/EG were carried out at a temperature of 298 K using MathCAD™[49]. The value of the dependent variable $\left(\Delta\mu_s^0\right)$ was computed as the sum of the contributions (a)-(d) defined above as functions of the aggregation number s and monomer mole fraction x_1 (the independent variables). This value and x_1 were introduced into equation [4–27] to obtain the distribution x_s from which the total surfactant concentration was calculated *via* $x_{total} = x_1 + x_{mic}$ where x_{mic} denotes the mole fraction of surfactant in the micellised form given by $x_{mic} = \sum_s sx_s$.

The size-dependent variables $s_{n,app}$ and $s_{n,app}$, representing the apparent weight and number average aggregation numbers respectively, were calcuated *via*

$$s_{w,app} = \frac{x_1 + \sum_s s^2 x_s}{x_1 + \sum_s sx_s}, \quad s_{n,app} = \frac{x_1 + \sum_s sx_s}{x_1 + \sum_s x_s}$$

for $s = 2$ to ∞. The variation of x_1, x_{mic}, $s_{n,app}$ and $s_{n,app}$ with x_{total} reveals the location of the cmc. In order to compare calculated cmc's of the APFO/H_2O and APFO/EG systems with those determined experimentally, a single cmc is calculated[39] as the value of $x_{total} = x_1 + x_{mic}$ where 10% of the surfactant exists in the micellised form i.e. where $x_1 = 9x_{mic}$. An alternative definition[50] of the cmc is that concentration where half the total concentration exists as monomer and half as micelles i.e where any additional dissolved surfactant has an equal probability of entering a micelle or

remaining as monomer. The former definition seems the most reasonable in this work since conductivity is sensitive to the monomer concentration and should reveal the presence of aggregates well before the condition in the latter definition is met.

4.4.3 Results of calculations and comparison with experiment.

The size-dependent variables x_1, x_{mic}, $s_{n,app}$ and $s_{n,app}$ calculated for APFO in water and ethylene glycol are plotted in Figure 4.15 against total concentration x_{total} up to roughly twice the calculated cmc. Calculated cmc's are represented by dotted lines and their values and those determined from conductivity are shown in Table 4.3.

Table 4.3 Comparison of calculated and measured cmc's (mole fraction) at 298 K.

	Calculated	Measured
APFO/H_2O	4.08×10^{-4}	4.56×10^{-4}
APFO/EG	2.09×10^{-2}	6.51×10^{-3}

The absolute values of the calculated cmc's are strongly dependent on the transfer free energy term and in view of the assumptions made with respect to the transfer of fluorocarbons from water the agreement between calculated and measured cmc's of APFO/H_2O is pleasing. However, the model predicts a roughly three-fold greater cmc in ethylene glycol than that measured by conductivity. Some variation between experimental and calculated values is expected since the former value is technique-dependent. Cmc's are determined by the observation of a break in a measured property of the solution as a function of total surfactant concentration and different experimental techniques measure different solution properties. For example, surface tension and conductivity depend largely on the monomer concentration hence a plot of monomer concentration *vs* total concentration is appropriate. The technique of dye solubilisation depends on the concentration of surfactant in the micellised form - here a plot of x_{mic} *vs* total concentration is appropriate. Light scattering techniques depend on the average mass of species in solution so $s_{n,app}$ should be plotted. Properties such as osmotic pressure, vapour pressure and freezing point depression depend on the number of distinct species and $s_{n,app}$ is appropriate. Examination of Figure 4.15(a) shows breaks in these parameters for APFO/H_2O at virtually the same concentration. Figure 4.15(b) shows that surfactant aggregation in ethylene glycol occurs over a wide concentration range and the exact value of the cmc depends on which parameters are being followed i.e. the term 'critical micelle concentration' is not meaningful in non-aqueous solvents. However, the three-fold difference between calculated and experimental APFO/EG cmc's cannot be simply explained by the indeterminacy of an exact cmc value and the difference probably originates in an underestimation of the transfer free energy term $\left(\Delta\mu_s^0\right)_{\text{trans}}$.

Figure 4.15 Calculated size dependent variables for APFO in (a) water and (b) ethylene glycol at 298 K as a function of total surfactant mole fraction. Symbols: $s_{n,app}$, apparent weight average aggregation number; $s_{n,app}$ apparent number average aggregation number; x_1, monomer mole fraction; x_{mic}, micellised mole fraction; x_{total}, total mole fraction. The dotted lines represent the calculated cmc's as $x_1 = 9x_{mic}$ (see text) which are $x_1 = 4.08\text{x}10^{-4}$ in water and $x_1 = 0.0209$ in ethylene glycol.

(a) APFO/water.

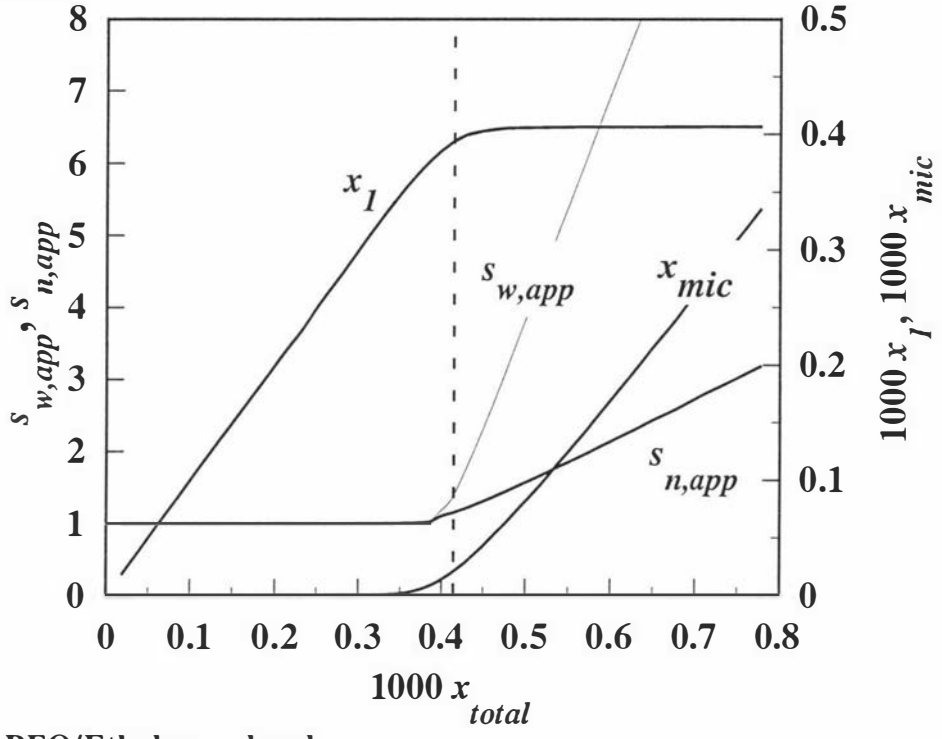

(b) APFO/Ethylene glycol.

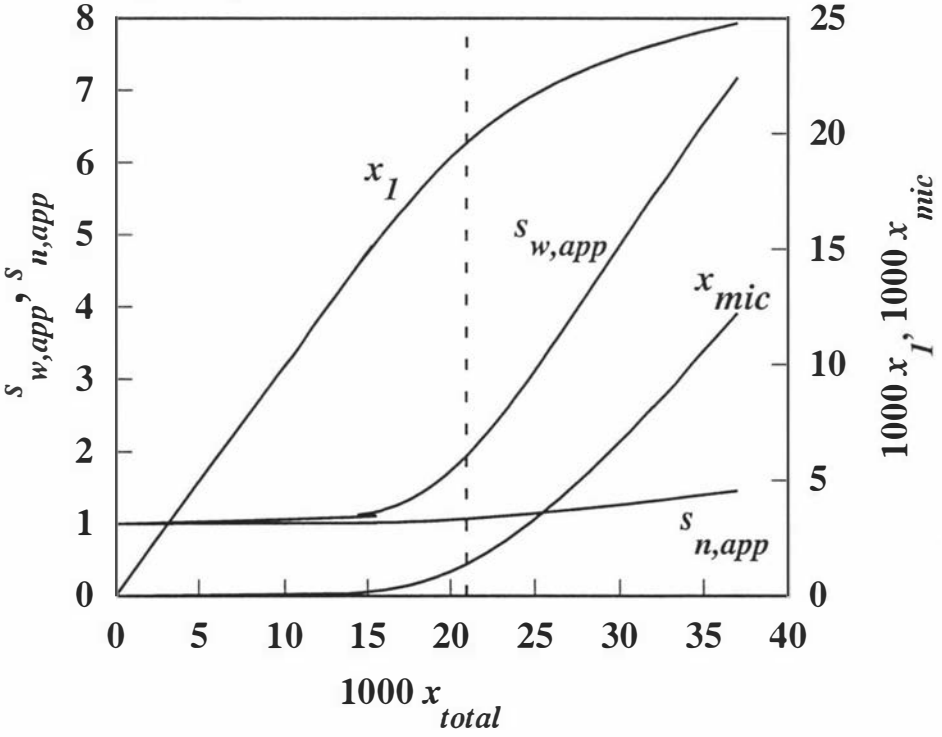

4.4.4 Solvent-dependent micellisation free energies.

These will be discussed with reference to micellisation in pure H_2O and ethylene glycol then their predicted variation in H_2O/EG mixtures will be discussed. Figure 4.16 shows the free energy contributions (a)-(d) to $\left(\Delta\mu_s^0 / kT\right)$ for APFO/H_2O and APFO/EG as functions of aggregation number s at the calculated cmc's. Differences in the aggregation of APFO in water and ethylene glycol can be qualitatively understood by comparison of the solvent-dependent contributions. The three solvent-dependent free energy contributions, the transfer free energy, the electrostatic headgroup repulsion free energy, and the interfacial free energy all show major differences between water and ethylene glycol.

(a) Transfer Free Energy.

This is the only negative contribution and is responsible for the formation of aggregates. It is independent of the aggregation number but strongly influences the magnitude of the cmc. The micelle size is affected only indirectly by $\left(\Delta\mu_s^0 / kT\right)_{\text{trans}}$ since changes in the cmc alters the ionic strength and hence $\left(\Delta\mu_s^0 / kT\right)_{\text{ionic}}$. The greatly reduced $\left(\Delta\mu_s^0 / kT\right)_{\text{trans}}$ value in ethylene glycol is responsible for the increase in cmc.

All other free energy contributions are positive and all influence both s and the cmc.

(b) Electrostatic Headgroup Repulsion Free Energy.

At the same ionic strength, differences in this term between the two solvents must originate in the difference in their relative permittivity. Thus, lowering ε_r by substituting ethylene glycol for water should increase this free energy term. However, at the calculated cmc concentrations, comparing the two terms in Figure 4.16(a) and (b) shows the opposite to be true. The increase in $\left(\Delta\mu_s^0 / kT\right)_{\text{ionic}}$ caused by the decrease in ε_r upon substituting EG for water is more than compensated for by the reduction in electrostatic headgroup repulsion due to the higher ionic strength of the ethylene glycol solutions at cmc concentrations. This term then would have the effect of *reducing* the cmc in ethylene glycol and cannot be responsible for the observed increase. Furthermore, decreasing ionic headgroup repulsion would cause an increase in aggregation number, at odds with experimental observation.

(c) Interfacial Free Energy.

This term decreases with aggregation number and serves to limit the growth of aggregates. It is smaller in ethylene glycol than water due to lower γ_{int} and, on substituting ethylene glycol for water, the change in this term is primarily responsible for the shift in the distribution of micelles to lower values (see Figure 4.17). A smaller

$\left(\Delta\mu_s^0/kT\right)_{\text{int}}$ value leads to a lower cmc so cannot be responsible for the observed increase in cmc.

Figure 4.16 Contributions to the standard free energy change associated with aggregation of APFO at 298 K as a function of aggregation number s at the cmc's in (a) water, with $x_1 = 4.08\text{x}10^{-4}$, and (b) ethylene glycol, with $x_1 = 0.0209$.

(a) APFO/Water

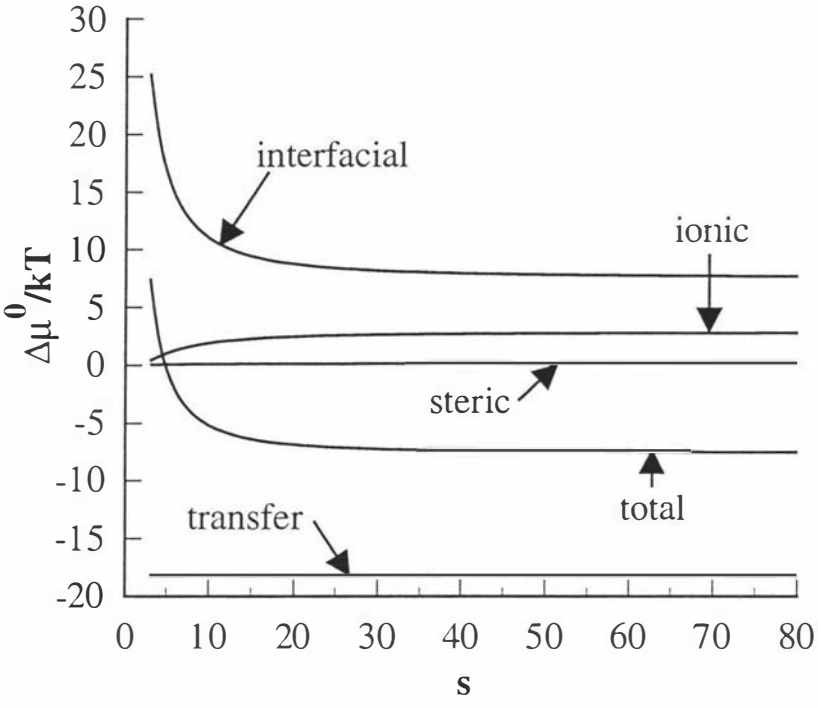

(b) APFO/Ethylene glycol.

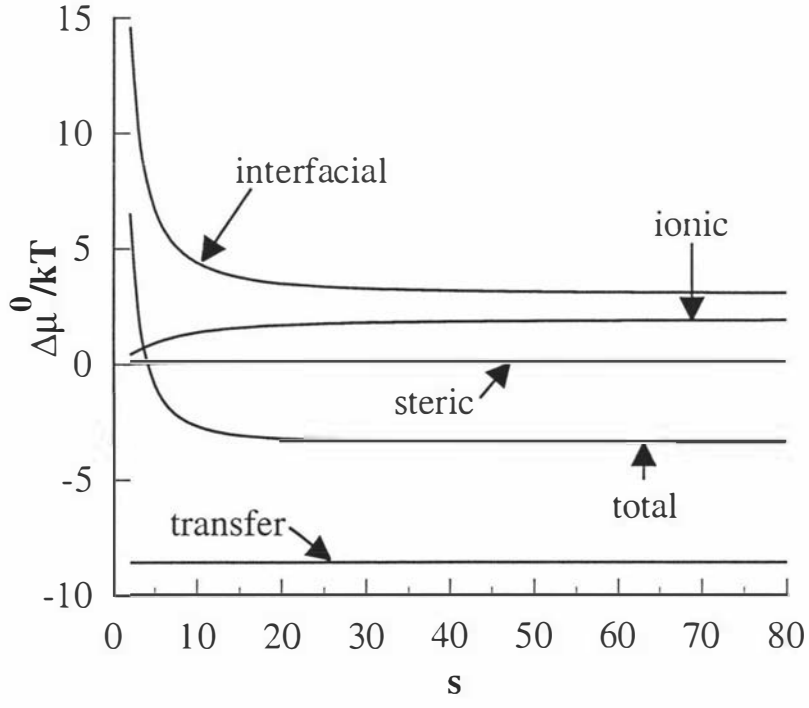

Figure 4.17 Calculated size distributions of APFO in ethylene glycol and water at the cmc's of $x_1 = 0.0209$ and $x_1 = 4.08 \times 10^{-4}$ respectively. Their respective aggregation number distribution maxima occur at 11 and 34.

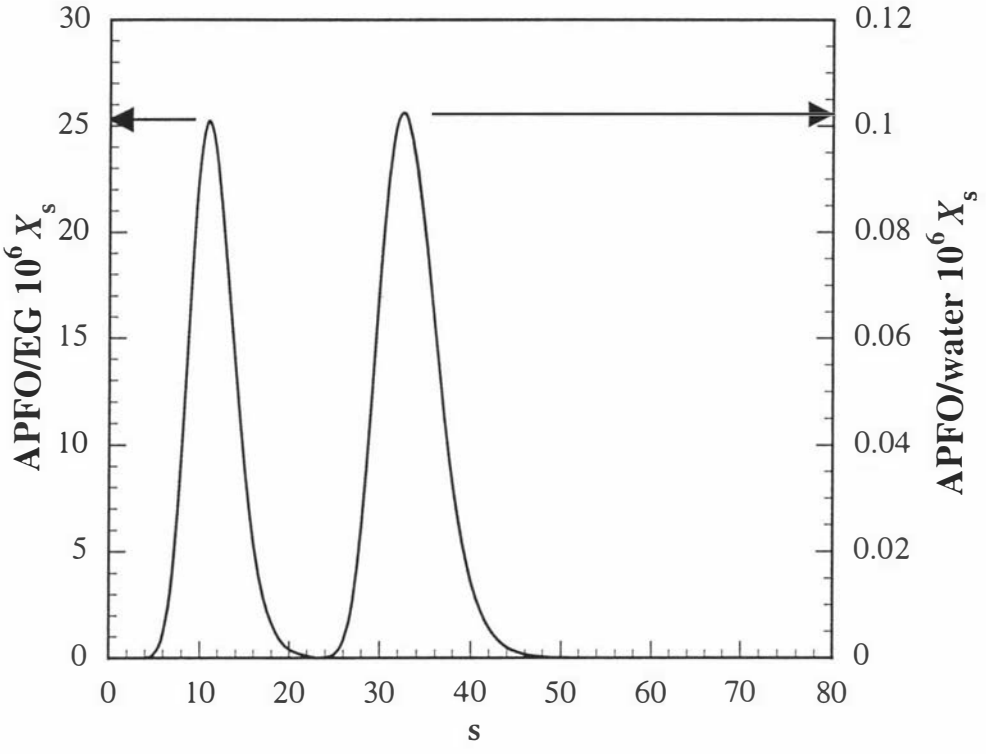

4.4.4.1 Application to H_2O/EG mixtures

In view of the reasonably successful prediction of the APFO/H_2O cmc, the approach used to discuss the aggregation behaviour of APFO in H_2O/EG mixtures will be to consider the variation of the solvent-dependent free energy contributions i.e. $\left(\Delta\mu_s^0/kT\right)_{\text{trans}}$, $\left(\Delta\mu_s^0/kT\right)_{\text{ionic}}$, $\left(\Delta\mu_s^0/kT\right)_{\text{int}}$ and $\left(\Delta\mu_s^0/kT\right)_{\text{total}}$ with EG concentration based on experimentally determined solvent dependent-parameters, where available, normalised to those values predicted by the model for APFO/H_2O, where appropriate. The variation of relevant solvent-dependent parameters with EG composition is shown in Figure 4.18. The derivation of these quantities is discussed in the relevant sections below.

Figure 4.18 Variation in solvent-dependent parameters for ethylene glycol/water solutions with ethylene glycol composition at 298 K

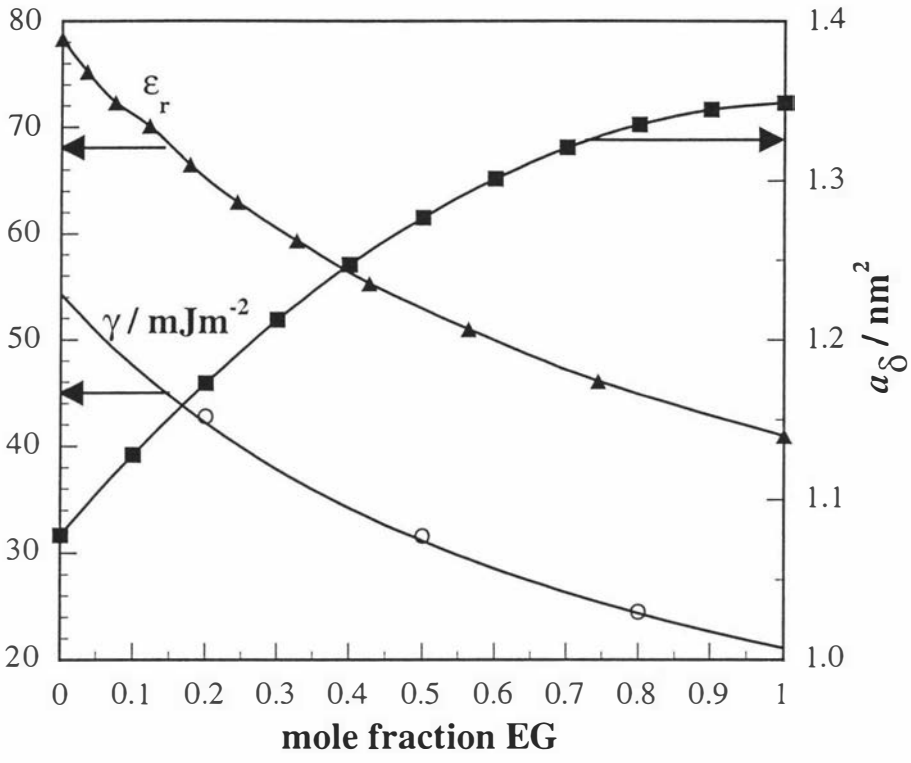

4.4.4.2 Calculation of solvent-dependent free energy contributions.

(a) Transfer Free Energy.

Nagarajan applies the Flory-Huggins equation to the binary H_2O/EG system (ignoring the presence of surfactant) to obtain an expression for $\left(\Delta\mu_s^0 / kT\right)_{\text{trans}}$ thus

$$\left(\Delta\mu_s^0\right)_{\text{trans,mix}} = \phi_{\text{EG}}\left(\Delta\mu_s^0\right)_{\text{trans,EG}} + \phi_{\text{W}}\left(\Delta\mu_s^0\right)_{\text{trans,W}} - \phi_{\text{EG}} \ln\frac{V_{\text{EG}}}{V_{\text{mix}}} - \phi_{\text{W}} \ln\frac{V_{\text{W}}}{V_{\text{mix}}} + \chi_{\text{mix}}\phi_{\text{W}}\phi_{\text{EG}}$$

where $\left(\Delta\mu_s^0\right)_{\text{trans,EG}}$ and $\left(\Delta\mu_s^0\right)_{\text{trans,W}}$ are given by equation [4–28], ϕ is the volume fraction of solvent defined as

$$\phi_{\text{EG}} = x_{\text{EG}} V_{\text{EG}} / V_{\text{mix}} = (1 - \phi_{\text{W}})$$

with $V_{\text{mix}} = x_{\text{EG}} V_{\text{EG}} + x_{\text{W}} V_{\text{W}}$ and solvent molar volumes $V_{\text{W}} = 18.0\ \text{cm}^3\ \text{mol}^{-1}$ and $V_{\text{EG}} = 55.8\ \text{cm}^3\ \text{mol}^{-1}$. x_{W} and x_{EG} are the bulk mole fractions of water and ethylene glycol respectively, and $\chi_{\text{mix}} = -2.3$ at 298 K. χ_{mix} is the Flory interaction parameter

between water and ethylene glycol which Nagarajan estimates‡ from an undiscussed computational method. A negative value indicates that EG-H_2O water attraction is greater than the mean of H_2O-H_2O and EG-EG attractions.

(b) Electrostatic Headgroup Repulsion Free Energy.

The expression for $\left(\Delta\mu_s^0/kT\right)_{\text{ionic}}$ given by equation [4–29] contains three solvent-dependent terms, the ionic strength c, the relative permittivity ε_r, and the average optimal headgroup area a_δ at the centre of the charge on the carboxylate headgroup at the cmc. The latter two quantities are shown in Figure 4.18. ε_r has been determined at a range of temperatures and compositions by Corradini[51]. In this calculation it was assumed that a_δ for APFO/H_2O had that value predicted by Nagarajan's model at s = 34 corresponding to the maximum in the aggregate size distribution at the cmc at 298 K i.e. a_δ = 1.08 nm^2. The variation in the average optimal headgroup area with ethylene glycol composition has been determined from the SAXS measurements presented in Chapter 5 for w = 0.5 APFO at 311 K and it was assumed to vary in the same way at the cmc at 298 K i.e. the values from SAXS were normalised to a_δ = 1.08 nm^2. This assumption gives a_δ = 1.36 nm^2 for APFO/EG which compares favourably with the value of 1.35 nm^2 calculated at s = 11 corresponding to the maximum in the aggregate size distribution at the cmc at 298 K. For the purposes of this comparison, c was taken to be equal to the experimentally determined cmc values shown in Figure 4.10 expressed as molecules/dm^3. It will be shown below that the change in $\left(\Delta\mu_s^0/kT\right)_{\text{total}}$ with ethylene glycol composition is insensitive to changes in $\left(\Delta\mu_s^0/kT\right)_{\text{ionic}}$.

(c) Interfacial Free Energy.

The free energy term $\left(\Delta\mu_s^0/kT\right)_{\text{int}}$ given by equation [4–30] contains two solvent-dependent terms, the fluorocarbon/solvent interfacial tension γ_{int} and the average optimal headgroup area a_0 at the fluorocarbon/solvent interface at the cmc. γ_{int} was estimated by the method outlined in Chapter 6 and is plotted again in Figure 4.18. a_0 was calculated in the same way as a_δ above i.e. by normalising SAXS data to the value of a_0 for APFO/H_2O calculated at s = 34 corresponding to the maximum in the aggregate size distribution at the cmc at 298 K i.e. a_0 = 0.81 nm^2.

---

‡ The validity of the value of χ_{mix} calculated by Nagarajan may be drawn into question in view of the arguments presented in Chapter 6.

4.4.4.3 Results of calculations.

The variation of solvent-dependent free energy contributions with ethylene glycol composition are shown in Figure 4.19. The absolute magnitudes of $\left(\Delta\mu_s^0/kT\right)_{\text{trans}}$ and $\left(\Delta\mu_s^0/kT\right)_{\text{int}}$ contributions shift to lower values with ethylene glycol composition. The variation of $\left(\Delta\mu_s^0/kT\right)_{\text{ionic}}$ shows a complicated behaviour best illustrated by Figure 4.20 which shows the same values plotted in Figure 4.19 normalised to their values in pure water. The form of $\left(\Delta\mu_s^0/kT\right)_{\text{ionic}}$ is a consequence of the opposing effects of the monotonically decreasing ε_r, which increases $\left(\Delta\mu_s^0/kT\right)_{\text{ionic}}$, and the ionic strength, an increase in which leads to a lower $\left(\Delta\mu_s^0/kT\right)_{\text{ionic}}$. The maximum in $\left(\Delta\mu_s^0/kT\right)_{\text{ionic}}$ at low EG concentration corresponds to the minimum in experimental cmc's shown in Figure 4.10. Thereafter, $\left(\Delta\mu_s^0/kT\right)_{\text{ionic}}$ decreases as the cmc increases. Figure 4.19, however, shows that $\left(\Delta\mu_s^0/kT\right)_{\text{total}}$ is insensitive to changes in electrostatic free energy and decreases steadily with EG composition. This would lead to increasing cmc's with increasing EG composition i.e. Nagarajan's model cannot explain the minima in cmc's of fluorocarbon surfactants. Nonetheless , the change in $\left(\Delta\mu_s^0/kT\right)_{\text{total}}$ successfully predicts a decreasing average aggregation number *s* with ethylene glycol composition consistent with experiment.

Figure 4.19 Variation of solvent-dependent free energies with ethylene glycol composition at 298 K.

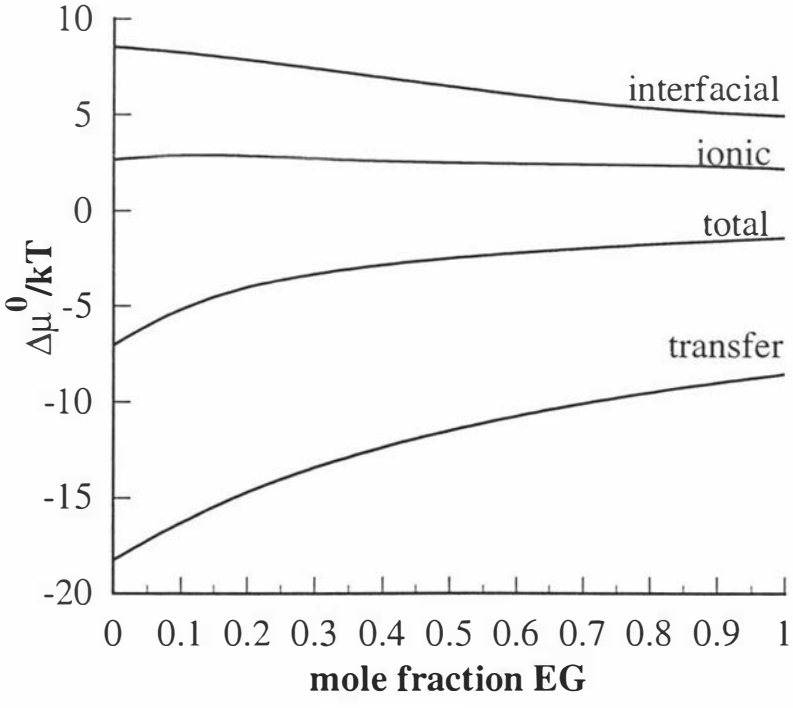

Figure 4.20 Variation of the solvent-dependent free energies in Figure 4.19, normalised to their values in pure water, with ethylene glycol composition at 298 K.

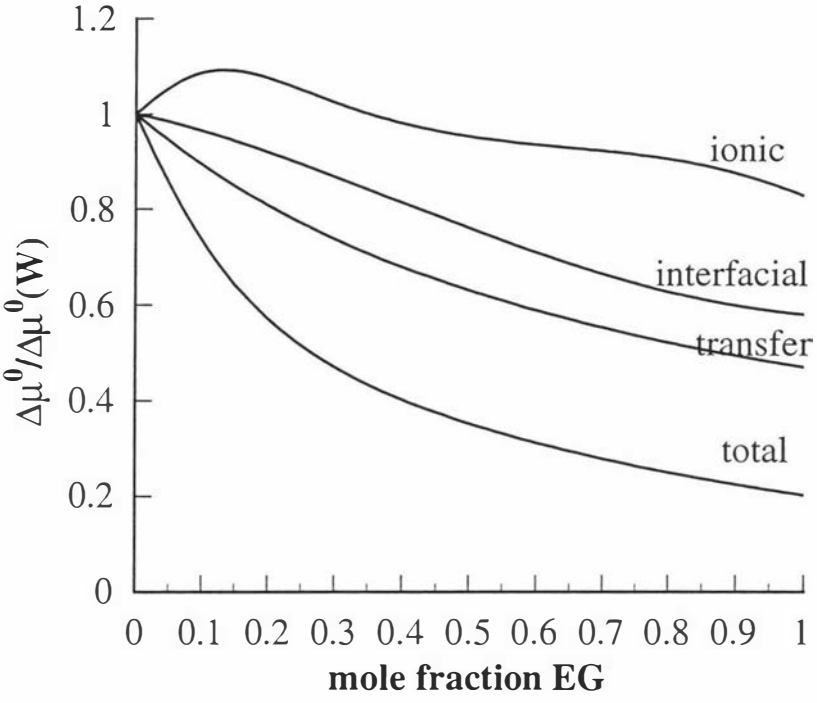

4.4.5 The effect of temperature in Nagarajan's model.

The minima in experimentally determined aqueous APFO cmc's with temperature are not predicted by Nagarajan's model, which predicts a monotonically decreasing cmc with decreasing temperature.

4.4.6 Summary of Nagarajan's model predictions.

Applying Nagarajan's phenomenological model to the effect of changing solvent on the aggregation of APFO has provided a useful insight into the origin of the increase in critical micelle concentrations and the shift in the distribution of micelle aggregation numbers to lower values upon substituting ethylene glycol for water at constant temperature.

4.4.6.1 Effect on cmc.

The increase in cmc accompanying the substitution of EG for water lies in the much reduced magnitude of the transfer free energy which outweighs the opposing effects of the reduction in the other solvent-dependent free energy terms i.e. electrostatic headgroup repulsion and interfacial free energies. However, the model cannot explain the experimentally-determined minimum in mixed solvents cmc's. In view of the strong dependence of the cmc on the transfer free energy, the inadequacies in the model

lie in the almost complete lack of experimental data for this free energy contribution for perfluorocarbons and consequently, the assumptions necessary for its estimation.

4.4.6.2 Effect on average aggregation number *s*.

Shifts in the distribution of micelle aggregation numbers upon changing solvents are only indirectly affected by changes in transfer free energy since this remains constant with *s* but influences the cmc and hence the ionic strength. In the pure solvent systems, the decrease in relative permittivity accompanying the substitution of EG for water does not cause an expected shift in the distribution of micelle aggregation numbers to higher values since the increase in cmc, and hence the ionic strength of the solutions, more than compensates for this effect, leading to a decrease in ionic headgroup repulsion. Thus the origin of the decrease in average aggregation number on substituting EG for water can solely be attributed to the reduction in the fluorocarbon/solvent interfacial tension. This also explains the shift to lower *s* in the EG/H_2O solvent mixtures. This conclusion highlights the importance of the interfacial tension in governing the self-assembly of perfluorocarbon surfactants which will be further emphasised by the NMR and SAXS measurements presented in Chapter 5.

4.5 Discussion of experimental cmc results.

The experimentally-determined cmc results will now be discussed with reference to the mass-action and phase separation models and the results of Nagarajan's phenomenological model.

4.5.1 The isotope effect on micellisation.

Substituting D_2O for H_2O has two effects on APFO micellisation: (i) it displaces the cmc's to higher concentration, and (ii) it displaces the minimum in the temperature dependence of the cmc's to higher temperature.

4.5.1.1 The isotope effect on cmc's.

The experimental result that the isotope effect displaces cmc's of APFO to higher concentration is in agreement with previous studies on the isotope effect on CsPFO[4] micellisation. In aqueous hydrocarbon surfactant systems, substituting D_2O for H_2O displaces hydrocarbon surfactant cmc's to lower concentration. Figure 4.21 compares the temperature-dependence of the isotope effect on two hydrocarbon surfactants, SDS[1] and DTAB[3], with CsPFO[4], all of which were determined by conductivity.

Figure 4.21 Comparison of cmc's of CsPFO[4] (circles), SDS[1] (squares) and DTAB[3] (triangles) in D_2O (closed points) and H_2O (open points) as a function of temperature. Lines are fits to data points with degree-three polynomials. The isotope effect on the cmc's of CsPFO is the same for APFO shown in Figure 4.8 but opposite to the effect on the hydrocarbon surfactants SDS and DTAB.

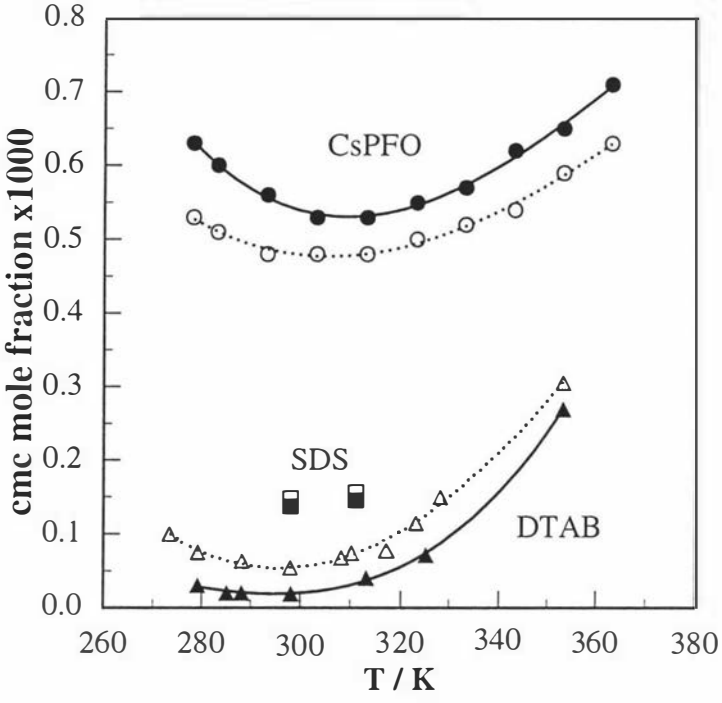

The isotope effect on hydrocarbon surfactant chainlength at 298 K has been studied by Berr[2] for alkyltrimethylammonium bromides (C_nTAB with n=12,14 and 16) using surface tension, and Chang[1] for sodium alkylsulphates (SD_nS with n=8,10,12 and 14) using electrical conductivity measurements. Table 4.4 shows that, for hydrocarbon surfactants, in all but one case the isotope effect was to displace the cmc's to lower values. It is reasonable to attribute the anomalously higher cmc of C_{12}TAB (=DTAB) in D_2O to experimental error in view of the data from Emerson[3] on the same system shown in Figure 4.21. There is a large difference between the absolute values of the cmc of C_{12}TAB (=DTAB) obtained by the two groups. It is not unusual to find different cmc values when determined by different experimental methods since they monitor variation in different solution properties with surfactant concentration. This was discussed in section 4.4.3. However, a five-fold difference cannot be accounted for by this factor.

Table 4.4 The isotope effect on hydrocarbon surfactant chain length at 298 K.

	n	cmc mole fraction x1000	
		H_2O	D_2O
DTAB[3] (=C_{12}TAB)	12	0.0544	0.0191
C_nTAB[2]	12	0.241	0.245
	14	0.0617	0.0597
	16	0.0181	0.0148
SD_nS[1]	8	2.51	2.40
	10	0.611	0.571
	12	0.148	0.138
	14	0.0400	0.0356

Having established that the opposite isotope effect on surfactant cmc's is a real phenomenon, the origin of the difference can be speculated upon. The fact that a minimum appears at all is just one of the many peculiarities associated with water. The increase in cmc at lower temperature has been attributed to the "possible dehydration of the ionic headgroup of micellised surfactant with respect to the monomer below 298 K[44, 52]" though (unhelpfully) no further elucidation of, nor literature references to, this statement were given.

The cmc curves do not appear to converge at any temperature, as would be expected if the two solvents were to become "normal" solvents at high temperature (~160°C), as suggested by Shinoda[53].

Following the oft-quoted argument of Frank and Evans[52], the driving force for surfactant aggregation is the entropy increase associated with the release of structured water ("icebergs") around the hydrophobic solute. Since it is generally accepted that D_2O is more structured than H_2O, this cannot explain the increased solubility in D_2O at all temperatures.

Even though Nagarajan's model does not directly account for the isotope effect, a simple explanation within the framework of his model can be derived from solubility considerations (at least in the case of perfluorocarbon surfactants) that explains both the minima in temperature-dependence of the cmc's and the isotope effect. The cmc can be viewed as a "solubility limit" for a surfactant. In this context, the isotope effect on cmc's implies that fluorocarbons are more soluble in D_2O than H_2O. There is a very little literature data on the solubility of perfluoroalkanes. The only data available[32] that compares solubilities in water and heavy water are for CF_4 and C_2F_6 over a narrow temperature range and these are shown in Figure 4.22. The Figure shows that over the temperature range investigated (5-30°C) perfluoroalkanes are indeed more soluble in D_2O than H_2O and the non-monotonic variation in solubilities with temperature may

imply the existence of minima at higher temperature. The corresponding thermodynamic free energies of solubilisation ΔG°(gas→aq.) are shown in Figure 4.23.

Figure 4.22 Solubilites of perfluoroalkanes in H_2O (open points) and D_2O (closed points) as a function of temperature.

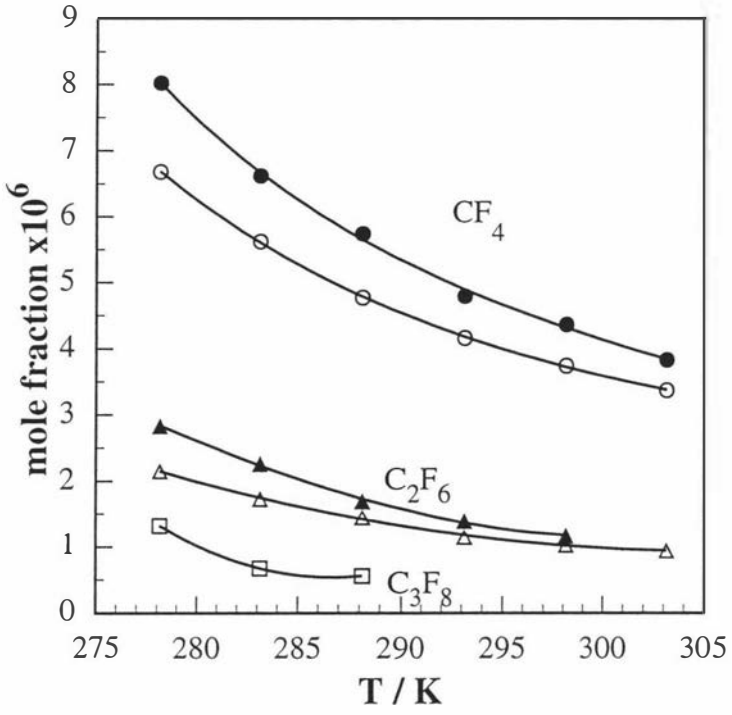

Figure 4.23 Transfer free energy ΔG°(gas→aq.) of perfluoroalkanes in H_2O (open points) and D_2O (closed points) as a function of temperature.

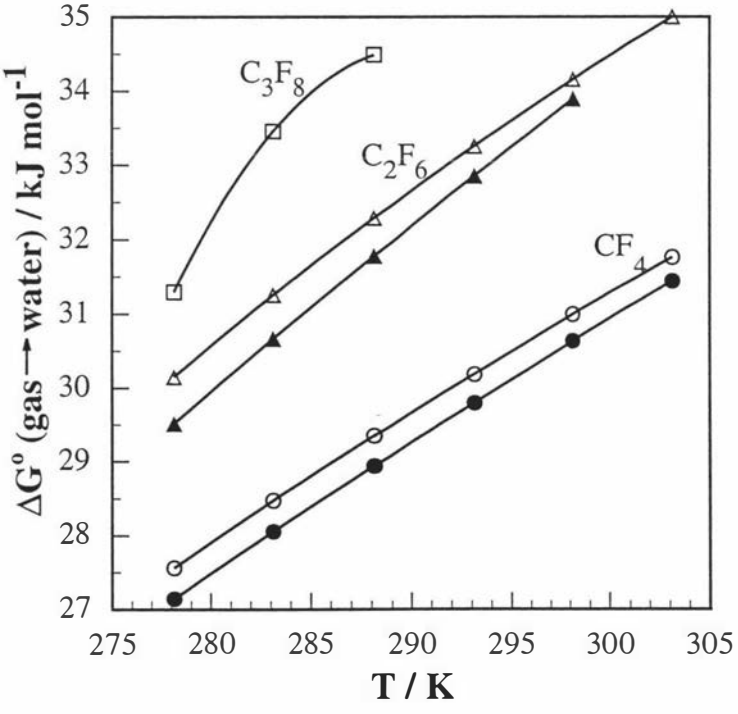

ΔG°(gas→aq.) can be related[28, 29] to the expression appropriate for micelle formation ΔG°(aq.→liq.) i.e. the free energy change accompanying the transfer of a fluorocarbon dissolved in water to the micelle interior (entirely equivalent to $\left(\Delta\mu_s^0 / kT\right)_{\text{trans}}$ in Nagarajan's model) *via* the free energy of vaporisation $\Delta G^{\circ}_{\text{vap}}$ thus

[**4–32**] $$-\Delta G^{\circ}(\text{aq.} \rightarrow \text{liq.}) = \Delta G^{\circ}_{\text{vap}} - \Delta G^{\circ}(\text{gas} \rightarrow \text{aq.}).$$

If the isotope effect evident in Figure 4.22 can be extrapolated to the chainlength of interest i.e. C_7F_{16} (a rather speculative assertion considering the lack of data), and since $\Delta G^{\circ}_{\text{vap}}$ is independent of solvent, then the isotope effect on the cmc's can be explained simply as due to the transfer free energy ΔG°(aq.→liq.) being smaller in magnitude (less negative) in D_2O than H_2O leading to perfluorocarbon surfactants having greater cmc's in D_2O than H_2O.

The isotope effect on hydrocarbon surfactants cannot be explained by an analagous argument since the isotope effect on methane, ethane[32] and propane[54] solubility acts *in the same direction* as that for perfluoroalkanes. It may be asserted, then, that the isotope effect on hydrocarbon surfactant cmc's is the anomalous one. This behaviour of hydrocarbons may be explicable by, in the case of longer-chain alkanes, the contribution of chain entropy (considered to be negligible in perfluoroalkylchains), and possibly enthalpy, dominating ΔG°(aq.→liq.).

Boden *et al*[4] attributed the difference in behaviour between hydrocarbon and fluorocarbon surfactants to differences in the interactions of their respective hydrophobic moities with the solvents. They considered the trade-off between the free energy change $\Delta\mu_2^{cav}$ associated with the work of forming a cavity large enough to accommodate the surfactant in the solvent, and the free energy change $\Delta\mu_2^{att}$ associated with the attractive Lennard-Jones solute-solvent intermolecular interaction. On substituting D_2O for H_2O the number density of solvent molecules decreases, resulting in a more positive $\Delta\mu_2^{cav}$ and a less negative $\Delta\mu_2^{att}$. The higher cmc's of perfluorocarbon surfactants in D_2O indicate that $\Delta\mu_2^{cav}$ dominates $\Delta\mu_2^{att}$ resulting in the surfactant monomer having a lower free energy and consequently a higher solubility in D_2O. This is in keeping with the larger molecular volumes and consequently large values of $\Delta\mu_2^{cav}$ for perfluorocarbon chains and the lower $\Delta\mu_2^{att}$ values evidenced by weaker fluorocarbon chain-chain interactions compared to hydrocarbon chain-chain interactions. The higher hydrocarbon surfactant cmc's in H_2O compared to D_2O

indicate that $\Delta\mu_2^{art}$ must dominate $\Delta\mu_2^{cav}$ which is consistent with their smaller volumes and stronger chain-chain interactions.

4.5.1.2 The isotope effect on the cmc minimum.

In common with many other systems[53], the temperature-dependences of APFO/H_2O and APFO/D_2O cmc's are well-correlated (>0.993) by symmetrical parabolas. Table 4.5 compares the temperatures T^* at the minima in the temperature-dependences of the cmc's shown in Figure 4.8 and Figure 4.21 fitted with symmetric parabolic curves. The isotope effect on the temperature-dependence of the cmc's of fluorocarbon surfactants is to shift the minimum to higher temperature whereas, in the case of DTAB cmc's, any isotope effect on the minimum is unclear. In view of the lack of data on other surfactant systems available for comparison, the significance of the shift in T^* remains uncertain.

With reference to the phase-separation model, the minimum corresponds to $\Delta H_s^0 = 0$ which is discussed below.

Table 4.5 Comparison of T^*, the temperature at the minimum in the temperature-dependence of the cmc's.

	H_2O	D_2O	isotope effect
APFO	311.1 K	317.3 K	+6.2 K
CsPFO[4]	305.2 K	309.2 K	+4.0 K
DTAB[3]	295.4 K	295.0 K	-0.4 K

4.5.1.3 Experimental thermodynamic parameters of aqueous APFO micellisation.

Figure 4.24 shows the thermodynamic parameters of APFO/H_2O (dotted line) and APFO/D_2O (solid line) micellisation determined using the phase separation model *via* equations [4–14], [4–15] and [4–16]. The corresponding parameters determined using the mass-action model *via* equations [4–13], [4–15] and [4–16] are shown in Figure 4.25. The latter parameters depend on the estimation of the free ion fraction α by equation [4–17] and $d\alpha/dT$ which are plotted in Figure 4.12, the form of which requires some discussion. It is uncertain whether the crossover in α at lower temperature truly reflects the free counterion fraction or is due to the invalidity of some of the assumptions used in its derivation since there is no independent data available for comparison. A drop in α at low temperature using conductivity was observed by Smith[56] in both the CsPFO/H_2O and CsPFO/D_2O systems. It was

assumed in that work that the drop was due to experimental error and the low temperature data discarded. Furthermore, it was assumed that there was no difference in α between CsPFO/H_2O and CsPFO/D_2O. Considering some of the unrealistic assumptions inherent to the mass-action (e.g. s is invariant with temperature) and phase separation (e.g. s is infinite) models the thermodynamic parameters extracted are restricted to qualitative interpretation only. With this in mind, the approach by Smith to the mass-action model was adopted here.

Figures 4.24 and 4.25 show that values of ΔG for both models are negative, indicating that the formation of micelles is favourable, and this quantity remains essentially constant with temperature showing compensation behaviour common to aqueous systems. At low temperature the large and positive ΔH implies unfavourable fluorocarbon chain-chain interactions, and that it is the entropy of the solvent that drives micelle formation. Furthermore, at low temperature ΔS is more positive in D_2O than H_2O reflecting the generally accepted higher degree of structure in heavy water. As temperature is increased, both ΔS and ΔH become more negative indicating (a) that the solvents are becoming less structured, and (b) that fluorocarbon chain-chain interactions are becoming more favourable and begin to dominate ΔG. Within the phase separation model, the minimum in the temperature dependence of the cmc's coincides with $\Delta H = 0$ and indicates this crossover from a dominance of entropic contributions at low temperature to a dominance of enthalpic contributions to ΔG. The difference in the form of the curves for D_2O and H_2O i.e. the upturn in H_2O values at higher temperatures in both Figures cannot be explained at present.

Figure 4.24 Thermodynamic parameters of APFO/H_2O (dotted line) and APFO/D_2O (solid line) micellisation determined using the **phase separation model** *via* equations[4–14], [4–15] and [4–16].

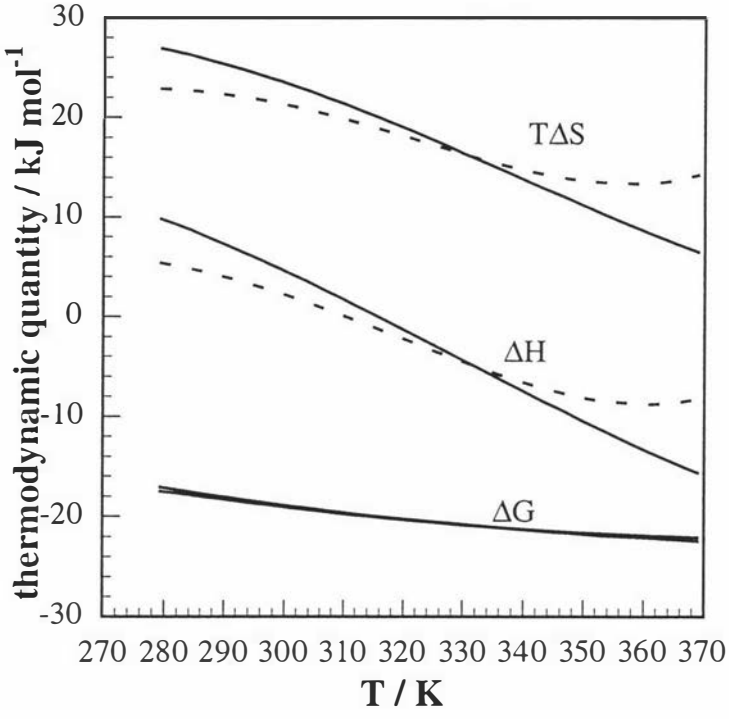

Figure 4.25 Thermodynamic parameters of APFO/H_2O (solid points) and APFO/D_2O (open points) micellisation determined using the **mass-action model** (equations [4–13], [4–15] and [4–16].

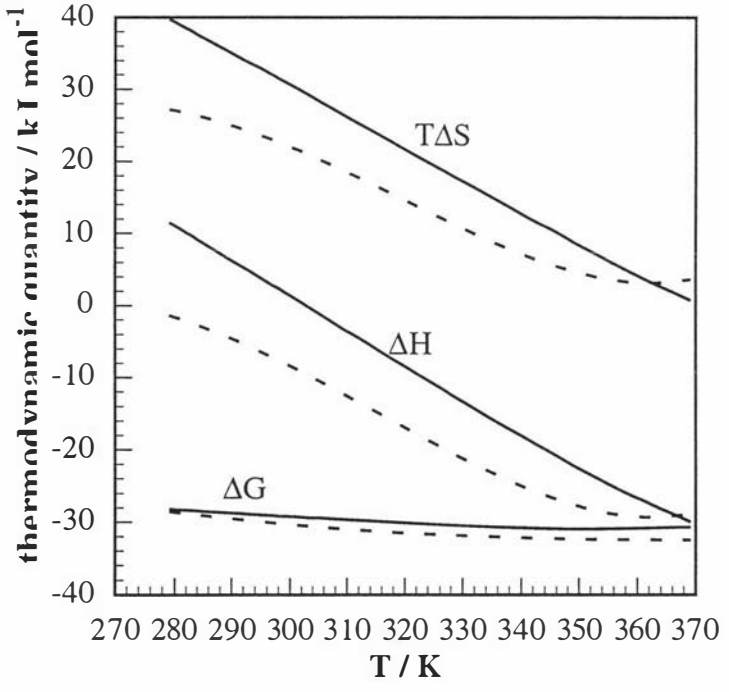

4.5.2 Surfactant aggregation in ethylene glycol - does a cmc exist?

This section discusses the conductivity results for APFO in EG and EG/water mixtures and addresses the validity of the concept of a critical micelle concentration in non-aqueous solvents.

The aggregation behaviour of APFO in EG is illustrated by the variation of the conductivity *vs* concentration curves at 295 K shown in Figure 4.26. Initially the conductivity varies linearly with concentration according to equation [4–1], then the slope of the curve gradually lessens indicating the onset of aggregation, when the conductivity is given by equation [4–4]. Thus conductivity reveals that APFO aggregates do form in non-aqueous solvents, but since no abrupt change in slope occurs, aggregation occurs over a wide concentration range.

A good insight into the effect of ethylene glycol on the conductivity of APFO in ethylene glycol/water solutions is provided by Figure 4.27, which shows the variation of the difference $\Delta d\kappa/dc$ in conductivity *vs* concentration slopes above and below the cmc's as the composition of ethylene glycol is increased at 298 K. Since the cmc is calculated as the intersection of lines with these slopes and α is calculated as their ratio, it is clear that any random errors (or, more importantly,

Figure 4.26 Conductivity *vs* concentration for the APFO/EG system at 295 K. The dotted line represents the cmc calculated from the fitting method described in section 4.1.2. The selection of points above the cmc to fit linearly is subjective, and it may be that the curve never become linear.

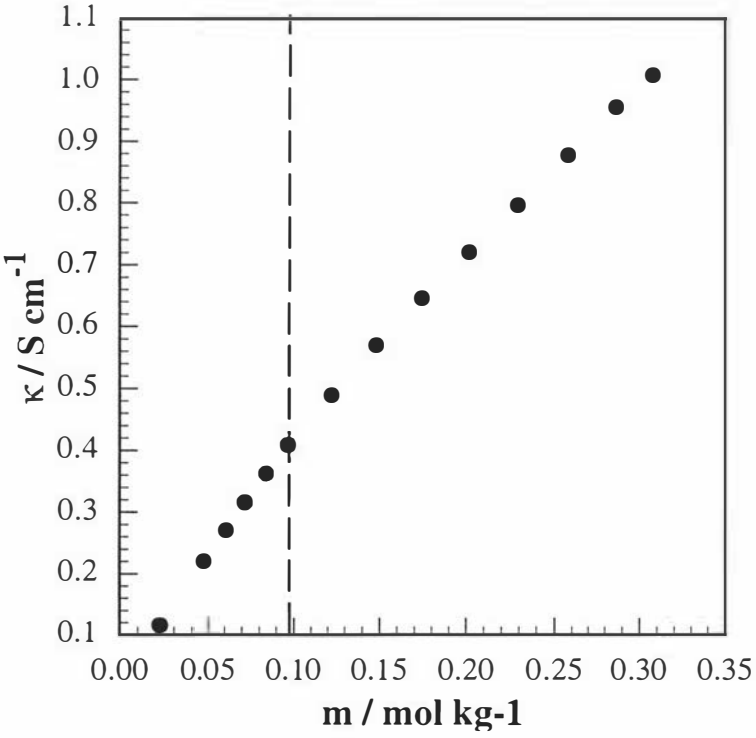

Figure 4.27 The difference in slope of the conductivity *vs* concentration curves above and below the cmc's, $\Delta d\kappa/dc$ in APFO/EG/H_2O systems as a function of ethylene glycol composition at 298 K. The line is a visual guide only.

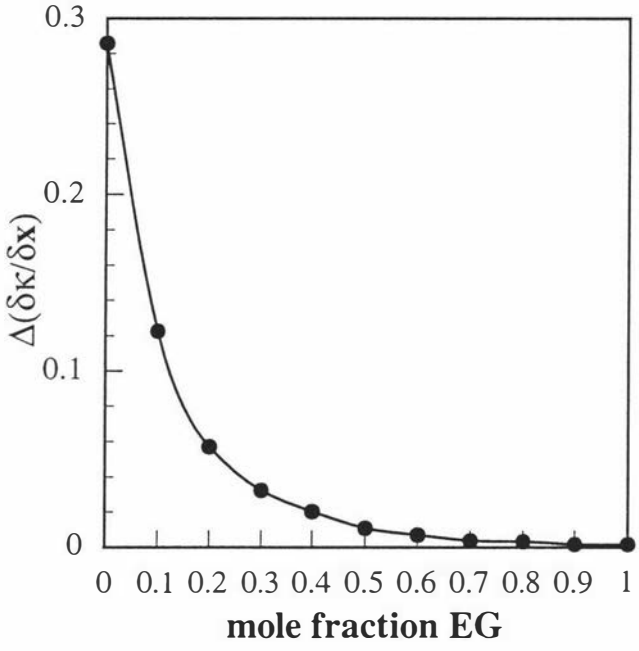

non-random influences) associated with the slope determination become rapidly more significant with increasing EG composition. The problem increases with increasing temperature because of the increased range over which aggregation occurs. In the absence of a well defined linear region above the cmc in the conductivity *vs* concentration plots it is clear that the cmc obtained by linear extrapolation is not a well-defined quantity. Thus, at the temperatures examined here for the APFO/EG system, a *critical* micelle concentration cannot be experimentally determined by conductivity, though the concept of a cmc may be appropriate at very low temperatures. In that temperature regime formal cmc's may fall below the solubility curve, though they may still be accessible since ethylene glycol solutions have been shown[22] to supercool to very low temperatures (-160°C).

4.5.2.1 Experimental thermodynamic parameters of APFO/EG micellisation.

Thermodynamic properties were not extracted using the mass-action or phase separation models because they have been shown to be unsuitable models for APFO/EG micellisation. For example, the mass-action model assumes that one equilibrium constant i.e the value of K in equations [4–7] and [4–9] is constant and

that one aggregation number dominates. These have been shown to be invalid assumptions for the APFO/EG system. The phase separation model assumes that *s* is infinite and, whilst it is self-evident that *s* is finite in the APFO/water system, it is much larger for this system than it is for the APFO/EG system and the model remains a reasonable approximation for APFO/water.

However, the application of Nagarajan's model to APFO/EG micellisation successfully predicts aggregation occurring at higher surfactant concentrations i.e higher "cmc's" (largely as a consequence of decreased transfer free energy) and smaller average aggregation numbers (largely as a consequence of decreased interfacial tension) consistent with both the conductivity results presented in this Chapter and the SAXS and NMR results to be presented in Chapter 5.

4.5.2.2 Surfactant aggregation in solvent/water mixtures.

Generally, the addition of cosolvent to water at constant temperature causes cmc's to increase and average aggregation numbers to decrease (as evidenced by the increase in free ion fraction irrespective of the change in cmc and the fluorocarbon surfactant). Nagarajan's model can account for these trends on the basis of decreases in transfer free energy and lowering of interfacial tension. However, his model cannot explain the small minimum in cmc with small concentrations of cosolvent though it appears to be a phenomenon common to perfluorocarbon (and some hydrocarbon) surfactants. Figure 4.28 summarises the cmc's of all known perfluorocarbon surfactants in the presence of cosolvents up to $x_{solvent} = 0.1$ reduced to their values in pure H_2O (APFO-open circle, LiPOS-open square[7]) or D_2O (closed points, CsPFO[6]). There is insufficent data to clearly correlate the trends in cmc's of different surfactants with the effect of cosolvent on bulk solvent properties, made worse by the isotope effect. However, considering only the points relating to the effect of cosolvent on CsPFO/D_2O cmc's, a (rather tentative) correlation presents itself with the location and depth of the minimum in cmc's with cosolvent concentration i.e. the depth of the minimum is shifted to higher surfactant concentration with increasing interfacial tension of the cosolvent (FA>NMF>DMF>DMA). In addition, the location of the minimum is shifted to lower cosolvent mole fraction with increasing interfacial tension: The point representing formamide may have passed through the minimum, the NMF points show the minimum, and DMF and DMA are yet to pass through it. The minima in APFO/EG/H_2O and LiPOS/EG/H_2O cmc curves occur at the EG concentrations shown in Figure [4.28] .

The increase in free ion fraction for CsPFO/D_2O shown in Figure 4.29 is consistent with both a decrease in aggregation number at all compositions and with a

reduction in interfacial tension. There appears to be no correlation between changes in bulk relative permittivity and the reduced values plotted in either figure.

Figure 4.28 Cmc's of all known perfluorocarbon surfactants in the presence of cosolvents up to $x_{solvent} = 0.1$ reduced to their values in pure H_2O (APFO-open circle, LiPOS-open square[7]) or D_2O (closed points, CsPFO[6]).

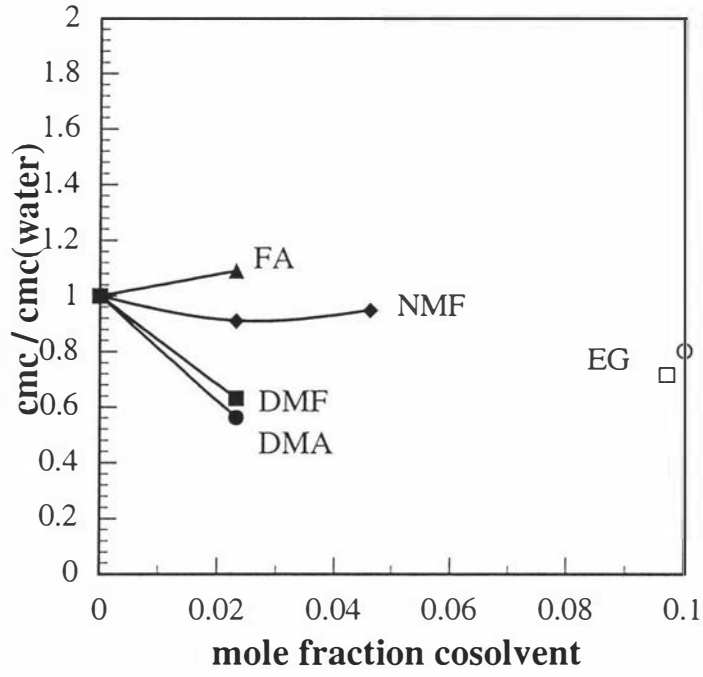

Figure 4.29 Estimated free ion fractions α of all known perfluorocarbon surfactants in the presence of cosolvents up to $x_{solvent}$=0.1 reduced to their values in pure H_2O (APFO-open circle) or D_2O (closed points, CsPFO[6]). The increase in α for the CsPFO/D_2O/cosolvent data can be correlated with decreasing interfacial tensions.

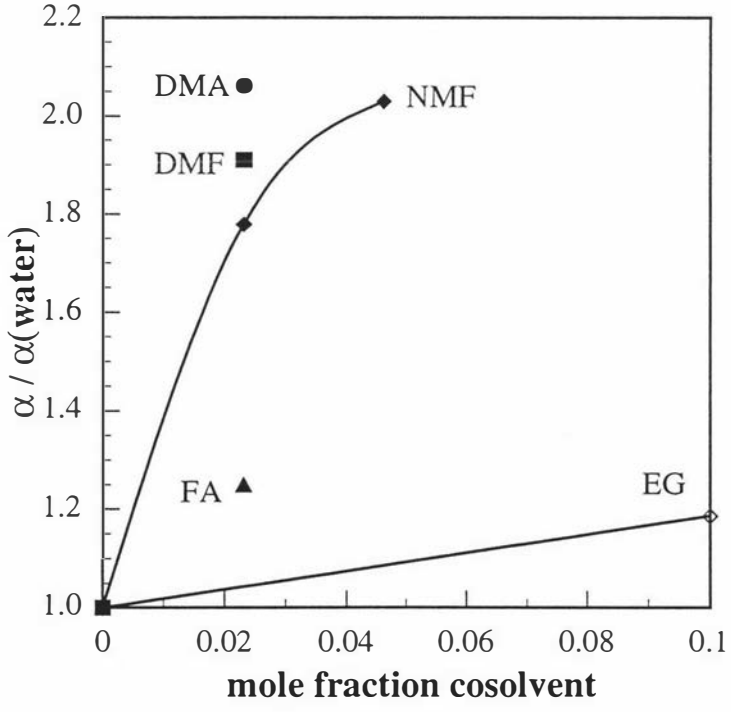

4.6 References.

1. Chang, J.N. and E.W. Kaler, *J. Phys. Chem.* **1985**, *89*, 2996.

2. Berr, S.S., *J. Phys. Chem.* **1987**, *91*, 4760.

3. Emerson, M.F. and A. Holtzer, *J. Phys. Chem.* **1967**, *71*, 3320.

4. Boden, N., K.W. Jolley, and M.H. Smith, *J. Phys. Chem.* **1993**, *97*, 7678.

5. Callaghan, A., *et al.*, *Langmuir* **1993**, *9*, 3422.

6. Thomsen, S.J, M.Sc. Thesis, Dept. of Chemistry, Massey University, New Zealand. 1994.

7. Esumi, K. and S. Ogiri, *Colloids and Surfaces A* **1995**, *94*, 107.

8. Atkins, P. *Physical Chemistry*; Editor Ed.; Oxford University Press: Oxford, 1982;

9. Heiks, J.R., *et al.*, *J. Phys. Chem.* **1954**, *58*, 488.

10. Kissa, E. *Fluorinated Surfactants*; Marcel Dekker, Inc: New York, 1994; Vol. 50, 469.

11. Evans, D.F. and P.J. Wightman, *J. Colloid Interface Sci.* **1982**, *86*, 515.

12. Evans, D.F., *et al.*, *J. Solution Chem.* **1984**, *13*, 87.

13. Ramadan, M.S., D.F. Evans, and S. Philson, *J. Phys. Chem.* **1985**, *89*, 3405.

14. Ramadan, M.S., D.F. Evans, and R. Lumry, *J. Phys. Chem.* **1983**, *87*, 4538.

15. Hoffmann, H. and W. Ulbricht, *Z. Physikalische Chemie Neue Folge* **1977**, *106*, 167.

16. Zana, R., *J. Colloid Interface Sci.* **1980**, *78*, 330.

17. Mendez Sierra, J., *et al.*, *Colloids and Surfaces A* **1996**, *117*, 143.

18. Asakawa, T., *et al.*, *Langmuir* **1995**, *11*, 2376.

19. Boden, N., S.A. Corne, and K.W. Jolley, *Chem. Phys. Lett.* **1984**, *105*, 99.

20. Mukerjee, P., *et al.*, *J. Phys. Chem.* **1985**, *89*, 5308.

21. Mukerjee, P., K. Mysels, and P. Kapuan, *Journal of Physical Chemistry* **1967**, *71*, 4166.

22. Harding, R., *to be submitted,* in *Chemistry*. 1997, Leeds University: Leeds.

23. Gelbart, W., A. Ben-Shaul, and D. Roux, ed. *Micelles, Membranes, Microemulsions, and Monolayers*. 1st ed. Partially Ordered Systems, ed. L. Lam and D. Langevin. 1994, Springer-Verlag, Inc: New York. 608.

24. Nagarajan, R. and C.-C. Wang, *Langmuir* **1995**, *11*, 4673.

25. Nagarajan, R. and C. Wang, *Journal of Colloid and Interface Science* **1996**, *178*, 471.

26. Nagarajan, R., *Journal of Colloid and Polymer Science* **1998**, *submitted for publication*,

27. Rabolt, J. and B. Franconi, *Macromolecules* **1978**, *11*, 740.

28. Abraham, M., *Journal of the Chemical Society, Faraday Transactions I* **1984**, *80*, 153.

29. Abraham, M. and E. Matteoli, *J. Chem. Soc., Faraday Transactions I* **1988**, *84*, 1985.

30. Pierotti, G., C. Deal, and E. Derr, *Industrial and Engineering Chemistry* **1959**, *51*, 95.

31. Hildebrand, J. and R. Scott *The Solubility of Nonelectrolytes*; Reinhold: New York, 1950;

32. Wen, W.-Y. and J.A. Muccitelli, *Journal of Solution Chemistry* **1979**, *8*, 225.

33. Scharlin, P. and R. Battino, *Journal of Chemical and Engineering Data* **1995**, *40*, 167.

34. Park, T., *et al.*, *Journal of Chemical and Engineering Data* **1982**, *27*, 324.

35. Abraham, M., . 1997,

36. Shinoda, K., M. Hato, and T. Hayashi, *J. Phys. Chem.* **1972**, *76* , 909.

37. Boden, N., *et al.*, *J. Chem. Phys.* **1990**, *93*, 9096.

38. Boden, N., *et al.*, *J. Chem. Phys.* **1995**, *103*, 5712.

39. Tanford, C. *The Hydrophobic Effect*; Editor Ed.; Wiley: New York, 1980;

40. Mitchell, D. and B. Ninham, *Journal of Physical Chemistry* **1983**, *87*, 2996.

41. Fowkes, F.M., *Industrial and Engineering Chemistry* **1964**, *56*, 40.

42. Good, R.J. and E. Elbing, *Industrial and Engineering Chemistry* **1970**, *62*, 54.

43. Girifalco, L. and R. Good, *Journal of Physical Chemistry* **1957**, *61*, 904.

44. Nagarajan, R. and E. Ruckenstein, *Langmuir* **1991**, *7*, 2934.

45. Burkitt, S., *et al.*, *Colloid and Polymer Science* **1987**, *265*, 619.

46. Brandao, M., , in *Chemistry*. 1997, Leeds University: Leeds.

47. MacKintosh, F.C., S.A. Safran, and P.A. Pincus, *Europhysics Letters* **1990**, *12*, 697.

48. Safran, S.A., *et al.*, *J. Phys. France* **1990**, *51*, 503.

49. Mathsoft, I., *MathCAD*. 1989, Mathsoft, Inc: Cambridge, Mass.

50. Hartley, G. *Aqueous Solutions of Paraffinic Chain Salts*; Editor Ed.; Hermann: Paris, 1936;

51. Corradini, F., *et al.*, *Journal of the chemical society, Faraday Transactions* **1993**, *89*, 123.

52. Evans, D. and H. Wennerstrom *The Colloidal Domain*;; VCH: New York, 1994; 515.

53. Shinoda, K., *Journal of Physical Chemistry* **1977**, *81*, 1300.

54. Arnett, E. and D. McKelvey, *Solvent Isotope Effect on Thermodynamics of Nonreacting Solutes.*, in *Solute-Solvent Interactions.*, J. Coetzee and C. Ritchie, Ed. 1969, Marcel Dekker: NY. p. 343.

55. La Mesa, C., *J. Phys. Chem.* **1990**, *94*, 323.

56. Smith, M.H., Ph.D. Thesis, Dept. of Chemistry, Massey University, New Zealand. 1990

57. Owenson, B. and L.R. Pratt, *J. Phys. Chem.* **1984**, *88*, 2905.

58. Puvvada, S. and D. Blankschtein, *Journal of Chemical Physics* **1990**, *92*, 3710.

59. Shinoda, K. and K. Katsura, *J. Phys. Chem.* **1964**, *68*, 1568.

60. Woolley, E.M. and T.E. Burchfield, *J. Phys. Chem.* **1985**, *89*, 714.

61. Rusanov, A., *Advances in Colloid and Interface Science* **1993**, *45*, 1.

62. Eriksson, J.C.,*et al* , *J. Chem. Soc, Faraday Trans 2* **1984**, *81*, 833.

63. Blankschtein, D., G.M. Thurston, and G.B. Benedek, *J. Chem. Phys.* **1986**, *85*, 7268.

64. Nagarajan, R. and E. Ruckenstein, *Langmuir* **1991**, *7*, 2934.

65. Israelachvili, J.N., D.J. Mitchell, and B.W. Ninham, *Faraday Trans. II* **1976**, *72*, 1525.

66. Corkill, J., J. Goodman, and J. Tate, *Thermodynamics of Micelle Formation,* in *Hydrogen-Bonded Solvent Systems,* A.J. Covington, P, Editor. 1968, Taylor and Francis Ltd: London. p. 181.

67. Mitchell, D. and B. Ninham, *Journal of Physical Chemistry* **1983**, *87*, 2996.

68. Ljunggren, S. and J. Eriksson, *J. Chem.Soc., Faraday Transactions II* **1986**, *82*, 913.

79. Nagarajan, R., *Colloids and Surfaces A* **1993**, *71*, 39.

5. Effect of Solvent at High Surfactant Concentration.

Chapter 4 examined the effect of substituting ethylene glycol (EG) for H_2O and EG/H_2O mixtures on the micellisation of APFO and it was concluded that one effect was to cause a shift in the distribution of micelle size to lower aggregation numbers i.e micelles get smaller. A direct measure of micelle size can be obtained by small angle x-ray diffraction spectroscopy (SAXS) and one object of this Chapter is to explicitly show the effect of changing solvent on the size of APFO micelles. SAXS can be used provided the number density of the diffracting particles is high enough to obtain sufficiently intense diffraction patterns. This is not the case at cmc concentrations, and so a temperature-concentration regime was chosen to enable the use of SAXS. The choice was influenced by the NMR investigation of the liquid crystal phases of the closely related caesium pentadecafluorooctanoate/heavy water (CsPFO/D_2O) surfactant system to be presented in the first section of this Chapter. Here it will be shown that, in the presence of the cosolvents formamide (FA), *N*-methylformamide (NMF), *N,N*-dimethylformamide (DMF), *N,N*-dimethylacetamide (DMA) and EG, the temperature T_{IN} at which the transition of the $w = 0.5$ CsPFO/D_2O system from an isotropic (I) solution of discotic micelles to a nematic (N_D) phase of discotic micelles occurs is shifted to lower temperature, and this effect is coupled to a decrease in micelle size. The variation in micelle size will be shown indirectly from NMR ^2H quadrupole splittings, and another object of this Chapter is to use SAXS to explicitly show the size variation. However, the CsPFO/D_2O system is not amenable to SAXS investigation owing to the strong absorption of x-rays by the heavy Cs^+ ion, but since the aqueous APFO and CsPFO solutions exhibit a universal liquid crystal phase behaviour[1], the effect of cosolvent on both systems will be assumed to be the same. Thus for the SAXS investigation, the APFO/H_2O concentration was chosen to be $w = 0.5$ and temperatures were chosen to be a few degrees above $T_{IN} = 305.9$ K[2] for this surfactant system.

This Chapter consists of two parts: in section 5.1, NMR measurements will be presented to show the effect of cosolvent on T_{IN} of $w = 0.5$ CsPFO/D_2O, and in section 5.2, SAXS measurements will be presented to show changes in $w = 0.5$ APFO/H_2O micelle size accompanying the substitution of (i) EG and EG/H_2O mixtures for H_2O, and (ii) DMF/H_2O and DMA/H_2O mixtures for H_2O. SAXS results on the effect of temperature on micelle size will also be presented.

It will be shown that the depression of liquid crystal phase transition temperatures caused by cosolvents originates in changes in micelle size as a consequence of their effect on micelle/solvent interfacial tension. Furthermore, the

SAXS results will be interpreted within Nagarajan's statistical thermodynamic model for surfactant self-assembly presented in Chapter 4.

5.1 NMR investigation of w = 0.5 CsPFO/D_2O/cosolvents.

The method for determining the liquid crystal phase transitions from NMR quadrupole splittings measurements will be briefly described, then ^2H quadrupole splittings will be used to show (a) the variation in micelle size with cosolvent concentration and temperature, and (b) that cosolvent is uniformly distributed around the micelle and that the proportion of cosolvent:water at the interface does not vary with temperature.

5.1.1 Determining T_{IN} by NMR.

The phase transition temperatures were determined from ^{133}Cs NMR measurements. In a binary w = 0.5 CsPFO/D_2O sample both the I - to - N_D and N_D - to - lamellar (L_D) transitions are first order[3, 4] and the temperatures of the upper and lower boundaries to the I/N_D phase coexistence regime, T_{IN} and T_{NI} respectively, can be precisely located by either ^2H[3, 5] or ^{133}Cs[4, 6] NMR. The corresponding temperatures for the N_D/L_D phase coexistence regime, T_{NL} and T_{LN} respectively, are, however, best obtained from ^{133}Cs measurements which yield an order of magnitude improvement in the resolution of the NMR spectra from the coexisting phases[4].

5.1.2 The effect of cosolvent on T_{IN}.

The effect of added cosolvent on the I - to - N_D phase transition temperatures is shown in Figure 5.2. The Figure shows that in all cases increasing the cosolvent concentration results in a displacement of the phase transition temperatures to successively lower values and that at corresponding cosolvent mole fractions the order of effectiveness in depressing the phase transition temperatures is DMA> DMF>NMF>EG>FA. It should be noted that this order parallels the order of the interfacial tensions between cosolvent/water and a perfluorocarbon self-assembled monolayer (SAM) (presented in Chapter 6) but this will be discussed in section 5.2.

Figure 5.1 The effect of added cosolvent on the w = 0.5 CsPFO/D_2O I - to - N_D phase transition temperatures. Above the lines an isotropic (I) phase exists and below the lines a mixed isotropic/nematic (I/N_D) phase exists. For clarity, the subsequent N_D - to - L_D transitions at lower temperatures are not shown but are described in the text. Closed points indicate values determined in this study and open points indicate values determined from previous work[7].

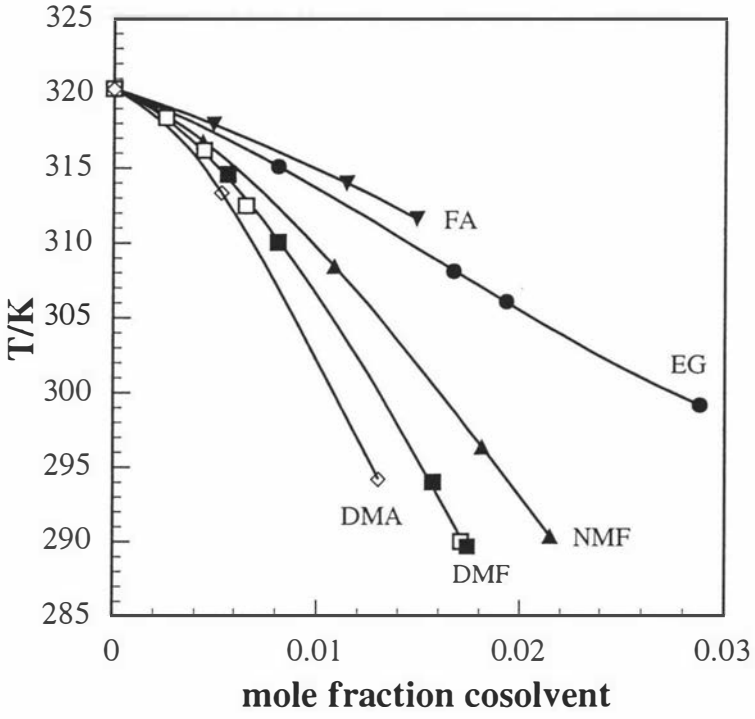

The phase behaviour of the w = 0.5 CsPFO/D_2O sample is preserved in the sense that both the I - to - N_D and N_D - to - L_D transitions remain first order and there are no significant changes in either T_{IN}-T_{NI} or T_{NL}-T_{LN} over the full cosolvent temperature and concentration ranges. For all cosolvents T_{IN}-T_{LN} increases with increasing cosolvent concentration to an extent which is roughly proportional to the depression in the phase transition temperatures. Thus, at a DMA mole fraction of 0.0130 the depression in T_{IN} is 29.11 K and T_{IN}-T_{LN} is 8.33 K (*c.f.* 5.23 K for the pure w = 0.5 CsPFO/D_2O sample). The corresponding values at a FA mole fraction of 0.0114 are 6.32 and 6.31 K respectively.

5.1.3 Obtaining micelle sizes from NMR.

Variations in micelle size were monitored by ^2H NMR. The NMR spectrum for a deuterium spin (spin quantum number I = 1) in heavy water in a macroscopically aligned uniaxial nematic or lamellar mesophase is a doublet with separation $\Delta\tilde{\nu}$ referred to as the partially averaged quadrupole splitting, given by[3]

[5–1] $$\Delta\tilde{\nu}(\phi) = \tfrac{3}{2}\left|\tilde{q}_{zz}\right|_s SP_2(\cos\phi)$$

where ϕ (= 0° in this study) is the angle between the mesophase director **n** and the magnetic field **B** and S is the second-rank orientational order parameter representing the ensemble average of the orientational fluctuations of the micellar axes with respect to **n**. $|\tilde{q}_{zz}|_s$ is the partially averaged component of the nuclear-quadrupole-electric-field-gradient interaction tensor measured parallel to **n** in a perfectly ordered mesophase; it is given by[3]

$$|\tilde{q}_{zz}|_s = \langle P_2(\cos\alpha)\rangle_s \chi_D (x_s/x_w) n_b S_{OD},$$

where χ_D is the quadrupole coupling constant for a water molecule, x_s and x_w are, respectively, the mole fractions of surfactant and water, n_b is the number of water molecules bound to each surfactant molecule, and S_{OD} is an "order parameter" representing the averaging due to the local reorientational motion of these water molecules. The quantity $\langle P_2(\cos\alpha)\rangle_s = \left\langle \frac{3}{2}\cos^2\alpha - \frac{1}{2}\right\rangle_s$, where α is the angle between the normal to the surface and the symmetry axis of the micelle and the angular brackets denote an average over the surface, accounts for the diffusive motion of the molecule over the surface of a micelle. $\langle P_2(\cos\alpha)\rangle_s$ is a function of, and may be calculated from, the micelle axial ratio R/L where R is the half-thickness of the disk and L is the radius of the disk in the plane of symmetry[3]. As a micelle grows the R/L ratio decreases and the magnitude of $\langle P_2(\cos\alpha)\rangle_s$ increases. It has been established from studies on the CsPFO/D_2O[3] and APFO/D_2O[5] systems that over the temperature and concentration ranges of the nematic and lamellar phases the product $\chi_D n_b S_{OD}$ is essentially constant, and independent of the fraction of bound counterions. In this study the value of x_s/x_w is also the same for all samples and thus changes in the magnitude of the quadrupole splittings with temperature or cosolvent concentration are a consequence of changes in S and $\langle P_2(\cos\alpha)\rangle_s$ only.

The temperature dependence of the partially averaged ^2H quadrupole splittings normalised to their values at T_{NI} of D_2O (circles) for a ($x_{DMF} = 0.0174$) $w = 0.5$ CsPFO/D_2O /DMF-d_7 sample is illustrated in Figure 5.2.

Figure 5.2 Temperature dependence of the partially averaged ^{2}H quadrupole splittings $\Delta\tilde{\nu}$ of a (x_{DMF} = 0.0174) w = 0.5 CsPFO/D_2O/DMF-d_7 sample normalised to their values at T_{NI}: T_{LN} = 281.92(1) K, T_{NI} = 289.12(1) K, and T_{IN} = 289.70(2) K. For D_2O (circles), $\Delta\tilde{\nu}(T_{NI})$ = 200 Hz, for the CD_3 group *trans* to the formyl deuteron (—), $\Delta\tilde{\nu}(T_{NI})$ = 1260 Hz, for the CD_3 group *cis* to the formyl deuteron (|), $\Delta\tilde{\nu}(T_{NI})$ = 1800 Hz and for the formyl deuteron (×) $\Delta\tilde{\nu}(T_{NI})$ = 3110 Hz.

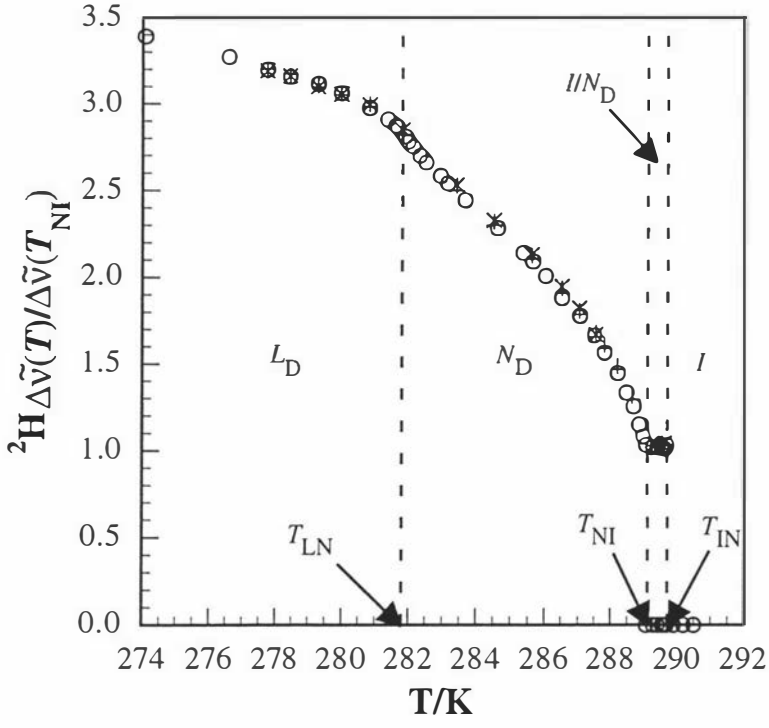

Similar temperature dependences of the ^{2}H quadrupole splittings of heavy water are obtained for all the samples studied, with the phase transition lines simply being displaced in temperature. The rapid increase in $\Delta\tilde{\nu}$ with decreasing temperature in the N_D phase is primarily due to an increase in S, whilst the more gradual increase in $\Delta\tilde{\nu}$ with decreasing temperature in the lamellar phase is primarily due to an increase in $\langle P_2(\cos\alpha)\rangle_s$[3]. In the lamellar phase, therefore, variations in $\Delta\tilde{\nu}$ largely reflect changes in the micelle size (R/L ratio). This will also be the case at both T_{NI} and T_{LN} since, in view of the negligible effects of added cosolvent on the temperature ranges of the two-phase coexistence regions, it is reasonable to assume a constant value of S at both these temperatures. Thus, at the phase transition temperatures T_{NI} and T_{LN} and in the lamellar phase, to a first approximation changes in $\Delta\tilde{\nu}$ may be related solely to changes in the micelle axial R/L ratio.

5.1.4 Variation of micelle size with temperature and cosolvent concentration from NMR.

The effect of cosolvent concentration on the ^2H quadrupole splittings of heavy water of lamellar phase samples at 297.0 K is shown in Figure 5.3 and the ^2H quadrupole splittings at T_{NI} and T_{LN} as a function of cosolvent concentration are shown in Figure 5.4. Assuming that the sole cause of any change in quadrupole splittings is due to a change in micelle size, Figure 5.3 shows that with increasing cosolvent concentration at 279.0 K, the distribution of micelle sizes is displaced to lower aggregation numbers and that at a given cosolvent concentration the order of efficacy of the cosolvents in decreasing the micelle sizes parallels that for decreasing the phase transition temperatures in Figure 5.1 i.e DMA>DMF>NMF>EG>FA. Figure 5.4 shows that at both T_{NI} and T_{LN} the quadrupole splittings remain essentially constant. This is indicative of phase transitions driven by predominantly hard particle interactions between discotic micelles[8]. As the cosolvent concentration increases there is a decrease in micelle size and it is necessary to go to increasingly lower temperatures (increase the micelle sizes) in order to re-establish the critical axial ratios at the new phase transition temperatures. Thus, the effect of cosolvent on the self-organisation (liquid crystal behaviour) of perflurocarbon surfactant systems can be understood by their effect on surfactant self-assembly. This will be addressed in section 5.2 on the interpretation of SAXS measurements.

Figure 5.3 The dependence of the partially averaged ^2H quadrupole splittings of heavy water on cosolvent mole fraction along 279.0 K isotherms in the lamellar phases of $w = 0.5$ CsPFO/D_2O/cosolvent systems: FA (inverted triangles), EG (circles), NMF (triangles), DMF (squares), and DMA (diamonds). Closed points were determined in this study and open points were determined from previous work[7].

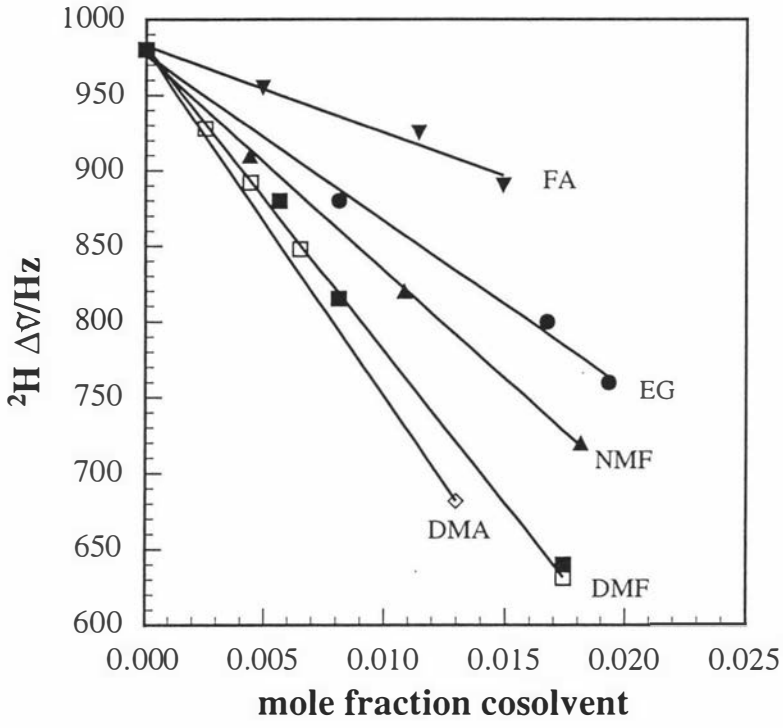

Figure 5.4 The dependence of the partially averaged ^2H quadrupole splittings $\Delta\tilde{\nu}$ of heavy water at T_{NI} and T_{LN} on the cosolvent mole fraction as measured for the (all $w = 0.5$) CsPFO/D_2O/FA (inverted triangles), CsPFO/D_2O/EG (circles), CsPFO/D_2O/NMF (triangles), CsPFO/D_2O/DMF (squares), and CsPFO/D_2O/DMA (diamonds) systems. Closed points were determined in this study and open points were determined in previous work[7].

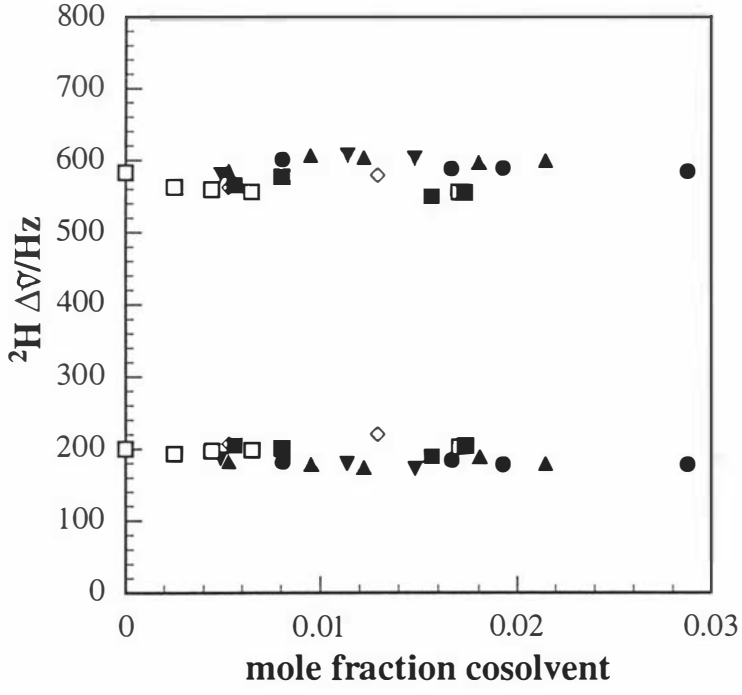

5.1.5 ^{2}H quadrupole splittings of DMF-d_7.

Figure 5.2 compares the temperature dependences of the normalised ^{2}H quadrupole splittings of DMF-d_7 i.e. the molecule $(CD_3)_2CDO$ with those of heavy water for the (x_{DMF} = 0.0174) w = 0.5 CsPFO/D_2O/DMF-d_7 sample.

It has previously been shown[6] that the temperature dependence of the ^{2}H quadrupole splittings of heavy water given by equation [5-1] can be ascribed to changes in just S and $\langle P_2(\cos\alpha)\rangle_s$ with temperature. This was demonstrated by the agreement between the reduced ^{2}H quadrupole splittings ($\Delta\tilde{\nu}_T/\Delta\tilde{\nu}_{T_{NI}}$) and the corresponding reduced $S\langle P_2(\cos\alpha)\rangle_s$ values. The agreement is excellent, not only through the nematic phase, but deep into the lamellar phase as well.

The expression for $|\tilde{q}_{zz}|_s$ in equation [5-1] for DMF-d_7 quadrupole splittings is

$$|\tilde{q}_{zz}|_s = \langle P_2(\cos\alpha)\rangle_s \chi_D f S_{X-D},$$

where f represents the fraction of cosolvent molecules bound to the micelle surface and there will be three distinct values for the ^{2}H quadrupole coupling constants χ_D and the X-D bond "order parameters" corresponding to the three deuterium sites. The fact that ^{2}H quadrupole splittings of DMF-d_7 are observed at all shows that DMF is present at the surface. The correspondence of the reduced values throughout the nematic and well into the lamellar phase indicate that, like the heavy water molecules, the DMF molecules are also statistically distributed uniformly over the micelle surface, and furthermore, that $\chi_D f S_{X-D}$ values must also be constant, and hence the proportion of DMF-d_7:D_2O around the micelle does not vary with temperature.

5.2 SAXS investigation of w = 0.5 APFO/H_2O/cosolvents.

The micellar structural parameters derived from SAXS will first be described and the effect of added cosolvent on micelle size will be presented. Then the results will be interpreted within Nagarajan's statistical thermodynamic model for surfactant self-assembly presented in Chapter 4 to obtain an expression for the micelle/solvent interfacial tension.

5.2.1 Deriving micellar structural parameters from SAXS.

Experimental SAXS details and the method for converting a measured x-ray diffraction ring diameter d to the centre-to-centre distance between diffracting planes d_0 and micellar volumes V_m are described in Chapter 2, section 2.8.4. The micellar volume V_m thus obtained was used to calculate micellar structural parameters by adopting the geometric model for a disklike aggregates formulated by McMullen, Ben-Shaul and Gelbart (MBG)[9].

The MBG disk model consists of the oblate right-circular cylinder surrounded by a semi-toroidal rim depicted in Figure 5.5. The half-thickness of the disk $R_{2\delta}$ is fixed as the sum of the length of the fluorocarbon chain R = 1.086 nm and twice the radius δ = 0.118 nm of the carboxylate headgroup i.e $R_{2\delta}$ = R + 2δ. L is the radius of the disk defined as the distance from the rotational axis of symmetry to the extreme edge of the semi-toroid through the plane of symmetry and is obtained as the solution to the quadratic equation with coefficents a, b and c given by[10]

$$a = 2\pi R_{2\delta}$$

$$b = R_{2\delta}^2\left(\pi^2 - 4\pi\right)$$

$$c = R_{2\delta}^3\left(\tfrac{10}{3}\pi - \pi^2\right) - V_m.$$

Figure 5.5 MBG disk model used in calculations.

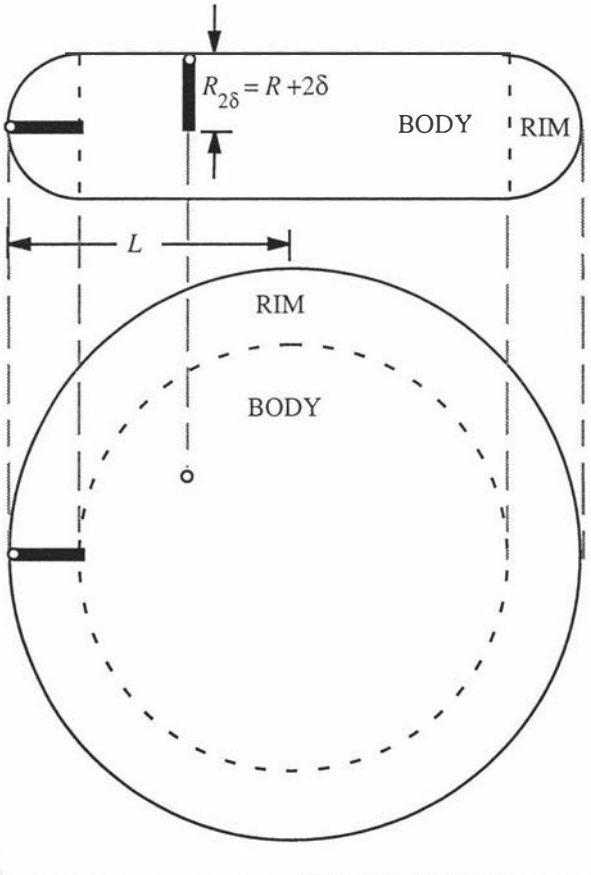

The aggregation number s is calculated assuming the entire volume is occupied by PFO^- ions, thus

$$s = \frac{V_m}{V_{mon}}$$

where $V_{mon} = 0.364\ nm^3$. The above assumption leads to a value of s which should be regarded as an upper limit to the true aggregation number.

The number of molecules in the semi-toroidal rim s_{rim}, is given by[10]

$$s_{rim} = \frac{\pi}{2}\sqrt{\frac{3}{2}s_{min}}\sqrt{s + s_{min}\left(\frac{3\pi^2}{32} - 1\right)} - s_{min}\left(\frac{3\pi^2}{16} - 1\right)$$

where s_{min} is the minimum aggregation number defined as

$$s_{min} = \frac{4}{3}\pi\frac{R_{2\delta}^3}{V_{mon}}.$$

The surface area per molecule in the semi-toroidal rim is

$$a_{rim} = \left(2\pi R_{2\delta}\left(L - R_{2\delta}\right) + 4\pi R_{2\delta}^2\right)/s_{rim}$$

and the surface area per molecule in the cylindrical body is

$$a_{body} = \frac{V_{mon}}{R_{2\delta}}.$$

The average surface area per molecule is thus

$$a_{2\delta} = \left(a_{body}\left(s - s_{rim}\right) + a_{rim}s_{rim}\right)/s.$$

The structural parameters defined above, and the raw data from which they were derived are tabulated in Table 5.1(a) for the w = 0.5 APFO/H_2O/EG system over $0 \le x_{EG} \le 1$ at 311 K, Table 5.1(b) for the w = 0.5 APFO/H_2O/EG system at x_{EG} = 0.1 at different temperatures, and Table 5.2 for the w = 0.5 APFO/H_2O/EG, APFO/H_2O/DMF and APFO/H_2O/DMA systems over $0 \le x_{cosolvent} < 0.021$ at 308 K. Included in the tables are values for the micellar axial ratio $R_{2\delta}/L$ where larger values mean smaller micelles.

Table 5.1 Micelle structural parameters obtained from SAXS measurements of w = 0.5 APFO/H_2O/EG in the isotropic phase.

(a) T = 311 K

x_{EG}	d/mm	d_0/nm	ϕ	V_m /nm^3	L /nm	s	$a_{2\delta}$	$R_{2\delta}/L$
0	8.40	4.40	0.348	38.51	2.639	105.8	0.5489	0.500
0.1	9.70	3.81	0.351	25.22	2.136	69.3	0.6147	0.618
0.2	10.50	3.52	0.353	20.00	1.902	54.9	0.6571	0.694
0.3	11.20	3.30	0.356	16.62	1.734	45.7	0.6947	0.761
0.4	11.40	3.24	0.358	15.85	1.693	43.5	0.7049	0.780
0.5	12.00	3.08	0.361	13.70	1.574	37.6	0.7378	0.839
0.6	12.56	2.94	0.363	12.02	1.474	33.0	0.7693	0.895
0.7	12.89	2.87	0.365	11.18	1.422	30.7	0.7876	0.928
0.8	13.08	2.83	0.368	10.79	1.397	29.6	0.7968	0.945
0.9	13.32	2.77	0.370	10.27	1.363	28.2	0.8099	0.969
1	13.40	2.76	0.372	10.14	1.354	27.9	0.8133	0.975

(b) x_{EG} = 0.1

T/K	d/mm	d_0/nm	ϕ	V_m /nm^3	L /nm	s	$a_{2\delta}$	$R_{2\delta}/L$
311	9.70	3.810	0.351	25.22	2.136	69.3	0.6147	0.618
307	9.65	3.830	0.351	25.62	2.152	70.4	0.6120	0.613
303	9.56	3.866	0.351	26.35	2.183	72.4	0.6072	0.605
299	9.50	3.891	0.351	26.85	2.204	73.8	0.6040	0.599
295	9.40	3.932	0.351	27.72	2.239	76.1	0.5987	0.590

Table 5.2 Micelle structural parameters obtained from SAXS measurements of w = 0.5 APFO/H_2O/cosolvent at 308 K.

$x_{cosolvent}$	d/mm	d_0/nm	ϕ	V_m /nm^3	L /nm	s	$a_{2\delta}$	$R_{2\delta}/L$
EG								
0.0000	7.94	46.55	0.348	45.60	2.872	125.3	0.5264	0.4597
0.0051	8.05	45.91	0.348	43.75	2.813	120.2	0.5317	0.4692
0.0102	8.18	45.18	0.348	41.70	2.746	114.6	0.5381	0.4807
0.0152	8.26	44.75	0.348	40.50	2.706	111.3	0.5420	0.4877
0.0203	8.41	43.95	0.348	38.37	2.634	105.4	0.5495	0.5011
DMF								
0.0000	7.94	46.55	0.348	45.60	2.872	125.3	0.5264	0.4597
0.0049	8.11	45.57	0.348	42.79	2.782	117.6	0.5346	0.4745
0.0101	8.32	44.42	0.348	39.63	2.677	108.9	0.5450	0.4931
0.0153	8.45	43.74	0.348	37.83	2.616	103.9	0.5514	0.5047
0.0208	8.66	42.68	0.348	35.14	2.521	96.5	0.5620	0.5236
DMA								
0.0000	7.94	46.55	0.348	45.60	2.872	125.3	0.5264	0.4597
0.0051	8.15	45.35	0.348	42.16	2.761	115.8	0.5366	0.4780
0.0099	8.40	44.00	0.348	38.51	2.639	105.8	0.5489	0.5002
0.0153	8.65	42.73	0.348	35.27	2.525	96.9	0.5614	0.5227
0.0203	8.90	41.53	0.348	32.38	2.420	88.9	0.5742	0.5455

5.2.2 Variation of micelle size with temperature and cosolvent concentration from SAXS.

The aggregation numbers and values of $R_{2\delta}/L$ are shown in Figure 5.6 and Figure 5.7. Figure 5.6(a) shows that increasing ethylene glycol concentration at constant temperature causes a decrease in aggregation number and micelle size (larger $R_{2\delta}/L$), and that in pure ethylene glycol $R_{2\delta}/L \approx 1$ indicating that the micelles are very nearly spherical. Figure 5.6(b) shows that the effect of decreasing temperature is to cause an increase in s and micelle size (smaller $R_{2\delta}/L$). Figure 5.7 shows that, at constant temperature and corresponding concentration, different cosolvents decrease micelle size in the order of their effect on the perfluorocarbon SAM/solvent interfacial tensions shown in Figure 6.2, Chapter 6 i.e., in the order of greatest effect, DMA>DMF>EG.

The previously established[1] universal nature of the liquid crystal behaviour of APFO and CsPFO in aqueous solution allows the effect of cosolvent on the two systems to be compared. In section 5.1, the depression of the $w = 0.5$ CsPFO/D_2O phase transitions by cosolvents was explained by changes in micelle size i.e. at constant temperature, the addition of cosolvent causes micelles to get smaller and, since the phase transitions are driven by hard particle interactions i.e. micelles must be of a critical size, the system must be cooled to regain that critical size hence T_{IN} is shifted to lower temperature. In that section, the variation in micelle size was inferred from the variation in ^2H quadrupole splittings. In this section the variation in micelle size with cosolvent has been shown explicitly and the explanation confirmed.

Figure 5.6 Aggregation numbers (open points) and values for the ratio $R_{2\delta}/L$ (closed points) for for the w = 0.5 APFO/H_2O/EG system (a) over $0 \leq x_{EG} \leq 1$ at 311 K, and (b) for the w = 0.5 APFO/H_2O/EG system at x_{EG} = 0.1 at different temperatures. $R_{2\delta}/L$ is a measure of micelle size (larger values mean smaller micelles).

(a) T = 311 K

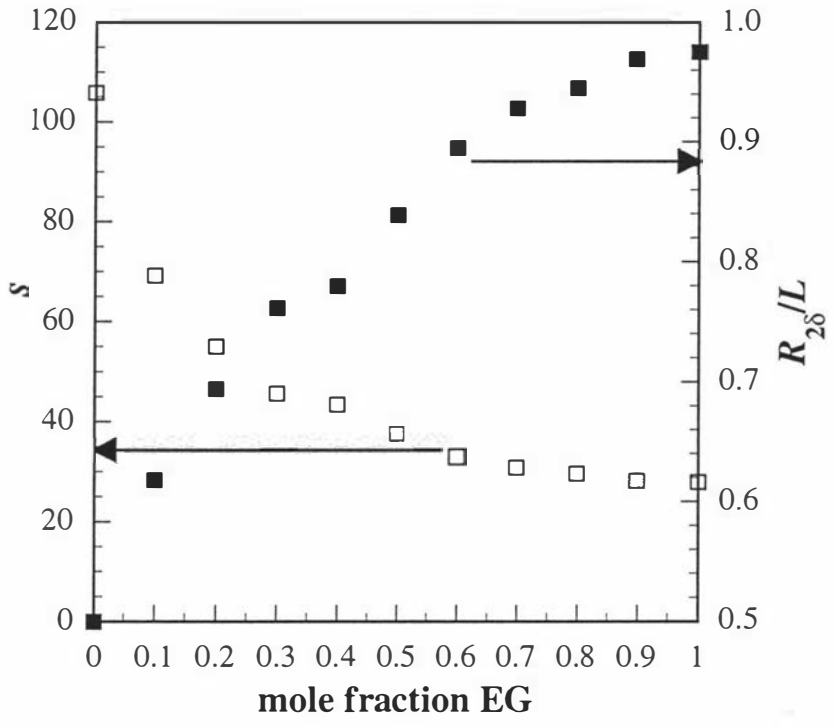

(b) x_{EG} = 0.1.

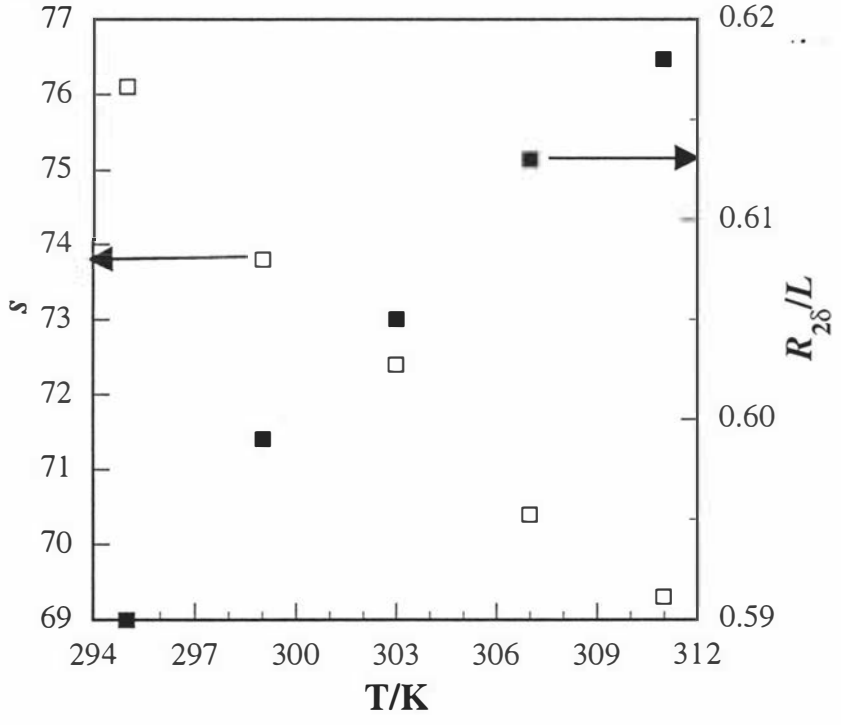

Figure 5.7 Aggregation numbers (open points, dashed lines) and values for the ratio $R_{2\delta}/L$ (closed points, solid lines) for w = 0.5 APFO/H_2O/EG, APFO/H_2O/DMF and APFO/H_2O/DMA systems over $0 \leq x_{cosolvent} < 0.021$ at 308 K. $R_{2\delta}/L$ is a measure of micelle size (larger values mean smaller micelles).

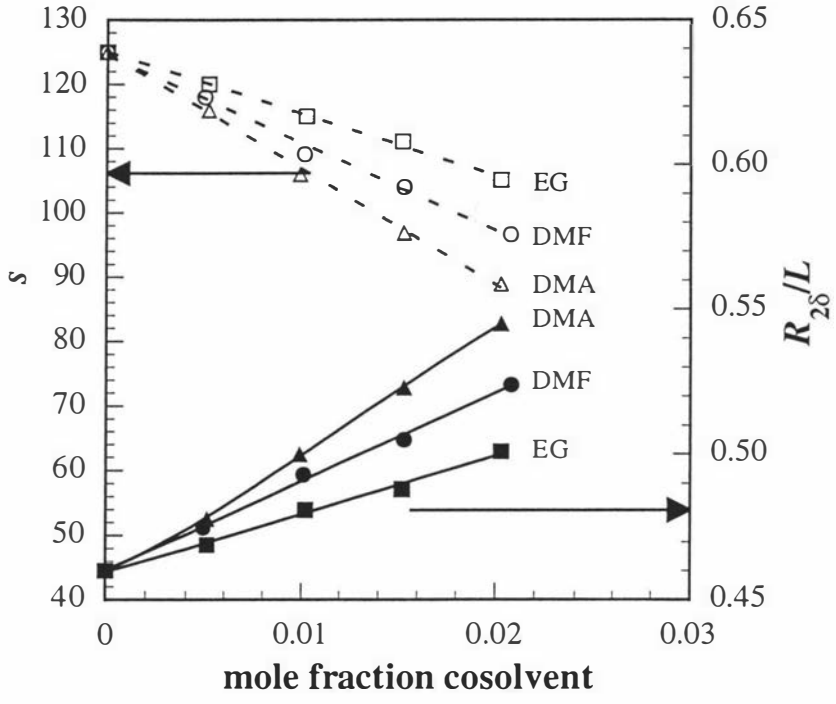

5. 2. 3 Calculation of γ_{int} from SAXS.

Prevailing phenomenological models for self-assembly share the common feature of partitioning the free energy of micellisation into headgroup and tail contributions. $\Delta\mu_s^0$ partitioned in this way and expressed as a function of the headgroup area a of a surfactant ion within a micelle (of arbitrary geometry) is

[5-2] $$\Delta\mu_s^0(a) = h(a) + g(a)$$

where $h(a)$ and $g(a)$ represent the headgroup and tail contributions respectively. The average headgroup area $\tilde{a}$ of a surfactant ion in a micelle, defined as the value of a that minimises equation [5-2] can be obtained by solving

[5-3] $$\frac{d}{da}\left\{\Delta\mu_s^0(a)\right\} = 0$$

Assuming g(a) is invariant with s and hence a, Tanford[11] applied the "principle of opposing forces" to obtain a form of equation [5-3] as

$$\frac{d}{da}\left\{\gamma_{int}a + c/a\right\} = 0$$

where the term in γ_{int}, the hydrocarbon/water interfacial tension, is attractive, and the term in c, a constant comprising the predominantly electrostatic interactions between headgroups, is repulsive. Solving this equation gives

$$\tilde{a} = \sqrt{\frac{c}{\gamma_{int}}}$$

The approach adopted in this section is to evaluate c within Nagarajan's statistical thermodynamic model for surfactant self-assembly (presented in Chapter 4) to obtain an expression for γ_{int} using the values of $a_{2\delta}$ obtained from SAXS. Values of γ_{int} calculated in this way will be compared to the interfacial tension measured at the interface between a self-assembled perfluorocarbon monolayer (SAM) and the solvent presented in Chapter 6. Within Nagarajan's model, $g(a)$ is comprised of the free energy of transfer of the surfactant tail $\left(\Delta\mu_s^0\right)_{trans}$ and the free energy of deformation of the tail inside the micelle $\left(\Delta\mu_s^0\right)_{def}$. The former free energy term does not vary with s (and hence a) and the latter will be assumed to be negligble for perfluorocarbon surfactants (for reasons previously outlined in Chapter 4) i.e. $dg(a)/da \approx 0$. Hence the effect of changing solvent must originate in changes $h(a)$, and equation [5-3] becomes

[**5-4**] $$\frac{d}{da}\left\{\left(\Delta\mu_s^0\right)_{ionic}(a)+\left(\Delta\mu_s^0\right)_{int}(a)+\left(\Delta\mu_s^0\right)_{steric}(a)\right\}=0$$

Derivatives of expressions for each contribution to $h(a)$ will be now be developed.

$\left(\Delta\mu_s^0\right)_{ionic}$ is given by equation [4-28] and its derivative can be obtained parametrically by

[**5-5**] $$\frac{d}{da}\left\{\left(\Delta\mu_s^0\right)_{ionic}(a)\right\}=\frac{d}{dS}\left\{\left(\Delta\mu_s^0\right)_{ionic}(S)\right\}\cdot\frac{dS}{da}$$

with

$$\frac{dS}{da}=\frac{d}{da}\left\{\frac{e}{a\sqrt{8ckT\varepsilon}}\right\}=\frac{-e}{a^2\sqrt{8ckT\varepsilon}}$$

The expression for $\frac{d}{dS}\left\{\left(\Delta\mu_s^0\right)_{ionic}(S)\right\}$ is simple to obtain from equation [4-28] but is very lengthy and will be omitted.

$\left(\Delta\mu_s^0\right)_{int}$ is given by equation [4-29] and its derivative with respect to a is

[**5-6**] $$\frac{d}{da}\left\{\left(\Delta\mu_s^0\right)_{int}(a)\right\}=\frac{d}{da}\left\{\gamma_{int}\left(a-a_p\right)\right\}=\gamma_{int}$$

$\left(\Delta\mu_s^0\right)_{steric}$ is given by equation [4-30] and its derivative is given by

[5-7] $$\frac{d}{da}\left\{\left(\Delta\mu_s^0\right)_{\text{steric}}(a)\right\} = \frac{-d}{da}kT\ln\left(1-\frac{a_p}{a}\right) = \frac{-kTa_p}{a^2\left(1-a_p/a\right)}$$

Thus an expression for the interfacial tension is obtained as a function of $\tilde{a}$ *via* rearrangement of equation [5-4] as

[5-8] $$\gamma_{\text{int}}\left(\tilde{a}\right) = -\frac{d}{dS}\left\{\left(\Delta\mu_s^0\right)_{\text{ionic}}(S)\right\}\cdot\frac{-e}{\tilde{a}^2\sqrt{8ckT\varepsilon}} + \frac{kTa_p}{\tilde{a}^2\left(1-a_p/\tilde{a}\right)}$$

It is not appropriate to insert the values of $a_{2\delta}$ measured from SAXS into equation [5-8] since $a_{2\delta}$ represents the average headgroup area of a surfactant molecule at the distance $R+2\delta$ from the micelle centre, whereas the average values appearing in equation [5-8] occur at $R+\delta$ for the steric and ionic contributions and at R for the interfacial contribution. However, the average headgroup areas at these distances can easily be evaluated in terms of $a_{2\delta}$ from geometric considerations. If it is assumed that $a_{2\delta}$ represents the base area of the cone swept out by a PFO^- ion in a micelle shown in Figure 5.1, then the radii of the base areas at each distance from the micelle centre are related by

$$\frac{r_{2\delta}}{R+2\delta} = \frac{r_{\delta}}{R+\delta} = \frac{r}{R} = \sin\theta$$

and the areas at each distance are related by

[5-9] $$a_{2\delta} = \left(\frac{R+2\delta}{R+\delta}\right)^2 a_{\delta} = \left(\frac{R+2\delta}{R}\right)^2 a_0.$$

Then the values of $\tilde{a}$ appearing in equation [5-8] can be expressed in terms of $a_{2\delta}$ by multiplication by the appropriate factor given in equation [5-9].

In applying the expression for $\left(\Delta\mu_s^0\right)_{\text{ionic}}$ given by equation [4-28] to the MBG disk model, a *caveat* is recognised in that this equation represents an approximate analytical solution to the Poisson-Boltzmann equation in *spherical* geometry. Whilst corresponding solutions appropriate to prolate ellipsoidal, infinite (prolate) cylindrical, and infinite bilayer geometries have been published[12], a solution appropriate for the MBG disk model cannot be found nor formulated at present. The disk model of Eriksson and Ljunggren[13] used the expression for spherical geometry and the same approximation is adopted here.

Figure 5.8 Average headgroup areas a as base areas of the cone swept out by a surfactant molecule in a micelle (see text for details).

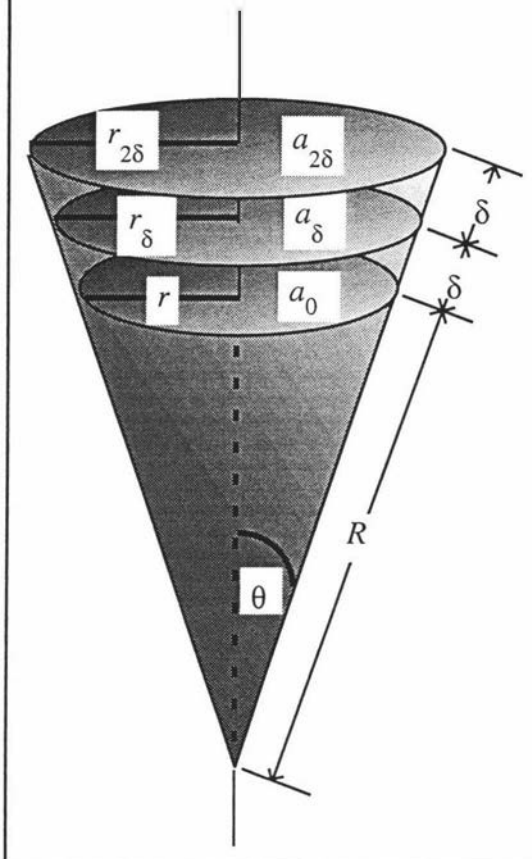

Calculations of γ_{int} for the APFO/H_2O/EG, APFO/H_2O/DMF and APFO/H_2O/DMA systems were carried out using equation [5-8] with the input parameters of $a_{2\delta}$ in Tables 5.1 and 5.2 (multiplied by the appropriate factor in equation [5-9]), ε_r, T and c = cmc/molecules dm^{-3}. The cmc's for the APFO/H_2O/DMF and APFO/H_2O/DMA systems are unknown and were approximated by the values measured[7] for the CsPFO/D_2O/cosolvent systems (presented in Chapter 4) normalised to the value for the pure APFO/H_2O system i.e. 0.0254 mol dm^{-3}. Values for the relative permittivities of H_2O/DMF and H_2O/DMA mixtures at the temperature of interest are also unknown and were approximated by their values measured by Rohdewald[14] at 298 K.

The calculated values of γ_{int} for APFO/H_2O/EG at 311 K and those values based on the measurements against a self-assembled perfluorocarbon monolayer (SAM) presented in Chapter 6 at 298 K are plotted against EG mole fraction in Figure 5.9. It

is pleasing that the form of the two curves is similar, with both showing negative deviations from ideality. Nagarajan[15] adopted an approximation for γ_{int} which predicted positive deviations from ideality. Furthermore, there is a linear relationship between the two sets of data which is shown in Figure 5.10. The results of the calculations of γ_{int} for the APFO/H_2O/EG, APFO/H_2O/DMF and APFO/H_2O/DMA systems at 308 K are shown in Figure 5.11. Again, the form of the two sets of interfacial tensions closely parallel one another, with the order of the effect of different cosolvents being preserved. Differences in magnitude between the two sets of data in both Figure 5.10 and Figure 5.11 cannot be simply explained by the significant differences in temperature since, assuming the proportion of cosolvent:water at the surface does not vary with temperature, which was shown to be the case for DMF-d_7 in section 5.1.5, if γ_{int} should change with temperature then it is expected to decrease with increasing temperature, whereas the Figures show the opposite effect. In view of the number of assumptions involved in calculating γ_{int} by equation [5-8] i.e. (a) the application of a dilute solution model, which ignores intermicellar interactions in influencing micelle size, to a high surfactant concentration regime, where these interactions are present, and (b) equating the ionic strength c to the cmc, it would be speculative to attribute the discrepancies between the two sets of γ_{int} values to a physical phenomenon. However, the approach has been useful in demonstrating the importance of interfacial tension in surfactant self-assembly, and the linear relationship in Figure 5.10 deserves future attention.

Figure 5.9 Calculated interfacial tensions between EG/H_2O mixtures and (i) an APFO micelle at 311 K, calculated from x-ray measurements using equation [5-8], and (ii) a self-assembled perfluorocarbon monolayer (SAM) (upper curve, calculated using equation [6-5]) at 298 K plotted as a function of EG mole fraction.

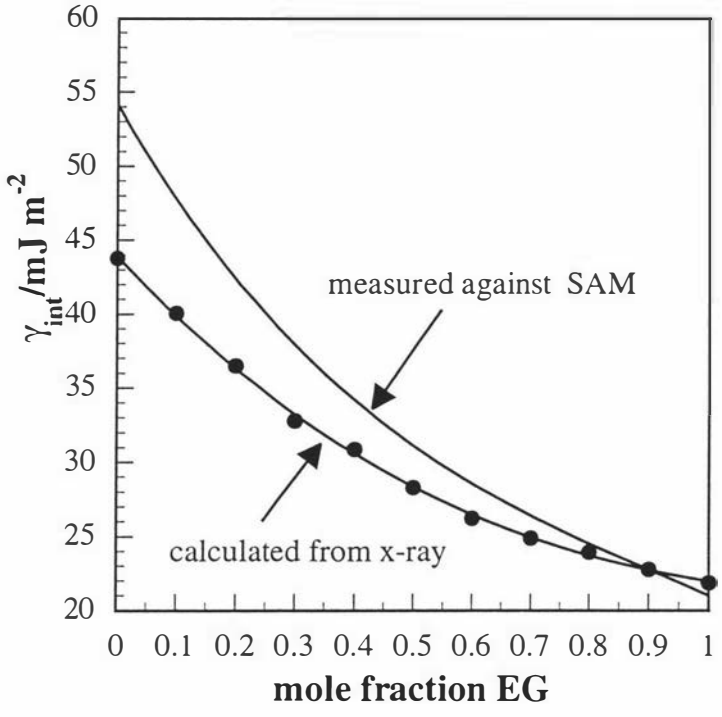

Figure 5.10 The linear relationship between the interfacial tensions shown in Figure 5.9.

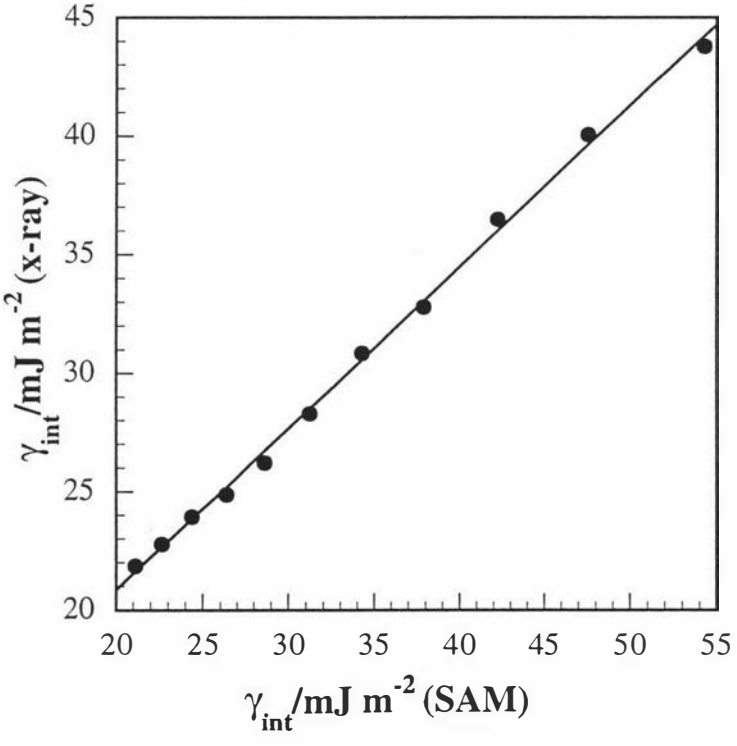

Figure 5.11 Calculated interfacial tensions between cosolvent/H_2O mixtures and (i) an APFO micelle at 308 K (open points), calculated from x-ray measurements using equation [5-8], and (ii) a self-assembled perfluorocarbon monolayer (SAM) (closed points), calculated using equation [6-5]) at 298 K plotted as a function of cosolvent mole fraction.

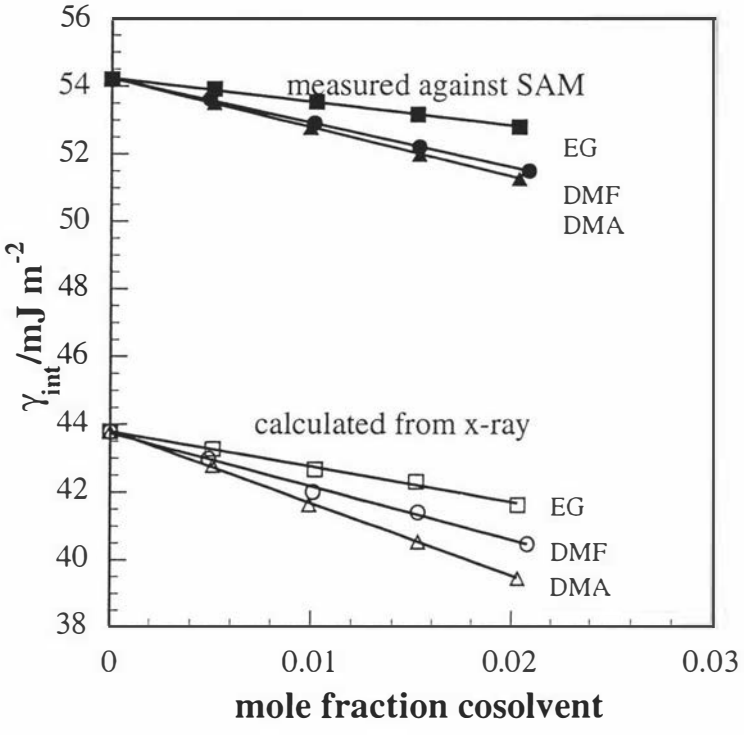

5.3 Summary.

This Chapter has demonstrated the importance of the micelle/solvent interfacial tension in governing the self-assembly of perflurocarbon surfactants. At constant temperature, increasing the cosolvent concentration in the APFO/H_2O/cosolvent systems was shown to decrease the micelle size because of their effect on the micelle/solvent interfacial tension. At constant EG/water concentration, decreasing the temperature was shown to increase the micelle size. Thus it has been shown that the effect of cosolvents on the self-organisation of CsPFO/D_2O is explained by their effect on the surfactant self-assembly i.e. the liquid crystal phase transition temperatures are shifted to lower values because the cosolvents decrease the micelle size (because of their effect on the micelle/solvent interfacial tension) and, since the phase transitions are determined by hard-particle interactions, in order for a phase transition to occur the temperature must be lowered to restore the micelle size.

5.4 References.

1. Boden, N., *et al.*, *Phys. Rev. Lett.* **1991**, *66*, 2883.
2. Edwards, P., *et al.*, *Langmuir* **1997**, *13*, 2665.
3. Boden, N., S.A. Corne, and K.W. Jolley, *J. Phys. Chem.* **1987**, *91*, 4092.
4. Boden, N., K.W. Jolley, and M.H. Smith, *Liq. Cryst.* **1989**, *6*, 481.
5. Boden, N., *et al.*, *J. Chem. Phys.* **1990**, *93*, 9096.
6. Boden, N., K.W. Jolley, and M.H. Smith, *J. Phys. Chem.* **1993**, *97*, 7678.
7. Thomsen, S.J., M.Sc. Thesis, Dept. of Chemistry, Massey University, New Zealand. **1994**
8. Granek, R., *et al.*, *Journal of Chemical Physics* **1994**, *101*, 4331.
9. McMullen, W.E., A. Ben-Shaul, and W.M. Gelbart, *J. Colloid Interface Sci.* **1984**, *98*, 523.
10. Boden, N., *et al.*, *J. Chem. Phys.* **1995**, *103*, 5712.
11. Tanford, C. *The Hydrophobic Effect*; Wiley: New York, 1980;
12. Nagarajan, R. and E. Ruckenstein, *Langmuir* **1991**, *7*, 2934.
13. Ljunggren, S. and J. Eriksson, *J. Chem. Soc., Faraday Transactions II* **1986**, *82*, 913.
14. Rohdewald, P. and M. Moldner, *J. Phys. Chem.* **1973**, *77*, 373.
15. Nagarajan, R., *Journal of Colloid and Polymer Science* **1998**, *submitted for publication*,

6. Calculation of Interfacial Tensions in Ternary Systems.

It was assumed in calculations in previous Chapters that the micellar interfacial tension can be approximated by the interfacial tension measured between aqueous solvent mixtures and a self-assembled perfluorocarbon monolayer (SAM). This Chapter outlines a method for estimating interfacial tensions from known data and compares the method with the experimentally-determined solvent/SAM interfacial tensions. The Chapter concludes with a discussion of the validity of approximating the solvent/micelle interface by the solvent/SAM interface.

The Fowkes equation[1] (equation [6–1]) for the estimation of interfacial tensions between two pure and immiscible or partly miscible phases is a well known and widely used relation, though it's validity has been the subject of ongoing discussion[3-8]. Nagarajan[9, 10] used a modified[6, 7] form of the equation to estimate hydrocarbon/water and hydrocarbon/ethylene glycol micellar interfacial tensions at the

The Fowkes Equation[1] for Estimation of Interfacial Tension.

[**6–1**] $$\gamma_{12} = \gamma_1 + \gamma_2 - 2\sqrt{\gamma_1^d \gamma_2^d}\,.$$

The equation is simply an expression for the summation of forces at the interface between phases 1 and 2, as shown in the figure[1] below. γ is the surface tension of the pure phase, and $\sqrt{\gamma_1^d \gamma_2^d}$ is the geometric mean of the dispersive components of the interfacial tension γ^d (Berthelot's Hypothesis[1]) which can be estimated from available data[2].

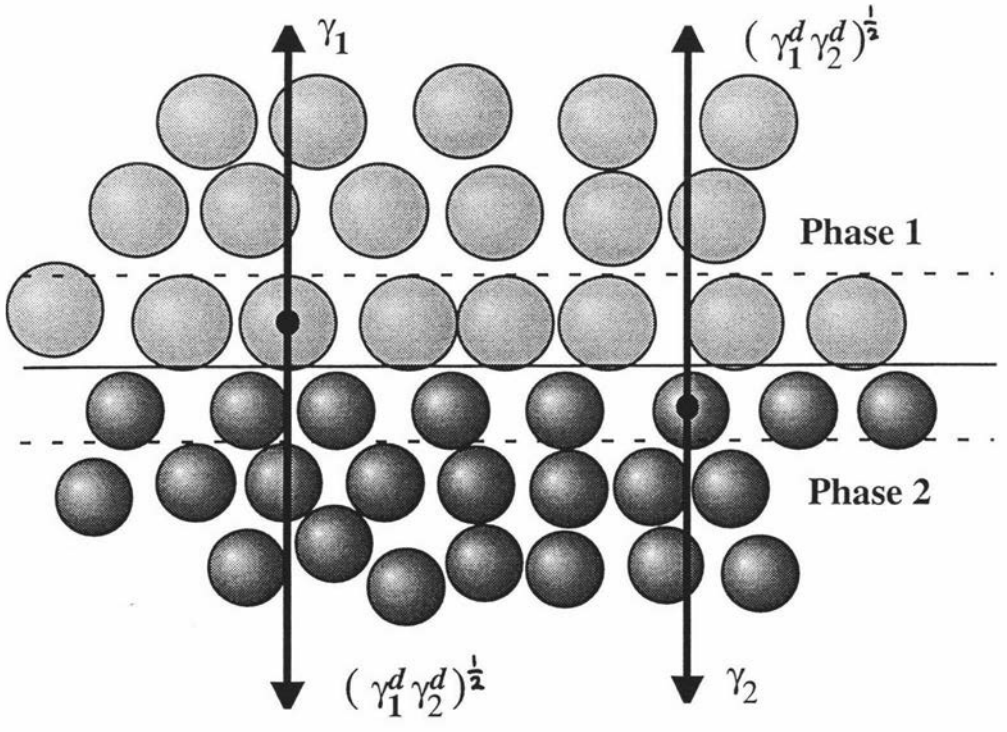

micellar surface (see Chapter 4). However, the situation becomes complex when the solvent consists of a binary mixture of miscible liquids. In this case there will be competition between, for example, water and ethylene glycol for sites at the solvent/fluorocarbon interface. Nagarajan[11] used an approach based on Prigogine theory to both estimate the surface composition at the EG/H_2O solvent/hydrocarbon interface and the interfacial tension. His approach used the Flory interaction parameter χ_{mix} which was derived from an unexplained computational method and successfully predicts an interfacial excess of EG over all EG compositions. However, the same theory predicts an interfacial tension that is *greater* than the sum of the molar products of the individual pure solvent/hydrocarbon interfacial tensions i.e the bulk solvent/hydrocarbon interfacial tension. It is difficult to reconcile a predicted surface excess of one component leading to an interfacial tension dominated by the other component, and using Nagarajan's approach to estimate the EG/H_2O solvent/fluorocarbon interfacial tension would not reproduce the experimentally-determined data to be presented below. Furthermore, values of χ_{mix} are unavailable for the other solvents of interest. Nagarajan also used χ_{mix} in his expression for the free energies of transfer from EG/water mixtures and, in view of the above arguments, the validity of that expression is also drawn into question. It will be shown in the next section that a theoretical method involving the Fowkes equation can closely reproduce experimental data for the interfacial tensions between several mixed solvents and a self-assembled fluorocarbon monolayer (SAM).

6.1 A Phenomenological Method for Calculating Interfacial Tension.

The competition between solvent components for sites at a solvent/fluorocarbon interface can be formalised as an "interaction potential" E dominated by, in the case of alkanes or perfluoroalkanes, wholly dispersive forces. Acting against this potential is the entropy favouring random dispersal of the binary solvent components. The approach used here combines an expression for E and the Fowkes equation. It is similar to that approach used to derive the Langmuir equation for adsorption at solid interfaces but with the difference in the areas occupied by water and cosolvent at the interface taken into account. Both approaches ignore water-cosolvent interactions and assume that the surface is ideal. In the case of a perfluorocarbon SAM, the surface has been shown to be highly uniform[12]. The idealised interface between fluorocarbon and solvent is depicted in Figure 6.1. Solvent molecules at the surface (denoted "σ") and in the bulk ("b") will possess chemical potentials according to

$$\mu_a^\sigma = \mu_a^{0,\sigma} + kT \ln x_a^\sigma$$
$$\mu_a^b = \mu_a^{0,b} + kT \ln x_a^b$$

and

$$\mu_w^\sigma = \mu_w^{0,\sigma} + kT \ln x_w^\sigma$$
$$\mu_w^b = \mu_w^{0,b} + kT \ln x_w^b .$$

where "a" and "w" denote cosolvent and water respectively. The condition of equilibrium requires μ^σ and μ^b to be equal, leading to the following expressions for the mole fractions of each solvent component at the surface

[6–2]

$$x_a^\sigma = x_a^b \exp(-E_a / kT)$$
$$x_w^\sigma = x_w^b \exp(-E_w / kT)$$

where $E = \mu^{0,b} - \mu^{0,\sigma}$ represents the "interaction potential" of each solvent. Equation [6–2] can be written in terms of the total mole fraction X of each solvent component since $X = x^\sigma + x^b$, thus

[6–3]

$$x_a^\sigma = X_a / \left[1 + \exp(-E_a / kT)\right]$$
$$x_w^\sigma = X_w / \left[1 + \exp(-E_w / kT)\right] .$$

Now the above equations [6–3] can be used to construct an expression for the effective interfacial tension γ_{eff} at the fluorocarbon-solution interface assuming that γ_{eff} may be expressed as

[6–4]

$$\gamma_{eff} = \theta \cdot \gamma_{fa} + (1-\theta) \cdot \gamma_{fw}$$

where θ is the fraction of the surface covered by cosolvent, and γ_{fa} and γ_{fw} are the fluorocarbon-cosolvent and fluorocarbon-water interfacial tensions respectively. θ can be written

[6–5]

$$\theta = \frac{x_a^\sigma \cdot A_a}{x_a^\sigma \cdot A_a + x_w^\sigma \cdot A_w} = \frac{A_a}{A_a + \frac{x_w^\sigma}{x_a^\sigma} \cdot A_w}$$

where x_a^σ and x_w^σ are the surface mole fractions of cosolvent and water respectively, and A_a and A_w are the effective cross-sectional areas of cosolvent and water molecules projected onto the surface, calculated from their molecular masses and densities assuming they are spherical (while they may not structurally approximate spheres, it is assumed that they present an effectively circular profile at the interface due to rapid reorientation).

A phenomenological expression for the effective interfacial tension has thus been derived in terms of known quantities. Values for the "interaction potential" E can

be calculated as the product of A / m^2 and the work of adhesion W / J m^{-2}. W was estimated using the expression[2] for the work of adhesion of one solvent component to the fluorocarbon surface in a medium of the other solvent component i.e.

[6–6] $$W_{fla/w} = \gamma_{fw} + \gamma_{aw} - \gamma_{fa}.$$

With the aforementioned assumption that water-cosolvent interactions can be ignored, equation [6–6] reduces to

[6–7] $$W_{fla/w} = \gamma_{fw} - \gamma_{fa}.$$

6.1.1 Numerical calculations of interfacial tension and comparison with experimental data.

The solvents of interest (chosen for reasons outlined in the Introduction) and their physical properties required for calculations using the above method are tabulated in Table 6.1. Surface tensions γ were obtained from Israelachvili[2] except for DMA[13]. Values for the dispersive components of the surface tension γ^d represent averages of data from Kwok[4] and Israelachvili[2]. Values for their interfacial tension of the pure solvents against a perfluorocarbon self-assembled monolayer (SAM) γ_{fa} were calculated from contact angle data obtained in collaboration with the Centre for Self Organising Molecular Systems (SOMS), The University, Leeds, UK (described below). W was calculated from equation [6–7], A was calculated from the solvents' molecular masses and densities[13], and the interaction potential E was calculated as $E = WA$. The perfluorocarbon surface tension γ_f was taken to be[14] 19 m Jm^{-2}. Using the above data, calculations for the effective interfacial tension γ_{eff} between perfluorocarbon and binary aqueous solvent mixtures were implemented in Microsoft Excel©[15] and

Figure 6.1 Idealised equilibrium between solvent molecules at the micellar surface (σ) and in the bulk (b). x and μ represent the mole fractions and chemical potentials in each environment.

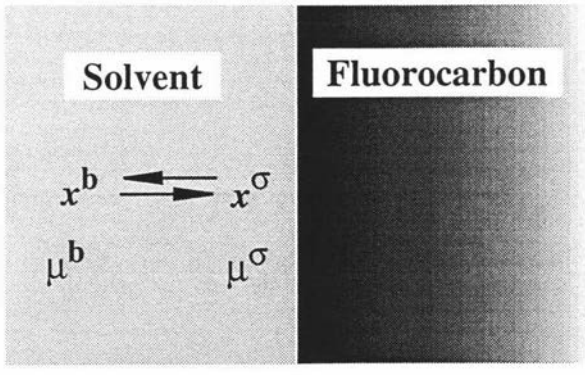

Table 6.1 Properties of solvents used in calculations (T = 295 K). Quantities and their source or derivation are explained in the text.

solvent	γ / mJ m^{-2}	γ^d / mJ m^{-2}	γ_{fa} / mJ m^{-2}	W / mJ m^{-2}	A / nm^2	E / kT
water	72.1	19	54.3	0.0	0.116	1.51
FA	58.0	28	33.6	22.2	0.197	1.08
EG	48.1	29	21.1	33.0	0.248	2.01
NMF	40.2	29	13.3	41.0	0.255	2.57
DMF	37.1	30	7.7	45.0	0.298	3.29
DMA	32.4	29	7.0	48.6	0.320	3.82

MathCAD™[16] as functions of the independent variable X, the total mole fraction of cosolvent in water. The accuracy of the estimated γ_{eff} values was tested by experimentally measuring the interfacial tensions of binary solvent mixtures against a fluorocarbon SAM. The SAM surface has been shown[12] to be a highly uniform monolayer consisting of $C_{10}F_{21}$- chains aligned normally to a gold-coated glass slide.

Contact angle measurements[12] against the SAM were carried out on all solvents in Table 6.1 except for NMF at cosolvent/water mole fractions of 0, 0.2, 0.5, 0.8 and 1. Surface tension γ_a measurements (see Chapter 2) were carried out at corresponding concentrations on solvent mixtures where literature data[17-19] was unavailable, and the fluorocarbon/solvent interfacial tension γ_{fa} calculated from Young's equation $\gamma_{fa} = \gamma_f - \gamma_a \cos\vartheta$ where ϑ is the measured contact angle. The close agreement between calculated values and those obtained experimentally is shown in Table 6.2 and Figure 6.2.

Table 6.2 Comparison of measured and calculated interfacial tensions of cosolvent-water mixtures against a perfluorocarbon SAM at cosolvent mole fractions X_a. Measured values have an error of ±0.5 mJ m^{-2}. Experimental NMF data was not available.

	Interfacial Tension γ_{fa} / mJ m^{-2}					
X_a	0.2		0.5		0.8	
	meas.	calc.	meas.	calc.	meas.	calc.
FA	48.6	48.2	41.9	41.4	36.6	36.4
EG	42.8	42.7	31.6	31.7	24.5	24.6
DMF	34.9	35.8	19.9	20.5	12.0	11.7
DMA	33.8	34.0	18.2	18.8	10.1	10.6

Figure 6.2 Interfacial tensions between a perfluorocarbon self-assembled monolayer (SAM) and binary aqueous solvent mixtures as a function of cosolvent mole fraction. Lines represent interfacial tensions calculated *via* equation [6-4] and points were determined experimentally. Experimental contact angle data for NMF was unavailable.

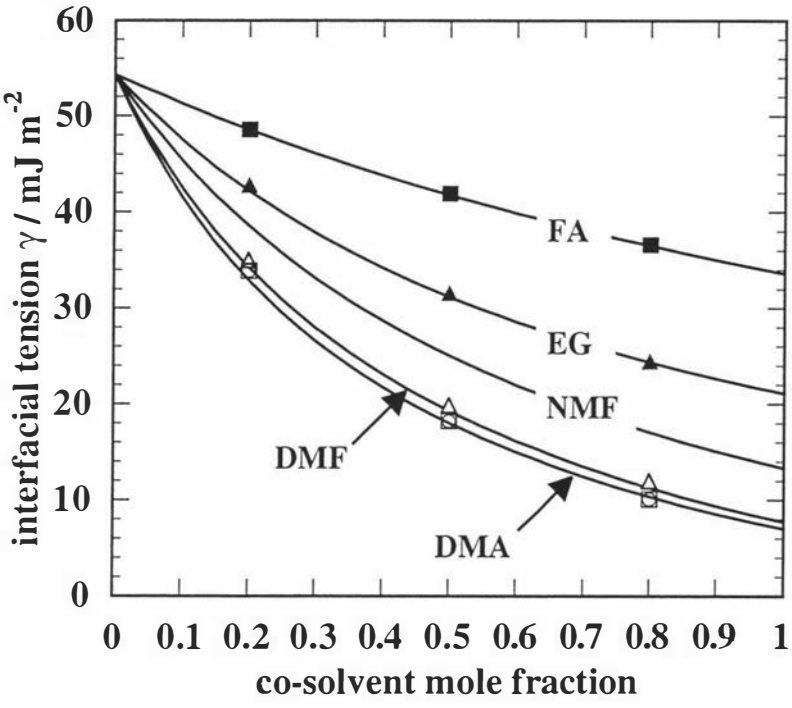

6.1.2 Discussion and application to the micellar interface.

The close agreement between theory and experiment evident in Figure 6.2 is pleasing considering the number of assumptions and simplifications invoked, and it would be interesting to apply the method to ternary solvent mixtures should data become available. However, some discussion is required about the use of a perfluorocarbon SAM as an approximation for the APFO/solvent micellar interface. It is reasonably certain that (a) a proportion of the cosolvents in solution are present at the micellar interface since this was shown to be the case in Chapter 5 for DMF-d_7 by ^{2}H NMR measurements on the very similar CsPFO/DMF-d_7/^2H_2O system, and (b) electrostatic repulsion and steric hindrance between surfactant headgroups will ensure that at least some solvophobic surface is exposed to the solvent.

In the case of the SAM, solvent molecules were assumed to be attracted to the interface *via* dispersive forces only. At the micellar interface, there will be an additional attraction *via* carboxylate ion-dipole interactions, the magnitude of which depends on the solvent dipole moments according to[21]

$$\hat{E}_{ion-dipole} = -\frac{e_q^2 m^2}{3(4\pi\varepsilon_0\varepsilon_r)^2 kTr^4} \quad \text{for } kT > \frac{e_q m}{4\pi\varepsilon_0\varepsilon_r r^2}.$$

The carat on $\hat{E}$ denotes a spatially averaged quantity, m is the dipole moment, and r is the distance from the point charge to the centre of the dipole. Other quantities have their usual meanings. The non-aqueous solvents of interest here all possess high dipole moments (see Table 6.3) which are, with the exception of ethylene glycol, of the same magnitude. Two consequences of this extra attraction are (a) that there may be an enhanced attraction for the interface in the case of the amides over ethylene glycol, and (b) that the spatial averaging of the ion-dipole effect may reduce the area occupied by the solvents at the interface i.e. the amides will spend a greater time oriented with the partially positive nitrogen atom closer to the interface. The situation becomes exceedingly complex with the consideration of ammonium ion-dipole interactions coupled with ammonium ion-carboxylate headgroup interactions.

Table 6.3 Dipole moments of solvent molecules[19].

	Water	FA	EG	NMF	DMF	DMA
m / Debye	1.84	3.68	2.28	3.86	3.90	3.79

Further interactions could be considered, such as ion-induced dipole interactions, which increase with the polarizability. Though the polarizabilities and differences in polarizability between these solvents will be small, they increase with the number of substituted methyl groups and could provide a further difference in affinity for the surface. Polarizability has been discussed in Chapter 3 with respect to the higher apparent affinity of tetraalkylammonium ions over ammonium ions for the micellar surface.

Another consideration is the assumption of the complete miscibility of water and cosolvents. There is the possibility that the least hydrophilic solvent i.e. DMA may become partially insoluble in water at low temperature and/or high concentrations, which would lead to a further attraction for the micellar interface.

A final consideration is to recognise that the concept of an interfacial tension, which is a bulk property, may not apply on a molecular scale in the case where there are insufficient cosolvent molecules present at the interface to collectively constitute a change in this bulk property.

In summary, it is recognised that the affinity of cosolvent molecules for the micellar interface will almost certainly not be solely a function of dispersive forces, as was assumed above for the solvent/SAM interface, but will consist of a very complex combination of dispersive, electrostatic, and ion-dipole forces between all species in solution i.e. ammonium ions, PFO^- ions, micelles, water, and cosolvent molecules, all

of which will vary with surfactant concentration, cosolvent concentration, and solution ionic strength. However, it appears from the results presented in previous Chapters that using the solvent/SAM interfacial tension to approximate the solvent/micelle interacial tension is valid to first order.

6.2 References.

1. Fowkes, F.M., *Industrial and Engineering Chemistry* **1964**, *56*, 40.
2. Israelachvili, J. *Intermolecular and Surface Forces*; Academic Press Ltd: London, 1991; 353.
3. Johnson, R. and R. Dettre, *Langmuir* **1989**, *5*, 293.
4. Kwok, D.Y., D. Li, and A.W. Neumann, *Colloids and Surfaces A* **1994**, *89*, 181.
5. Kwok, D., *et al.*, *Langmuir* **1995**, *11*, 2669.
6. Good, R.J. and E. Elbing, *Industrial and Engineering Chemistry* **1970**, *62*, 54.
7. Girifalco, L. and R. Good, *Journal of Physical Chemistry* **1957**, *61*, 904.
8. van Oss, C., R. Good, and M. Chaudhury, *Langmuir* **1988**, *4*, 884.
9. Nagarajan, R. and E. Ruckenstein, *Langmuir* **1991**, *7*, 2934.
10. Nagarajan, R. and C. Wang, *Journal of Colloid and Interface Science* **1996**, *178*, 471.
11. Nagarajan, R., *Journal of Colloid and Polymer Science* **1998**, *submitted for publication*,
12. Harding, R., *to be submitted,* in *Chemistry*. 1997, Leeds University: Leeds.
13. Weast, R.C. *Handbook of Chemistry and Physics*; The Chemical Rubber Co. Ohio: 1971;
14. Boden, N., *et al.*, *Mol. Cryst. Liq. Cryst.* **1987**, *152*, 37.
15. Microsoft, *Microsoft Excel*. 1985, Microsoft Corporation:
16. Mathsoft., *MathCAD*. 1989, Mathsoft, Inc: Cambridge, Mass.
17. Khossravi, D. and K. Connors, *Journal of Solution Chemistry* **1993**, *22*, 321.
18. Hoke, B. and J. Chen, *Journal of chemical engineering data* **1991**, *36*, 322.
19. Dean, J. *Lange's Handbook of Chemistry*; Editor Ed.; McGraw-Hill Book Co: 1985;
20. Thomsen, S., M.Sc. Thesis, Dept. of Chemistry, Massey University: New Zealand. **1994**
21. Evans, D. and H. Wennerstrom *The Colloidal Domain*;.; VCH.: NY, 1994; 515.

Conclusions

The characterisation of tetralkylsubstituted ammonium perfluorocarboxylate surfactants by rheological techniques has shown (a) that the alkyl-substitution on the ammonium ion promotes the formation of very long entangled rodlike micelles, and (b) the mean length of the rods goes through a maximum with increasing surfactant concentration. However, the technique cannot distinguish the transition from rods to disks that must occur in these systems. Further avenues for study are (a) to fully characterise these surfactants' isotropic phases *via* the determination of the temperature-dependence of the viscoelasticity and the use of complementary techniques such as light and x-ray scattering, which may delineate the rod-to-disk transition, and (b) the determination of the liquid crystal phase boundaries of TEAHFN.

The effect of changing solvent on the self-organisation of perfluorocarbon surfactants i.e. on their liquid crystal phase behaviour, has been shown to originate in the solvent's effect on surfactant self-assembly. A phenomenological statistical thermodynamic model, adapted for perfluorocarbon surfactant self-assembly, successfully predicted several features in accordance with experiment: (a) it quantitatively predicted critical micelle concentrations in H_2O that are in reasonable agreement with those determined experimentally, (b) it predicted aggregation to occur at higher surfactant concentrations in ethylene glycol than H_2O, and over a wider surfactant concentration range, and (c) it predicted that the effect of changing solvent shifts the micelle size distribution to lower aggregation numbers largely as a consequence of changes in the interfacial tension. However, the model should be refined by the determination of both long-chain *n*-perfluorocarbon and *n*-hydrocarbon solubilities in H_2O, D_2O and non-aqueous solvents. This would (a) clarify the opposite isotope effect on hydrocarbon and perfluorocarbon surfactant cmc's, and (b) allow more accurate quantitative predictions of surfactant self-assembly in non-aqueous solvents.

Appendix A: Polynomials from conductance measurements.

Table A1 Coefficients of the polynomials for the conductance in *E*/mV:
$G/S = aE^4 + bE^3 + cE^2 + dE + e$

(a) H_2O

w	a	b	c	d	e
0.001	-6.52E-07	2.985E-06	1.545E-06	1.525E-04	1.680E-04
0.003	-1.60E-06	7.031E-06	4.512E-06	4.096E-04	4.459E-04
0.005	-7.75E-06	4.748E-05	-6.664E-05	7.254E-04	7.243E-04
0.007	2.90E-08	-1.579E-05	9.891E-05	8.505E-04	1.055E-03
0.009	2.15E-06	-3.620E-05	1.702E-04	1.022E-03	1.333E-03
0.011	-1.17E-05	6.434E-05	-7.072E-06	1.330E-03	1.642E-03
0.013	-2.28E-05	1.453E-04	-7.722E-05	1.313E-03	1.925E-03
0.015	-1.60E-05	1.092E-04	1.932E-07	1.419E-03	2.046E-03
0.017	-9.97E-06	7.408E-05	9.690E-05	1.437E-03	2.157E-03
0.019	-8.92E-06	7.718E-05	9.272E-05	1.550E-03	2.254E-03
0.021	-3.59E-06	-1.961E-05	5.258E-04	1.167E-03	2.264E-03
0.023	5.84E-06	-4.126E-05	4.202E-04	1.514E-03	2.535E-03
0.025	-2.39E-06	3.545E-05	1.843E-04	1.817E-03	2.429E-03
0.030	2.54E-06	-1.207E-05	3.376E-04	2.268E-03	2.845E-03

(b) D_2O

w	a	b	c	d	e
0.003	-1.09E-06	5.46E-06	3.98E-06	4.10E-04	3.64E-04
0.006	6.85E-07	-1.50E-05	9.14E-05	6.74E-04	7.27E-04
0.008	-3.39E-06	9.89E-06	4.87E-05	9.62E-04	9.78E-04
0.010	-3.77E-06	1.58E-05	4.18E-05	1.19E-03	1.18E-03
0.012	-2.96E-05	2.09E-04	-3.40E-04	1.52E-03	1.41E-03
0.014	-1.65E-05	1.17E-04	-5.03E-05	1.26E-03	1.70E-03
0.016	-7.44E-06	5.92E-05	9.58E-05	1.23E-03	1.81E-03
0.018	-2.25E-06	2.55E-05	1.85E-04	1.28E-03	1.88E-03
0.020	-2.50E-06	3.32E-05	1.51E-04	1.50E-03	1.97E-03
0.022	-1.65E-06	2.29E-05	2.10E-04	1.55E-03	2.06E-03
0.024	-7.75E-06	6.60E-05	1.12E-04	1.80E-03	2.08E-03
0.026	-6.56E-06	5.40E-05	2.08E-04	1.61E-03	2.46E-03
0.028	1.30E-06	1.58E-06	2.86E-04	1.93E-03	2.25E-03
0.030	-4.37E-06	3.63E-05	2.26E-04	2.12E-03	2.32E-03
0.035	-1.63E-06	8.68E-06	3.36E-04	2.37E-03	2.49E-03
0.040	5.64E-05	-6.78E-04	3.43E-03	-3.50E-03	7.38E-03

Table A1 (continued)

(**c**) Ethylene glycol

w	b	c	d	e
0.010	-5.09E-07	4.46E-05	8.34E-05	6.13E-05
0.020	-9.93E-07	8.27E-05	1.57E-04	1.16E-04
0.025	-7.33E-07	9.97E-05	1.93E-04	1.44E-04
0.030	-6.80E-07	1.16E-04	2.29E-04	1.67E-04
0.035	-1.33E-06	1.34E-04	2.61E-04	1.93E-04
0.040	-6.72E-06	1.67E-04	2.84E-04	2.19E-04
0.050	-7.11E-06	2.04E-04	3.40E-04	2.60E-04
0.060	-4.00E-06	2.21E-04	4.10E-04	2.99E-04
0.070	-6.37E-06	2.61E-04	4.56E-04	3.42E-04
0.080	-2.24E-06	2.82E-04	5.14E-04	3.79E-04
0.090	-6.51E-06	3.21E-04	5.62E-04	4.22E-04
0.100	-6.90E-06	3.58E-04	6.11E-04	4.68E-04
0.110	-3.51E-06	3.75E-04	6.77E-04	5.08E-04
0.120	-1.42E-05	4.38E-04	6.83E-04	5.39E-04

Appendix B: Data extracted from conductance measurements.

Table B1 Critical micelle concentrations (cmc) and free ion fractions α from linear fits to points above (denoted "2") and below ("1") the cmc. w is weight fraction and x is mole fraction.
(a) H_2O

T/°C	gradient S_1	y_1-intercept	gradient S_2	y_2-intercept	$a = S_2/S_1$	cmc w	cmc 10^3x
6	1.74E-01	2.26E-05	6.65E-02	1.36E-03	0.383	0.01088	0.5099
7	1.79E-01	2.55E-05	6.81E-02	1.40E-03	0.380	0.01081	0.5069
8	1.84E-01	2.81E-05	7.31E-02	1.37E-03	0.398	0.01074	0.5034
9	1.88E-01	3.06E-05	7.13E-02	1.47E-03	0.378	0.01068	0.5005
10	1.93E-01	3.29E-05	7.29E-02	1.50E-03	0.378	0.01061	0.4975
11	1.97E-01	3.53E-05	7.47E-02	1.53E-03	0.378	0.01055	0.4945
12	2.02E-01	3.77E-05	7.82E-02	1.53E-03	0.386	0.01048	0.4910
14	2.12E-01	4.22E-05	8.27E-02	1.58E-03	0.390	0.01034	0.4846
16	2.22E-01	4.66E-05	8.75E-02	1.63E-03	0.394	0.01022	0.4787
18	2.32E-01	5.08E-05	9.27E-02	1.67E-03	0.399	0.01009	0.4727
20	2.43E-01	5.48E-05	9.81E-02	1.72E-03	0.404	0.00997	0.4671
22	2.55E-01	5.16E-05	1.04E-01	1.76E-03	0.406	0.00987	0.4624
24	2.78E-01	5.50E-05	1.15E-01	1.85E-03	0.416	0.00978	0.4582
25	2.72E-01	5.42E-05	1.12E-01	1.83E-03	0.413	0.00974	0.4560
26	2.78E-01	5.50E-05	1.15E-01	1.85E-03	0.416	0.00970	0.4543
28	2.89E-01	5.66E-05	1.22E-01	1.90E-03	0.421	0.00963	0.4509
30	3.01E-01	5.82E-05	1.28E-01	1.95E-03	0.425	0.00957	0.4483
32	3.13E-01	5.97E-05	1.34E-01	2.00E-03	0.430	0.00953	0.4462
34	3.25E-01	6.13E-05	1.41E-01	2.06E-03	0.434	0.00950	0.4449
36	3.37E-01	6.30E-05	1.48E-01	2.12E-03	0.438	0.00948	0.4441
38	3.48E-01	6.47E-05	1.54E-01	2.17E-03	0.442	0.00948	0.4441
40	3.61E-01	6.65E-05	1.61E-01	2.24E-03	0.446	0.00950	0.4449
44	3.85E-01	7.06E-05	1.75E-01	2.37E-03	0.454	0.00957	0.4479
48	4.11E-01	7.55E-05	1.90E-01	2.52E-03	0.462	0.00969	0.4539
52	4.36E-01	8.11E-05	2.05E-01	2.68E-03	0.469	0.00986	0.4620
56	4.61E-01	8.72E-05	2.20E-01	2.85E-03	0.477	0.01008	0.4722
60	4.87E-01	9.62E-05	2.35E-01	3.06E-03	0.484	0.01033	0.4842
64	5.13E-01	9.65E-05	2.46E-01	3.36E-03	0.480	0.01061	0.4975
68	5.42E-01	9.60E-05	2.65E-01	3.56E-03	0.489	0.01084	0.5082
72	5.69E-01	9.49E-05	2.85E-01	3.73E-03	0.501	0.01125	0.5206
74	5.82E-01	9.40E-05	2.95E-01	3.81E-03	0.507	0.01140	0.5274
76	5.96E-01	9.30E-05	3.06E-01	3.90E-03	0.514	0.01171	0.5347
80	6.23E-01	9.03E-05	3.30E-01	4.05E-03	0.529	0.01251	0.5493
86	6.63E-01	8.29E-05	3.69E-01	4.21E-03	0.557	0.01295	0.5874
88	6.78E-01	7.45E-05	3.84E-01	4.24E-03	0.567	0.01316	0.5982
90	6.91E-01	6.67E-05	3.99E-01	4.26E-03	0.577	0.01350	0.6085
92	7.02E-01	6.01E-05	4.13E-01	4.26E-03	0.587	0.01451	0.6184
96	7.19E-01	5.07E-05	4.36E-01	4.24E-03	0.606	0.01478	0.6347

Table B1 (continued)

(b) D_2O

T/°C	gradient S_1	y_1-intercept	gradient S_2	y_2-intercept	$a = S_2/S_1$	cmc w	cmc 10^3x
6	1.41E-01	4.86E-05	5.26E-02	1.25E-03	0.373	0.01356	0.6372
7	1.46E-01	5.15E-05	5.58E-02	1.25E-03	0.382	0.01332	0.6258
8	1.50E-01	5.54E-05	5.86E-02	1.26E-03	0.390	0.01312	0.6164
9	1.55E-01	6.04E-05	6.16E-02	1.26E-03	0.398	0.01293	0.6075
10	1.58E-01	6.59E-05	6.43E-02	1.27E-03	0.406	0.01278	0.6001
11	1.62E-01	7.25E-05	6.71E-02	1.27E-03	0.414	0.01262	0.5928
12	1.66E-01	8.02E-05	7.01E-02	1.28E-03	0.422	0.01248	0.5858
14	1.74E-01	9.79E-05	7.24E-02	1.37E-03	0.416	0.01248	0.5765
16	1.91E-01	5.14E-05	7.78E-02	1.40E-03	0.408	0.01193	0.5599
18	2.00E-01	5.63E-05	8.38E-02	1.42E-03	0.418	0.01168	0.5482
20	2.10E-01	6.20E-05	8.98E-02	1.44E-03	0.427	0.01146	0.5378
22	2.20E-01	6.83E-05	9.60E-02	1.47E-03	0.436	0.01127	0.5285
24	2.30E-01	7.47E-05	1.02E-01	1.49E-03	0.444	0.01110	0.5206
25	2.35E-01	7.83E-05	1.05E-01	1.51E-03	0.448	0.01102	0.5168
26	2.40E-01	8.21E-05	1.08E-01	1.52E-03	0.452	0.01094	0.5131
28	2.50E-01	8.99E-05	1.15E-01	1.55E-03	0.460	0.01081	0.5067
30	2.60E-01	9.75E-05	1.21E-01	1.58E-03	0.467	0.01070	0.5014
32	2.71E-01	1.06E-04	1.28E-01	1.62E-03	0.474	0.01060	0.4968
34	2.81E-01	1.14E-04	1.35E-01	1.65E-03	0.480	0.01052	0.4932
36	2.92E-01	1.22E-04	1.42E-01	1.69E-03	0.487	0.01046	0.4904
38	3.02E-01	1.29E-04	1.49E-01	1.73E-03	0.492	0.01042	0.4885
40	3.13E-01	1.37E-04	1.56E-01	1.77E-03	0.498	0.01040	0.4873
44	3.35E-01	1.52E-04	1.70E-01	1.87E-03	0.508	0.01040	0.4873
48	3.58E-01	1.66E-04	1.85E-01	1.98E-03	0.517	0.01046	0.4903
52	3.82E-01	1.79E-04	2.01E-01	2.10E-03	0.525	0.01059	0.4962
56	4.05E-01	1.90E-04	2.16E-01	2.24E-03	0.532	0.01078	0.5053
60	4.31E-01	1.99E-04	2.32E-01	2.38E-03	0.540	0.01099	0.5154
64	4.55E-01	2.07E-04	2.49E-01	2.52E-03	0.547	0.01123	0.5269
68	4.81E-01	2.15E-04	2.66E-01	2.71E-03	0.553	0.01161	0.5446
70	4.93E-01	2.18E-04	2.74E-01	2.80E-03	0.556	0.01178	0.5528
72	5.06E-01	2.21E-04	2.83E-01	2.89E-03	0.560	0.01197	0.5617
74	5.18E-01	2.25E-04	2.92E-01	2.98E-03	0.563	0.01216	0.5710
76	5.31E-01	2.28E-04	3.01E-01	3.07E-03	0.567	0.01238	0.5815
80	5.49E-01	2.87E-04	3.20E-01	3.27E-03	0.583	0.01301	0.6113
84	5.76E-01	2.78E-04	3.40E-01	3.46E-03	0.590	0.01346	0.6328
86	5.89E-01	2.81E-04	3.47E-01	3.65E-03	0.589	0.01392	0.6547
88	6.00E-01	2.89E-04	3.56E-01	3.77E-03	0.593	0.01428	0.6716
90	6.10E-01	3.04E-04	3.65E-01	3.89E-03	0.598	0.01465	0.6896
92	6.18E-01	3.23E-04	3.73E-01	4.00E-03	0.604	0.01504	0.7080
96	6.34E-01	3.14E-04	3.81E-01	4.31E-03	0.601	0.01578	0.7435

Table B1 (continued)

(c) Ethylene glycol.

T/°C	gradient S_1	y_1-intercept	gradient S_2	y_2-intercept	$a = S_2/S_1$	cmc w	cmc 10^3x
2	4.62E-03	5.38E-05	5.66E-03	1.44E-05	0.03774	0.8155	5.633
3	4.84E-03	5.81E-05	5.96E-03	1.52E-05	0.03837	0.8122	5.666
4	5.06E-03	6.21E-05	6.24E-03	1.59E-05	0.03888	0.8096	5.695
5	5.28E-03	6.61E-05	6.53E-03	1.66E-05	0.03932	0.8076	5.721
6	5.53E-03	7.03E-05	6.86E-03	1.75E-05	0.03974	0.8060	5.748
7	5.82E-03	7.52E-05	7.23E-03	1.85E-05	0.04017	0.8045	5.776
8	6.10E-03	7.97E-05	7.59E-03	1.94E-05	0.04051	0.8036	5.801
9	6.39E-03	8.44E-05	7.96E-03	2.04E-05	0.04083	0.8031	5.825
10	6.67E-03	8.86E-05	8.31E-03	2.13E-05	0.04109	0.8029	5.846
11	6.98E-03	9.32E-05	8.69E-03	2.24E-05	0.04134	0.8029	5.867
12	7.30E-03	9.79E-05	9.09E-03	2.35E-05	0.04157	0.8031	5.886
14	7.99E-03	1.08E-04	9.94E-03	2.58E-05	0.04198	0.8041	5.923
16	8.71E-03	1.17E-04	1.08E-02	2.83E-05	0.04232	0.8056	5.954
18	9.50E-03	1.27E-04	1.18E-02	3.10E-05	0.04261	0.8076	5.983
20	1.03E-02	1.38E-04	1.28E-02	3.38E-05	0.04284	0.8098	6.006
22	1.12E-02	1.48E-04	1.38E-02	3.67E-05	0.04304	0.8122	6.027
24	1.21E-02	1.58E-04	1.48E-02	3.97E-05	0.04321	0.8145	6.043
26	1.30E-02	1.70E-04	1.60E-02	4.31E-05	0.04335	0.8171	6.058
28	1.41E-02	1.81E-04	1.72E-02	4.66E-05	0.04347	0.8196	6.068
30	1.51E-02	1.93E-04	1.84E-02	5.01E-05	0.04356	0.8220	6.076
32	1.62E-02	2.05E-04	1.97E-02	5.39E-05	0.04363	0.8244	6.081
34	1.74E-02	2.17E-04	2.10E-02	5.78E-05	0.04369	0.8267	6.083
36	1.86E-02	2.30E-04	2.24E-02	6.19E-05	0.04373	0.8289	6.082
38	1.98E-02	2.42E-04	2.38E-02	6.60E-05	0.04375	0.8309	6.079
40	2.11E-02	2.55E-04	2.53E-02	7.03E-05	0.04376	0.8329	6.073
42	2.24E-02	2.69E-04	2.69E-02	7.51E-05	0.04376	0.8348	6.065
44	2.38E-02	2.83E-04	2.84E-02	7.95E-05	0.04375	0.8364	6.056
46	2.52E-02	2.97E-04	3.00E-02	8.43E-05	0.04373	0.8380	6.044
48	2.67E-02	3.13E-04	3.18E-02	8.95E-05	0.04370	0.8396	6.028
50	2.83E-02	3.29E-04	3.37E-02	9.49E-05	0.04366	0.8410	6.011
52	2.99E-02	3.44E-04	3.55E-02	1.00E-04	0.04361	0.8422	5.993
54	3.15E-02	3.60E-04	3.73E-02	1.06E-04	0.04356	0.8433	5.972
56	3.31E-02	3.77E-04	3.92E-02	1.11E-04	0.04350	0.8443	5.951